Kinematic Simulation of Turbulent Flow and Particle Motions

Jimmy Chi Hung Fung

A dissertation submitted
to the University of Cambridge for the
degree of Doctor of Philosophy

Peterhouse

January 1990

Summary of Research

Kinematic simulation of turbulent flow and particle motions

J.C.H. Fung

This thesis describes a new method for simulating high Reynolds number turbulence which requires much less computing power. This involved both theoretical work – to understand and model the important processes – and computational work, to implement the model efficiently.

There are many different techniques for modelling particle dispersion in turbulent flow (e.g. K-theory and Random Flight) but they make assumptions about the fluid-particle interaction and require empirical coefficients. Theoretical work on the motion of bubbles and particles in idealised flows has shown that the instantaneous structure of the velocity field is important in determining particle trajectories, and that particle motion cannot currently be modelled reliably in terms of time- or ensemble-averaged fluid velocities. Therefore, the solution of many practical problems, requires the simulation of the instantaneous structure of a turbulent velocity field. This can now be provided with the very large computers and large amounts of computer time; even then, only low Reynolds number turbulence can be simulated.

In the method developed here, the velocity field of homogeneous isotropic turbulence is simulated by a large number of random Fourier modes varying in space and time. They are chosen so that the flow field has certain properties, namely (i) it satisfies continuity, (ii) the two point Eulerian spatial spectra have known form (e.g. the Kolmogorov inertial subrange), (iii) the time dependence is modelled by dividing the turbulence into large- and small-scales eddies, and by assuming that the large eddies advect the small eddies which also decorrelate as they are advected, (iv) the large- and small-scale Fourier modes are each statistically independent and Gaussian. Computations of the streamlines in a sequence of realisations of the flow show that they have a similar structure to that obtained from direct numerical simulations. New results for the statistics of high Reynolds number turbulent flows are obtained, for the velocity and pressure fields.

Particle statistics are obtained by computing the trajectories of many particles and taking the ensemble average. Particle dispersion has been computed for a range of particle parameters and the results agree well with experimental measurements such as those of Snyder and Lumley; this enables us to compute empirical coefficients (e.g. Lagrangian timescales) for use in simpler models such as Random Flight, and for modelling other processes such as combustion and mixing.

Rapid Distortion Theory is used to investigate the effects of high shear rate on the structure of homogeneous turbulence in chapter 4. The results show that an important effect of the shear acting on initially isotropic turbulence is the selective amplification of structures having large length scale in the mean flow direction.

Declaration

The research described in this thesis was carried out between October 1986 and October 1989 at the University of Cambridge in the Department of Applied Mathematics and Theoretical Physics. Unless stated otherwise in the text, the research described in the thesis represents my own original work and includes nothing which is the outcome of work done in collaboration. No part of the dissertation has been submitted for a degree, diploma or other qualification at any other university.

Acknowledgements

I would like to gratefully acknowledge the support of the following:

To my family

Contents

CHAPTER ONE

General Introduction

1.1 Introduction

The main subject of this thesis is the development of a new method for approximate simulation of turbulent flows, that cannot be simulated at present and to apply this method to new studies of particles in turbulent flows, especially high Reynolds number turbulent flows.

In many fields of turbulence research, it is as necessary to be able to compute or model actual flow fields as they evolve as it is to know the statistics of the turbulence (e.g. spectra, correlations etc). This is because many processes involving turbulence are not well enough understood to be quantified in terms of the statistics. For example the effect of turbulence on chemical reactions (e.g. Broadwell and Breidenthal 1982) or on particle trajectories (e.g. Maxey 1987, Brown & Hutchinson 1979) or on bubble concentration (e.g. Hunt *et al.* 1988a) can best be understood and modelled in terms of actual flow structures. One reason for this is that certain reactions or bubble concentrations are largely located in vortical regions of the flow, whilst particles appear to move in regions between vortices. These highly non-uniform processes and distributions cannot be modelled satisfactorily in terms of the statistics of the velocity field. Instead it is necessary to compute mixing of reacting species or the motion of bubbles and particles as they are transported in the actual flow.

When such studies have progressed further it is likely that reliable models will emerge relating the complex process to the statistics of the turbulence. For example several research groups are exploring the use of stochastic models for the fluctuating velocity at the site of a particle moving randomly through turbulence flows (e.g. random flight models). In studies of combustion and mixing, models are being developed based on the large scale deterministic flow structure within the turbulence (e.g. Broadwell and Breidenthal 1982, Peters and Williams 1988) There are also smaller scale processes, such as the coagulation of small particles or the break up of bubbles and transmission of waves through turbulence, where the small scale velocity field must be simulated.

We have emphasised these practical reasons for being able to compute and model actual

flow fields. But the study of the fundamental dynamics and kinematics of turbulence also requires simulations of actual flow fields. Certain important concepts can be explored even with simulations that are not quite accurate, such as the relations between Lagrangian and Eulerian statistics, the reasons for the skewness of the derivatives (is it entirely dynamical, i.e. vortex stretching, or is there also a kinematical explanation?)

There are also many aspects that can only be modelled directly with very accurate computation of all the small scale intermittent processes of turbulence; but such computational models do not yet exist.

There have been two different approaches for developing simulations of turbulent flow fields:

1.1.1 *Dynamical simulations*

Two methods have been developed for computational simulations of the full space and time velocity field of turbulence, namely, Direct Numerical simulations (DNS) and Large Eddy simulations (LES).

The basic principle of DNS is to solve the Navier-Stokes equation numerically (e.g. pseudospectral methods) to determine instantaneous velocities in a turbulent flow. With this approach no approximation of the governing equations is needed. But in order to ensure sufficient spatial and temporal resolution requirements adequately, and numerical stability, it is necessary to restrict the turbulent Reynolds number (based on the microscale) of the simulation to about 150 (Rogallo and Moin 1984; Meneguzzi and Pouquet 1989). In DNS the number of spatial grid points is determined by two constraints: first, the size of the computational domain must be large enough to accommodate the largest turbulence scales, and second, the grid spacing must be sufficiently fine to resolve the dissipation length scale, which is on the order of the Kolmogorov scale. (One can usually tell when not enough small-scales have been captured by pile-up of energy at the high wavenumber end of the spectrum.) It is well known that the range of scales widen rapidly as the Reynolds numbers increases. Also, the ratio of these two scales provides an estimate for the total number, N_g, of mesh points. At moderate Reynolds number $Re = 3300$ (based on the centerline velocity and channel half-width) of turbulent channel flow, roughly 4×10^6 grid points (Kim, Moin and Moser 1987). Such a computation requires the full capabilities of presently available supercomputers.

There have been a number of direct simulations of channel flows, boundary layer and homogeneous shear flows at these low Reynolds numbers. From an accurate DNS, all the statistics of the flow field can be computed and can be used to test the predictions of different, approximate turbulence 'models' (which are usually restricted to these moments) and leads to suggestions about how to improve them. Unfortunately as mentioned above, all DNS to date

fall into the range of 'low-Reynold-number turbulence', which does not matter so much for low order statistics in *shear* flow, but this means that DNS cannot be used with confidence to test those respects of models which are based on the assumption that the turbulence has a high Reynolds numbers (e.g. non shear flow or two-point statistics of shear flow).

This restriction on Reynolds number is avoided by decomposing the flow field variable into a large-scale field (the filtered field) and a residual field (the subgrid field), but at the cost of only approximately satisfy the governing equation. This is the method of Large Eddy Simulation (Lesieur 1987). The basic philosophy of LES is to compute explicitly the solution of the smoothed dynamical equations for the large scales, while assuming that the small scales act on the large scales like a stress. This stress is modelled as a local eddy viscosity acting on the large scales, which is of order $u_g \ell_g$ (where ℓ_g is the scale of the computational grid used and $u_g^2 = \int_{\ell_g^{-1}}^{\infty} E(k) \, dk$, $E(k)$ is the energy spectrum). The small scales in the inertial range are not explicitly modelled, but they are assumed to have an universal structure, that is, their statistics and their effect upon the large scales can be specified by small number of parameters as discussed above, whereas the structure of large eddies differ greatly from flow to flow (which is why universal models are elusive). In LES the resolution requirement are determined directly by the range of scales contributing to the desired statistics. For a fully developed turbulent channel flow (Moin and Kim 1982) for a Reynolds number of 13,800, based on the centerline velocity and channel half-width, the calculation were carried out with 516,096 grid points.

Both simulations with a higher spatial resolution are technically possible, but they are extremely time consuming, due to the numerous inputs-outputs between the central memory and the disk units. Alternative methods based on the parallel computations using several processors simultaneously, are only in the preliminary stage of their development. Both these methods require access to the largest computer systems or to databases of the computed velocity fields. Neither method reproduces velocity fields with all the details of the small scales required for studying turbulent flow at high Reynolds number.

The detailed structure in space and time of the small-scales are particularly important because they play a dominant role in problems of heat and mass transfer by turbulence (Batchelor and Townsend 1956). This further suggests why a simulation of the fine scale turbulence is important.

1.1.2 *Kinematic simulations*

Because of the computational expense and the limitations to their range of representation, other methods have been proposed to simulate certain aspects of turbulent flow fields. In some methods random flow fields are generated whose statistics agree with values obtained

from measurements or direct simulations, but the flow fields do not necessarily satisfy the dynamical equations. In other methods certain key *elements* in the flow fields are modelled such as vortices or stagnation regions etc, and then the strength and distribution of these key kinematical structure have to be estimated from experiment or other numerical simulations (e.g. Broadwell and Breidenthal 1982).

The former of these two methods is the approach developed in this study. We extend the methods of Kraichnan (1970) and Drummond *et al.* (1984), who studied turbulent diffusion using statistically independent random Fourier modes, but not a full spectrum. No attempt was made by these authors to model the details of the inertial range or the variation of the time dependent structure of turbulence on length scales. However, some important *concepts* emerged from these studies about the Lagrangian time scale and the role of molecular processes in turbulent diffusion.

The essential objective here is to simulate a random velocity field that has some *known* statistics (e.g. Eulerian spectra) and then to use this velocity field to predict some *new* results, which can be compared with experiments. If the simulation is at all useful it should also lead to some new *concepts*. The construction and use of Kinematic Simulations (KS) ought to be based on the results obtained from dynamical simulations and from experiments. One can also regard this simulation as a convenient way of providing an accessible repository or reference for most of our present knowledge of two point/two time Eulerian/Lagrangian statistics. It may enable investigators using turbulent flow fields to extract widely different statistics that are needed for different applications.

An important result of fluid motion is the transport both of the fluid itself and also of quantities embedded or suspended in it, such as dust, chemical contaminants, slit, or sand. It is well known that the average transport of such quantities is greatly enhanced if the fluid motion is turbulent (e.g. Hinze 1975). This is a result of the convection of these quantities by the irregular motion of the fluid. We term such convection by continua in irregular motion, dispersion, to distinguish it from its molecular counterpart, diffusion.

1.2 Particle dispersion

A primary objective in developing the new methods of KS has been to compute the motions of bubbles, droplets or particles in turbulent flow. There are many fundamental unanwsered questions about these motions, which we can investigate using this new method, and relate to methods of approximate modelling. Examples of environmental and industrial processes involve particles and bubbles are:

(i) Power industry

  – Particle and droplet dispersion in coal- and oil-fire burners

  – Formation and dispersion of bubbles in cooling circuits of nuclear power plants

  – Deposition and re-entrainment of particles in cooling circuits of nuclear power plants

(ii) Petroleum and Chemical industries

  – Two- and Three-phase pipe flows

  – Accidental release of volatile and hazardous liquids

  – Mixing and residence times in reactor vessels

(iii) Particle transport in the atmosphere

  – Soil erosion

  – Dispersion of dusts and sprays

  – Erosion by air-borne particles and droplets

(iv) Marine and alluvial sediment transport

  – Scour round coastal and sea bed structure

  – Siltation of dredged channels, irrigation channels and reservoirs

  – Transport of sediment and pollutants in the coastal zone

A better understanding of particle motions should lead to better models *and* to better designs for products and environmental solutions.

Although the concentration of particles in a fluid is a scalar, its behaviour is quite different from other scalars (temperature, moisture, gas species etc.) because the inertia and buoyancy forces acting on the particles are different to these acting on equivalent volume of fluid and therefore the particles do not follow the trajectories of the fluid particles. The behaviour of scalars in turbulent flow has been extensively studied with both experiments and theoretical models; the behaviour of particles has been studied less (Csanady 1963; Snyder and Lumley 1971; Pismen and Nir 1979; Wells and Stock 1983), mainly because of the experimental difficulties in measuring their movements. A number of general features have been derived from these experiments and computational simulations; but also some major questions have arisen which are still unanswered.

In general, the motion of a particle in a turbulent flow is governed by the combined effects of its inertia, the buoyancy forces acting on it and the drag caused by the difference of the particle velocity and that of the turbulent flow field. The first two effects cause the velocity difference and therefore the difference between the particle's trajectory and that of the fluid elements in the flow – the 'crossing-trajectories effect' (Yudine 1959). The movement of light particles is similar to that of fluid particle in the turbulent flow field, though any given particle always diverges from the path of any *given* fluid particles, but the movements of heavy particles are quite different from those of fluid particles and are determined by random forces acting on

them as they fall or rise through the flow (i.e. by the crossing-trajectories effect).

Thus, an essential part of any discussion of the particle velocity $\mathbf{u}_p$ is the nature of the turbulent velocity field *at* the location of the particle $\mathbf{u}_f(\mathbf{x}_p, t) = \mathbf{u}_{fp}(t)$, and the difference between the particle velocity $\mathbf{u}_p(t)$ and $\mathbf{u}_{fp}(t)$.

The influence of a buoyancy force on the trajectory-crossing effect is quite clear; it decreases the particle dispersion, because a fluid point will remain in the same eddy throughout the lifetime of the eddy, whilst a particle will fall from one eddy to another, so that the correlation between particle and fluid velocities decreases. However, the effect of the particle inertia on the trajectory-crossing effect is not so clear; because of its inertia, even a light particle cannot completely follow the highly curved fluid trajectories in a turbulent eddy, so for a light particle the auto-correlation and the timescale of $\mathbf{u}_{fp}(t)$ and of $\mathbf{u}_p$ may be *greater* than that for a fluid particle! But for a heavy particle the effect of inertia is to cause the particle r.m.s. velocity $\mathbf{u}_p'$ to be less than that of the fluid $\mathbf{u}_f'$ (Snyder and Lumley 1971) and so it cuts through many eddies and causes the correlation time for $\mathbf{u}_{fp}$ to be less than for $\mathbf{u}_f$ but the correlation time for $\mathbf{u}_p$ to be greater than for $\mathbf{u}_f$. Therefore, the effects of inertia on particle dispersion are quite complex. Since the particle diffusivity $\varkappa_p$ is the product of the particle mean-square fluctuating velocity $\mathbf{u}_p'^2$ and its integral timescale T_{Lp}, the above argument suggests that for *light* particles, $\varkappa_p$ does not differ much between solid and fluid particles, but for heavy particles, the decrease of $\mathbf{u}_p'^2$ and the increase of T_{Lp}, lead to a decrease in $\varkappa_p$. But this need careful evaluation. Buoyancy forces and inertial forces can act in combination, which also needs consideration.

1.2.1 *Particle motion*

To understand particle motion it is instructive to consider the variations of the fluid velocity seen by the particle and to divide them into spatial and temporal variations.

(a) *Spatial variation*

Consider a dense particle travelling towards an eddy (Fig. 1.1). A particle with low inertia will be swept part of the way around the eddy and then leave the eddy, to be swept part of the way around a neighbouring eddy. Although the particle trajectory is quite curved, the fluid velocity sampled by the particle $(\mathbf{u}(\mathbf{x}_p, t))$ – which is the important velocity in modelling the motion of the particle – does not change very much. The time scale for this velocity can then be greater than that for a fluid element retained by the eddy.

A particle with high inertia will cut through the eddy, and the fluid velocity which it samples will change very rapidly – more rapidly than that seen by a fluid element.

The most interesting case is that if the particle inertia lies within a certain range, the

Fig. 1.1 Show the difference of fluid velocity auto-correlation functions along the particle trajectories with different inertia parameters τ_p.

particle may penetrate into an eddy and become trapped there, spiralling out slowly. Thomas *et al.* (1983) have shown that 'trapping' certainly occurs for bubbles and light particles, but Kraichnan (1970) observed that it only occurs for dense particles in a static, two-dimensional flow field. Chung and Troutt (1988) observed some trapping of dense particles in their Discrete Vortex Method simulation of an axisymmetric jet, and Perkins and Hunt (1986) demonstrated that isolated vortices can trap dense particles in certain situations. The point is whether turbulent flow corresponds to these idealised flows and whether particles can be trapped by 'eddies'.

The introduction of a fall velocity also tends to increase the rate at which the fluid velocity 'seen' by the particle changes, either because the particle 'falls' from one eddy to the next, or because even if a particle is trapped it 'sees' a rapidly changing velocity field. This will be discussed in more detail in §3.8.

(b) *Temporal variation*

As the particle moves it experiences a velocity field which changes for two reasons. First (as described above), the fluid velocity *sampled* by the particle changes. Secondly, the fluid velocity field is itself changing in time. All that the particle perceives, however, is a velocity field which changes with time, although, as we have illustrated above, the rate at which the flow field appears to change depends on both the inertia and the fall velocity of the particle.

The response of the particle to this changing velocity field depends only on its inertia. Particles with high inertia are insensitive to the frequency velocity fluctuations and so remain correlated for longer periods. We will show that the velocity of the particle will only be affected with frequency $\omega > \tau_p^{-1}$ (or time scale $\lesssim \tau_p$) in §3.3.3.

1.2.2 *Current modelling techniques*

Physical models:

These are often used to model particle transport in complex flows, e.g. sediment transport in large-scale environmental flows or bubbles in two phase flows. Even for these kind of modelling many assumptions are necessary to model the transport rates correctly, for this reason some flows are modelled at full scale. Physical models are also expensive, and their results cannot easily be applied to other situations. But increasingly they are used in conjunction with mathematical models and then such an extension is possible.

Computational models:

Until now, predicting the behaviour of particles in a turbulent flow has been approached mainly in two ways, by:

– Eulerian methods in which properties of the particle motion are evaluated in space and time in a certain geometrical frame of reference. These methods of modelling turbulent dispersion use a set of moment equations which are derived by Reynolds-averaging of the Eulerian conservation equation for the mean and fluctuating concentration C. 'Closure' of the latter set of equations involves approximate relations among certain joint moments of the velocity and concentration fields. Such approximations depend on the concentration field itself and so are not uniformly valid for all concentration fields. They are usually 'fixed' for particular situations, such as two phase pipe flows.

– Lagrangian methods in which the motion of particles are computed along their trajectories, (if the turbulent flow is determined by a Eulerian calculation, we can then speak of a Eulerian-Lagrangian method). Calculation of concentration moments can be carried out for an arbitrary source distribution. The assumptions made in Lagrangian modelling thus do not depend on the concentration field of the source distribution and in this sense, are uniformly valid (provided the concentrations are weak and there are no interaction between the particles).

Different methods are now considered in detail:

I. Eulerian methods:

For many flows, a number of simpler models has been used. These require empirical coefficients which have to be obtained from experiments.

(a) *Turbulent diffusivities (K-theories)*

Turbulent diffusivities, say $\varkappa_{ij}(t)$ (assuming they are a function of time t alone for homogeneous turbulence), are usually defined in the following manner. Consider a scalar field $\theta(\mathbf{x}, t)$ advected by a velocity field $\mathbf{u}(\mathbf{x}, t)$ without changing as it moves (i.e. no molecular diffusion). It satisfies the following conservation equation:

$$\frac{\partial}{\partial t}\theta + (\mathbf{u}.\nabla)\theta = 0, \tag{1.2.1}$$

In this case the usual molecular diffusivity term can be omitted.

Decomposing $\theta(\mathbf{x}, t)$ and $\mathbf{u}(\mathbf{x}, t)$ into mean and fluctuating parts,

$$\theta(\mathbf{x}, t) = \langle \theta(\mathbf{x}, t) \rangle + \theta'(\mathbf{x}, t), \tag{1.2.2a}$$

$$\mathbf{u}(\mathbf{x}, t) = \langle \mathbf{u}(\mathbf{x}, t) \rangle + \mathbf{u}'(\mathbf{x}, t) \tag{1.2.2b}$$

and substituting (1.2.2) into (1.2.1) and averaging gives (with $\nabla.\mathbf{u}' = 0$):

$$\left\{ \frac{\partial}{\partial t} + \langle \mathbf{u}(\mathbf{x}, t) \rangle .\nabla \right\} \langle \theta(\mathbf{x}, t) \rangle = -\nabla. \left\{ \langle \mathbf{u}'(\mathbf{x}, t)\theta'(\mathbf{x}, t) \rangle \right\}. \tag{1.2.3}$$

In attempting to close this equation, it is sometimes assumed that the flux is proportional to the gradient of concentration, by analogy with molecular diffusion. i.e.

$$-\langle u_i'(\mathbf{x},t)\theta'(\mathbf{x},t)\rangle = \varkappa_{ij}\frac{\partial}{\partial x_j}\langle\theta(\mathbf{x},t)\rangle,\tag{1.2.4}$$

where $\varkappa_{ij}$ is defined in term of properties of the turbulence (e.g. Csanady 1963, Monin & Yaglom 1975). The order of magnitude of $\varkappa_{ij}$ is $u_o^2 T_L$ or $u_o L$. For this assumption to be valid it is at least necessary that the characteristic length scale of $\langle\theta(\mathbf{x},t)\rangle$, say L_θ, is *much greater* than the characteristic length scale of the transporting mechanism, which in this case can be taken to be an Eulerian integral length scale, say L (Corrsin 1973). It is also necessary that the p.d.f. of turbulence is close to Gaussian (Hunt 1982) and that $T_L \sim L/u_o$. (1.2.4) breaks down close to "point" sources but is asymptotically valid for large travel time.

Substituting (1.2.4) into (1.2.3) gives, for a statistically homogeneous flow,

$$\left\{\frac{\partial}{\partial t} + \langle\mathbf{u}(\mathbf{x},t)\rangle.\nabla\right\}\langle\theta(\mathbf{x},t)\rangle = \varkappa_{ij}(t)\frac{\partial^2}{\partial x_i\partial x_j}\langle\theta(\mathbf{x},t)\rangle.\tag{1.2.5}$$

This is the so-called diffusion equation for $\langle\theta(\mathbf{x},t)\rangle$ and when the turbulent intensity is large enough (e.g. $u_o L \gg \varkappa$) the equation can applied even in the presence of molecular diffusion, except near boundaries (Hunt 1985). In most problems of interest, $L = \mathcal{O}(L_\theta)$ since the diffusing mechanism is of the same scale as the property being diffused, the K-theories are fundamentally incorrect. However the errors are often small enough that the K-theories continue to be of practical value, provided the value of the diffusivity $\varkappa$ is known. But since $\varkappa$ takes on different values for different flows and different distribution of concentrations, it is not possible to estimate $\varkappa$ without further computational or experimental studies.

Since solid particles do not follow the flow, it is an even more tenuous hypothesis to assume that the diffusion of solid particle in a turbulent flow is described by a diffusion equation. Also the value of $\varkappa$ depends on the properties of the turbulence, the particle and distribution of particles.

(b) *Higher-order Eulerian closure model*

We will only describe the second-order modelling technique, the so-called one point closures. In this technique, equations are carried for the means, variances and fluxes, and these equations are closed by representing the third order quantities and certain other terms such as the pressure correlations, in terms of the second order quantities.

By using the Reynolds decomposition, the equations for the first and second moments can be written without approximation as:

$$\partial_t\langle C\rangle + \partial_j\langle C\rangle(U_j + V_j) + \partial_j\langle cu_j\rangle = 0,\tag{1.2.6a}$$

$$\partial_t \langle c^2 \rangle + 2\partial_i \langle C \rangle \langle cu_i \rangle + \partial_i \langle c^2 \rangle U_i + \partial_i \langle c^2 u_i \rangle + \partial_i \langle c^2 \rangle V_i = -2 \langle \epsilon_c \rangle, \qquad (1.2.6b)$$

$$\partial_t \langle cu_i \rangle + 2\partial_j \langle C \rangle \langle u_i u_j \rangle + \partial_j \langle cu_i \rangle U_j + \partial_j U_i \langle cu_j \rangle$$
$$+ \partial_j \langle cu_i u_j \rangle + \langle u_i \partial_j c \rangle V_j = - \langle c\partial_i p \rangle / \rho, \qquad (1.2.6c)$$

where ∂_t is a derivative with respective to time, and ∂_i is a derivative with respect to x_i; $\langle \epsilon_c \rangle$ is the dissipation rate of $\langle c^2 \rangle$; and C is the instantaneous value of the particle concentration, while $c = C - \langle C \rangle$ (Shih and Lumley 1986).

The (exact) equation for the third moments, can be interpreted as representing the tendency of turbulence (in the energy containing range) tending to relax to an isotropic Gaussian state in the absence of disturbing conditions such as inhomogeneity, buoyancy, chemical reactions and so forth.

Shih and Lumley (1986) approximated the third moments (e.g. $\langle cu_i u_j \rangle$) in terms of second moments and predicted C. Their results for C compare favourably with the experimental data of Wells and Stock (1983). It is not clear that the second order model outlined by Shih and Lumley is always satisfactory for the dispersion of particles. (The same models cannot predict $\langle \phi^2 \rangle$ for scalar, so it is unlikely that $\langle c^2 \rangle$ for particles can be modelled!) The basic assumption of the second order modelling is the field of a particular variable can be completely described by the scales of the energy-containing range, or in other words, that the spectrum is simple (Spalding 1971). A superposition of two scalar fields having different time scales and no longer has a simple spectrum, and hence cannot reasonably be described by equations having a single time scale (Pope 1983). While it is possible to construct multiple time scale models, they become extremely complex.

II. Lagrangian methods:

In the Lagrangian approach, diffusion of scalars or particles are related to the Lagrangian statistics of the turbulence, which are assumed to be known (by computation or experiment). They are physically more transparent than gradient transport or higher-order Eulerian closure models and simpler to compute, especially for different particle sizes or distributions. They also possess the computational advantages of being potentially more efficient than Eulerian methods generally (since calculations involve only those portions of the fluid which are marked and therefore of interest). In several methods in current practice (Gosman *et al.* 1981), Lagrangian methods are used to compute diffusion coefficients of particles $\varkappa_{ij}$ which are then used in Eulerian models for C (such as (1.2.6a)).

(a) *Brown and Hutchinson Model*

In this one-dimensional model (Brown and Hutchinson 1974), the fluid velocity fluctuations u_f, which particles pass through, are described by a simple auto-correlation function with a time constant which is independent of the particle size. The turbulent flow field is described by a sequence of eddies all of which have the same characteristic speed, U_e, the same characteristic length, ℓ_e, and the same characteristic decay time, t_e, but whose direction is random, characterized by a sign S_1, which can be either positive or negative with equal probability. The interaction time δt_i between the particle and ith eddy depends on the particle velocity v_i at the beginning of the ith step and the particle displacement s_i during the ith interaction (i.e. whether s_i is less or greater than ℓ_e), so δt_i is governing by the equation of motion (Hutchinson 1974), in any case, the maximum possible value δt_i is t_e. The trajectories of the particles are constructed in the following (Fig. 1.2): at the start of each time step Δt, say after certain no. of time steps $n\Delta t$ interacting with ith eddy. The value $n\Delta t$ is compared with δt_i. If $n\Delta t \geqslant \delta t_i$, a new eddy (U_e) id generated; if not, (U_e) retains the same value during time interval Δt. The equation of motion for the particle is solved for each particle-eddy interaction and their effects of many interactions are summing on a computer. After 20,000 particles, the mean square displacement of the particle can then be obtained. This model does not represent the range of characteristic scales for the flow dynamics as in real turbulence. This model (and its later refinements by Gosman 1981) is used for computation of the mean particle or droplet concentrations of sprays in chemical and automobile engineering, using (1.2.6a).
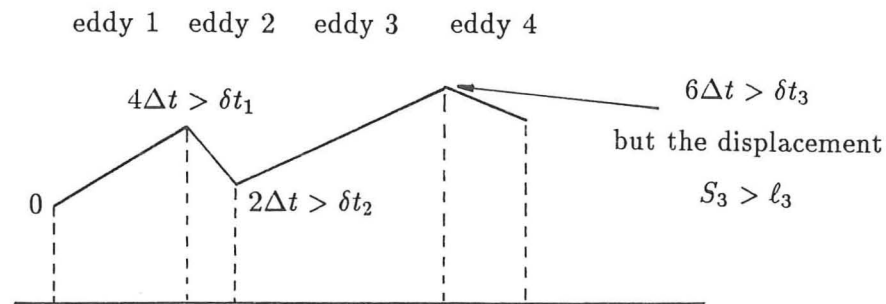
Fig. 1.2 Procedure for constructing the trajectory of a particle

(b) *Gouesbet et al. model*

In this three-dimensional model (Gouesbet, Desjonquéres and Berlemont 1987), at each step of time, the fluctuating velocity u_{f_i} is obtained from a random generation process complying with two physical conditions: (a) the r.m.s velocity $\langle u_{f_i} \rangle$ is known and u_{f_i} is assumed to be Gaussian; (b) using a two-parameter (T_L and the loop parameter m, linked to the occurrence and to the importance of the negative loops, in the function) Frenkiel family of Lagrangian
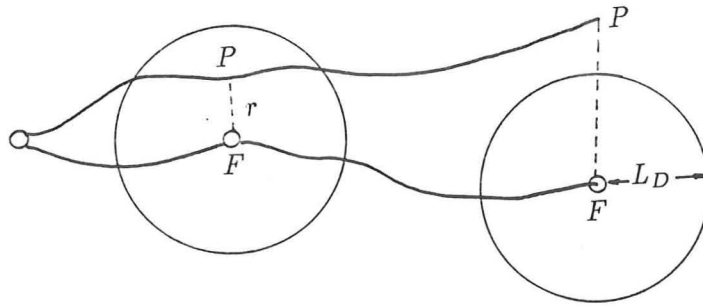
Fig. 1.3 Correlation length for the simulation.

velocity auto-correlation function for u_{f_i}.

To integrate the equation of motion for the particle and build the particle trajectory, one need the instantaneous fluid velocity $\mathbf{u}_{fp}$ at the particle position. In the simulation, Gouesbet *et al.* follow from the starting point and at the initial time, a particle and a fluid particle. The fluid particle trajectory is constructed according to the method explained in the previous paragraph. At each time step Δt, the fluid velocity, at point P of the particle position, $\mathbf{u}_{fp}$ is computed from the knowledge of the fluid velocity at the fluid particle position F, using Eulerian spatial correlations $\langle u_{f_i}(P)u_{f_j}(F)\rangle$.

The particle P will, sooner or later, leave a correlation domain, assumed to be a sphere of radius L_D (for isotropic turbulence, L_D is taken equal to $(L_{11} + L_{22})/2$), attach to the fluid particle F (Fig. 1.3). When the distance r between P and F becomes greater than the correlation length L_D, the fluid particle F is no longer followed and a new fluid particle is considered, at the particle position. The whole process produces a Lagrangian simulation of the particle trajectories.

This approach has been used to predict particle dispersion and the results compared well with the experiments by Snyder and Lumley (1971) and Wells and Stock (1983). The limitation of this methods is the difficulty of predicting precisely the various scales (e.g. T_L, L_D) involved in the formulation.

(c) *Random flight model*

Another more sophisticated (and flexible) method for simulating the motion of particles or bubbles in unsteady random velocity fields is the 'random flight models' (RFM) in which the fluid velocity seen by the particle is represented by a stochastic process. Thence the particle motion is computed and the trajectories of many particles give the mean concentration distribution. Because the particles are assumed to move independently, the results are applicable only to ensemble- or time-averaged diffusion and do not apply to the diffusion of a puff. The velocity seen by a particle is modelled by the Langevin equation, i.e. if $u_{fp}(t)$ is the velocity of
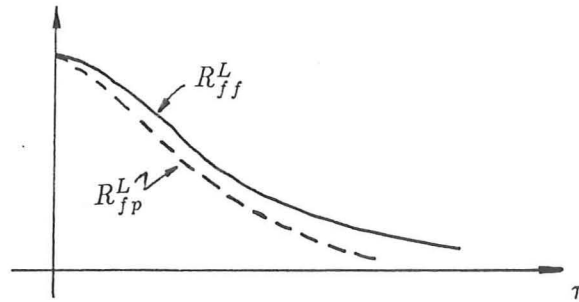
Fig. 1.4 The form of the auto-correlation functions of R_{fp}^L and R_{ff}^L

the fluid element at the particle, then:

$$du_{fp}(t) = -\frac{u_{fp}(t)}{T_L^*}dt + \sigma_{u_{fp}}\left(\frac{2}{T_L^*}\right)^{1/2}dU_t, \qquad (1.2.7)$$

where dU_t is a Gaussian, white-noise stochastic process (which represents the rapid random acceleration, which is uncorrelated from one timestep to the next) with mean zero and variance dt, also with initial condition that $u_{fp}(0)$ is a Gaussian random variable with mean zero and variance $\sigma_{u_{fp}}^2$. T_L^* is the time scale over which the velocity of the fluid along the particle trajectory is correlated while it undergoes the random acceleration. It is easily shown (Thomson 1984) that if T_l^*, $\sigma_{u_{fp}}$ are constants, $u_{fp}(t)$ is also Gaussian with mean zero and variance $\sigma_{u_{fp}}^2$ and that the auto-correlation is $R^L(\tau) = \exp(-\tau/T_L^*)$. Equation (1.2.7) allows the velocity u_{fp} to have a finite memory. When $t \gg T_L^*$, this memory does not have a significant effect and then the velocity u_{fp} may be thought of as a sequence of uncorrelated jumps.

If the particle is very light, $u_{fp} = u_f$ and then T_L^* is equal to the time scale of the fluid particles. It has been found in several flows that for diffusion of scalars, the random flight models gives a better description of dispersion for times less that about T_L than models with a diffusion coefficient $\varkappa$. Also for $t \gg T_L$ they are able to include more properties of the turbulence than the usual K-theory formulation (especially near the source, since the diffusion equation overestimates the dispersion near the source (Hunt 1985)). Random flight models can be computed with simple numerical methods (first order differential equations). Statistically stable solutions, however, are obtained only when the trajectories of thousands of particle are evaluated. A major drawback of this technique is that there is no theory which specifies T_L or T_L^* and the Lagrangian statistics of dU_t in terms of the (Eulerian) statistics of turbulent velocities measured at a number of fixed (or moving) points.

Hunt and Nalpanis (1985) used the RFM to model solid particle dispersion problems and assume that the velocity correlation of the velocity seen by the particle has the same form as $R^L(\tau)$ but with a timescale T_L^* that differ from T_L (Fig. 1.4). Because of the inertia of the

particle and 'trajectory-crossing' effect, T_L^* is reduced by a factor (i.e. the time over which velocities remain correlated is reduced) which will be reviewed in greater detail later. Based on this model for u_{fp}, the computations for u_p and the mean square displacement of the particle $\mathbf{x}_p$ were compared with the experimental data of Snyder and Lumley (1971).

Although these methods are useful and are relatively cheap in computing time, the basis of such approaches are not well understood. For example the stochastic model masks the presence of quasi-ordered structures, which may be present in turbulent flow. Furthermore, the systematic interaction of particles with such quasi-ordered structures or eddies may have a role in the suspension process, especially in cases where the terminal velocity of the particle is of the same order as the fluctuating fluid velocities.

(d) *Random walk model*

Rather than modelling the fluid velocity seen by the particles as a random process, a simple method is to model the *particle velocity u_p* as a stochastic process. It requires less computation than the Random Flight method, but the mean and fluctuating particle velocities and the integral time scales must be estimated directly. It has been used to model droplet and particle dispersion in the atmosphere, for example by Walklate (1987).

The main weaknesses of these models are:

– empirical coefficients which depend on both the particles and the flow, can vary through the flow and are difficult to estimate a *priori*.

– an assumption that the velocity field is described by simple statistics which neglect the influence of the structure of the flow.

– only first and second order moment quantities can be computed, whilst we often need extreme values, such as peak concentrations

– Lagrangian quantities such as particle residence times cannot be calculated.

– they cannot be used to investigate the fundamental mechanisms in particle-fluid interaction.

To investigate some of the fundamental mechanisms in particle dispersion we need a technique for simulating a turbulent velocity field. A full simulation is not practical because it requires a large amount of computing time and is limited to low Reynolds number turbulence and to simple boundary conditions. However there are simpler techniques which can reproduce the important features of a turbulent velocity field such as Discrete Vortex method.

(e) *Discrete vortex method*

In the early stages of free shear flows, large scale eddies or coherent structure form in which their vorticity is in the spanwise direction. Consequently, the large scale features of these flows

can be represented by a flow model in which only *one* component of vorticity. The vorticity is discretised into point sources which are released into the flow at each time step, and are then advected with the local fluid velocity. Empirical adjustments are needed to incorporate the effects of dissipation and to ensure that the solution remains stable, but the method reproduces many of the phenomena such as coalescence, roll-up and pairing, which characterise these types of flow. It has been used successfully to simulate the flow field and hence the particle trajectories for the cases of bubble entrainment in shear layer (Sene 1984), particle dispersion in an axisymmetric jet (Chung & Troutt 1988) and particle entrainment into a plane jet (Perkins & Hunt 1988a).

These models (a–e) have had some success in comparison with experimental data. In spite of these successes, the correct way to formulate such models has not been investigated in detail and a number of theoretical problems have recently been identified in connection with existing models. (In particular, Durbin's (1980a) model is only consistent with incompressibility if the trajectories are calculated forwards in time from the source to the receptor.)

The improvement of these models requires a better understanding of the basic physical processes which takes place and therefore, computations must be devoted to certain particular phenomena which have to be considered as being only a part of the real process.

The method described here can be consider as an intermediate way between very sophisticated and expensive numerical integration of the Navier-Stokes equation techniques and simple Stochastic models obtain by assuming some specific constants. Fig. 1.5 shown the diagram of overall research scheme.

1.2.3 *Analysis*

Taylor (1921) developed the first statistical theory of turbulent dispersion for relating the statistics of particle displacements to the statistics of the velocity field. The displacement of an individual diffusing particle is related to its velocity by

$$x(t) = \int_0^t u(t') \, dt', \tag{1.2.8}$$

where we have taken the x-components. From (1.2.8) the rate of change of $x^2(t)$ may be written, in a given realisation:

$$\frac{d}{dt}x^2(t) = 2x\frac{dx}{dt} = 2\int_0^t u(t)u(t') \, dt'. \tag{1.2.9}$$

If we now take ensemble averages on both sides and assume the stationary Lagrangian velocity
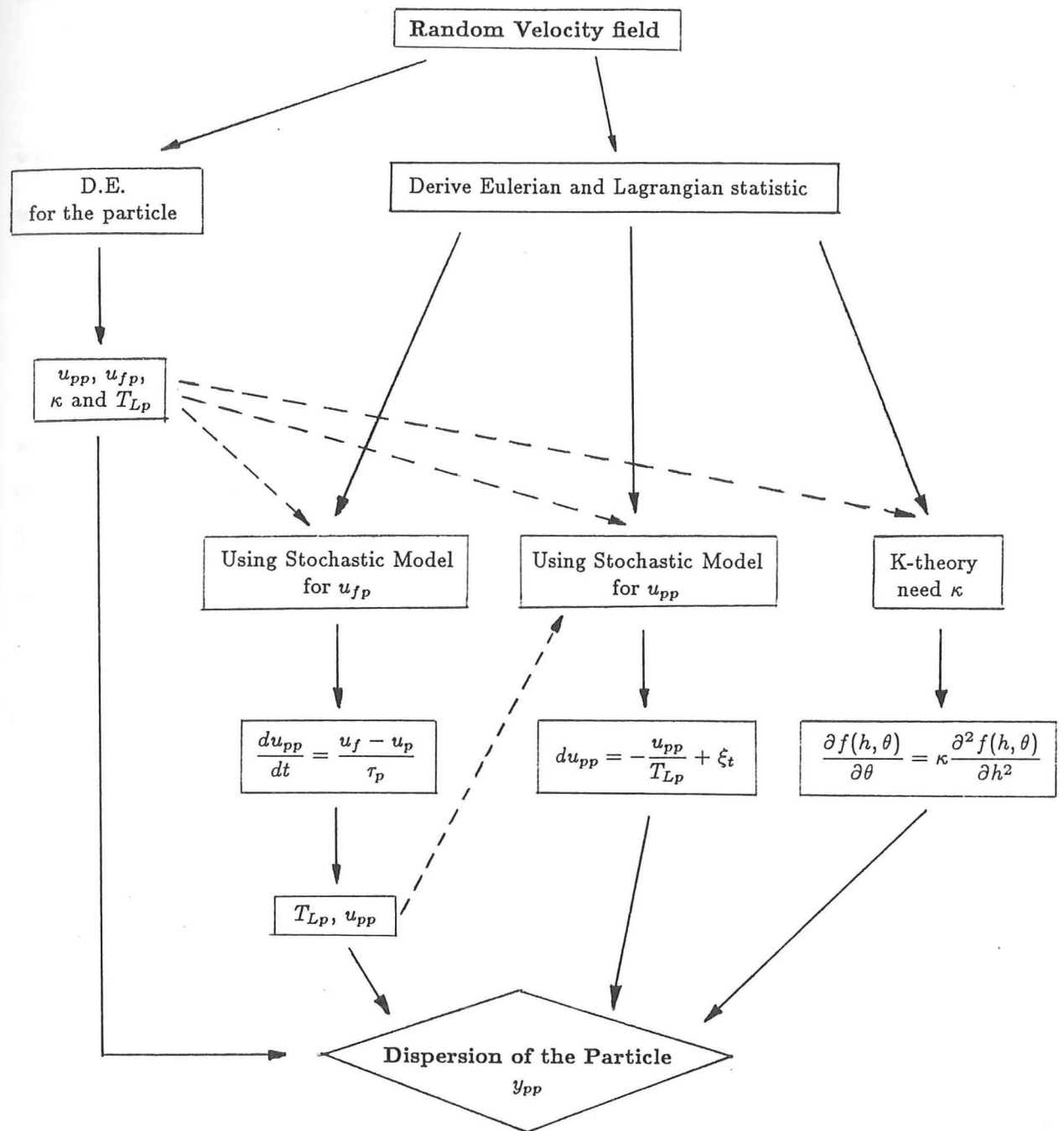
$f(h, \theta)dh$ — the probability of finding particle in the small element dh at position h and time θ.
u_{pp} — velocity of the particle along particle trajectory.
u_{fp} — velocity of the fluid along particle trajectory.
τ_p — inverse of inertia parameter.
T_{Lp} — Lagrangian time scale of the particle.
κ — diffusion coefficient.

Fig. 1.5

field is with zero mean, then

$$\frac{d}{dt}\left\langle x^2(t) \right\rangle = 2 \left\langle u^2 \right\rangle \int_0^t R_{ff}(t')\, dt', \tag{1.2.10}$$

where $R_{ff}(t') = \dfrac{\langle u(t)u(t+t')\rangle}{\langle u^2(t)\rangle}$ is the Lagrangian velocity auto-correlation and for stationary $u(t)$ is an even function of τ. On a further time-integration we find

$$\left\langle x^2(t)\right\rangle = 2\left\langle u^2 \right\rangle \int_0^t \int_0^{t'} R_{ff}(\tau)\, d\tau dt'$$

$$= 2\left\langle u^2 \right\rangle \int_0^t (t-\tau) R_{ff}(\tau)\, d\tau, \tag{1.2.11}$$

where the second form follows on partial integration. Therefore the moments of the displacement of a fluid particle are related kinematically to the Lagrangian velocity-correlation functions. The following limiting expressions are obtained from equation (1.2.11):

(i) When the time t is so small that $R_{ff}(\tau)$ approximates unity, equation (1.2.11) becomes

$$\left\langle x^2(t)\right\rangle = \left\langle u^2 \right\rangle t^2, \qquad \text{for} \qquad t \ll T_L, \tag{1.2.12a}$$

(ii) for large time t such that $\int_0^{t\to\infty} R_{ff}(\tau)\, d\tau = T_L \neq 0$, the Lagrangian velocity integral time scale, then

$$\left\langle x^2(t)\right\rangle = 2\left\langle u^2 \right\rangle T_L t, \qquad \text{for} \qquad t \gg T_L, \tag{1.2.12b}$$

so that $\langle x^2 \rangle$ increases at a uniform rate. By considering the probability distribution function of concentration C, this result is equivalent to the Eulerian approach, i.e. $\langle x^2 \rangle = \int x^2 C\, dx / C\, dx = 2\varkappa t$. Thus $\varkappa = 2\left\langle u^2 \right\rangle T_L$. (Note that only if $R(\tau) = e^{-\tau/T_L}$ is T_L defined in (1.2.10), same as in RFM.)

Thus the *Eulerian* dispersion variable $\varkappa$ can only be defined in terms of Lagrangian property of the turbulence. There is no rigorous theoretical method for predicting the dispersion rate $\varkappa$ or the form of the distribution from Eulerian quantities. Unfortunately, Lagrangian statistics are extremely difficult to obtain experimentally because they require measurements following the random motion of fluid particle. Nevertheless, some useful data have been obtained by Snyder and Lumley (1971) and Shlien and Corrsin (1974) in isotropic flows. In these experiments measurements are made from the spreading of the contaminant downstream from the source and hence assuming molecular diffusion can be neglected. Thus, the Lagrangian velocity correlation function is estimated; but not very accurately because it is difficult to follow the trajectories of the contaminants and so obtain their velocities at different points in time and to obtain the auto-correlation functions from the statistics from those $\langle \mathbf{x} \rangle$ involving such questionable techniques

as double differentiation of experimental curves (i.e. $\frac{d}{dt}\langle x^2\rangle = 2\langle u^2\rangle \int_0^t R_{11}(t')\,dt'$). Though the actual integral scale itself is well defined. More recently, Sato and Yamamoto (1987) have measured Lagrangian velocity auto-correlation in grid turbulence, by tracking small tracer particles optically and Yeung and Pope (1989) have computed higher-order Lagrangian statistics (velocity gradient and acceleration auto-correlations) using DNS in Taylor-scale Reynolds numbers in the range $38 - 93$. Taylor's analysis has proved a useful mean of analysing other flows. It has been extended to diffusion in three dimensional homogeneous, 'steady', non-isotropic turbulence (Batchelor 1949), to homogeneous, self-similarly decaying flows (Townsend 1954); and to shear flows and to inhomogeneous flows (reviewed by Hunt 1985).

All these results remain valid for the displacement of heavy particle $\mathbf{x}_p$ (Batchelor 1949) but the Lagrangian statistics of the velocity of the particles $\mathbf{u}_p$ are even less well understood. The motion of a particle in a turbulent fluid depends upon the characteristics of the particle and of the turbulent flow. Small particles show a fluctuating motion resulting from turbulent fluid motion. Generally speaking, a particle responds to turbulent fluctuations with a scale larger than the particle diameter. A particle which is much larger than the scale of turbulence shows relatively little velocity fluctuation. The effect of turbulence is then to modify the flow field around the particle, so that the drag may be affected. However, there are two basic mechanisms for the discrepancy between the diffusivities of fluid elements and foreign particles: a trend to increasing particle diffusivity due to inertial effects, characterised by the particle relaxation/response time, by which 'sluggish' particles do not follow completely the high frequency fluctuation of the turbulent medium. The response time of a particle is defined as $\tau_p = 2\rho_p a_p^2/9\mu$ where ρ_p is the particle density, a_p is the particle radius and μ is the fluid viscosity. This quantity represents the time required for a particle released from rest in a uniform flow, to reach 63% of the flow velocity (provided Stokes' drag law is applicable). It is simply a measure of the aerodynamic responsiveness of a particle. The ratio of the two time scales, τ_p/τ_f, also called the Stokes number, St, is used to measure the dimensionless response time of the particle motion to changes in the velocity of the surrounding fluid. It is plausible to assume that for $\mathrm{St} \gg 1$, the particles will not respond to the large eddies significantly and will exhibit little dispersion. For $\mathrm{St} \ll 1$, the particle will follow closely the streamlines in the flow and should disperse at the same rate. For Stokes numbers ranging between these two extremes, particles may be capture by the vortex structures but eventually they may be flung out of the structure, as seen by Yule (1980).

A counter-acting trend, usually stronger, the "crossing trajectories" effect (Yudine 1959), to decreasing diffusivity due to the particle falling out from the eddy where it was at an earlier

instant and therefore will lose its velocity correlation more rapidly than a fluid particle which changes its turbulent velocity only owing to "eddy-decay". Csanady (1963) in his analysis of the turbulent diffusion of heavy particle in the atmosphere which included the crossing-trajectories effect and ignored the particle inertia, suggested that the correlation will evidently be a function of W_g and τ, the time lag. Thus

$$g_{33}(\tau) = \langle u_3(t)u_3(t+\tau)\rangle / u'^2 = f(u'\tau/L, \; W_g\tau/L) \tag{1.2.13}$$

and $f(u'\tau/L, 0)$ corresponds to the Lagrangian case and $f(0, W_g\tau/L)$ to the Eulerian case in which the particle falls like a stone. For a large free falling speeds particle, the eddy-decay during $t = \tau$ may be neglected compared to the spatial change of correlations, so that the Lagrangian correlation at two points separated by the distance $W_g\tau$ where W_g is a finite free fall velocity, could be obtained from the fluid Eulerian space-time velocity auto-correlation in a frame of reference moving with the fluid mean velocity. Comparing these results with those for fluid point dispersion, he arrived at the following equations involving ratios of the longitudinal (33) and lateral (11) coefficients respectively

$$\frac{\varkappa_{p33}(\tau)}{\varkappa_{f33}(\tau)} = \left[1 + \frac{\beta^2 W_g^2}{u'^2}\right]^{-1/2}, \tag{1.2.14a}$$

$$\frac{\varkappa_{p11}(\tau)}{\varkappa_{f11}(\tau)} = \left[1 + \frac{4\beta^2 W_g^2}{u'^2}\right]^{-1/2}, \tag{1.2.14b}$$

where $\varkappa$ is the particle diffusivity, u' is the r.m.s. velocity in the direction of W_g and $\beta = u'T_L/L_E$ relates the Lagrangian integral time scale T_L, and the Eulerian integral lengthscale L_E and from theoretical considerations of Tennekes and Lumley (1972), they obtained $\beta = 2/3$. Note that in (1.2.14b), the coefficient is about 4 (rather than 1 as in (1.2.14a)) because the transverse integral scale on $\langle u_1(\mathbf{x})u_1(\mathbf{x}+r_3)\rangle$ is half the longitudinal integral scale based on $\langle u_1(\mathbf{x})u_1(\mathbf{x}+r_1)\rangle$ in isotropic turbulence. Therefore, it can be seen that the effect of constant free-fall velocity on the dispersion of particles in a turbulent flow is then to decrease the particle dispersion coefficient by approximately the inverse of the free-fall velocity. In the limit $W_g/u' \to \infty$, the diffusion coefficient normal to W_g is a half that parallel to W_g. Also, their results indicated an appreciable reduction of dispersion rates. But these formulae cannot be in general rigorously valid, as, for instance, when the drift is not constant or when it is not large enough to provide an Eulerian sampling out as assumed in the analysis.

However this model did not fit the measurement of Snyder and Lumley (1971) with one value of β (Hunt and Nalpanis (1985) suggested using (1.2.14a) for $\varkappa_{fp33}$ which is different to $\varkappa_p$). The reason for this failure is because even when the relative velocity v_R is small compared

with σ_u, one has to allow for the large spatial gradients of turbulent velocities. Over a small interval δx, the cross correlation of u is given by

$$\langle u(x + \delta x)u(x)\rangle = \langle u^2(x)\rangle - A_1 \frac{\sigma_u^{4/3}}{T_L^{2/3}}\delta x^{2/3}.$$

Clearly this results cannot be accommodated in a Stochastic Markov model for $u(x, t)$ in which $u(x, t)$ has a exponential velocity correlations since $\delta x \sim v_R\Delta t$. Hunt and Nalpanis (1985) by allowing for the large spatial gradient of turbulent velocity, derived a heuristic form for T_L for use in the random flight model, dependent on the time interval Δt,

$$T_L^* = T_L\left/\left[1 + A\left(\frac{v_R}{\sigma_u}\right)^{2/3}\left(\frac{T_L}{\Delta t}\right)^{1/3}\right]\right., \qquad (1.2.15)$$

where A is constant of order 1 which is determined from experimental measurements. Using (1.2.15) for simulations Walklate's (1987) model gave good agreement with the measurements of Snyder and Lumley (1971).

A drawback of the random walk technique is that it assumes a specific form for the Lagrangian correlation statistics, also from Hunt's formula it depends on the size of the time step Δt being chosen. Thus, in principle the velocity of the particle $\mathbf{u}_{fp}$ cannot be represented by a simple stochastic Markov processes.

Before moving on to the discussion of shear flow turbulence, we wish to mention two reliable Lagrangian experiments. In spite of the difficulties as described above, some important conclusions have been established.

Both laboratory investigations of the dispersion of particle have been performed in isotropic flows. Starting with Snyder & Lumley (1971) who measured the Lagrangian auto-correlation experimentally using particle of four different sizes and densities ranging from light particles that would closely follow the fluid fluctuations to heavy particle that would experience both inertia and crossing-trajectory effects. In their experiment Snyder and Lumley determined the lateral position of different particles as they are individually convected up the wind tunnel. Although decay, it could be corrected to stationarity. The main results were that (1) the auto-correlations of the particle velocity decreased much faster for heavy particles, (2) the particle velocity auto-correlations and the Eulerian spatial correlation have similar shapes, (3) the ratio of Eulerian to Lagrangian time scales is about 3, (4) the Lagrangian integral scale is closely approximated by L/u' where L is the Eulerian integral scale and u' is the turbulence intensity.

In order to understand the individual influence of inertia and the crossing-trajectories effect on the dispersion of particles, Wells & Stock (1983) investigated experimentally the dispersion

from a point source of charged spherical glass beads (5μm and 57μm diameter). Their inertia time scales differed by more than two order of magnitude in a horizontal wind tunnel with grid generated turbulence. The flow properties are similar to those used by Snyder & Lumley (1971), but with a vertical uniform electrostatic field. The field intensity could be varied, forcing the charged particles out of regions of correlated fluid at a higher than normal rate or vice versa, thereby inducing the effects of crossing trajectories or making the terminal velocity zero. In this way they could isolate the individual consequences of particle inertia and the crossing-trajectories effect on the dispersion process. Laser-Dopper anemometry was used to measure the distribution of particle concentration and velocity in several cross sections along the tunnel. The results showed that effect of crossing trajectories decreased the particle dispersion after a suitably long time from their release. Crossing-trajectory effects appear to be negligible when the drift velocity is less than the r.m.s. fluid velocity, a finding consistent with Reeks (1977). Both particle sizes gave nearly the same dispersion for the case of zero drift velocity.

However, since the particle were released at the grid, during the early stage of their motion the turbulence cannot be regarded even approximately as homogeneous and the law of initial period of decay of turbulence (Batchelor 1952) is not applicable. Scaling by conditions at the source cannot therefore be completely effective as a means of comparing their data with other measurements. Furthermore, the charge sections of the wind tunnel commenced $15M$, where M is the grid mech dimension, downstream of the grid so that the particles experienced a change in the external force field at that point, thus further obscuring the initial conditions.

It is apparent that although the experiments of Wells and Stock were designed to be comparable with that of Snyder and Lumley, there are considerable differences which make quantitative comparison between them difficult. The main problem is that proper scaling of the data is impossible because the source was located too close to the grid.

Thus, we will only use the experimental data of Snyder and Lumley to compare with our computing simulations of particles as shown in Chapter 2.

1.3 Homogeneous shear flow

Most of the discussion so far has been on homogeneous turbulent fields without a mean velocity gradient. In turbulent boundary layers and pipe flows there are several other important processes, including those associated with the inhomogeneity of the turbulence and with a mean velocity gradient. The difficulties encountered in considering all the turbulent processes simultaneously are very great. However, it may be possible to obtain some understanding of various processes by considering them separately. In this section, the effect of a uniform velocity gradient on a homogeneous turbulent field is considered.

If one linearizes (i.e. neglect terms quadratic in fluctuating quantities by Rapid Distortion Theory (RDT)) the homogeneous problem, one is left with the relatively trivial problem of the 'final period of decay' (Batchelor 1953, §5.4) which by its nature can provide no insight into the central problem of the energy cascade at high Reynolds number. However, if one linearize the the shear flow problem (of Orr-Sommerfeld type in plane shear flow) with solutions generally representing damped waves (see, e.g. Landahl 1967), then this provides a technique for study structure of turbulence (Pearson 1959) and the related problem of energy transfer to the turbulence.

It was Batchelor and Proudman (1954) who first presented a RDT of turbulent flows. It is assumed that distortion by mean influences take place on a time (spatial) scale small compared to the Lagrangian time (length) scale on which non-linear and viscous effect act, so that the turbulence interacts strongly with the mean flow but only weakly with itself. Starting with an isotropic spectrum they found the evolution of turbulent intensities in an arbitrary homogeneous straining flow. Pearson (1959) incorporated viscous terms into Batchelor and Proudman's theory and three cases of distortion were investigated; those of uniform rotation, uniform shear, and uniform irrotational distortion. For the first two, the total enegry associated with the turbulence was found to decay, but for the third it was found in general to increase without limit. Townsend (1970, 1976) has shown that RDT calculations, for the value of the total strain between about two to four, with a finite shear of about 63° imposed on initially isotropic turbulence, can reproduce quite accurately eight out of the nine principal correlation functions measured by Grant (1958) in a turbulent wake and stress ratios are also fairly well predicted – and this all on the basis of a linear calculation! More recently, Lee, Kim and Moin (1987) have demonstrated that applying the linear (RDT) distortion to an actual realisation of an initially homogeneous isotropic velocity field leads to velocity fields that contain many major large-scale coherent structures. These structures appear very *similar* in their scale, shape and distribution to structures that have been found in the Direction Simulations of homogeneous (uniform) shear flows and in the simulation and experiments of turbulent shear boundary layer.

In view of this similarity, RDT is used to investigate the effects of high shear rate on the structure of homogeneous turbulence in chapter 4. The results show that an important effect of the shear acting on initially isotropic turbulence is the selective amplification of structures having large length scale in the mean flow direction. The theory of RDT is based on the linearization of the basic equation of motion, and is intended to described the linear interactions between the large scale (energy containing) turbulent eddies and the mean velocity U. It is important to recognize that RDT works best when a turbulent flow is subjected to a large distortion; when $|S|q^2/\varepsilon \gg 1$, where $S \sim \mathcal{O}(\|\nabla \mathbf{U}\|)$, the time scale of the turbulence q^2/ε

is long compared to that of mean deformation, and so the turbulence does not have time to interact with itself for the duration of the distortion.

If one relaxes the rapid condition to consider distortions acting over time less than but of order T_L, there is then time for the large eddies to pass energy down a cascade to smaller eddies during the distortion. However turbulence/turbulence interactions between the large eddies themselves may still be ignored if the turbulence remains weaks. Lee, Kim & Moin (1987) have demonstrated by comparison with experiments that the linear theory of *rapidly* distorted flow can be applied to analysing the structure of slowly changing turbulent shear flow.

The RDT model clearly omits some important mechanisms which are present in such flows, notably non-linear transfer (energy cascade) process. Nevertheless it appears that the selective amplification of certain eddies by interaction with mean shear in the way described by RDT, is an important mechanism in the development and maintenance of the turbulence structure. Non-linear effect seem to limit the process rather than modify it.

This thesis is organized as follows. In Chapter 2 the method of Kinematic Simulation of homogeneous isotropic turbulent velocity field is presented. Using an accurate numerical scheme, of order 2700 fluid particles are tracked through the computed flow field, and hence time series of both Eulerian and Lagrangian velocites are obtained. The results reported include: Eulerian and Lagrangian velocity auto-correlations and spectra; 'Eulerian-Lagrangian' and 'Frozen Lagrangian' velocity spectra; pressure spectra. In Chapter 3 the simulation is employed to compute the individual motion on dispersion of small dense particles. New concepts and results are obtained for different statistics, in particular, from a Lagrangian point of view. The simulation results are compared with experiment of Snyder and Lumley (1971). One objective of this study is to obtain particle Lagrangian statistics from KS in relation to the stochastic models, such as random flight models. In Chapter 4, we use Rapid Distortion Theory, in which the exact equations for the fluctuating field are approximated in a way that is valid for very strong imposed mean strain rate, to examine the structure of flow under plane shear. Finally, certain details of chapters are presented in the Appendices (a)–(d).

CHAPTER TWO

Kinematic Simulation
of Homogeneous Turbulent Flows

2.1 Introduction

In the Kinematic Simulation presented here we represent the three dimensional velocity field
as sums of Fourier modes in space and time, with random coefficients chosen so that the flow
field has certain properties, namely:

(i)   it satisfies continuity;

(ii) it has the measured form of the Eulerian spatial spectrum for isotropic three-dimensional
      turbulence (in particular the Kolmogorov inertial subrange form);

(iii) the large scale eddies advect small scale eddies (by applying and extending the results of
      Tennekes 1975, Chase 1970 and Hunt *et al.* 1987);

(iv) the Fourier modes are statistically independent of each other and have Gaussian statistics.

The computed results are first shown to be consistent with the assumptions, and then
some interesting new results are obtained which are compared with measurements and direct
numerical simulations; in particular we find that:

(a)   for a fixed observer the main cause of high frequency fluctuations in the velocity is the
      advection of small eddies by large eddies. It is only for an observer moving with the eddies
      that the 'turn-over' of the small eddies determines the fluctuations in velocity;

(b)   the Eulerian fluctuating pressure field agrees approximately with the theoretical results of
      Batchelor (1953), Hinze (1975) and George *et al.* (1984);

(c)   the negative skewness of the derivatives $\left\langle (\partial u_i / \partial x_i)^3 \right\rangle$ (where $\langle \ \rangle$ denotes the ensemble
      average), usually ascribed to the intrinsic non-linearity of the turbulence (Batchelor and
      Townsend 1947), receives a significant contribution from the advection of small scales by
      non-uniform motion of large scales;

(d) the Lagrangian statistics of the velocity of a single particle, i.e. the time scale (T_L) and spectrum $\phi_{11}^L(\omega) \, (= C^L \varepsilon \omega^{-2})$, agree with the experimental values of Snyder and Lumley (1971), the inertial subrange form of Inoue (1951), and approximately with Hanna's (1980) value for C^L of 0.6;

(e) the Eulerian-Lagrangian spectrum of the velocities measured by an observer travelling with the large scales ϕ_{11}^{EL} has the form $C^{EL} \varepsilon \omega^{-2}$ (where C^{EL} is about $4.23 C^L$).

The Kinematic Simulation of homogeneous turbulence presented here is not grid-based, and does not require the solution of any set of equations, so it can be easily programmed on any computer. It takes a long time to run on a small computer; it is more convenient to use a large one! It is ideally suited to parallel computations. The method can be extended to allow for shear as discussed in Chapter 4 and for the effects of rigid walls or generation of turbulence at a density interface (Carruthers 1989), following the approach of Lee, Kim and Moin (1987) and Turfus and Hunt (1986).

There are some significant differences between the present work and large eddy simulations. Generally stated, our attitude has been to make use of the available experimental information to construct a model and see whether it is possible to throw some light on the dynamics of the problem. The large eddy simulation should be viewed, at least in our opinion, as an alternative to experiments to derive statistical averages, or three-dimensional visualizations of fluid motion and the structural aspects of the turbulent flow. These data has been used to determined certain parameters to be specified in Kinematic Simulations and some comparisons were made between LES and KS.

2.2 Method

We can represent the fluctuating velocity field, $\mathbf{u}(\mathbf{x}, t)$, moving with the mean flow in a homogeneous, turbulent flow by a Fourier transform over space and time. For simplicity, it is assumed that the turbulence is stationary in time; its decay is ignored.

$$\mathbf{u}(\mathbf{x}, t) = \int\limits_{-\infty}^{\infty} \int\limits_{-\infty}^{\infty} \int\limits_{-\infty}^{\infty} \int\limits_{-\infty}^{\infty} \mathbf{S}(\boldsymbol{\kappa}, \omega) \; e^{i\{\boldsymbol{\kappa}.\mathbf{x} + \omega t\}} \, d\boldsymbol{\kappa} \, d\omega, \tag{2.2.1}$$

where $\boldsymbol{\kappa}$ is the wave-vector, ω the frequency and $\mathbf{S}(\boldsymbol{\kappa}, \omega)$ is the four-dimensional Fourier Transform.

The wavenumber-frequency spectrum tensor is defined by the Fourier transform of the three-dimensional space and time autocorrelation function and is

$$\Psi_{ij}(\boldsymbol{\kappa}, \omega) = \frac{1}{(2\pi)^4} \int\limits_{-\infty}^{\infty} \int\limits_{-\infty}^{\infty} \int\limits_{-\infty}^{\infty} \int\limits_{-\infty}^{\infty} R_{ij}(\mathbf{x}, \tau) \; e^{-i\{\boldsymbol{\kappa}.\mathbf{x} + \omega\tau\}} \, d\mathbf{x} \, d\tau, \tag{2.2.2}$$

and its equivalent energy spectrum $\mathcal{E}(k,\omega)$, which is a function of k only, is given by

$$\mathcal{E}(k,\omega) = \int_A \Psi_{ii}(\boldsymbol{\kappa},\omega) \, dA(\boldsymbol{\kappa}), \tag{2.2.3}$$

the integration are over the surface of spheres of which dA is an element. The corresponding wavenumber energy spectrum tensor is defined as the spatial Fourier transform of $R_{ij}(\mathbf{x}, \tau = 0)$, which can be derived from Ψ_{ij} by,

$$\Phi_{ij}(\boldsymbol{\kappa}) = \int_{-\infty}^{\infty} \Psi_{ij}(\boldsymbol{\kappa},\omega) \, d\omega. \tag{2.2.4}$$

The Eulerian frequency spectrum of the velocity at a fixed point is

$$\phi_{ij}(\omega) = \int_{-\infty}^{\infty} R_{ij}(\mathbf{x} = 0, \tau)e^{-i\omega t} \, dt. \tag{2.2.5}$$

In order to discuss the statistical behaviour of the small scale turbulence, it is convenient to apply a wavenumber decomposition to the covariance. Therefore we will work with the wavenumber spectra at zero time separation τ, i.e.

$$\Phi_{ij}(\boldsymbol{\kappa}) = \frac{1}{(2\pi)^3} \int_{-\infty}^{\infty}\int_{-\infty}^{\infty}\int_{-\infty}^{\infty} R_{ij}(\mathbf{x}, \tau = 0)e^{-i\boldsymbol{\kappa}.\mathbf{x}} \, d\mathbf{x}, \tag{2.2.6}$$

which for isotropic turbulence (Batchelor 1953) is relation to the wavenumber-magnitude energy spectrum function $E(k)$ by

$$\Phi_{ij}(\boldsymbol{\kappa}) = \frac{E(k)}{4\pi k^4} \left(k^2 \delta_{ij} - k_i k_j\right), \tag{2.2.7}$$

where $k^2 = k_i k_i$. Note that

$$E(k) = \int_{-\infty}^{\infty} \mathcal{E}(k,\omega) \, d\omega. \tag{2.2.8}$$

The function $E(k)$ measures how much energy is contained between the wavenumber κ and $\kappa + d\kappa$, the total kinetic energy per unit mass of fluid is

$$\int_{-\infty}^{\infty} E(k) \, dk = \frac{1}{2} \langle \mathbf{u}^2 \rangle, \tag{2.2.9}$$

where the $\langle \ \rangle$ denotes the ensemble average. No way is known by which $E(k)$ may be measured directly. Experimental measurements are made of the longitudinal one-dimensional spectrum function $\phi_{11}(k_1)$, where

$$\int_{-\infty}^{\infty} \phi_{11}(k_1) \, dk_1 = \frac{1}{2} \langle u_1^2 \rangle, \tag{2.2.10}$$

which is related (Batchelor 1953) to $E(k)$ by

$$E(k) = k^3 \frac{d}{dk}\left[\frac{1}{k}\frac{d\phi(k)}{dk}\right]. \tag{2.2.11}$$

It should be noted that the factor $1/2$ is customarily used in the definition of $E(k)$, as in (2.2.10) (except by Stewart & Townsend 1951), but that the definition of $\phi_{11}(k_1)$ is not uniform in the literature. The form (2.2.11) above is used by Batchelor (1953). The function $\phi_{11}(k_1)$ is half of that defined above in the book of Hinze (1975) where the corresponding quantity is $E_1(k)$.

A complete statistical description of $\Psi_{ij}(\boldsymbol{\kappa},\omega)$ requires knowledge of the joint probability function for all variables of interest at all wavenumbers and frequencies, which allows a random flow field to be generated with any prescribed energy spectrum, an impossible goal to achieve. Therefore, statistical descriptions are always limited in what they can provide, and the challenge is to provide what is really essential, with minimum effort and maximum accuracy.

Thus the most important question is how does $\Phi_{ij}(\boldsymbol{\kappa})$ relate to $\Psi_{ij}(\boldsymbol{\kappa},\omega)$. Following Townsend (1966) and Tennekes (1975), Turfus and Hunt (1986) argued that, for an observer moving with the mean flow, the turbulent energy at a frequency ω is primarily associated with the larger, energy-containing eddies (variance U_o) advecting smaller eddies of scale k^{-1} ($= U_o/\omega$) past the observer. They further assume that at high Reynolds numbers, the dynamics of the advection effect can be analysed using a variant of Taylor's frozen turbulence approximation. Then they made the hypothesis that

$$\Phi_{ij}(\boldsymbol{\kappa},\omega) = \frac{1}{2}\delta(|\omega| - kU_o)\Phi_{ij}(\boldsymbol{\kappa}). \tag{2.2.12}$$

Physically, this corresponds to a constant 'sweeping' velocity U_o which advects the whole flow field past a stationary observer. We extend this idea of a sweeping velocity and model the flow field as a collection of small eddies being advected by larger, energy-containing eddies. The small eddies are also deformed by the straining caused by the large eddies, but Hunt *et al.* (1987) showed, computationally, that the advection of the small eddies appears account for the frequency spectra. Chase (1970) had shown earlier that this explains the forms of the spectra measured by Favre *et al.* (1957).

2.2.1 The velocity field

The method of discretisation of Kraichnan (1970) and Drummond *et al.* (1984) which we shall extend, essentially involves approximating the velocity field $\mathbf{u}(\mathbf{x},t)$ as a Fourier series with a finite number of modes:

$$\mathbf{u}(\mathbf{x},t) = \sum_{n=1}^{n=N_k} \sum_{m=1}^{m=M_\omega} [(\mathbf{a}_{mn}\wedge\widehat{\boldsymbol{\kappa}}_n)\cos\{\boldsymbol{\kappa}_n.\mathbf{x} + \omega_{mn}t\} + (\mathbf{b}_{mn}\wedge\widehat{\boldsymbol{\kappa}}_n)\sin\{\boldsymbol{\kappa}_n.\mathbf{x} + \omega_{mn}t\}], \tag{2.2.13}$$

where $\widehat{\boldsymbol{\kappa}}_n = \boldsymbol{\kappa}_n/k_n$ and $k_n = |\boldsymbol{\kappa}_n|$. The broad features of this formulation are these: the velocity field automatically satisfies the incompressibility condition, $\nabla.\mathbf{u} = 0$. All the energy is concentrated in N_k shells of radius k_n in wavenumber space; the energy spectrum $E(k)$ and wavenumbers k_n have to be specified. The variables $\mathbf{a}_{mn}$, $\mathbf{b}_{mn}$ and $\boldsymbol{\kappa}_n$ are randomly distributed and mutually independent. There is no dynamical interaction and therefore no correlation between the Fourier modes.

The time dependence of the turbulence is actually determined by the non-linear dynamical interactions between different modes (e.g. vortex stretching) and by the purely kinematic process of non-uniform unsteady advection of the vorticity field by the velocity field, which implies large-scale eddies advecting small-scale eddies (figure 2.1). The novel feature of our simulation is modelling these effects by choosing ω_{mn} and $\boldsymbol{\kappa}_n$ appropriately. Both effects imply that $\boldsymbol{\kappa}_n$ and ω_{mn} are slowly-varying functions of $\mathbf{x}$ and t.

The temporal structure of the flow is determined by the frequency ω. We divide the velocity field into large and small scale fields ($\mathbf{u}_\ell$ and $\mathbf{u}_s$ – see figure 2.2) using a critical wave number k_c to divide the wave number range. The velocity field is given by the sum of these two fields:

$$\mathbf{u}(\mathbf{x}, t) = \mathbf{u}_\ell(\mathbf{x}, t) + \mathbf{u}_s(\mathbf{x}, t). \qquad (2.2.14)$$

We then assume that the main cause of the temporal evolution of the velocity field is the non-uniform advection of the small scales by the large scales, and we model ω accordingly.

We assume that the *large eddies* move randomly and independently of each other; this corresponds to a random shift in the relative phases of the large modes. Alternatively they might be computed by a Large Eddy Simulation (Metcalfe 1988). The large scale motion is modelled by Fourier modes containing a random walk element:

$$\mathbf{u}_\ell(\mathbf{x}, t) = \sum_{n=1}^{N_c-1} \Big[(\mathbf{a}_n \wedge \widehat{\boldsymbol{\kappa}}_n) \cos \boldsymbol{\kappa}_n . \{\mathbf{x} - \boldsymbol{\chi}_n(\boldsymbol{\kappa}_n, t)\} + (\mathbf{b}_n \wedge \widehat{\boldsymbol{\kappa}}_n) \sin \boldsymbol{\kappa}_n . \{\mathbf{x} - \boldsymbol{\chi}_n(\boldsymbol{\kappa}_n, t)\} \Big], \quad (2.2.15)$$

where the vectors $\mathbf{a}_n$,$\mathbf{b}_n$ and $\boldsymbol{\kappa}_n$ are chosen as described in §2.2.5. $\boldsymbol{\chi}_n(\boldsymbol{\kappa}_n, t)$ is the displacement at time t of the large eddy of wave number $\boldsymbol{\kappa}_n$; at time $t = 0$, $\boldsymbol{\chi}_n(\boldsymbol{\kappa}_n, t) = 0$. We model the velocity $\mathbf{W}_n(t)$ of each of the large modes as a random, Gaussian velocity with zero mean and variance equal to the energy of the n-th mode, i.e. $\langle \mathbf{u}_\ell^n(\mathbf{x}, t)^2 \rangle$. Then we have:

$$\boldsymbol{\chi}_n(\boldsymbol{\kappa}_n, t) = \int_0^t \mathbf{W}_n(t') \, dt', \qquad (2.2.16)$$

It can be shown (see Appendix A) that this gives the typical form for the Eulerian correlation function, i.e.

$$R^E(\mathbf{x}, t) \propto \exp\left(-At^2\right) \qquad \text{for} \qquad |t| \ll T_{k_o} \qquad (2.2.17a)$$

and

$$R^E(\mathbf{x}, t) \propto \exp(-B|t|) \qquad \text{for} \qquad |t| \gg T_{k_o}, \qquad (2.2.17b)$$

where A and B are constants and T_{k_o} is the turn-over time of the smallest eddy.

The spatial structure of the small scale field is modelled in a similar way. We assume that there are two main causes for the temporal variation: the change of the small scale velocity of a fluid element (which occurs in the Lagrangian timescale T_L) by a random decorrelation ω'_n (see Appendix B) and the random velocity of advection of fluid elements by the most energetic eddies (on the time scale L/u_ℓ where L and u_ℓ are the length scale and rms velocity of the advected large eddy). The former process leads to a 'Lagrangian' frequency spectrum proportional to $\varepsilon \omega^{-2}$ while the latter leads to an 'Eulerian' frequency spectrum proportional to $\varepsilon^{2/3} u_\ell^{2/3} \omega^{-5/3}$. Therefore, we write

$$\mathbf{u}_s(\mathbf{x}, t) = \sum_{n=N_c}^{N_k} \left[(\mathbf{a}_n \wedge \widehat{\boldsymbol{\kappa}}_n) \cos[\boldsymbol{\kappa}_n . \mathbf{X} - \omega'_n t] + (\mathbf{b}_n \wedge \widehat{\boldsymbol{\kappa}}_n) \sin[\boldsymbol{\kappa}_n . \mathbf{X} - \omega'_n t] \right], \qquad (2.2.18)$$

where $\mathbf{X} = \mathbf{x} - \mathbf{x}_L$ and

$$\mathbf{x}_L(t) = \int_0^t \mathbf{u}_\ell(\mathbf{x}_L(t'), t') \, dt'. \qquad (2.2.19)$$

$\mathbf{a}_n$, $\mathbf{b}_n$ and $\widehat{\boldsymbol{\kappa}}_n$ are chosen as for $\mathbf{u}_\ell(\mathbf{x}, t)$, and $\mathbf{x}_L(t)$ defined the displacement of the small scale field by the large scale motion $\mathbf{u}_\ell$. Clearly $\mathbf{u}_\ell$ is the same for all $k > k_c$, since we have assumed that all small eddies are carried along by the large eddies. This would be a correct kinematical model if there were a gap in the spectrum, separating the wavenumber range into large and small scales. In reality, a high wavenumber eddy is imbedded in a continuous spectrum of eddies, and therefore a small 'small eddy' will be swept by larger 'small eddies' as well as by energy-containing eddies. However, we neglect this effect because the more energetic and longer lasting sweeping by the energy-containing (or large) eddies is assumed to be the dominant 'sweeping' process. (The results seem to support this assumption.) No attempt is made to smooth the transition between the large and small scale fields; this means that as k_c varies the frequency spectra and time correlations change (as described later).

In addition, the frequency distribution (in the frame moving with the large eddies) cannot be uniquely related to the value of k_n, the energy of k_n must be spread over a range of frequencies (Townsend 1966), but, without any measurements to indicate this range, it is simplest to specify that all energy of frequency ω is associated with the wavenumber k (see figure 2.3). This implies the delta-function form of the spectrum (2.2.12).

2.2.2 Eulerian spectra

We use the von Kármán energy spectrum (figure 2.2), which has been found to give reasonable agreement with many measurements in a range of turbulent flows:

$$E(k) = \frac{g_2 k^4}{(g_1 + k^2)^{17/6}}, \qquad (2.2.20)$$

where the numerical constants are given by (Hunt 1973):

$$g_1 = \frac{\pi \Gamma^2 \left(\frac{5}{6}\right)}{\Gamma^2 \left(\frac{1}{3}\right)} = 0.558, \qquad g_2 = \frac{55}{9} \frac{g_1^{5/6}}{\pi} = 1.196. \qquad (2.2.21)$$

This spectrum covers the range of wavenumbers from the largest permanent eddies (where $E(k) \propto k^4$) to the inertial subrange where $E(k) \propto k^{-5/3}$. Note that $E(k)$ is normalised to give

$$\int_0^\infty E(k)\, dk = \frac{1}{2} \left\langle \mathbf{u}(\mathbf{x}, t)^2 \right\rangle = \frac{3}{2}, \qquad (2.2.22a)$$

and the integral length scale derived from the energy spectrum (Monin and Yaglom 1975) becomes:

$$L_{11} = \frac{3\pi}{4} \int_0^\infty k^{-1} E(k)\, dk \bigg/ \int_0^\infty E(k)\, dk = 1. \qquad (2.2.22b)$$

The form of Eulerian energy spectrum corresponding to Kolmogorov's (1941) theory of the locally isotropic "inertial subrange" is

$$E(k) = \alpha_k \varepsilon^{2/3} k^{-5/3} \qquad \text{for} \qquad k_c \ll k \ll \eta^{-1}. \qquad (2.2.23)$$

This is the Kolmogorov spectrum, a cornerstone of turbulence. Where α_k is the Kolmogorov constant, ε is the rate of dissipation of kinetic energy per unit mass and η $(= (\nu^3/\varepsilon)^{1/4})$ is the Kolmogorov microscale, which characterises the dissipative scale. There is some variability in the measured value of α_k. Measurements in a tidal stream $(Re_\lambda \sim 2000)$ by Grant et al. (1962) give $\alpha_k = 1.44$ with a standard deviation of 0.07 (measured over four decades of $-5/3$ spectrum). In Gibson's (1963) measurements in a round jet $(Re_\lambda \sim 800)$, $\alpha_k = 1.57$ on the jet axis and $\alpha_k = 1.62$ at the half radius (measured over one decade of $-5/3$ spectrum). We have chosen $\alpha_k = 1.5$.

2.2.3 Time scale of small eddies

The scalings for ω_n lead to predictions for correlation and structure functions which can be tested.

Essentially, the current understanding is that the large scales of turbulence with velocity and length scales u_o and L_o are unsteady and change on a time scale L_o/u_o. In a frame of reference moving with the mean flow, the difference between the mean square velocity $\mathbf{u}$ at a time t and a time $(t + \tau)$ is given (following Tennekes 1975) by the Eulerian Time Structure Function

$$\mathbf{S}^E(\tau) = \frac{1}{2} \left\langle (\mathbf{u}(\mathbf{x}, t) - \mathbf{u}(\mathbf{x}, t + \tau))^2 \right\rangle. \tag{2.2.24}$$

If the Reynolds number, Re $(= u_o L_o/\nu)$, is very high and if τ is much larger than the Eulerian micro scale $\text{Re}^{-1/2} L_o/u_o$ and much smaller than the integral time scale L_o/u_o, then $\mathbf{S}^E(\tau)$ is determined by the change in velocity caused by small eddies being swept past by the observer by large eddies, so

$$S_{11}^E(\tau) = C_{11}^E (\varepsilon u_0 \tau)^{2/3} = \langle u_1(\mathbf{x}, t) u_1(\mathbf{x}, t + \tau) \rangle - \langle u_1(\mathbf{x}, t)^2 \rangle, \tag{2.2.25}$$

where u_0 is the r.m.s. velocity in one direction.

Now consider an observer moving with the large eddies and measuring the changes in the velocity (say on a scale k^{-1}, where k is in the inertial subrange). It is assumed that the observer moves at a velocity $\mathbf{V}_0$ which is locally averaged over a scale ℓ_0, where $k^{-1} \ll \ell_0 \ll L_o$. The structure function for the velocity at time t and $t + \tau$, measured in this randomly moving frame (which we call 'Eulerian-Lagrangian') is determined by eddies of scale k^{-1} with velocity $v_k \sim \varepsilon^{1/3} k^{-1/3}$. The velocities v_k of such eddies are changing on the time scale of the local strain rate, viz $\varepsilon^{-1/3} k^{-2/3}$. Also, in a time scale τ, the eddy moves a distance $\ell_k(\tau) \sim \tau v_k$ past a observer. The change in velocity $\Delta v_k(\tau)$ seen by the observer in this local length and time scale is of the order $\varepsilon^{1/3} \ell_k^{1/3}(\tau) \sim \varepsilon^{1/3} (\tau v_k)^{1/3}$, which is of the same order as v_k. Hence $\Delta v_k \sim \varepsilon^{1/3} (\tau \Delta v)^{1/3}$. Therefore, $\Delta v_k \sim \varepsilon^{1/2} \tau^{1/2}$ and

$$S_{11}^{EL}(\tau) = \langle u_1(\mathbf{x}, t) u_1(\mathbf{x} + \mathbf{V}_0 t, t + \tau) \rangle - \langle u_1(\mathbf{x}, t)^2 \rangle = 2\pi C^{EL} \varepsilon \tau. \tag{2.2.26}$$

If the observer actually travels with a fluid element (with displacement $\boldsymbol{\xi}(t) = \int_0^t \mathbf{u}(\mathbf{x}(t'), t') \, dt'$) as its velocity changes on this inertial-range time scale, a similar local *scaling* applies. Then, as Inoue (1951) first pointed out, the local Lagrangian structure function is

$$S_{11}^L(\tau) = \langle u_1(\mathbf{x}, t) u_1(\mathbf{x} + \boldsymbol{\xi}, t + \tau) \rangle - \langle u_1(\mathbf{x}, t)^2 \rangle = 2\pi C_{11}^L \varepsilon \tau \tag{2.2.27}$$

(see also Monin and Yaglom 1975).

To understand the difference between the 'Eulerian-Lagrangian' and Lagrangian structure functions, consider two observers starting at $\mathbf{x}_0$ at time t_0. At time τ later the (EL) observer

has moved a distance $\mathbf{V}_0\tau$, while the (L) observer has moved a distance $\int_{t_0}^{t_0+\tau} \mathbf{u}\, dt$; the distance ℓ between the observers at time τ is of order $\varepsilon^{1/2}\tau^{3/2}$ (see Appendix B). Therefore the difference between the root-mean-squared velocity of the observers is of order $\ell^{1/3}\varepsilon^{1/3} \sim \varepsilon^{1/2}\tau^{1/2}$, and so S_{11}^L cannot equal S_{11}^{EL}. But these two structure functions are of the same order, and the coefficients C_{11}^L, C_{11}^{EL} must also be of the same order. Since the small scale eddies $\mathbf{u}_s(\mathbf{x}, t)$ are advected by the large scales, the Eulerian-Lagrangian structure function determines the modelling of the time variation of the small scales. Incidentally it is also important because it determines the changes in velocity affecting particles or surfaces (e.g. flames) in a flow that moves with the large eddies, but not with the smallest inertial range eddies.

For the model of $\mathbf{u}_s(\mathbf{x}, t)$, the Eulerian-Lagrangian (EL) *correlation function* is

$$R^{EL}(\tau) = \langle \mathbf{u}_s^2 \rangle - S^{EL}(\tau)$$

$$= \langle \mathbf{u}_s(\mathbf{x}(t), t) . \mathbf{u}_s(\mathbf{x}(t+\tau), t+\tau) \rangle$$

$$= \sum_{n=0}^{\infty} \langle |\mathbf{a}_n|^2 \rangle e^{i\omega_n'\tau}.$$

For S_{11}^{EL} to have the high Reynolds number limit defined by (2.2.26) and for $E(k)$ to have the inertial range form of $k^{-5/3}$, it is necessary that

$$\omega_n' = \lambda \varepsilon^{1/3} k_n^{2/3}, \tag{2.2.28}$$

since in the inertial range the time scale is proportional to $\varepsilon^{-1/3}k^{-2/3}$. We choose $\lambda\varepsilon = 1.0$, to give the correct forms for the Eulerian and Lagrangian correlation functions; λ is a constant of order unity, which can be related to the measurable coefficient C^{EL} (see Appendix B):

$$\lambda \approx 2C^{EL}/(3\alpha_k). \tag{2.2.29}$$

Note that the change in the mean square velocity of fluid elements over short times depends only on ε and the isotropic structure of the small-scales, not on the critical wave number k_c.

2.2.4 Maximum, critical wavenumbers k_η, k_c and Reynolds number

Because we use a finite number of Fourier modes the energy spectrum must be truncated at some cut-off wavenumber k_η. The choice of k_η determines both the Reynolds number and the integration time step. In a viscous flow at high Reynolds number, the micro- and large scales are related through the Reynolds number by $\mathrm{Re}^{3/4} \sim \ell/\eta = k_\eta\ell$ (Batchelor 1953), where $\ell \sim v^3/\varepsilon$ is the length scale of the energy-containing eddies and $v^2 = \langle u_1^2 \rangle$ is the velocity variance. Thus increasing k_η increases the Reynolds number of the simulation. At separations less than k_η^{-1}, the velocity field is simply a uniform straining motion as assumed in many previous models

(Batchelor 1959). Increasing k_η also decreases the time step which can be used in computing velocities and trajectories of fluid elements since the time step must be less than the inverse of the highest frequencies in the flow, and this increases the computational time. In most of the simulations, we have used $k_\eta = 50$ and in some cases we have varied k_η between 50 and 300 to investigate the importance of the *size* of the inertial subrange and hence the Reynolds numbers.

The critical wave number k_c marks the division between the large and the small eddies, and determines the proportion of the total energy assigned to each of the velocity fields. We have no *a priori* argument for determining k_c, but we have found that the Eulerian and Lagrangian autocorrelations, $R_{11}^E(\tau)$ and $R_{11}^L(\tau)$ are sensitive to k_c. At small τ the velocity fluctuations seen by a stationary observer are caused primarily by large scale energetic eddies advecting small eddies past the observation point, whilst the fluctuating velocities experienced by a fluid element are due primarily to the time-evolution of the small scale field. Since the large scale eddies contain most of the energy, it follows that the Eulerian autocorrelation at small τ must decay faster than the Lagrangian autocorrelation (Shlien and Corrsin 1974, Tennekes 1975). That is, $R_{11}^L(\tau) > R_{11}^E(\tau)$ for small τ. There is some experimental evidence (Shlien and Corrsin 1974) and the theoretical argument of Reeks (1977) that at large τ, $R_{11}^E(\tau) > R_{11}^L(\tau)$, implying that the curves must cross (see figure 2.8). It is clear from (2.2.15) that the change in $\partial \mathbf{u}_\ell / \partial t$ associated with changing k_c (N_c) is of order $\left| (\mathbf{a}_{N_c-1} \wedge \widehat{\boldsymbol{\kappa}}_{N_c-1}) . \dfrac{\partial \chi_{N_c-1}}{\partial t} \right| \sim |(\mathbf{a}_{N_c-1} \wedge \widehat{\boldsymbol{\kappa}}_{N_c-1}) . \mathbf{W}_{N_c-1}|$. But the change in $|\partial \mathbf{u}_s / \partial t|$ is of order $\left| (\mathbf{a}_{N_c} \wedge \widehat{\boldsymbol{\kappa}}_{N_c}) . \dfrac{\partial \mathbf{x}_L}{\partial t} - \omega_n' \right| \sim |(\mathbf{a}_{N_c} \wedge \widehat{\boldsymbol{\kappa}}_{N_c}) . (\mathbf{u}_\ell - \omega_n')|$. Since $|\mathbf{W}_{N_c-1}| < |\mathbf{u}_\ell|$. It follows that as k_c decreases, $|\partial \mathbf{u} / \partial t| \sim |(\mathbf{a}_{N_c} \wedge \widehat{\boldsymbol{\kappa}}_{N_c}) . (\mathbf{u}_\ell - \omega_n')|$, and as k_c increases, $|\partial \mathbf{u} / \partial t| \sim |(\mathbf{a}_{N_c-1} \wedge \widehat{\boldsymbol{\kappa}}_{N_c-1}) . \mathbf{W}_{N_c-1}|$, since $|\mathbf{W}_{N_c}| > |\mathbf{u}_\ell|$, it follows that as k_c decreases, $\partial u / \partial t$ decreases and R^E increases. Therefore, a small value of k_c, $R_{11}^E(\tau)$ always exceeded $R_{11}^L(\tau)$, and there was no crossover. Conversely, for large values of k_c, $R_{11}^L(\tau)$ always exceeded $R_{11}^E(\tau)$. However there was a narrow band of k_c, in which the two curves crossed in the expected manner at $\tau \approx 2.5$, and we located k_c within this band (at $k_c = 5.0$, somewhat arbitrarily) since this generated the appropriate forms for the two curves. This apportions the energy 5.8 to 4.2 between the large and the small scale fields. For most practical purposes, this sensitivity of the Eulerian time correlation function/frequency spectra is the most unsatisfactory feature of KS. It is clear that spatially determined variables – such as pressure – are much less sensitive to the choice of k_c, as we have found.

To determine the Reynolds number we use the relationship Re $\sim (k_\eta \langle u_1^2 \rangle^{3/2} / \varepsilon)^{4/3}$ derived above and estimate the dissipation rate ε from the universal spectrum for the inertial subrange (2.2.23). Since the von Kármán spectrum (2.2.20) tends to this form at high wave number, we equate the energy in the small scale field $E_s(k)$ to the energy in the equivalent range of the

inertial subrange spectrum :

$$E_s(k) = \int_{k_c}^{k_\eta} \frac{g_2 k^4}{(g_1 + k^2)^{17/6}} \, dk \;=\; \frac{3}{2} \langle u_{1s}^2 \rangle \;=\; \alpha_k \varepsilon^{2/3} \int_{k_c}^{k_\eta} k^{-5/3} \, dk$$

from which

$$\varepsilon = \left[\frac{\langle u_{1s}^2 \rangle}{\alpha_k} \left(\frac{1}{k_c^{2/3}} - \frac{1}{k_\eta^{2/3}} \right)^{-1} \right]^{3/2} .$$

For this model, $k_c = 5.0$, $k_\eta = 50.0$ and $\langle u_{1s}^2 \rangle = 0.42$, giving $\varepsilon = 1.066$ and a Reynolds number of 170. Full details of all the parameters are given in table 2.1.

2.2.5 Determination of k_n, κ_n, $\mathbf{a}_n$ and $\mathbf{b}_n$

The values of k_n have to be chosen by discretising the wave number space into a finite number of modes N_k. We use 6 modes for the large eddies ($0 < k_n < 5.0$) and 32 modes for the small eddies $5.0 \leq k_n \leq 50$. The wave numbers are distributed as follows:

$$0 < k_n < 5.0, \qquad k_n = 5.0 \times n/7, \qquad\qquad n = 1, 2, \ldots, 6;$$

$$5.0 \leq k_n \leq 50, \qquad k_n = 5.0(50/5.0)^{\left(\frac{n-7}{31}\right)}, \qquad n = 7, 8, \ldots, 38.$$

A geometric progression has been chosen for the small scale wave numbers to ensure that each mode carries approximately the same energy and to exclude the possibility of cyclic repetition of the velocity field.

The unit vectors $\widehat{\kappa}_n$ are chosen at random from a population distributed isotropically on the surface of a unit sphere. The energy E_n at each wave number k_n is obtained by integrating the energy spectrum:

$$E_n = \gamma \int_{k_n}^{k_{n+1}} E(k) \, dk, \tag{2.2.30}$$

where $\gamma = \int\limits_{0}^{\infty} E(k) \, dk \Big/ \int\limits_{0}^{k_\eta} E(k) \, dk$ – a factor to compensate for the energy contained beyond k_η. The energy is assigned to each wavenumber k_n through the choice of $\mathbf{a}_n$ and $\mathbf{b}_n$.

For each mode to be independent and the velocity field to be non-divergent, statistically stationary, homogeneous and isotropic, it is necessary that:

$\mathbf{a}_{mn}$, $\mathbf{b}_{mn}$, κ_n are independent of each other; $\hfill (2.2.31a)$

the distribution of κ_n is isotropic; $\hfill (2.2.31b)$

$\langle (\mathbf{a}_{mn})_i \rangle = \langle (\mathbf{b}_{mn})_i \rangle = 0, \qquad\qquad i = 1, 2, 3 ; \hfill (2.2.31c)$

$\langle (\mathbf{a}_{mn})_i (\mathbf{a}_{mn})_j \rangle = \langle (\mathbf{b}_{mn})_i (\mathbf{b}_{mn})_j \rangle = 0, \qquad i \neq j ; \hfill (2.2.31d)$

$\langle (\mathbf{a}_{mn})_i^2 \rangle = \langle (\mathbf{b}_{mn})_i^2 \rangle , \qquad\qquad i = 1, 2, 3. \hfill (2.2.31e)$

k_c	k_η	N_k	$\langle u_\ell^2 \rangle$	$\langle u_s^2 \rangle$	ε	L	Δt	Re
5.0	50	32	0.58	0.42	1.066	1.00	0.0075	170
5.0	100	64	0.55	0.45	1.037	1.00	0.0075	470
5.0	200	128	0.53	0.47	1.006	1.00	0.0050	1270
5.0	300	256	0.51	0.49	1.036	1.00	0.0030	2180

Table 2.1.

Then from (2.13), the energy at each wavenumber is given by

$$\langle \mathbf{u}_n^2 \rangle = \left\langle \left| \mathbf{a}_n \wedge \widehat{\boldsymbol{\kappa}}_n \right|^2 \cos^2 \left(\boldsymbol{\kappa}_n . \mathbf{x} + \omega_{mn} t \right) \right\rangle + \left\langle \left| \mathbf{b}_n \wedge \widehat{\boldsymbol{\kappa}}_n \right|^2 \sin^2 \left(\boldsymbol{\kappa}_n . \mathbf{x} + \omega_{mn} t \right) \right\rangle \quad (2.2.32)$$

We scale the velocity so that $\langle (u^2)_1 \rangle = \langle (u^2)_2 \rangle = \langle (u^2)_3 \rangle = 1$, so $\langle |\mathbf{u}|^2 \rangle = 3$. The energy spectrum $E(k) = \frac{3}{2}\mathbf{P}(k)$ where $\mathbf{P}(k)$ is the probability distribution of k-mode in k-space. Substituting in equations $(2.0a - e)$, (2.32) reduces to

$$\langle \mathbf{u}_n^2 \rangle = \frac{2}{3} \left\langle |\mathbf{a}_n|^2 \right\rangle = \frac{2}{3} \left\langle |\mathbf{b}_n|^2 \right\rangle = \gamma \int_{k_n}^{q k_n} \mathbf{P}(k) \, dk. \quad (2.2.33)$$

Therefore $\mathbf{a}_n$ and $\mathbf{b}_n$ have to be chosen from distributions which satisfy $(2.0a - e)$ and (2.33). We have used two different methods to do this.

In this study, the vectors $\{\mathbf{a}_n\}$ and $\{\mathbf{b}_n\}$ are picked independently from a three dimensional Gaussian distribution with a mean vector $\begin{pmatrix} 0 \\ 0 \\ 0 \end{pmatrix}$ and covariance matrix $\langle \mathbf{u}_n^2 \rangle \times \begin{pmatrix} 1 & 0 & 0 \\ 0 & 1 & 0 \\ 0 & 0 & 1 \end{pmatrix}$.

Alternatively, $\{\mathbf{a}_n\}$ and $\{\mathbf{b}_n\}$ can be distributed isotropically on a sphere with $|\mathbf{a}_n| = |\mathbf{b}_n|$ and their magnitude are chosen as described above.

All the parameters $\boldsymbol{\kappa}_n$, $\mathbf{a}_n$ and $\mathbf{b}_n$ are chosen afresh for each realisation. Experiments were made to verify that increasing the number of modes N did not change the results to within the statistical errors.

2.2.6 Eulerian space-time spectra

There can be no general form for the large scale space-time structure, because the dynamics of the large scales as they interact with each other depend sensitively on the nature of the large scale eddies, which are determined by the boundary and initial conditions throughout the lifetime of the flow.

Note that there are no precise data on the three dimensional space-time structure function for high Reynolds numbers, but from the assumptions made in §2.2.1 and §2.2.2 regarding the

spatial structure and the form of the space-time structure, we can calculate analytically the approximate form for the space-time spectra. We show here how this calculation is done and then in §2.3 we compare our simulations with these approximate forms.

Our simulation is based on the *assumption* that the large scale Gaussian velocity field $\mathbf{u}_\ell(\mathbf{x}, t)$ randomly advects the small scale field $\mathbf{u}_s(\mathbf{x}, t)$ (see figures 2.1 and 2.4a). It follows from (2.2.18), (2.2.23) and (2.2.28) that at small scales ($k > k_c$), the wavenumber-frequency energy spectrum has the approximate form

$$\mathcal{E}(k, \omega) = \frac{1}{2} E(k) \left[\frac{\exp\left\{ -\frac{1}{2}\omega_+^2 \Big/ (akU_0)^2 \right\}}{\sqrt{2\pi}(akU_0)} + \frac{\exp\left\{ -\frac{1}{2}\omega_-^2 \Big/ (akU_0)^2 \right\}}{\sqrt{2\pi}(akU_0)} \right], \qquad (2.2.34)$$

where $U_0^2 = \frac{1}{3} \langle |\mathbf{U}|^2 \rangle$, $\omega_+ = \left(\omega + \varepsilon^{1/3} k^{2/3} \right)$ and $\omega_- = \left(\omega - \varepsilon^{1/3} k^{2/3} \right)$. This expression is exactly follows from the model and $a = 1$ if the large scales are uniform advective motions and the small scales do not change with time. (Chase 1970 and Hunt *et al.* 1987 derived the first term in this equation). The second terms in ω_+ and ω_- represent the decorrelation of the small scales as they are advected. When the frequency ω corresponds to large eddies advecting small eddies (i.e. $\omega \sim kU_0$), the second term is much smaller than the first, and then, in a fixed frame, the spectrum has the form

$$\mathcal{E}(k, \omega) = \frac{1}{2} E(k) \frac{\exp\left\{ -\frac{1}{2}\omega^2 \Big/ (akU_0)^2 \right\}}{\sqrt{2\pi}(akU_0)} \qquad (2.2.35)$$

In a frame *moving* with the large eddies, the effective velocity of translation is zero, then

$$\mathcal{E}(k, \omega)^{(EL)} = \frac{1}{2} E(k) \left[\delta \left(\omega + \varepsilon^{-1/3} k^{2/3} \right) + \delta \left(\omega - \varepsilon^{-1/3} k^{2/3} \right) \right]. \qquad (2.2.36)$$

This delta function is an idealization of a narrow band spectrum - studied in more details by Malik (1990).

For high Reynolds number turbulence in the inertial subrange, if the dominant contribution to the kinetic energy at a frequency ω is made by large-scale advection of eddies in the inertial subrange, then the Eulerian frequency spectrum $\phi_{11}^E(\omega)$ of one component of velocity, say u_1, measured at a point (moving with the mean flow) has the form (Tennekes 1975):

$$\phi_{11}^E(\omega) = \int_0^\infty \mathcal{E}(k, \omega)\, d\omega = C^E (\varepsilon U_0)^{2/3} \omega^{-5/3}, \qquad (2.2.37)$$

where C^E is constant for a given flow and U_0 is the velocity of the largest scales of the turbulence. If the large scales are isotropic and the Reynolds number is large enough for there to be a large separation in scales between the energy-containing eddies and those in the inertial subrange, then C^E should be independent of the large scales and should be a universal constant.

In the inertial subrange where $E(k) = \alpha_k \varepsilon^{2/3} k^{-5/3}$, it follows that, by integrating the first term in (2.2.34), the frequency spectrum at a point has the form given in (2.2.37), and the constant C^E is

$$C^E = \frac{4a^{2/3}\alpha_k}{3 \times 2^{2/3}\sqrt{\pi}}\Gamma\left(\frac{5}{6}\right) = 0.8 \qquad \text{for} \qquad a = 1.0. \tag{2.2.38}$$

Again we are *assuming* that the spatial variation of the large scales does not affect $\mathcal{E}(\omega, k)$.

The form of this model for $\mathcal{E}(k, \omega)$ agrees with the results of a Direct Numerical Simulation of homogeneous turbulence by Hunt *et al.* (1987). They found that the wavenumber-frequency energy spectrum had a similar form to the advective term in (2.2.34), namely

$$\mathcal{E}(k, \omega) = \alpha_k \varepsilon^{2/3} k^{-5/3} \frac{\exp\left\{-\frac{1}{2}\omega^2 \big/ (akU_0)^2\right\}}{\sqrt{2\pi}(akU_0)}. \tag{2.2.39}$$

But the coefficient a was approximately equal to 0.5, rather than 1. This was probably due to the low Reynolds number of the simulation, in which there was no inertial range. In §2.3 we compare our simulation with (2.2.37) and (2.2.38), which are approximate deductions based on the forms we have chosen for the large and small scale fields, but which neglect the *spatial variation* of the large scales.

2.2.7 Pressure

From any simulation of a velocity field it is possible to compute the pressure field, and Kinematic Simulation is no exception. We first review the principles underlying the calculation of the fluctuating pressure field, and then compare out results with theoretical predictions in §2.5. The pressure is related to the velocity field by the equation

$$\frac{1}{\rho}\nabla p = -\frac{\partial \mathbf{u}}{\partial t} - (\mathbf{u}.\nabla)\mathbf{u}. \tag{2.2.40}$$

Decomposing the velocity and pressure fields into large and small scale fields, we obtain:

$$-\frac{1}{\rho}\nabla(p_\ell + p_s) = \frac{\partial}{\partial t}(\mathbf{u}_\ell + \mathbf{u}_s) + (\mathbf{u}_\ell + \mathbf{u}_s).\nabla(\mathbf{u}_\ell + \mathbf{u}_s). \tag{2.2.41}$$

Averaging the pressure over a small region in space, with characteristic length L, yields the equation for the large scale pressure field:

$$-\frac{1}{\rho}\nabla p_\ell = \frac{\partial}{\partial t}\mathbf{u}_\ell + \mathbf{u}_\ell.\nabla \mathbf{u}_\ell + \langle\!\langle \mathbf{u}_s.\nabla \mathbf{u}_s \rangle\!\rangle, \tag{2.2.42}$$

where $\langle\!\langle\ \rangle\!\rangle$ denotes the spatial average, $\langle\!\langle \mathbf{u}_s \rangle\!\rangle = 0$ and $\langle\!\langle \mathbf{u}_\ell \rangle\!\rangle = \mathbf{u}_\ell$. Subtracting this from (2.41), yields the small scale pressure field:

$$-\frac{1}{\rho}\nabla p_s = \frac{\partial}{\partial t}\mathbf{u}_s + \mathbf{u}_s.\nabla \mathbf{u}_s - \langle\!\langle \mathbf{u}_s.\nabla \mathbf{u}_s \rangle\!\rangle + \mathbf{u}_s.\nabla \mathbf{u}_\ell + \mathbf{u}_\ell.\nabla \mathbf{u}_s. \tag{2.2.43}$$

Assuming that the small scale field is statistically stationary, isotropic and locally homogeneous, Kolmogorov's hypothesis implies that statistical quantities $\langle\!\langle u_{si}u_{sj}(\mathbf{x},t)\rangle\!\rangle$, $\langle\!\langle u_{\ell i}(\mathbf{x},t)\rangle\!\rangle$ do not vary appreciably over a small region (with characteristic length L); i.e.,

$$\frac{\partial}{\partial x_i}\langle\!\langle u_{si}u_{sj}(\mathbf{x},t)\rangle\!\rangle = 0, \qquad \frac{\partial}{\partial x_i}\langle\!\langle u_{\ell i}(\mathbf{x},t)\rangle\!\rangle = 0, \qquad \text{for} \qquad |\mathbf{x}'-\mathbf{x}| < L. \quad (2.2.44)$$

Substituting these into (2.42) gives the equation for the large scale pressure field:

$$-\frac{1}{\rho}\nabla p_\ell = \frac{\partial}{\partial t}\mathbf{u}_\ell + \mathbf{u}_\ell.\nabla\mathbf{u}_\ell \qquad \text{for} \qquad |\mathbf{x}'-\mathbf{x}| < L. \quad (2.2.45)$$

In a frame of reference moving with the large scale velocity $\mathbf{u}_\ell(\mathbf{x},t)$, the small scale pressure field (2.43) also reduces to

$$-\frac{1}{\rho}\nabla p_s = \frac{\partial}{\partial t}\mathbf{u}_s + \mathbf{u}_s.\nabla\mathbf{u}_s \qquad \text{for} \qquad |\mathbf{x}'-\mathbf{x}| < L, \quad (2.2.46)$$

where p_s is now the small scale pressure field in a frame, moving with the large scale velocity $\mathbf{u}_\ell$.

Taking the divergence of the equations (2.45) and (2.46) yields the Poisson equations for the two pressure fields:

$$\frac{1}{\rho}\nabla^2 p_\ell(\mathbf{x}) = -\frac{\partial^2 u_{\ell i}u_{\ell j}}{\partial x_i\partial x_j} \qquad \text{and} \qquad \frac{1}{\rho}\nabla^2 p_s(\mathbf{x}) = -\frac{\partial^2 u_{si}u_{sj}}{\partial x_i\partial x_j}, \quad (2.2.47)$$

where repeated suffixes are summed over the values 1, 2 and 3, ∇^2 is the Laplacian operator, p represents the instantaneous static pressure, ρ is the density and u_i is the instantaneous velocity of the i component. Therefore the pressure is related to the spatial derivatives of the velocity field by the Poisson equation. It is not directly related to the time dependence of the turbulence.

The pressure can therefore be computed as a function of known Fourier coefficients (and therefore insensitive to the choice of k_c). If we write the two velocity components as

$$u_i = \sum_n (\mathbf{a}_n)_i \sin\left(\boldsymbol{\kappa}_n.\mathbf{x} + (\boldsymbol{\psi}_n)_i\right), u_j = \sum_m (\mathbf{a}_m)_j \sin\left(\boldsymbol{\kappa}_m.\mathbf{x} + (\boldsymbol{\psi}_m)_j\right), \quad (2.2.48)$$

then the product of the two velocities is given by

$$u_i u_j = \sum_n \sum_m \frac{1}{2}(\mathbf{a}_n)_i(\mathbf{a}_m)_j\left\{\cos\left[(\boldsymbol{\kappa}_n-\boldsymbol{\kappa}_m).\mathbf{x} + (\boldsymbol{\psi}_n)_i - (\boldsymbol{\psi}_m)_j\right] - \cos\left[(\boldsymbol{\kappa}_n+\boldsymbol{\kappa}_m).\mathbf{x} + (\boldsymbol{\psi}_n)_i + (\boldsymbol{\psi}_m)_j\right]\right\}.$$

Taking the divergence of $u_i u_j$, we have

$$\frac{\partial^2}{\partial x_i\partial x_j}u_i u_j = -\frac{1}{2}\sum_n\sum_m(\mathbf{a}_n)_i(\mathbf{a}_m)_j\left\{(\boldsymbol{\kappa}_n-\boldsymbol{\kappa}_m)_i(\boldsymbol{\kappa}_n-\boldsymbol{\kappa}_m)_j \cos\left[(\boldsymbol{\kappa}_n-\boldsymbol{\kappa}_m).\mathbf{x} + (\boldsymbol{\psi}_n)_i - (\boldsymbol{\psi}_m)_j\right]\right.$$

$$\left. - (\boldsymbol{\kappa}_n+\boldsymbol{\kappa}_m)_i(\boldsymbol{\kappa}_n+\boldsymbol{\kappa}_m)_j \cos\left[(\boldsymbol{\kappa}_n+\boldsymbol{\kappa}_m).\mathbf{x} + (\boldsymbol{\psi}_n)_i + (\boldsymbol{\psi}_m)_j\right]\right\}. \quad (2.2.49)$$

Substituting (2.49) into (2.47) leads to

$$\frac{p}{\rho} = \sum_n \sum_m \left\{ h_{nmij} \cos\left[(\boldsymbol{\kappa}_n - \boldsymbol{\kappa}_m).\mathbf{x} + (\boldsymbol{\psi}_n)_i - (\boldsymbol{\psi}_m)_j \right] \right.$$

$$\left. + g_{nmij} \cos\left[(\boldsymbol{\kappa}_n + \boldsymbol{\kappa}_m).\mathbf{x} + (\boldsymbol{\psi}_n)_i + (\boldsymbol{\psi}_m)_j \right] \right\}, \tag{2.2.50}$$

where

$$h_{nmij} = -\frac{1}{2}(\mathbf{a}_n)_i(\mathbf{a}_m)_j(\boldsymbol{\kappa}_n - \boldsymbol{\kappa}_m)_i(\boldsymbol{\kappa}_n - \boldsymbol{\kappa}_m)_j / (\boldsymbol{\kappa}_n - \boldsymbol{\kappa}_m)^2 \tag{2.2.51a}$$

and

$$g_{nmij} = \frac{1}{2}(\mathbf{a}_n)_i(\mathbf{a}_m)_j(\boldsymbol{\kappa}_n + \boldsymbol{\kappa}_m)_i(\boldsymbol{\kappa}_n + \boldsymbol{\kappa}_m)_j / (\boldsymbol{\kappa}_n + \boldsymbol{\kappa}_m)^2. \tag{2.2.51b}$$

Therefore the large and small scale pressure fields can be computed from the known Fourier coefficients for the large and small scale fields. This is a double sum over all possible wavenumber pairs, and is computationally very expensive.

2.2.8 Computational method

The fluid velocity at $(\mathbf{x}, t)$ is given (2.2.15 and 2.2.18) in terms of the large scale field at $\mathbf{x}(t)$ and the small scale field at

$$\mathbf{X} = \mathbf{x}(t) - \int_0^t \mathbf{u}_\ell(\mathbf{x}(t'), t')\, dt', \tag{2.2.52}$$

where $\int_0^t \mathbf{u}_\ell(\mathbf{x}(t'), t')\, dt'$ is a Lagrangian integration following a fluid element through the large scale field. $\mathbf{X}$ therefore represents the origin of a fluid element which passes through $\mathbf{x}$ at t; this term models both the advection and the distortion of the small scale field by the large scale field. In order to compute the fluid velocity at $(\mathbf{x}, t)$ it is necessary to evaluate (2.2.52) where $u_\ell(\mathbf{x}, t)$ is known explicitly as a function of $\mathbf{x}$ and t and is given by (2.2.15).

In principle, this backward integration needs to be carried out every time the fluid velocity is evaluated, and this would require an increasingly large amount of computing time as the solution progressed in time, since each backward integration has to be carried out over the elapsed time. There are some simplifications which reduce the number of computations required. If we define the set of starting points $\mathbf{X}(\tau)$ as the solutions to (2.2.52) obtained as time progresses, then we find that these form a smooth curve (see figure 2.5) and that it is possible to extrapolate the values of $\mathbf{X}(\tau)$ up to 5 time steps ahead with reasonably accuracy. This therefore requires that the full backwards integration only needs to be carried out at every 5th time step, with the intermediate values of $\mathbf{X}$ obtained by extrapolation from previous values. The results obtained

with this method differ negligibly from those obtained by carrying out the backward integration at every time step.

For each run of the simulation, statistical quantities were obtained by taking the ensemble average of many realisations; most of the results in this study were computed from independent 100 realisations of the velocity field. All the spectra in this study were obtained using fast Fourier transform of 100 digital records, each of which contained 1024 samples. It is important to take the average of many realisations (rather than just allowing the simulation to run for a long time) because the initial choice of wave vectors, although random, determines much of the 'structure' of the velocity field. Since most of the energy is concentrated in the first few wavenumbers on the large scale motions. Consequently, in any realisation considerable anisotropic is present, even through the fields are statistically isotropic. However, these effects have no substantial bearing on the statistics we seek from average results. Because directional differences appear to be largely averaged out by temporal fluctuations, and statistical isotropy prevails strongly.

The Eulerian velocity field is computed at fixed points. Lagrangian statistics are obtained by tracking fluid elements through the flow. We integrate the equation of motion

$$\frac{\partial}{\partial t}\mathbf{x}(\mathbf{a}, t) = \mathbf{u}\left[\mathbf{x}(\mathbf{a}, t), t\right], \qquad \text{with} \qquad \mathbf{x}(\mathbf{a}, 0) = \mathbf{a}, \qquad (2.2.53)$$

using an extended Runge-Kutta scheme modified by Drummond *et al.* (1984).

For each realisation of the velocity field the trajectories of 27 particles were computed simultaneously. The particles were released at the nodes of a $3 \times 3 \times 3$ lattice, spaced 6 integral length scales apart to minimise any initial correlation between the motion of the different particles. They were then tracked simultaneously for the required number of time steps and as many realisations as possible were generated, in order to produce accurate statistics. Spatial homogeneity is crucial because it enable us to treat each particle as representing a different realisations of the underlying stochastic process. This justifies taking ensemble averages over all 2700 particles.

The time step is determined by the need to track the motion of fluid elements at the smallest length scales. The smallest wavelength is $2\pi/k_{38}$, which is about $0.12L_{11}$, where $L_{11}(= 1.0)$ is the integral length scale. Taking the rms velocity $\sigma_u(= 1.0)$ as a typical local velocity, the smallest time scale is of order $0.12L_{11}/\sigma_u$ and we require Δt to be about $1/10^{\text{th}}$ of this, *i.e.* $\Delta t < 0.012L_{11}/\sigma_u$. After some tests to ensure that the results were independent of Δt to within the statistical errors, we chose $\Delta t = 0.0075$. The computations were carried out in single precision on the Cray-2 computer at UKAEA Harwell Laboratories and in double precision on the IBM (3080) computer at University of Cambridge.

with this method differ negligibly from those obtained by carrying out the backward integration at every time step.

For each run of the simulation, statistical quantities were obtained by taking the ensemble average of many realisations; most of the results in this study were computed from independent 100 realisations of the velocity field. All the spectra in this study were obtained using fast Fourier transform of 100 digital records, each of which contained 1024 samples. It is important to take the average of many realisations (rather than just allowing the simulation to run for a long time) because the initial choice of wave vectors, although random, determines much of the 'structure' of the velocity field. Since most of the energy is concentrated in the first few wavenumbers on the large scale motions. Consequently, in any realisation considerable anisotropic is present, even through the fields are statistically isotropic. However, these effects have no substantial bearing on the statistics we seek from average results. Because directional differences appear to be largely averaged out by temporal fluctuations, and statistical isotropy prevails strongly.

The Eulerian velocity field is computed at fixed points. Lagrangian statistics are obtained by tracking fluid elements through the flow. We integrate the equation of motion

$$\frac{\partial}{\partial t}\mathbf{x}(\mathbf{a}, t) = \mathbf{u}\left[\mathbf{x}(\mathbf{a}, t), t\right], \qquad \text{with} \qquad \mathbf{x}(\mathbf{a}, 0) = \mathbf{a}, \qquad (2.2.53)$$

using an extended Runge-Kutta scheme modified by Drummond *et al.* (1984).

For each realisation of the velocity field the trajectories of 27 particles were computed simultaneously. The particles were released at the nodes of a $3 \times 3 \times 3$ lattice, spaced 6 integral length scales apart to minimise any initial correlation between the motion of the different particles. They were then tracked simultaneously for the required number of time steps and as many realisations as possible were generated, in order to produce accurate statistics. Spatial homogeneity is crucial because it enable us to treat each particle as representing a different realisations of the underlying stochastic process. This justifies taking ensemble averages over all 2700 particles.

The time step is determined by the need to track the motion of fluid elements at the smallest length scales. The smallest wavelength is $2\pi/k_{38}$, which is about $0.12L_{11}$, where $L_{11}(= 1.0)$ is the integral length scale. Taking the rms velocity $\sigma_u(= 1.0)$ as a typical local velocity, the smallest time scale is of order $0.12L_{11}/\sigma_u$ and we require Δt to be about $1/10^{\text{th}}$ of this, *i.e.* $\Delta t < 0.012L_{11}/\sigma_u$. After some tests to ensure that the results were independent of Δt to within the statistical errors, we chose $\Delta t = 0.0075$. The computations were carried out in single precision on the Cray-2 computer at UKAEA Harwell Laboratories and in double precision on the IBM (3080) computer at University of Cambridge.

The method that we have developed is particularly useful and easy to implement on parallel computers. Since we are investigating passive fluid particles, each processor in the parallel array can be assigned a particle and then the full efficiency of the parallel machine can be exploited.

2.2.9 Continuity

The 'sweeping' of the small scales by the large scales is non-uniform in space, so continuity is not explicitly satisfied. Taking the gradient of the velocity field yields terms such as $(\mathbf{a}_n \wedge \hat{\boldsymbol{\kappa}}_n).\nabla(\boldsymbol{\kappa}_n.\mathbf{x}_L)$ which are non-zero because $\mathbf{x}_L$ – the displacement due to the large scales – is a function of $\mathbf{x}$. In order to satisfy continuity it is necessary for the wavenumber $\boldsymbol{\kappa}$ (and therefore frequency ω') to be function of time.

Consider the small scale velocity field represented in complex form by

$$u_i(\mathbf{x}, t) = \sum_{n=-N}^{N} A_i^{(n)} \exp i \left\{ \kappa_j^{(n)} X_j - \omega'_n t \right\}, \tag{2.2.54}$$

where

$$A_i^{(n)} = \epsilon_{ijk}(a_k^{(n)} \hat{\kappa}_j^{(n)} - b_k^{(n)} \hat{\kappa}_j^{(n)}),$$

and the Fourier coefficients $a_i^{(n)}$ is not a function of time. Let $u = u_s$ and $U = u_\ell$, then to second order, X_j can be expressed in term of gradients of the large scale sweeping motion,

$$X_j = x_j + \int_0^t U_j(\mathbf{x}, t) \, dt$$

$$= x_j + \int_0^t U_j(0) \, dt + x_k \int_0^t \frac{\partial U_j}{\partial x_k} \, dt + \mathcal{O}\left(\frac{\partial U_j}{\partial x_k}\right)^2. \tag{2.2.55}$$

Note that for conservation of wave-fronts (Townsend 1976), the wave-vector must satisfy the differential equation

$$\frac{\partial k_j}{\partial t} + U_j \frac{\partial k_j}{\partial x_i} + k_j \frac{\partial U_j}{\partial x_i} = 0.$$

Thus the wave-vector $\boldsymbol{\kappa}$ of the small scale velocity field varies in time and slowly in space. Taking the divergence of u_i in (2.2.54), together with (2.2.55), we obtain

$$\frac{\partial u_i}{\partial x_i} = \sum_n i \left\{ A_i^{(n)} k_i^{(n)}(t) + A_i^{(n)} k_j^{(n)} \int \frac{\partial U_j}{\partial x_i} \, dt + A_i^{(n)} X_j \frac{\partial k_j}{\partial x_i} \right\} \exp i \left\{ k_j^{(n)} X_j - \omega' t \right\}. \tag{2.2.56}$$

But

$$k_i(t) = k_i(t = 0) + \int_0^t \frac{\partial k_i}{\partial t} \, dt,$$

substituting this into (2.2.56), and the condition of incompressibility, $\partial u_i/\partial x_i = 0$, requires that for each wave-number mode, we must have (dropping the superscript n)

$$A_i k_i(t=0) + A_i \left[\int_0^t \left(\frac{\partial k_j}{\partial t} + U_j \frac{\partial k_j}{\partial x_i} + k_j \frac{\partial U_j}{\partial x_i} \right) \, dt \right] + A_i x_j \frac{\partial k_j}{\partial x_i} = 0. \qquad (2.2.57)$$

Then continuity can be satisfied by satisfying three additional conditions namely:

(1) $A_i k_i(t=0) = 0$ (this is satisfied by (2.2.0));

(2) $k_j(\mathbf{x}) = $ constant (over any region of effectively uniform straining);

(3) Let k_j vary with *time* such that

$$\frac{\partial k_i}{\partial t} = -k_j \frac{\partial U_j}{\partial x_i}. \qquad (2.2.58)$$

The equation (2.2.58) describes the rotation and distortion of the small scale wavenumber motion by the large scale velocity gradients. Therefore, in the region where the large scale velocity field varies slowly, and k_i varies with time, the error in $\partial u_i/\partial x_i$ will now be proportional to $\partial^2 U/\partial x^2 \sim (\ell/L)^2$.

Consequently if k is varying slowly with time, ω' must also be vary with time. Then the correct form for the Eulerian-Lagrangian autocorrelation function, (see Appendix B), would be from (B1)

$$R^{(EL)}(\tau) = \sum_{n=-\infty}^{\infty} \langle \mathbf{a}_n^2 \rangle \exp i \left[\left\{ -k_j \frac{\partial U_j}{\partial x_i} x_i \tau + k_j \frac{\partial U_j}{\partial x_i} \tau \int_0^t u_i(\mathbf{x}, t) \, dt + \omega'_n \tau \right\} \right], \qquad (2.2.59)$$

where we have used the fact that $\partial k_i/\partial t = k_j \partial U_j/\partial x_i$. Since the flow field is stationary in time, we let $t = 0$, so (2.2.59) can be rewritten as

$$R^{EL}(\tau) = \sum_{n=-\infty}^{\infty} \langle \mathbf{a}_n^2 \rangle \exp(i\omega''_n \tau), \qquad (2.2.60)$$

where

$$\omega''_n = \omega'_n - k_j^{(n)} \frac{\partial U_j}{\partial x_i} x_i, \qquad (2.2.61)$$

since $R^{EL}(\tau)$ must be independent of $\mathbf{x}$ and from (B3), it follows that

$$\omega'_n = \lambda \varepsilon^{2/3} k_n^{2/3} + k_j^{(n)} \frac{\partial U_j}{\partial x_i} x_i. \qquad (2.2.62)$$

This method results in an error in the continuity equation which is second order rather than first order (if changes in κ and ω are neglected). However it also make the computation about 40% more expensive.

To enable us to examine the first and second order errors in the continuity equation, consider an arbitrary cube with volume V fixed relative to Eulerian co-ordinates and entirely within the fluid. Fluid moves into or out of this volume at points over its surface. Let ds_p be an element of the surface (its direction is the outward normal) and $\mathbf{u}_p$ be the velocity at the position of this element, it is the component of $\mathbf{u}_p$ parallel to ds_p that transfers fluid out of V. Thus, the outward flux (flow per unit time) through the element is $\mathbf{u}_p.\mathbf{s}_p$. Hence the flux across any two opposite faces is

$$\Im^{(i)} = \int_{\mathcal{S}} \mathbf{u}_p.d\mathbf{s}_p, \qquad \text{where} \qquad i = 1, 2 \text{ or } 3.$$

The integration is over any two opposite faces of which ds_p is an element. The total error $\mathcal{J}$ in the continuity equation is

$$\mathcal{J} = \sum_{i=1}^{3} \Im^{(i)}.$$

This is negligible if it is much smaller than the flux across any two opposite faces for all time, i.e. if

$$\mathcal{J} \Big/ \Im^{(j)}_{+-} \ll 1, \qquad \text{for} \qquad j = 1, 2 \text{ or } 3.$$

A number of test for both first and second orders using cubes of different sizes showed that the inequality was well satisfied (typical ratio ≈ 0.1) even when the size of the cube $L = L_{11}$, the case where we would expect the largest errors as shown in figure 2.6 for the first order case, the ratio is even smaller for the second order case (though the result are not plotted here). In view of the computations expense involved in considering κ and ω as variables, and the small errors involved in ignoring this variation, in subsequent computations, κ and ω are therefore as constants.

2.3 Simulation results for Eulerian field

According to the Kolmogorov (1941) hypothesis, at high Reynolds numbers, small-scale statistics scaled by Kolmogorov scales are universal. In this section, we focus on the physical significance of the Eulerian statistics obtained from KS at high Reynolds numbers, also with the aim of checking various statistics of dependence.

2.3.1 One point statistical test of the flow field

Various quantities have been calculated in order to check that the flow field has the desired properties. These show that, for a large number of realisations ($\geqslant 100$):

(a) $\langle \mathbf{u}(\mathbf{x}, t) \rangle \to 0 \pm 0.03$;

(b) $\langle \mathbf{x}(t) \rangle \to 0 \pm 0.02$;

(c) $\langle u_i^2(\mathbf{x}, t) \rangle \to 1 \pm 0.05$, $\quad i = 1, 2, 3$, for all $\mathbf{x}$ and t (isotropic, homogeneous and stationary).

The existence of an approximately normal distribution of the velocity at one point has been known for many years. It is not easy to determine whether this has been accomplished, but statistical quantities of order three and higher (e.g. skewness and flatness) are often used as indicators. Figure 2.7 shows that the computed flatness factors $\langle u_i^4 \rangle / 3(\langle u_i^2 \rangle)^2$ and $\langle u_i^6 \rangle / 7.5 \langle u_i^2 \rangle^3$ converge to the theoretical values of 1.0 and 2.0 respectively (Gaussian values), and the skewness factors $\langle u_1^3 \rangle / \langle u_1^2 \rangle^{3/2}$ and $\langle u_1^5 \rangle / \langle u_1^2 \rangle^{5/2}$ converge to the theoretical value of 0.0.

2.3.2 Eulerian time scale

The simulation has been defined to satisfy four constraints; (i) Gaussian statistics; (ii) the form for the space-time structure of the large scale motions; (iii) the Eulerian wavenumber spectrum and (iv) the small scale 'Eulerian-Lagrangian' structure function. In order to test whether these constraints are sufficient to define a satisfactory model, we have computed the Eulerian and Lagrangian space-time correlations and spectra and have compared these with results obtained by other investigators.

The autocorrelation of the fluctuating velocity at a point, $R_{11}^E(\tau)$, is presented in figure 2.8. It is positive for all τ. The integral time scale T_{11}^E is defined as $\int\limits_0^\infty R_{11}^E(\tau)\, d\tau$ (Taylor 1921) but it can be difficult to calculate this from a record of finite duration (Comte-Bellot and Corrsin 1971) so we define it as the value value of τ at which R_{11}^E falls to $1/e$ of its value at $\tau = 0.0$. On this basis we obtain $T_{11}^E = 0.8$.

Several authors (e.g. Philip 1967, Pasquill 1974) have suggested that the Lagrangian correlation and the Eulerian temporal correlations are identical in shape but with a different scale for the independent variable (i.e. $R^L(\tau) = R^E(\beta^E \tau)$). The grid turbulence measurements of Favre *et al.* (1957) and numerical simulations of Moser and Moin (1984) for channel flow, Squires (1988) for decaying grid turbulence and Hunt *et al.* (1987) for stationary, homogeneous turbulence indicate that the value of $T_{11}^E = T_E$, normalised in terms of the rms velocity and the integral length scale L_{11} has a range of values given by

$$\beta^E T_E = L_{11} \Big/ \sqrt{\langle u_1^2 \rangle}, \tag{2.3.1}$$

where $1 \leq \beta^E \leq 2$. Snyder and Lumley (1971) inferred a value of $\beta^E \simeq 3$ by interpreting their heavy-particle correlations as representative of Eulerian correlations and light-particle results as representative of Lagrangian correlations. Pasquill (1974) suggested that for atmospheric turbulence β^E is independent of the turbulent field and proposed a value of $\beta^E = 4$, based on

experiments. But from our simulation of high Reynolds number turbulence we obtain $\beta^E \simeq$ 1.25, which is somewhat less than the values obtained by other workers. Two other runs with $k_c = 2.5$ and 10.0 were made and the results are listed in Table 2.4.

2.3.3 Eulerian frequency

Figure 2.9 shows the computed form of $\phi_{11}^E(\omega)$. Over most of the inertial range ($10 < k < 50$), there is a slope of $-5/3$ showing that the advection has a much larger effect on the frequency spectrum than the decorrelation of the small eddies. The computed value of $C^E = 0.82$. This is close to the value of 0.8 derived in (2.2.38) on the assumption that the spatial variation in the large scale velocity does not affect the spectrum. For other statistics this is an inappropriate assumption, as we show in the next section.

2.3.4 The spatial structure function

The spatial structure function $D_{11}(r,0,0)$ measures the correlation of fluid velocities at different locations in the flow:

$$D_{11}(r,0,0) = \left\langle [u_1(x+r,t) - u_1(x,t)]^2 \right\rangle. \tag{2.3.2}$$

In the inertial subrange it can only depend on ε, by dimensional arguments. From the Fourier transform of the spectrum for an infinite inertial subrange, we have

$$D_{11}(r,0,0) = C'\varepsilon^{2/3} r^{2/3}, \tag{2.3.3}$$

where $C' = \dfrac{27}{55}\Gamma\left(\dfrac{1}{3}\right)\alpha_k$ (Batchelor 1953).

In a real turbulent flow, in which the inertial subrange is not infinite, one would expect the two-thirds law to be obeyed up to a distance k_c^{-1}, comparable with a typical length scale of the flow. As the distance r increases beyond this, the structure function will continue to increase, but at a slower rate. For an energy spectrum truncated at k_c and k_η the truncated structure function can be obtained by taking the Fourier transform of the spectrum in the range $k_c < k < k_\eta$. Assuming $\phi_{11} \propto k^{-5/3}$ we have:

$$D_{11}(r,0,0) = 2\int_{k_c}^{k_\eta} \phi_{11}(k_1)\left(1 - \cos k_1 r\right)\,dk_1$$

$$\approx \frac{18\alpha_k}{55}\varepsilon^{2/3} r^{2/3}\left[\frac{3}{2}\Gamma\left(\frac{1}{3}\right) + \frac{3}{4}(k_c r)^{4/3} - 3(k_\eta r)^{-2/3}\right]. \tag{2.3.4}$$

The difference between the truncated and infinite forms of the structure function is given by:

$$\frac{0.5(k_c r)^{4/3} - 2(k_\eta r)^{-2/3}}{\Gamma\left(\frac{1}{3}\right)}.$$

For $k_\eta/k_c = 10$, the maximum difference in the range $0.05 < r < 0.15$ is about 40%, but as k_η/k_c is increased the difference decreases; for $k_\eta/k_c = 100$, 200 and 300 the maximum difference drops to 28%, 15% and 10% respectively.

The structure function is plotted in figure 2.10. The straight line portion has a slope of approximately 2/3 and the constant C' is equal to 1.7; this should be compared with the experimental value of 2.0 ± 0.1 (Townsend 1976). The correction terms in (2.3.4) explain the sensitivity of various statistics to the extent of the inertial range.

2.3.5 The skewness factor

The dimensionless skewness factor S for the velocity gradient $\partial u/\partial x$ is defined as

$$S = \left\langle \left(\frac{\partial u_1}{\partial x_1} \right)^3 \right\rangle \bigg/ \left[\left\langle \left(\frac{\partial u_1}{\partial x_1} \right)^2 \right\rangle \right]^{3/2} \tag{2.3.5}$$

(Batchelor and Townsend 1947). This is *negative* in a turbulent flow and is usually explained in terms of vortex lines being stretched by the tendency of fluid elements to move apart. Measurements in grid turbulence (Batchelor and Townsend 1947, Stewart 1951) show that at sufficiently large Reynolds numbers S tends to a constant value of about -0.3, and Direct Numerical Simulation at moderate Reynolds numbers gives a value of -0.5 (Orszag and Patterson 1972).

However, the negative skewness can also be affected by the kinematics of the turbulent flow, i.e. by non-uniform sweeping of the small scales by the large – 'wave-packing'. This contribution to S can be estimated by considering separately the third moments of derivatives of the large and small scale velocity fields:

$$\left\langle \left[\frac{\partial (u_\ell + u_s)}{\partial x} \right]^3 \right\rangle = \left\langle \left(\frac{\partial u_\ell}{\partial x} \right)^3 \right\rangle + \left\langle \left(\frac{\partial u_s}{\partial x} \right)^3 \right\rangle + 3 \left\langle \left(\frac{\partial u_\ell}{\partial x} \right)^2 \frac{\partial u_s}{\partial x} \right\rangle + 3 \left\langle \left(\frac{\partial u_s}{\partial x} \right)^2 \frac{\partial u_\ell}{\partial x} \right\rangle. \tag{2.3.6}$$

In our simulation, the first two terms on the right hand side are zero since both u_ℓ and u_s are Gaussian and the magnitude of the third term is small compared with the fourth since the spatial variation of u_ℓ is small. Therefore (2.3.6) becomes:

$$\left\langle \left(\frac{\partial (u_\ell + u_s)}{\partial x} \right)^3 \right\rangle \sim 3 \left\langle \left(\frac{\partial u_s}{\partial x} \right)^2 \frac{\partial u_\ell}{\partial x} \right\rangle. \tag{2.3.7}$$

Consider a stagnation region in the flow (figure 4b). Along a streamline leading into the region $\partial u_\ell/\partial x < 0$; from the analysis of wave number evolution (2.2.57), $|k_1|$ – and therefore $(\partial u_s/\partial x)^2$ – increases with time. Along a streamline leading out of the region $\partial u_\ell/\partial x > 0$ and $(\partial u_s/\partial x)^2$ decreases with time. Thus on streamlines where $\partial u_\ell/\partial x < 0$, S is large and negative; where $\partial u_\ell/\partial x > 0$, S is small and positive. Figure 2.11 shows the evolution of the skewness of the

longitudinal velocity-derivative, defined as (2.3.5); for demonstration purposes, the simulation was done with 2 modes in the large scales and 6 modes in the small scales. The skewness is zero to begin with, because the initial turbulence is Gaussian, but it decreases to about -0.15 as time progresses; this is about half the experimental value of -0.3. It seems that this is an important effect which is usually overlooked in explanations of the skewness of turbulence. The kinematic contribution to S would be higher if the model also allowed the large 'small scale eddies' to sweep the small 'small scale eddies' (see §2.1.1).

2.3.6 *How can we quantify 'Structure' in a flow* ?

Many measurements in turbulent flows and experiments published during the past 20 years, clearly show large scale characteristic flow patterns in turbulence shear flows. These patterns, often called coherent structures, retain their coherence over relatively long distances in the dominant flow direction. From a conceptual standpoint, these observations suggest that the turbulent motion is comprised of "quasi-deterministic" unsteady large scale eddy motions and fine grained random fluctuations. The identification of certain significant regions in a flow can provide an important method for analysing the dynamics of the flow and might enable us to simplify the way in which we model some flows. Recent experimental and computational research (Maxey 1987, Hunt *et al.* 1988a) has shown that bubbles tend to concentrate in low-pressure regions, whilst denser particles, especially if buoyancy forces are important, tend to concentrate in the streaming regions between eddies. But those particles that are entrained into eddy regions can remain there for long periods.

Flow visualisation can be used to identify structures and infer their qualitative topology. However, detection as well as detailed investigation of the structure of the flow is complicated by the large dispersion in the shape, size, orientation, strength and convection velocity of the structure. Structures typically undergo cycles of formation, growth and decay. Moreover, there is no generally agreed way of classifying the structure of the flow. The aim of the study in this section is to use the criteria for defining different flow zones which has been developed at CTR (Hunt *et al.* 1988b) and test the variability and reliability of the criteria.

I. Zone algorithms

Following Perry and Chong (1987) and Hunt *et al.* (1988b), we consider the flow to be composed of four different types of region – eddy, shear, streaming and convergence – and seek a set of criteria for distinguishing between them. As an initial criterion we use the second invariant, II, to define regions of large scale irrotational/rotational motion:

$$\Pi = \frac{\partial u_i}{\partial x_j} \frac{\partial u_j}{\partial x_i} = \frac{1}{4} \left\{ \overbrace{\left(\frac{\partial u_i}{\partial x_j} + \frac{\partial u_j}{\partial x_i} \right)^2}^{\text{strain rate}} - \overbrace{\left(\frac{\partial u_i}{\partial x_j} - \frac{\partial u_j}{\partial x_i} \right)^2}^{\text{vorticity}} \right\} = \frac{1}{4} \left(S_{ij}^2 - \Omega_{ij}^2 \right). \qquad (2.3.8)$$

To distinguish the four regions, we use some threshold values of Π, says, Π_E, Π_C and Π_S. We define eddy regions (E) as strong swirling zones with vorticity in which fluid particles typically have a long residence time. Irrotational swirling motion outside the zones is excluded. Therefore, we define eddy regions as those points where $\Pi < -\Pi_E$, — high vorticity as compared with the irrotational straining. Shear region (SH) are defined to have significant vorticity but without a circulating flow pattern, so the criteria for Π is same as for eddy regions, i.e. $\Pi < -\Pi_E$. Convergence regions (C) are defined as regions where there is irrotational straining motion and where there is strong convergence and divergence of streamlines. The criteria for the convergence zones must be such as to avoid the irrotational swirling flow around vortices. Therefore, we require $\Pi > \Pi_C$ — high strain rate as compared with the vorticity. Streaming regions (S) are defined as where the flow is moving relatively fast but without significant distortion or rotation. These zones are the main passages for fluid particles to be transported across the flow. Therefore, we require $|\Pi| < \Pi_S$ for weak curvature and convergence.

Plate 1 shows the velocity vectors superimposed on the second invariant. Although there is some agreement there are a number of reasons for introducing a further set of criteria. Firstly, the existing criteria simply divide the flow field into four, whereas we expect there to be regions of random small-scale motion as well. Secondly, each of the four classes is too all-embracing – a region may have high vorticity without being an eddy, for example. So we introduce four further criteria. For eddies, we require that the pressure is low so that if the flow is rotational, then the streamlines tend to curve around them (Hunt *et al.* 1988b). A criterion is that $p < p_E$, where p_E is a threshold value. It is the elliptic dependence of the pressure on $\mathbf{u}$ that allow us to make such a condition local in $\mathbf{x}$. Similarly, convergence zones are regions of high pressure, so $p > p_C$. The pressure criterion avoids the possibility of irrotational swirl. Shear zones are regions of moderate pressures, i.e $-p_E < p < p_C$. Plate 2 shows the velocity vectors superimposed on the pressure field, and there is good agreement between the pressure and the eddy and convergence regions. Finally, for the streaming region, we require that the velocity exceeds a characteristic velocity, u_S. The full set of criteria can then be illustrated:

eddy (E)	Shear (SH)	streaming (S)	convergence (C)
$\Pi < -\Pi_E$	$\Pi < -\Pi_E$	$|\Pi| < \Pi_S$	$\Pi > \Pi_C$
$p < -p_E$	$-p_E < p < p_C$	$|u| > u_S$	$p > p_C$

These criteria are made mutually exclusive by choosing $\Pi_S \leqslant \min(\Pi_E, \Pi_C)$, but they are not exhaustive, and much of a given turbulent flow field remains unclassified.

Following Wray and Hunt (1989), the values of the parameters are chosen as:

$$\Pi_E = \frac{1}{2}\Pi_{\text{rms}}; \qquad p_E = \frac{1}{2}p_{\text{rms}}; \qquad \Pi_C = \Pi_{\text{rms}}; \qquad p_C = p_{\text{rms}};$$

$$\Pi_S = \min(\Pi_E, \Pi_C) \qquad \text{and} \qquad u_S = u_{\text{rms}},$$

(2.3.9)

where the pressure and velocity rms values are taken relative to the global means.

The next set of observations over the flow and the results obtained therefrom seem consistent with the identification of different zones by Direct Numerical Simulation at low Reynolds number at CTR by Hunt *et al.* (1986).

II. The general features found for the flow regions are:

(a) *Eddy regions*:

Figure 2.12 shows a typical plane of the flow field generated by KS at an instance of time. The arrows represent the velocity vectors on the plane. Red indicates eddy regions and orange indicates shear regions. The region algorithms seems to have correctly identified eddies at the locations of $x = 1.2$, $y = 0.65$ and $x = 2.4$, $y = 0.2$. Other areas, for instance, $x = 2.3$, $y = 0.5$ do not show swirling flow *in this plane*. However, by examining the $y - z$ plane at $x = 2.3$, it was clear that there was a swirling motion in that plane. The typical diameter of these zones using the criteria is about $L/8$ and distributed uniformly in space. Not all eddy zones were circular in the cross section, a few were quite elongated in the plane being examined.

(b) *Shear regions*:

They seem to be regions of shear flow which are a part of the large-scale eddy structure but the curvature of the flow is small, for instance, at $x = 1.8$, $y = 0.25$ and $x = 2.0$, $y = 2.2$. Some of the zones tends to lie at the edge of the eddies, for example at $x = 1.7$, $y = 0.5$. Also, some zones are nearly straight shear layers on the edges of streaming zones, as at $x = 2.1$, $y = 2.3$. The longest extend is about $L/2$.

(c) *Streaming regions:*

The principal features of these regions (green in Figure 2.13) are often associated with a large-scale motion and the curvature is small. They are generally elongated and their typical size is about $0.3L$ and their longest extend is just under L.

(d) *Convergence regions:*

These zones (blue in Figure 2.13) are isolated and have similar size as that of eddy zones. These seem to be generally the collision points of streams, usually as oblique collision, as at $x = 1.3$, $y = 0.1$. Also, with a stagnation point in the zone somewhere, as at $x = 0.6$, $y = 2.0$.

Overall, there is good agreement (see Plate 3) between the observed structure and the regions determined on the zone algorithms, especially remembering that the criteria refer to 3-D space whilst the vectors are plotted in a 2-D plane. We hope that this approach will enable us to begin to classify, *quantitatively*, the importance of structure in particle dispersion.

By looking at the statistics (time average) of various quantities taken over the four zone types and compare them with each other, we wound be able to comment on their role and distinguish various features of the turbulent processes occurring in the flow, for example, kinetic energy production, enstrophy production and strain rate – these turbulent statistics should have great interest to turbulence modellers.

As shown in the table 2.2, the fraction of total volume occupied by the four regions, only about 45% of the total volume is classified as any of the four zone types, and most of that is in the stream regions. Furthermore, the streams dominates energy contributions. Eddy and shear zones dominate contributions to the total enstrophy (important for slow chemical reactions, transport of bubbles and particles) and the convergence zones, though quite small in size, dominate contribution to the total strain rate square, $\int S_{ij}S_{ji}dV$ (important for fast chemical reaction).

In a three-dimensional turbulent flow there are large coherent eddies or vortices, but because vorticity diffuses out of these regions or because vorticity is torn off the eddies when they interact, there has to be much smaller-scale chaotic vorticity in the flow between the large vortices. When vorticity finds itself in a strain-rate field (convergence zones), it is subject to stretching. On the basis of conservation of angular momentum, we expect that the vorticity in the direction of a positive strain rate is amplified, while the vorticity in the direction of a negative strain rate is attenuated. This effect is sketched in Figure 2.14. To quantify the *nature* of the strain, we use the third invariance of the strain tensor, S_{ij}, defined as

$$\mathrm{III} = S_{ij}S_{jk}S_{ki}. \tag{2.3.10}$$

regions	eddy	shear	streaming	convergence	undefined
volume (%)	8.0	6.0	28.0	3.0	55.0
energy contributions (%)	6.7	6.3	38.7	2.5	45.8
enstrophy $|\omega|^2$(%)	29.5	13.9	15.1	1.5	40.0
strain rate square (%)	7.5	5.3	16.7	5.9	64.6
energy contributions/volume	0.8	1.0	1.4	0.8	0.8
enstrophy/volume	3.7	2.3	0.5	0.5	0.7
strain rate square/volume	0.9	0.9	0.6	2.0	1.2

Table 2.2. Von Kárman energy spectrum

For $III > 0$ or $III < 0$ corresponds to one positive and two negative strains or two positive and one negative strains (i.e. elongating or flattening a material sphere in this zone). Processes of reaction depends on the nature of irrotational straining in the C and E zones.

The first thing to note is that the present model (KS), there is no vortex-stretching mechanism (dynamical process). However, as described in section 2.3.5, in Fourier space, 'wave packing' and 'wave stretching' correspond to $III < 0$ and $III > 0$ respectively and hence lead to a negative skewness. In order to quantify this effect, we have computed the third invariant, III, over the flow. Regions where III are positive and negative are indicated by shaded and unshaded areas, on a background of the indicated flow zones in Figure 2.15a.

As expected, the initial field ($t = 0$) is Gaussian and there is no 'wave packing', although III consists of positive and negative values over the flow, but the mean value of $III(t = 0)$ is approximately equal to zero. Eddy and convergence zones are uniformly distributed in space and have no preference of accumulation in either positive or negative III. However, after one integral time scale, T_L, when 'wave-packing' has taken place, it is found that, in the convergence zones, more than 3/4 of the area has $III < 0$, whilst in the eddy zones, more than 3/5 of the area has $III > 0$ (Figure 2.15b). In addition, the maximum positive and negative values of III is located in these zones. The mean value of the third invariant $III(t \approx T_L)$ over the whole flow, contribute a net negative III (i.e. negative skewness), moreover, the main negative contribution to III comes from the convergence zones (convergence zones correlate very strongly with negative III).

III. Reliability of the algorithms for different flows

Are the same criteria (2.3.9) applicable to different types of turbulent flows (spectra)? So far the discussion has centre around the turbulent with von Kárman energy spectrum. A model could be considered useful only if it is able to provide insight into a wider class of flows. For

regions	eddy	shear	streaming	convergence	undefined
volume (%)	13.2	14.6	16.5	7.5	48.2
energy contributions (%)	13.5	12.7	26.5	7.2	40.5
enstrophy $\|\omega\|^2$ (%)	27.7	23.7	12.5	4.0	40.0
strain rate square (%)	9.5	10.1	13.2	15.1	52.1
energy contributions/volume	1.0	0.9	1.6	1.0	0.8
enstrophy/volume	2.1	1.6	0.8	0.5	0.8
strain rate square/volume	0.7	0.7	0.8	2.0	1.1

Table 2.3. exponential decaying energy spectrum

instance, how much of the space should be occupied by eddy, shear, convergence and streaming regions with different flows? How strong of different processes should they be? Answering such questions, we have simulated a new flow field with exponential decay spectrum which has the form $k^2 e^{-ak}$. By applying the same criteria, we have determined the four zones and are shown in Figures 2.16 and 2.17. The agreement seems to be even better than the previous case with Von Kármán energy spectrum. Therefore, it seems that the criteria work well for different type of the flows.

The space occupied by different zones changes significantly with the different flows (spectra) as shown in table 2.3, especially in the shear and convergence zones, both of them occupied more than double of the volumes as compared with the von Kármán energy spectrum. However, the volumes of eddy and streaming zones only decrease slightly. Yet again, only one-half the total volume is classified into any of the four regions. The changes of the volume ratio between different zones is expected since the Lagrangian integral time scale (which depends on how a fluid particle moves through the flow) of the exponential decaying spectrum should be greater than that of the von Kármán spectrum. Therefore, the fluid particle trajectories in the exponential spectrum flow are rather straight, but the length scale over which the velocity is decorrelated is smaller, as in the case of shear zones (curvature small). Also, it occupies less eddy zones which make the velocity of a fluid particle keep changing.

However, the ratios of production of energy contributions, enstrophy and strain rate square to the volume of different zones do not change very much. This indicates that the eddy and shear regions contribute most of production of the enstrophy, streaming to production of energy, whilst convergence to the production of strain rate square.

To what extend does the structure of the flow change as the energy spectrum $E(k)$ changes? Using KS we have computed velocity fields for the von Kármán spectrum and for an exponential decay spectrum, with wave numbers in the range $0 < k \leq 40$. We can see that the structure of

the von Kármán spectrum makes the vorticity distribution 'spotty' with small regions of high vorticity as compared with the exponential decay spectrum, which distributes vorticity more evenly in space.

IV. Big whorls carry little whorls

The interaction of large and small scale eddies in the temporally-developing turbulence has been investigated by plotting the sequence of vorticity contours, ω_3, on top of the velocity vectors in the $x - y$ plane at different times. Figures 2.18a, b display that the weak vortices (Green) move in the direction of high velocity, for example, at $x = 0.3$, $y = 2.0$ and $x = 2.0$, $y = 1.5$ at $t = 0$ being advected to $x = 0.5$, $y = 1.7$ and $x = 2.0$, $y = 2.0$ after $t = 0.5T_L$ later. On the other hand, strong vortices (Orange) move very little under the advection of the velocity, for instance, $x = 0.5$, $y = 1.7$ and $x = 1.0$, $y = 1.0$ hardly move at all after $t = 0.5T_L$ later. This random movement of vortical regions under the action of larger scales has been studied by Hunt *et al.* (1987).

2.4 One point Lagrangian statistics in inertial subrange

Lagrangian statistical quantities are of fundamental important in the understand of turbulence, especially turbulence dispersion and transport processes (Taylor 1921, Monin and Yaglom 1971). We shall in the rest of this section examine several Lagrangian quantities as well as comparison of results with the experimental data.

2.4.1 Lagrangian integral time scale

The Lagrangian integral time scale is defined as $T_L = \int_0^\infty R^L(\tau)\, d\tau$ where $R^L(\tau)$ is the Lagrangian autocorrelation function, i.e.,

$$R^L(\tau) = \frac{\langle u_i(\mathbf{x}(t), t) u_i(\mathbf{x}(t+\tau), t+\tau) \rangle}{\sqrt{\langle u_i^2(\mathbf{x}(t), t) \rangle \langle u_i^2(\mathbf{x}(t+\tau), t+\tau) \rangle}}. \tag{2.4.1}$$

T_L can also be obtained from the mean square displacement of fluid elements; Taylor (1921) showed that

$$\langle \mathbf{x}^2(t) \rangle \simeq \langle \mathbf{u}^2(\mathbf{x}, t) \rangle t^2 \,, \qquad \text{for} \quad t \ll T_L, \tag{2.4.2}$$

$$\langle \mathbf{x}^2(t) \rangle \simeq 2 \langle \mathbf{u}^2(\mathbf{x}, t) \rangle T_L t \,, \qquad \text{for} \quad t \gg T_L. \tag{2.4.3}$$

Figure 2.19 shows a graph of $\log\{\langle \mathbf{x}^2(t) \rangle\}$ against $\log\{t\}$; as predicted, the graph has a slope of 2 at small times, and a slope of 1 at large times. From the graph and figure 2.8 we estimate

that $T_L \approx 0.52$, but we consider this to be a lower bound, since the curve does not extend to very large values of t.

Figure 2.20 shows the effective diffusivity, κ, as a function of time. The value of κ rises from zero, and after a few correlation times settles down to a fixed value ($\simeq 0.52$), which it then maintains within statistical errors. This agrees with the value calculated from the mean square displacement of the particle.

2.4.2 Lagrangian microscale

The Lagrangian microscale, τ_L, is defined as

$$R^L(\tau) = 1 - \frac{\tau^2}{\tau_L^2} + O(\tau^4) \, . \tag{2.4.4}$$

Since it is directly related to the curvature of Lagrangian velocity autocorrelation function $R^L(\tau)$ at the origin (see e.g. Tennekes and Lumley 1972), the microscale is important when velocity autocorrelations at small time lag are examined. Substituting this into the relationship $\frac{1}{2} \langle x_i^2 \rangle = \langle u_i^2 \rangle \int_o^\tau (\tau - \tau') R^L(\tau') \, d\tau'$, we have

$$\frac{1}{2} \langle x_i^2 \rangle = \frac{\tau^2}{2} \left[1 - \frac{1}{6} \frac{\tau^2}{\tau_L^2} \right] , \qquad \text{as} \qquad \tau \to 0. \tag{2.4.5}$$

The Lagrangian microscale can therefore be determined by plotting $\left(1 - \langle x_i^2 \rangle / \tau^2 \right)$ against $\left(\tau^2 \right)$ and estimating the slope of the curve as τ^2 tends to zero (figure 2.21). This yields a value for τ_L of 0.4.

2.4.3 Time scale

An interesting quantity is the non-dimensional constant β^L – the Lagrangian equivalent of the Eulerian constant β^E (see 2.3.1), this is defined as:

$$\beta^L T_L = L_{11} / \sqrt{\langle u_i^2 \rangle}, \tag{2.4.6}$$

where u_i is the rms velocity of one component and L_{11} is the integral length scale as defined in (2.2.22). Experiments and simulations indicate that $\beta^L \approx 1$ for grid turbulence (Snyder and Lumley 1971), and boundary layer turbulence (Durbin and Hunt 1980). However we obtain a value of $\beta^L \approx 1.92$ in high Reynolds number turbulence. We have also tested the sensitivity of β^L to the critical wave number k_c and the results appear in table 2.4; these show that β^L is not very sensitive to k_c. The ratio of the Lagrangian integral timescale to the eddy-turnover time is given in table 2.4and the ratios show a dependence on k_c. In a recent direct numerical

k_c/L	k_η/L	ε	u_ℓ^2/u_s^2	$u_\ell^3 k_c/\varepsilon$	β^L	β^E	T_L/T_E
2.5	50.0	0.7190	0.6393	4.4004	1.80	2.00	1.11
5.0	50.0	0.8215	1.3810	14.5706	1.92	1.25	0.65
10.0	50.0	0.7850	2.8961	42.4210	2.17	1.14	0.53

Table 2.4.

simulation of isotropic turbulence (Re_λ in the range 38–93) Yeung and Pope (1989) found $T_L/T_E \approx 0.8$. This ratio is quite plausibly flow dependent too: measurements suggest it to be ≈ 1.0 in grid turbulence (Shlien and Corrsin 1974), but ≈ 1.7 in the near-ground convective boundary layer (Hanna 1981).

2.4.4 Lagrangian spectrum in inertial subrange

Inoue (1951) applied the Kolmogorov theory to an analysis of the Lagrangian velocity spectrum. For frequencies in the inertial subrange, he obtained

$$\phi_{11}^L(\omega) = C^L \varepsilon \omega^{-2} \qquad \text{for} \qquad \omega_{\mathcal{L}} \ll \omega \ll \omega_\eta, \qquad (2.4.7)$$

where $\omega_{\mathcal{L}}$ refers to the energy-containing part of the Lagrangian spectrum, and ω_η ($= \sqrt{\varepsilon/\nu}$) is the Kolmogorov frequency. C^L is a universal constant of order 1, although its exact value is uncertain. One of the purposes of this exercise is to verify that $\phi_{11}^L(\omega) \propto \omega^{-2}$ and to obtain an estimate for C^L.

We have computed the Lagrangian spectrum $\phi_{11}^L(\omega)$ and the spectrum is plotted in figure 2.22. Over most of the frequency range the spectrum is a straight line with a slope of -2; the deviation at high frequencies is caused by noise from the numerical integration. From the graph we obtain $C^L \varepsilon = 0.58$, giving $C^L = 0.54$. This is consistent with measurements by Hanna (1980) in the atmospheric boundary layer using balloons and tetroons which suggest that $C^L = 0.6 \pm 0.3$. From the direct numerical simulation at $\text{R}_\lambda = 90$, Yeung and Pope (1989) predicted that C^L should be somewhat greater than 0.64.

As a check we have also computed C^L from the velocity autocorrelation. Taking the Fourier transform of the spectrum (2.4.7) yields the autocorrelation

$$R^L(\tau) = \int_{-\infty}^{\infty} \phi_{11}^L(\omega) e^{i\omega\tau}\, d\omega \; = \lim_{b \to 0} \int_{-\infty}^{\infty} \frac{C^L \varepsilon}{b^2 + \omega^2} e^{i\omega\tau}\, d\omega$$

$$= \langle u_1^2 \rangle - \pi C^L \varepsilon \tau \qquad \text{for} \qquad \tau_L \ll \tau \ll T_L. \qquad (2.4.8)$$

From the measured autocorrelation we obtain $C^L = 0.52$ which agrees with our earlier estimate.

2.4.5 The 'Eulerian-Lagrangian' spectrum

In §2.2.6 we calculated the 'Eulerian-Lagrangian' autocorrelation in a frame moving with the large eddies. The Eulerian-Lagrangian spectrum $\phi_{ij}^{EL}(\omega)$ can be obtained from the Fourier transform of this autocorrelation:

$$\phi_{11}^{EL}(\omega) = C^{EL}\varepsilon\omega^{-2}. \tag{2.4.9}$$

We have computed $\phi_{11}^{EL}(\omega)$ for different values of k_η and these are shown in figure 2.23. There is a region with a slope of -2 and the extent of this region increases with k_η. From the graph we estimate $C^{EL} \approx 2.3$. In Appendix B we show how C^{EL} can also be computed for a flow with a large inertial subrange, and derive the result $C^{EL} \approx \frac{3}{2}\alpha_k\lambda$. Substituting in appropriate values ($\alpha_k = 1.5, \lambda\varepsilon^{1/3} = 1.0, \varepsilon = 1.066$) we obtain $C^{EL} = 2.20$ (which agrees well with the measured value) and $C^{EL}/C^L \approx 4.07$.

2.4.6 'Frozen-Lagrangian' spectra

To what extent do the Lagrangian spectra and the time structure function depend on the *unsteadiness* of the velocity field? We have simulated 'frozen turbulence' (i.e. there is no time dependence) and we have computed the Lagrangian spectrum $\phi_{u_{11}}^{FL}(\omega) = \phi_{(u_\ell + u_s)_{11}}^{FL}(\omega)$ of $\mathbf{u}(\mathbf{x}) = \mathbf{u}_\ell(\mathbf{x}) + \mathbf{u}_s(\mathbf{x})$ for different sizes of inertial subrange. The spectra are shown in figure 2.24a. The straight line portions of the spectra have a slope of $-5/3$ (and the range increases as k_η increases) showing that the velocity fluctuations of particles are caused by being swept through the small eddies by the large eddies. This does not happen if the small eddies are themselves swept by the large eddies. The energy in this spectrum is lower than in the Eulerian spectrum $\phi_{11}^E(\omega)$ for all frequencies but higher than in the corresponding Lagrangian spectrum $\phi_{11}^L(\omega)$ at high frequencies; this is an important effect for the turbulent interface problem (Carruthers and Hunt 1986). Therefore to simulate the high frequency velocity and displacement of particles it is *necessary* to simulate the time dependence of the velocity field.

We also computed the Lagrangian velocity spectrum $\phi_{u_{s11}}^{FL}(\omega)$ for the small scale turbulence $\mathbf{u}_s(\mathbf{x})$ (in a frame moving with the large scales), with the time evolution of the small scales 'turned-off', i.e. $\omega_n' = 0$. This spectrum is shown in figure 2.24b. This also produced a result different from that in the time dependent velocity field, which was that $\phi_{u_{s11}}^{FL}$ is proportional to $\omega^{-5/3}$ (fig. 2.24b).

From dimensional arguments, we must have

$$\phi_{u_{s11}}^{FL} = C_{u_s}^{FL}(\varepsilon u_{1s})^{2/3}\omega^{-5/3}$$

and

k_c/L	k_η/L	ε	u_ℓ^2/u_s^2	$u_\ell^3 k_c/\varepsilon$	C_p
1.5	50.0	0.6377	0.3060	0.266	0.407
3.0	50.0	0.7582	0.9690	1.365	0.429
5.0	50.0	1.0660	1.3810	2.072	0.457
7.0	50.0	0.8045	2.8628	5.550	0.501
5.0	25.0	0.8638	2.2725	3.347	0.376
5.0	100.0	1.0365	1.2053	1.946	0.465

Table 2.5.

$$\phi_{u_{11}}^{FL} = C_u^{FL}(\varepsilon u_1)^{2/3}\omega^{-5/3},$$

where u_{1s} and u_1 are the r.m.s. velocity of $\mathbf{u}_s$ and $\mathbf{u}$ in one component, from our simulation, we obtained

$$C_{u_s}^{FL} = 1.12$$

and

$$C_u^{FL} = 1.22.$$

2.5 Pressure field

2.5.1 *The mean-square pressure fluctuation*

Batchelor (1953) obtained an integral expression for the correlation $P(r)$ between the fluctuating pressures at points r apart in a homogeneous isotropic turbulence. He showed how the mean-square fluctuating pressure $\langle \tilde{p}^2 \rangle$ depended on the velocity spectrum $E(k)$, and, in particular, how the maximum contribution to $\langle \tilde{p}^2 \rangle$ came from wavenumbers near the maximum of $E(k)$; that is, the energy-containing range of the spectrum. Using the experimental results of Proudman (1951), he was able to evaluate the expression for $P(r)$ numerically, and compute the pressure coefficient C_p, where

$$C_p = \langle p^2 \rangle / \rho^2 \left(\langle u^2 \rangle \right)^2. \qquad (2.5.1)$$

For *moderate* Reynolds numbers he found $C_p = 0.34$. Hinze (1975) attempted to compute C_p for *high* Reynolds numbers turbulence, by assuming Gaussian and simple exponential decay functions for the velocity correlation, i.e. $f(r) = \exp\left(-|r|/L\right)$, where L is the integral length scale of the flow. He obtained $C_p = 0.5$. This is close to the value obtained by Uberoi (1953) from the measured double velocity-correlation from experimental data. George *et al.* (1984) assumed an empirical spectrum suggested by von Kármán and followed the analysis of Batchelor (1953) to obtain $C_p = 0.42$.

Using KS1, we have evaluated $\langle p^2 \rangle$ by computing the pressure at 4900 different points at one instant in time and then taking the ensemble average. We have tested the sensitivity of the constant C_p by varying both the separation between the large and small scale fields (k_c) and the cut-off wavenumber k_η. The results are shown in table 2.5. The simulations all suggest that $0.4 < C_p < 0.5$, with the exception of $k_\eta / L = 25.0$; since this is a very low Reynolds number, the hypothesis that the small scales are advected by the large scales is questionable. For the high Reynolds number turbulence, however, there is very good agreement between the experimental and theoretical results and this simulation.

2.5.2 Pressure spectra

In previous investigations (e.g. George *et al.* 1984) it has been suggested that pressure fluctuations at small scales have been *caused* by the motions of eddies on that scale, and not by interaction between small scales and large scales. George *et al.* (1984) found $\phi_{pp}(k_1) \propto \varepsilon^{4/3} k_1^{-7/3}$ in the inertial subrange and the corresponding three-dimensional pressure spectrum (Monin & Yaglom 1975) is given by

$$E_{pp}(k) = \alpha_{kp} \varepsilon^{4/3} k^{-7/3} \quad \text{for} \quad k_0 \ll k \ll \eta^{-1} , \tag{2.5.2}$$

where α_{kp} is a universal constant analogous to the Kolmogorov constant for the velocity spectrum. Batchelor (1953) calculated the value of α_{kp} by using the zero-fourth-cumulant hypothesis for the velocity and assuming a simple transition function $B_{11}(y) = (\nu\varepsilon)^{-1/2} D_{11}(\eta y)$ of the form

$$B_{11}(y) = \frac{y^2/15}{\left[1 + (15C)^{-3/2} y^2\right]^{2/3}} ,$$

which is valid for both $y \ll 1$ and $y \gg 1$, for the velocity structure function D_{11}. According to his results, $\alpha_{kp} \approx 0.354 C^{3/2}$ where $C = 2$ determined from experiments, so $\alpha_{kp} \approx 1$.

It can be seen that the pressure spectrum decreases with increasing wavenumber more rapidly than the velocity spectrum, so that the small scale motions are of lesser importance in the pressure fluctuations than in the velocity fluctuations. Hunt *et al.* (1987) suggested that as the large scale eddies advect the small eddies, they also advect the small scale pressure fluctuations. Analogously to the velocity spectrum $\mathcal{E}(k,\omega)$ (2.34), the $k - \omega$ power spectrum of pressure fluctuations is expected to have the form

$$\mathcal{E}_{pp}(k,\omega) = E_{pp}(k) \exp\left[-\frac{1}{2}\omega^2 \big/ (a_p k U_0)^2\right] \bigg/ \left(\sqrt{2\pi}(a_p k U_0)\right) . \tag{2.5.3}$$

We have computed the pressure spectrum in wavenumber space and this is plotted in figure 2.25. There is an appreciable region having a slope of $-7/3$ as predicted by the theory, and the

constant α_{kp} obtained from figure 2.25, is given by $\alpha_{kp}\varepsilon^{4/3} = 1.0$, so $\alpha_{kp} = 0.92$. This is close to the value $\alpha_{kp} \approx 1.0$ obtained by Batchelor's (1953).

Hunt *et al.* (1987) applied similar arguments as in §2.7, using $\phi_{pp}(\omega) = 4 \int \mathcal{E}_{pp}(k,\omega)\, dk$ and obtained:

$$\phi_{pp}(\omega) = \frac{4\alpha_{kp}}{2^{1/3}\sqrt{\pi}}\Gamma\left(\frac{7}{6}\right)(a_p\varepsilon U_0)^{4/3}(\omega)^{-7/3}. \qquad (2.5.4)$$

Taking their value of $a_p = 1.0$, this gives

$$\phi_{pp} \approx 0.2\omega^{-7/3}. \qquad (2.5.5)$$

This result ($\phi_{pp}(\omega) \propto \omega^{-7/3}$) was also obtained by Chase (1970).

The calculated pressure frequency spectrum is presented on figure 2.26. We find that the spectrum $\phi_{pp}(\omega)$ follows the $\omega^{-7/3}$ law predicted by Hunt *et al.* (1987) very closely, but the $-7/3$ law extends over only one decade. This may explain why the constant of proportionality of 1.14 does not agree with value of 0.2 predicted from the asymptotic theory for an infinitely large $(-5/3)$ range.

Finally, summary of the comparison of turbulent velocity statistics between KS and DNS, experiment or theory is given in table 2.6. Also, additional studies were made with the propose of checking the sensitivity of the method to these various assumption and and the extent of some variability between the simulations is given in Appendix C.

2.6 Conclusion

We have shown how it is possible to simulate the unsteady random velocity field whose statistics agree with the known values of two-point space-time Eulerian and Lagrangian statistics. This Kinematic Simulation should be very useful in many studies which require such a flow fields, and where there is no model for the small scale at present – it is a kind of 'small eddy simulation' that might complement Large Eddy Simulation. There is no representation of the energy transfer from large scales to the smaller, dissipative eddies. The simulated flow contains some arbitrary features, which affect some statistics more than others, in particular, Eulerian statistics and their higher order statistics do not agree with experimental values. The reason is the simulation does not represent the dynamical processes in turbulence, which affect higher order statistics. But we suspect it is not very important to simulate these details aspect of the flow when modelling dispersion, combustion and two phase flow etc... We are not, however, primarily interested here in the dynamics of the field; we are interested in its effects on something imbedded in it. While such effect are dynamical, they depend on the field only through

its kinematical specification. Following the work by Lee, Kim and Moin (1987) and Turfus and Hunt (1986), it is possible to extend this simulation to include other effects such as shear and the presence of the boundaries (see Chapter 4).

Turbulent velocity statistics

Statistics	Form	Kinematic simulations	DNS, experiment or theory
Eulerian spectrum	$C^{(E)}(\varepsilon U_0)^{2/3}\omega^{-5/3}$	$C^{(E)} \simeq 0.82$	0.75 theory (Hunt 1986)
Lagrangian spectrum	$C^{(L)}\varepsilon\omega^{-2}$	$C^{(L)} \simeq 0.54$	0.6 ± 0.3 experiment (Hanna 1980)
Eulerian-Lagrangian spectrum	$C^{(EL)}\varepsilon\omega^{-2}$	$C^{(EL)} \simeq 2.20$	$C^{(EL)} \sim C^{(L)}$ theory (Hunt 1988)
Frozen Lagrangian spectrum	$C^{(FL)}(\varepsilon U_0)^{2/3}\omega^{-5/3}$	$C^{(FL)} \simeq 1.22$ and $T_L^F \simeq T_L$	—
Spatial structure function	$C'\varepsilon^{2/3}r^{2/3}$	$C' \simeq 1.70$	2.0 experiment (Townsend 1976)
Mean square pressure fluctuation	$\langle p^2 \rangle \big/ \rho^2 \left[\langle u^2 \rangle \right]^2 = C_p$	$C_p \simeq 0.46$	$0.34 \lesssim C_p \lesssim 0.5$ theory (Batchelor 1951) (Hinze 1975)
Pressure spectra k- and ω-space	$E_{pp}(k) = \alpha_{kp}\varepsilon^{4/3}k^{-7/3}$	$\alpha_{kp} \simeq 0.92$	1.0 theory (Batchelor 1953)
	$\phi_{pp}(\omega) = A\alpha_{kp}(\varepsilon U_0)^{4/3}\omega^{-7/3}$	$A \simeq 1.0$	0.17 theory (Hunt 1986)
Skewness (S)	$\left\langle \left(\dfrac{\partial u}{\partial x}\right)^3 \right\rangle \Big/ \left[\left\langle \left(\dfrac{\partial u}{\partial x}\right)^2 \right\rangle \right]^{3/2}$	$S \simeq -0.17$	-0.3 experiment (Stewart 1951)

Table 2.6

II Invariant Contours

II > 0

II = 0
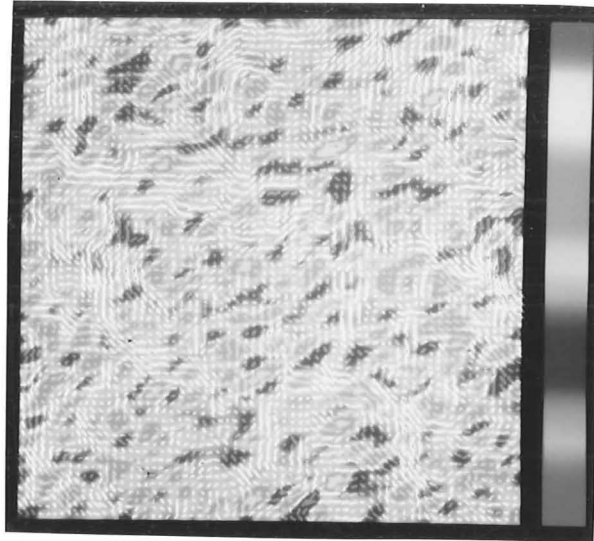
II < 0

Plate 1

Pressure Contours
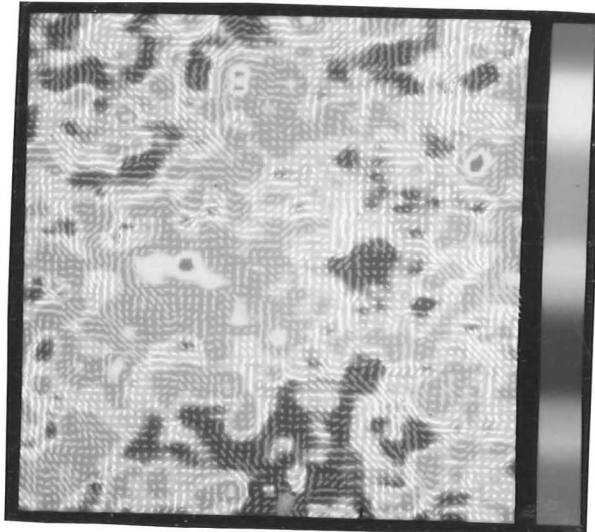
p < 0

p = 0

p > 0

Plate 2

Eddy, Streaming & Convergence Regions
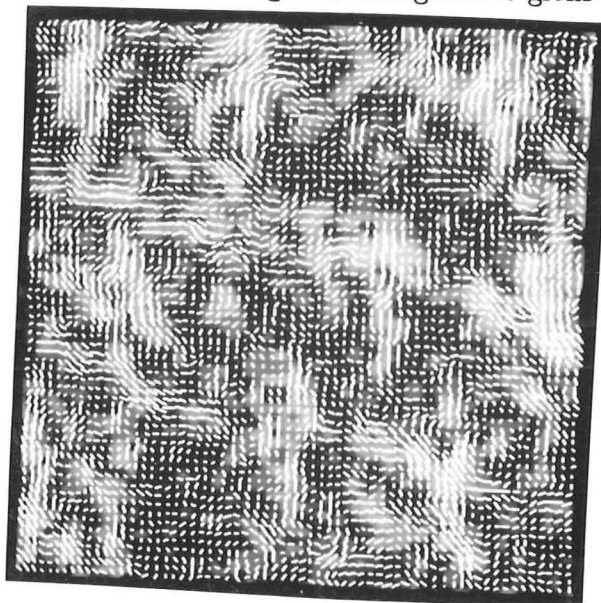
Red – eddy

Green – streaming

Blue – convergence

Plate 3
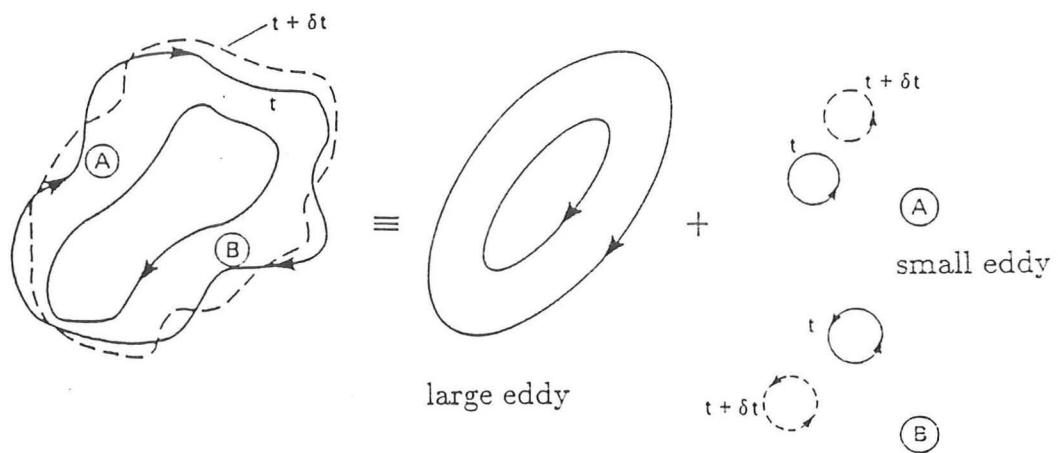
Fig. 2.1   Flow field composed of large scale eddies and small scale eddies that are transported by the large scales.
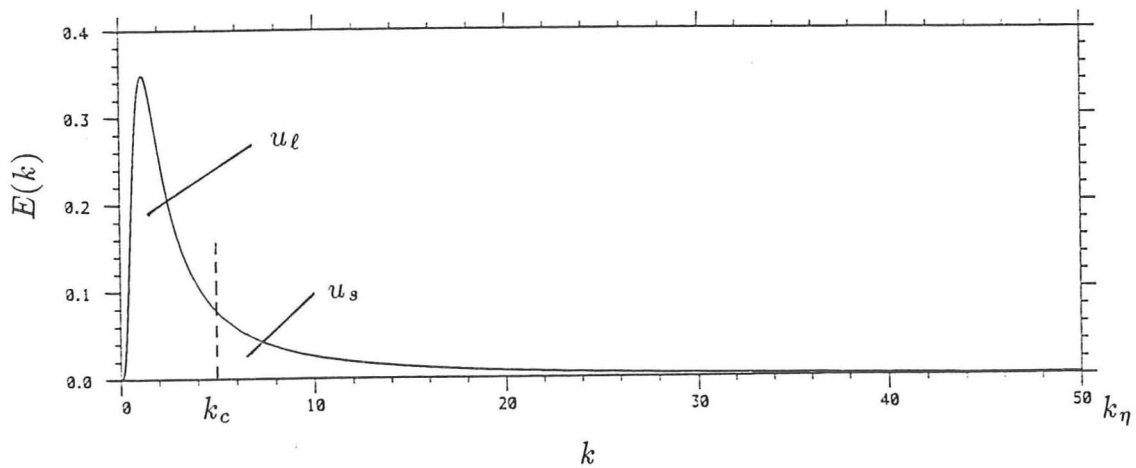
Fig. 2.2   Splitting the von Kármán energy spectrum into large and small scales. $E(k) \to k^4$ as $k \to 0$ and $E(k) \to k^{-5/3}$ as $k \to \infty$.

$$\mathcal{E}(k,\omega) = \frac{\exp\left\{\dfrac{-\omega^2}{2k^2\sigma_u^2}\right\}}{\sqrt{2\pi}k\sigma_u}$$
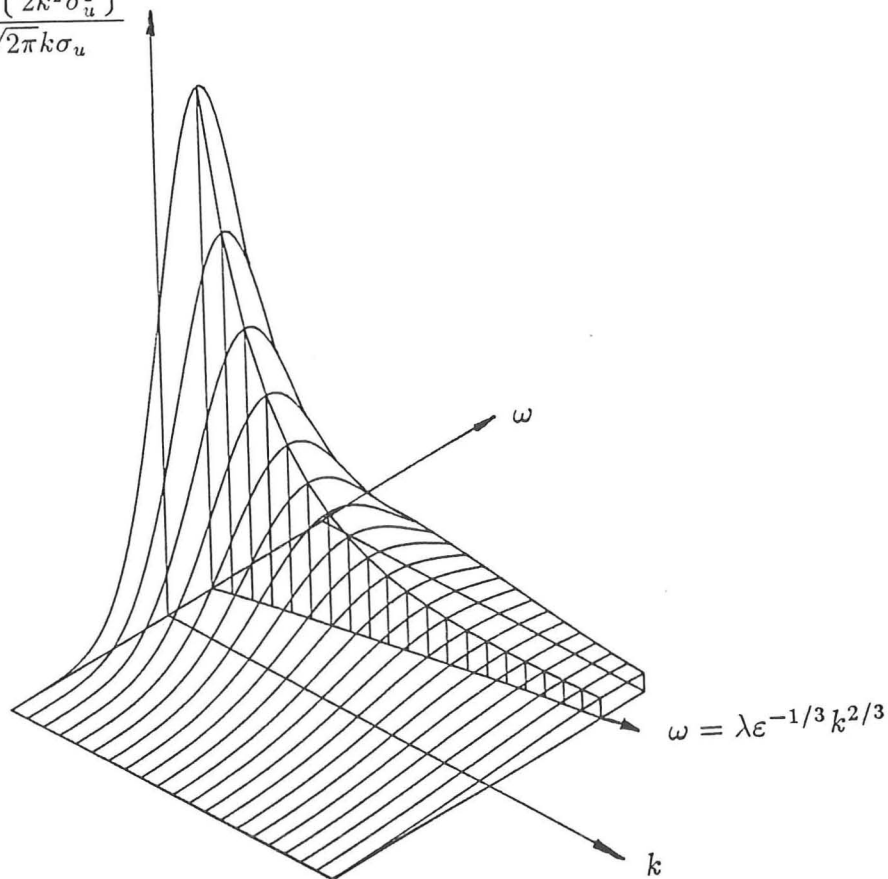
Fig. 2.3   The probability distribution of ω, the peaks are at $\pm\lambda\varepsilon^{1/3}k^{2/3}$ for a given k. In this model, ω is a δ-function, i.e. $\omega_n = \delta(\omega_n \pm \lambda\varepsilon^{1/3}k^{2/3})$.
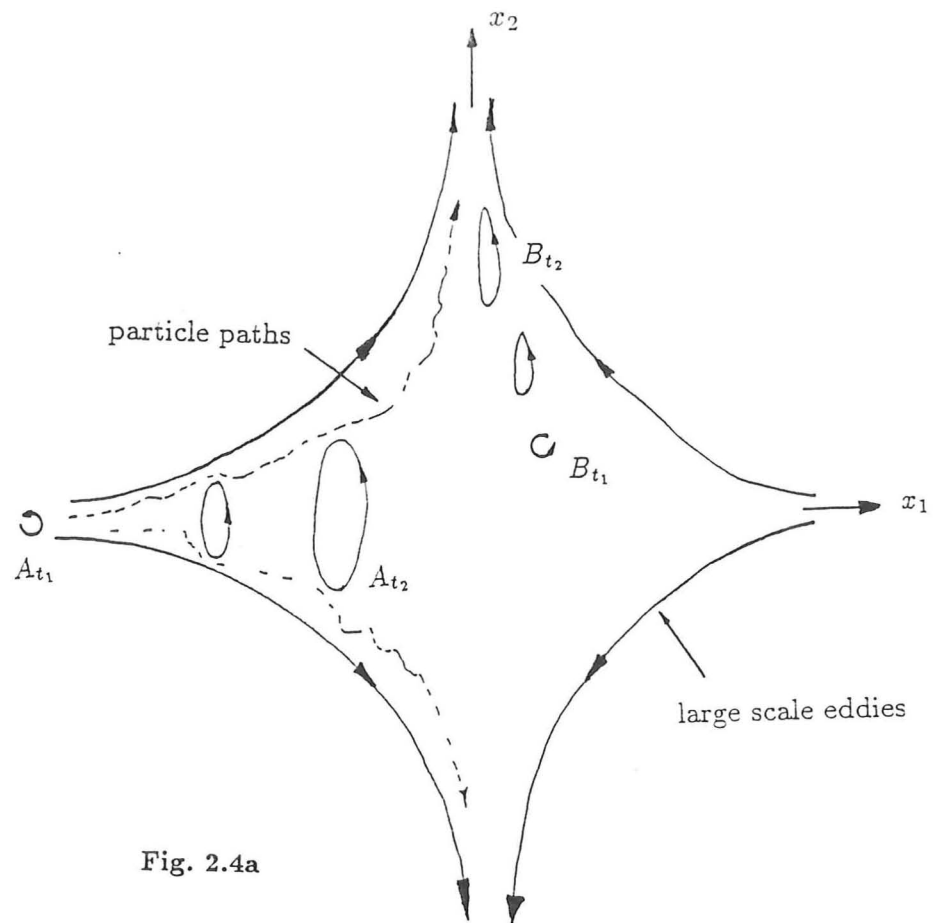
Fig. 2.4a
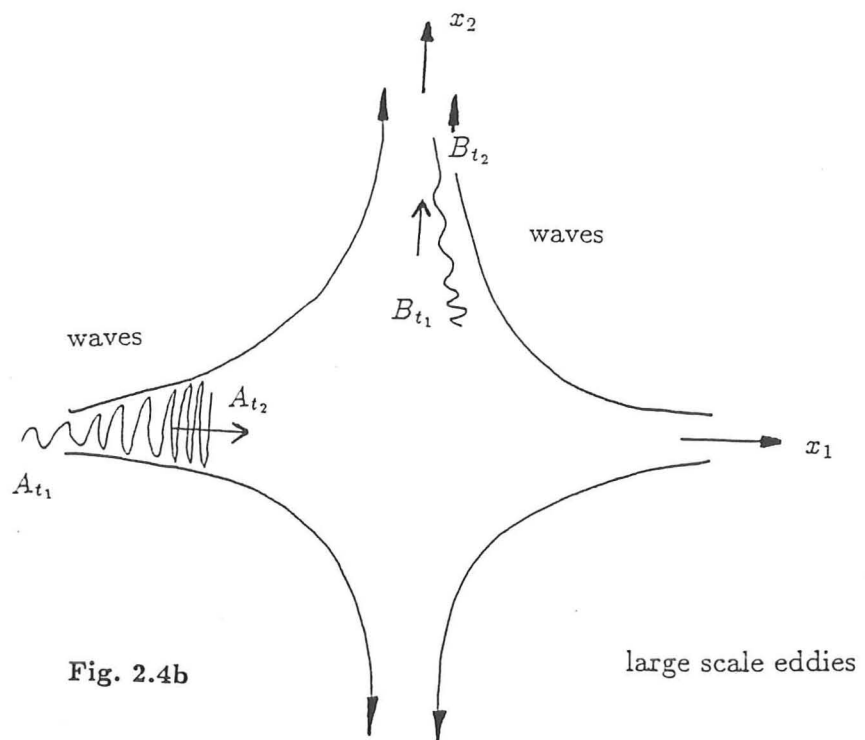
Fig. 2.4b

Fig. 2.4   (a) Small eddies carried around by the large eddies and squashed in a convergence region. (b) Wave being compressed or stretched in a convergence region.
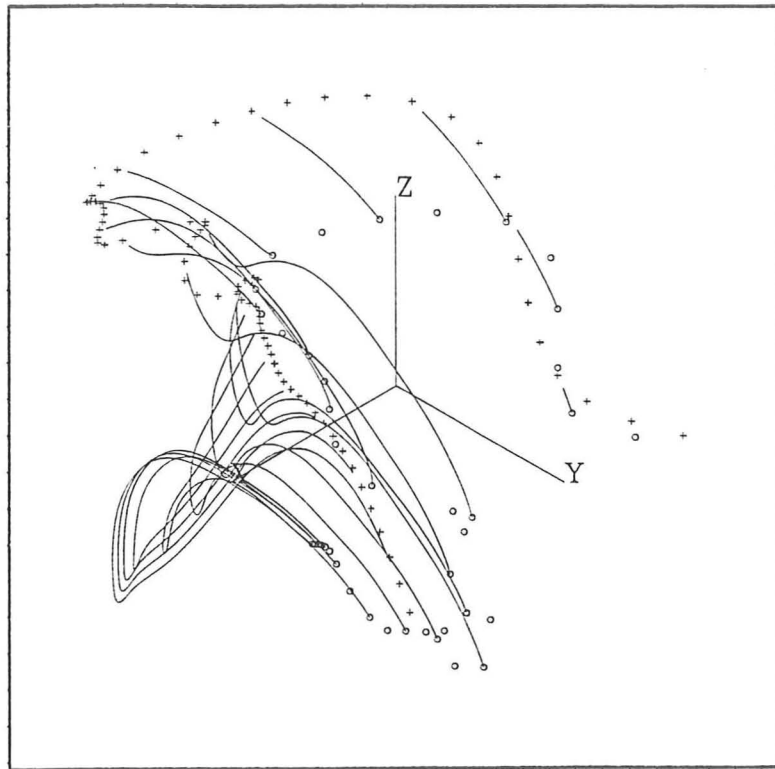
Fig. 2.5   Showing the small eddies being advected by the larger ones + + + +   particle
trajectories, o o o o   position of small eddy at time $t = 0$, ——— trajectories of
small eddies.
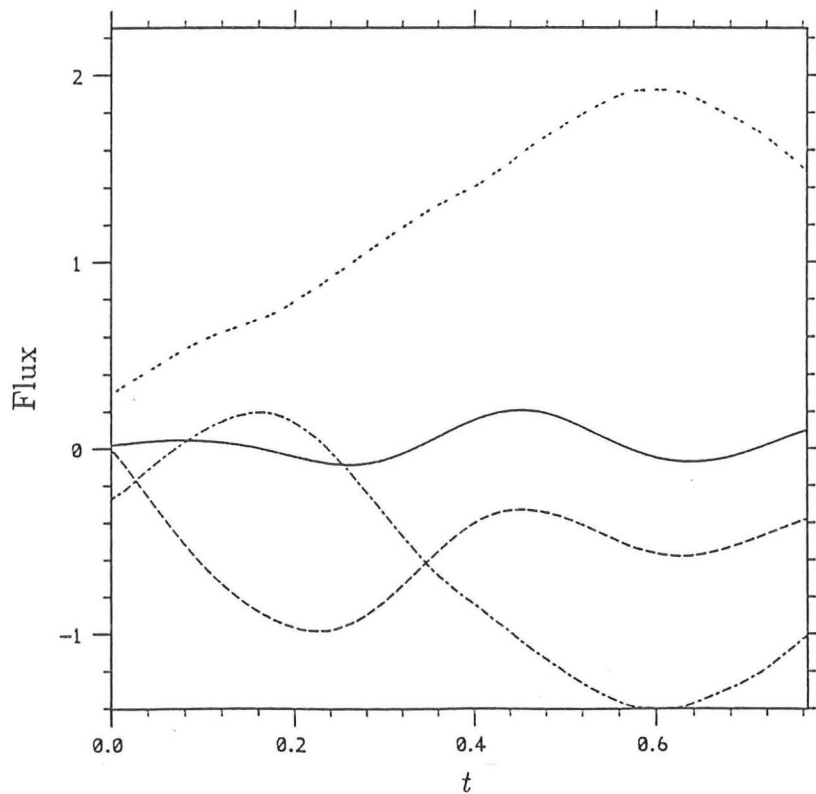
Fig. 2.6   Dashed lines are the flux across any two opposite faces, solid line is the total flux
across the box.
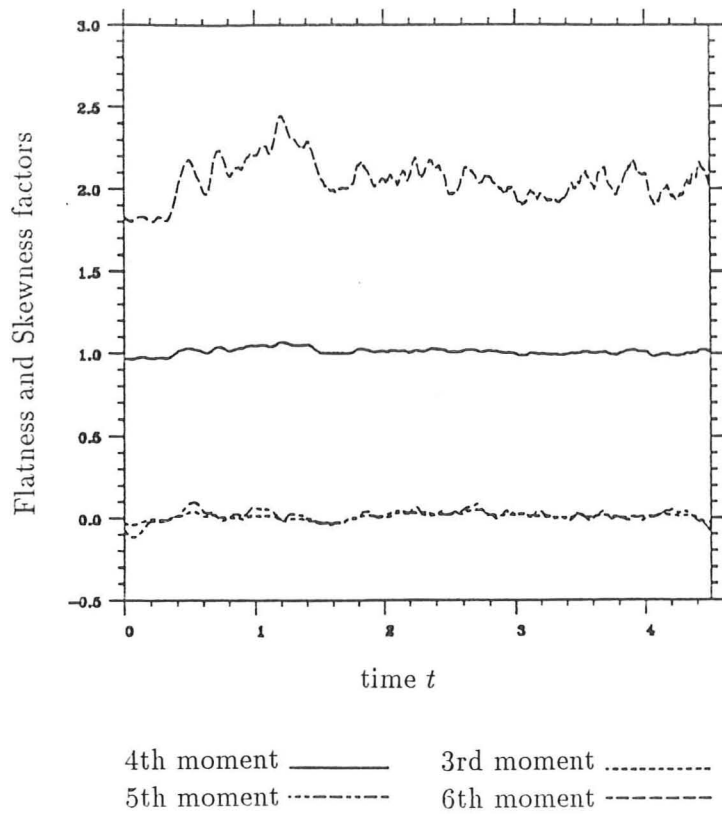
Fig. 2.7   Flatness and skewness factors of the velocity field.
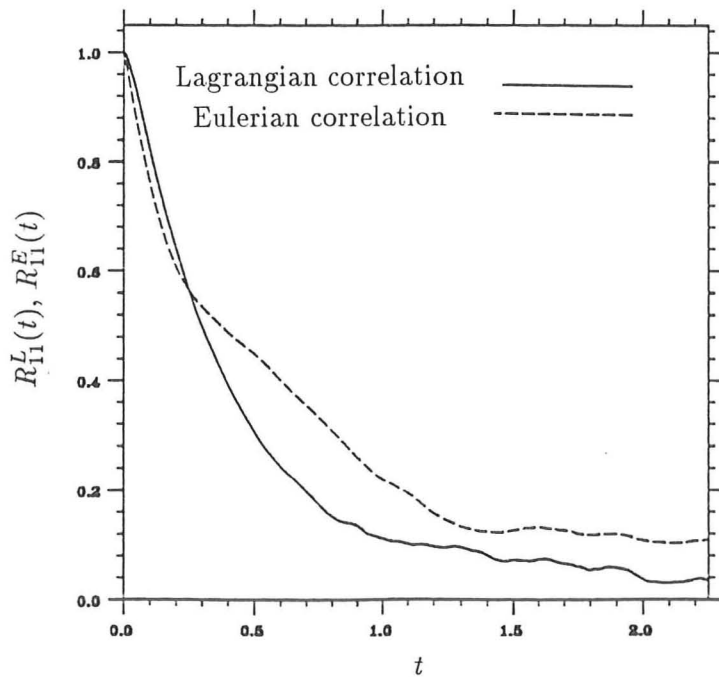
Fig. 2.8   The Eulerian and Lagrangian auto-correlation functions, there is a crossover at $k_c \approx 2.5$.
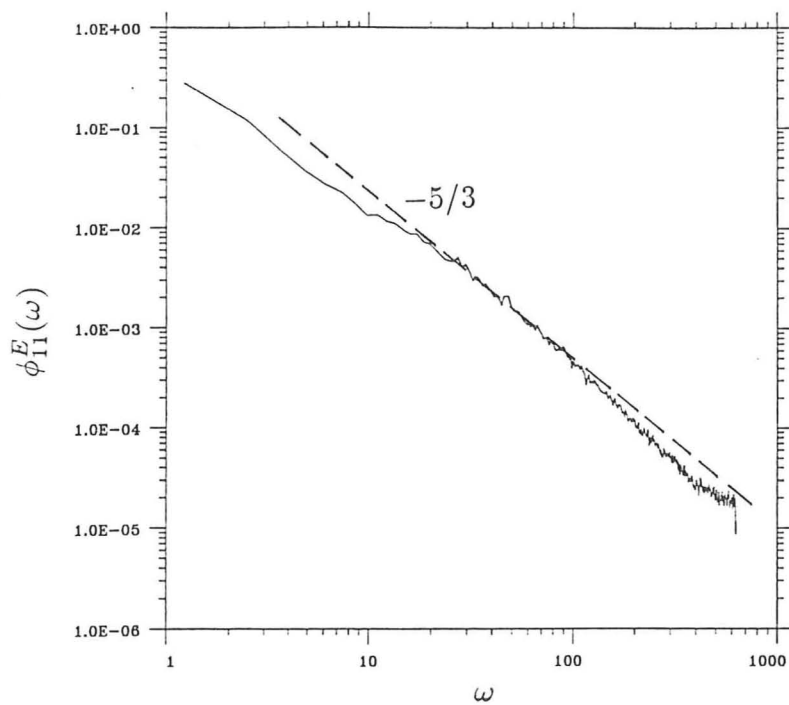
Fig. 2.9   Average Eulerian spectrum $\phi_{11}^E(\omega)$ with a $-5/3$-slope.
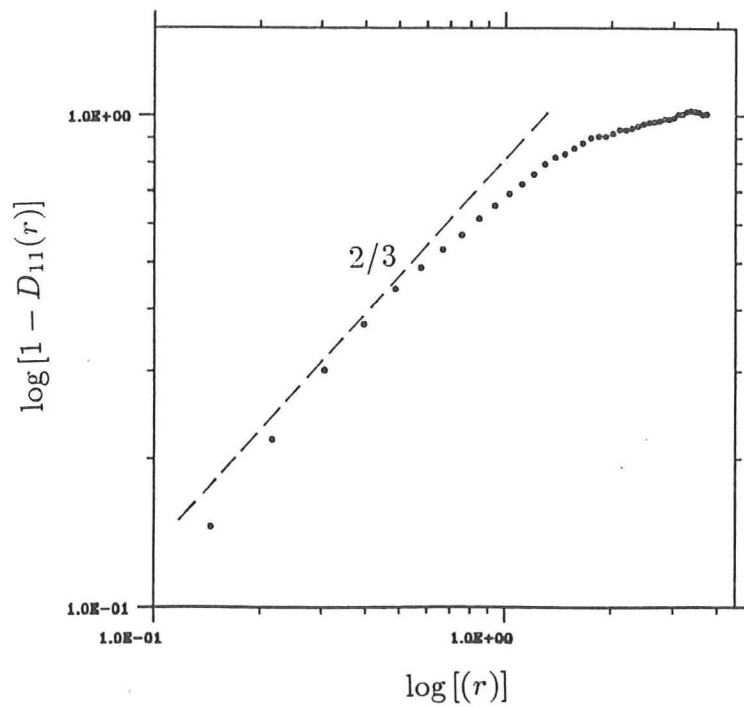
Fig. 2.10   The structure function $D_{11}(r)$ with a 2/3-slope over a limited range.
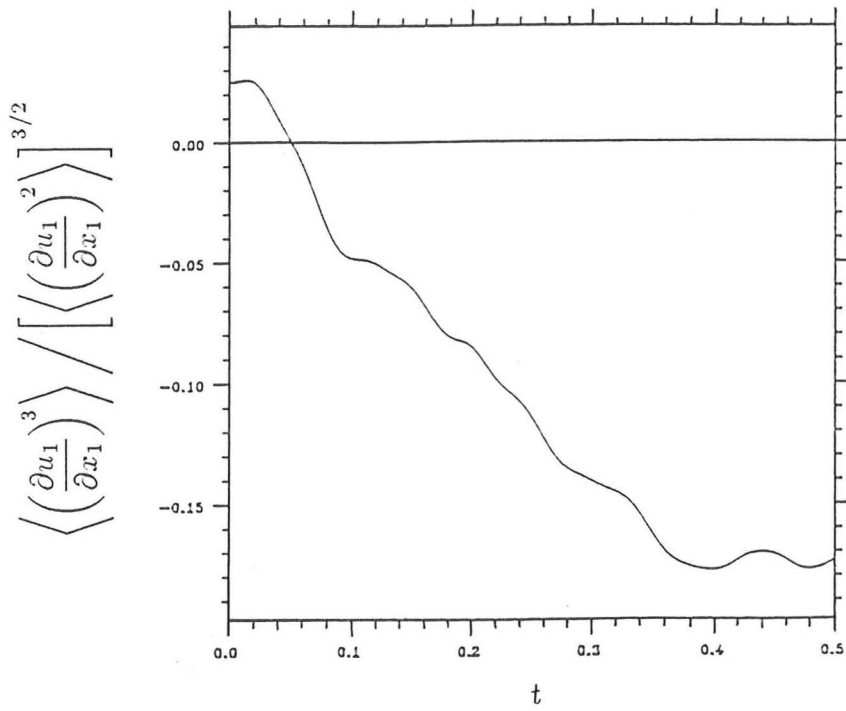
Fig. 2.11   The skewness of the longitudinal velocity-derivative, converging to -0.15.
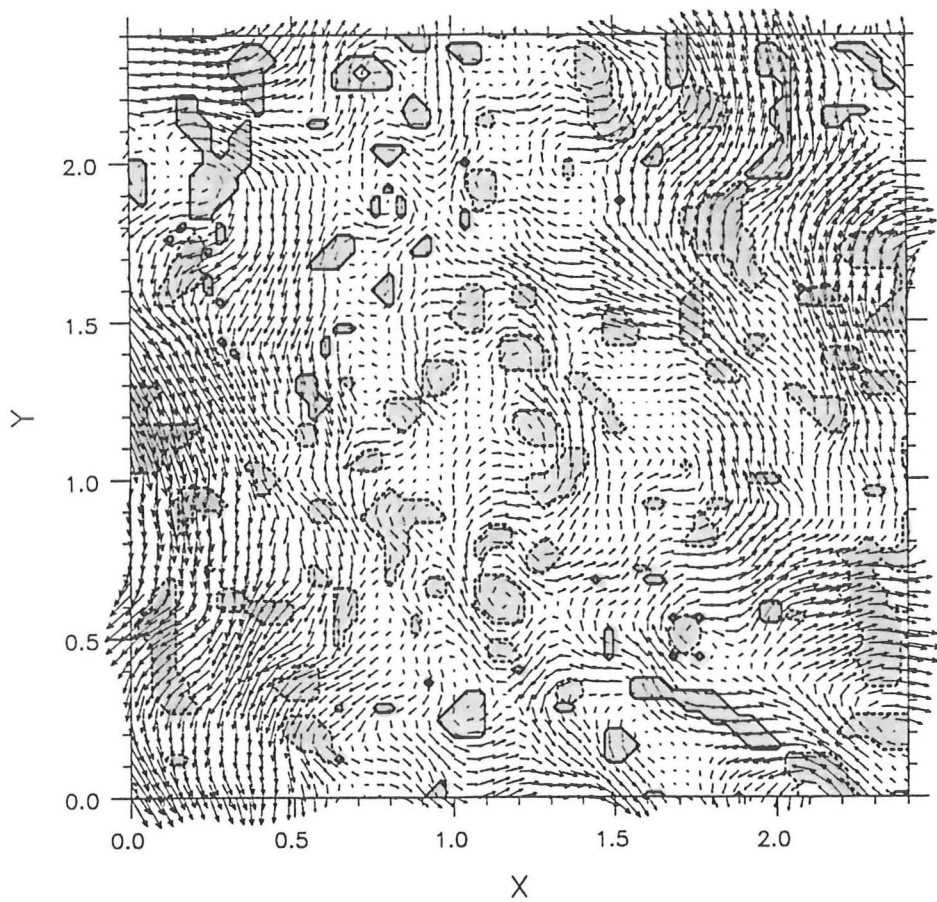
Fig. 2.12   Shear and eddy zones together with the velocity vectors of von Kárman energy spectrum. Orange: Shear zones ($\Pi < -\Pi_E$; $-p_E < p < p_C$); Red: Eddies ($\Pi < -\Pi_E$; $p < -p_E$).
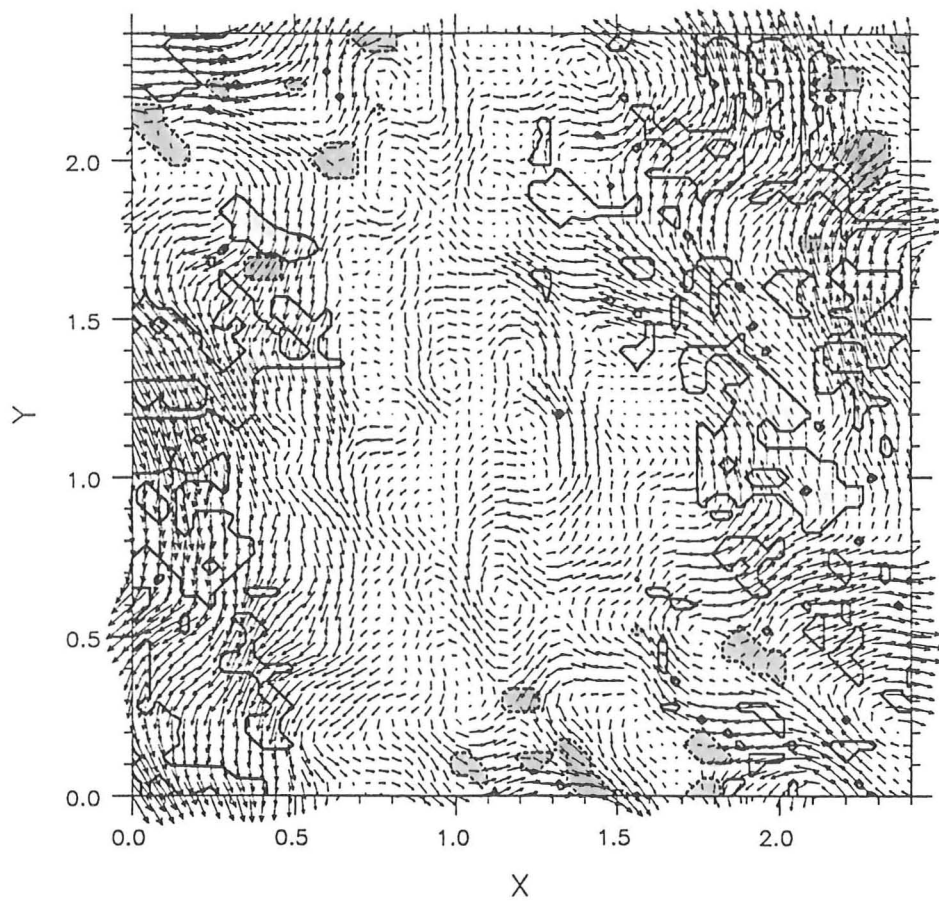
Fig. 2.13 Stream and convergence zones together with the velocity vectors of von Kárman energy spectrum. Green: Stream zones ($\Pi < -\Pi_S$; $u^2 > u_{\text{rms}}^2$); Blue: Convergence zones ($\Pi > \Pi_C$; $p > -p_C$).
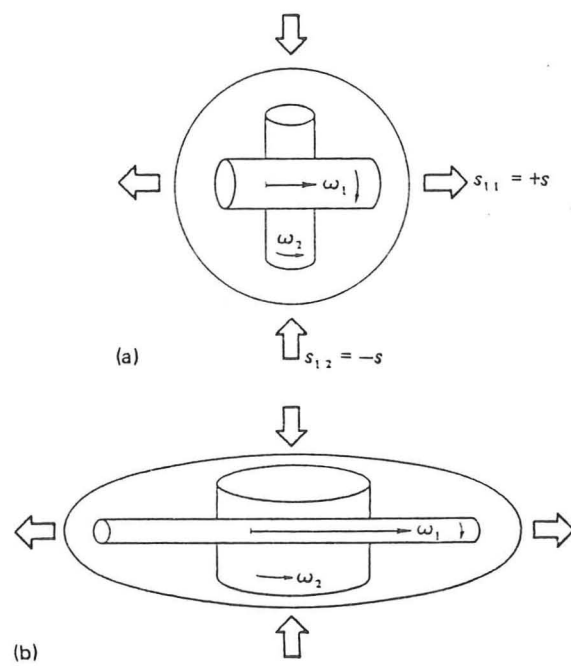
Fig. 2.14   Vorticity stretching in a strain-rate field: (a) before stretching (b) after stretching.
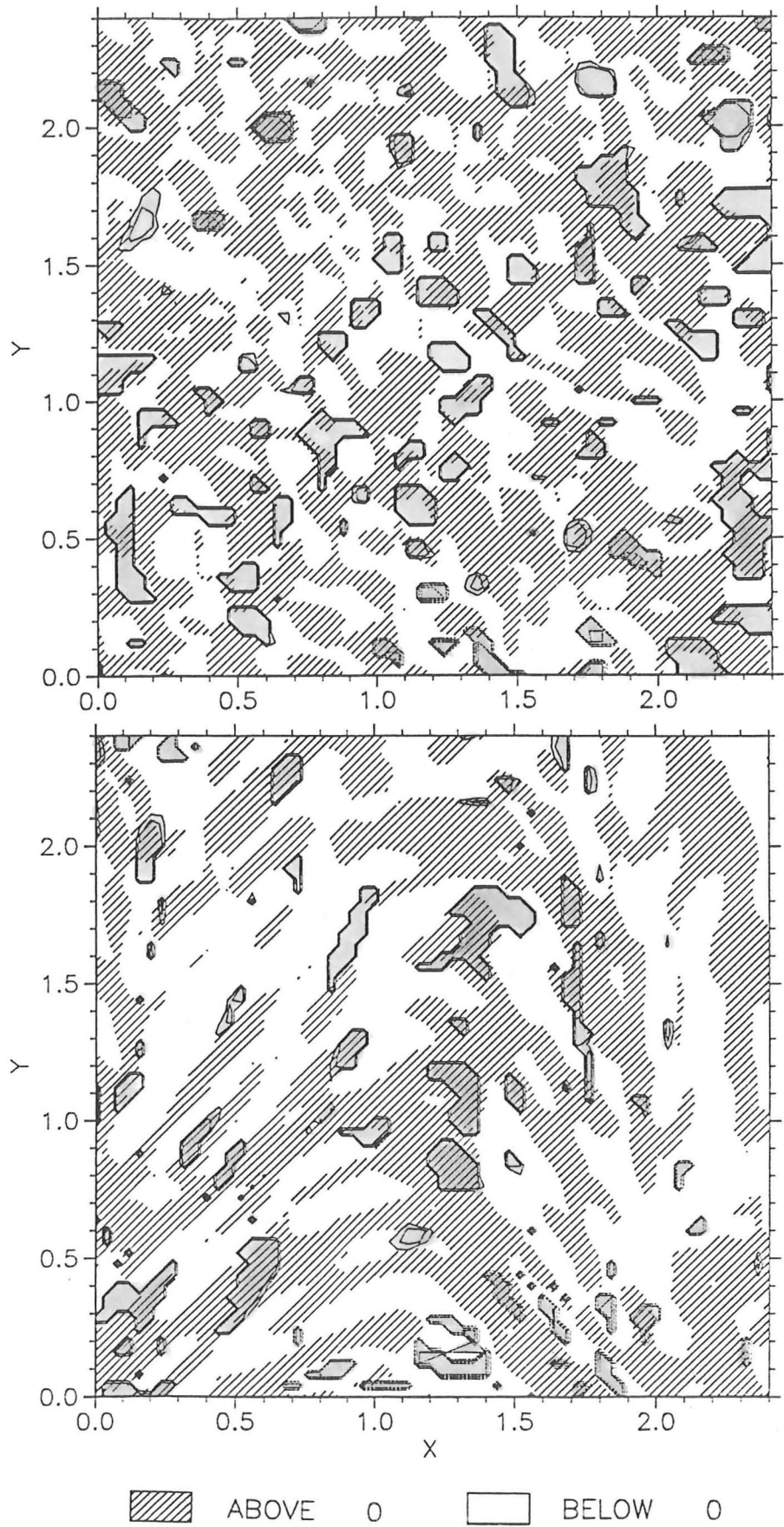
Fig. 2.15 Eddy and convergence zones show with the value of III. Shaded areas are positive and unshades areas are negative of III. Red: Eddies ($\Pi < -\Pi_E$; $p < -p_E$); Blue: convergence zones ($\Pi > \Pi_C$; $p > -p_C$). (a) at $t = 0$ and (b) at $t \approx T_L$.
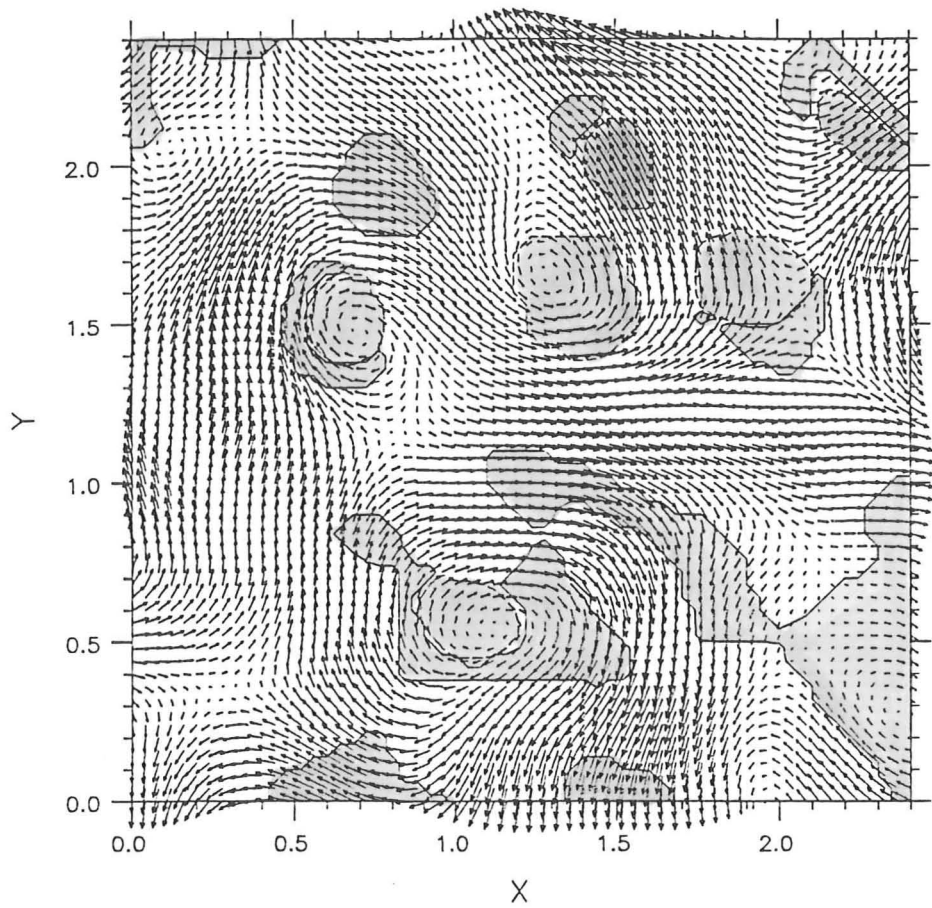
Fig. 2.16   Shear and eddy zones together with the velocity vectors of exponential energy spectrum. Orange: Shear zones ($\Pi < -\Pi_E$; $-p_E < p < p_C$); Red: Eddies ($\Pi < -\Pi_E$; $p < -p_E$).
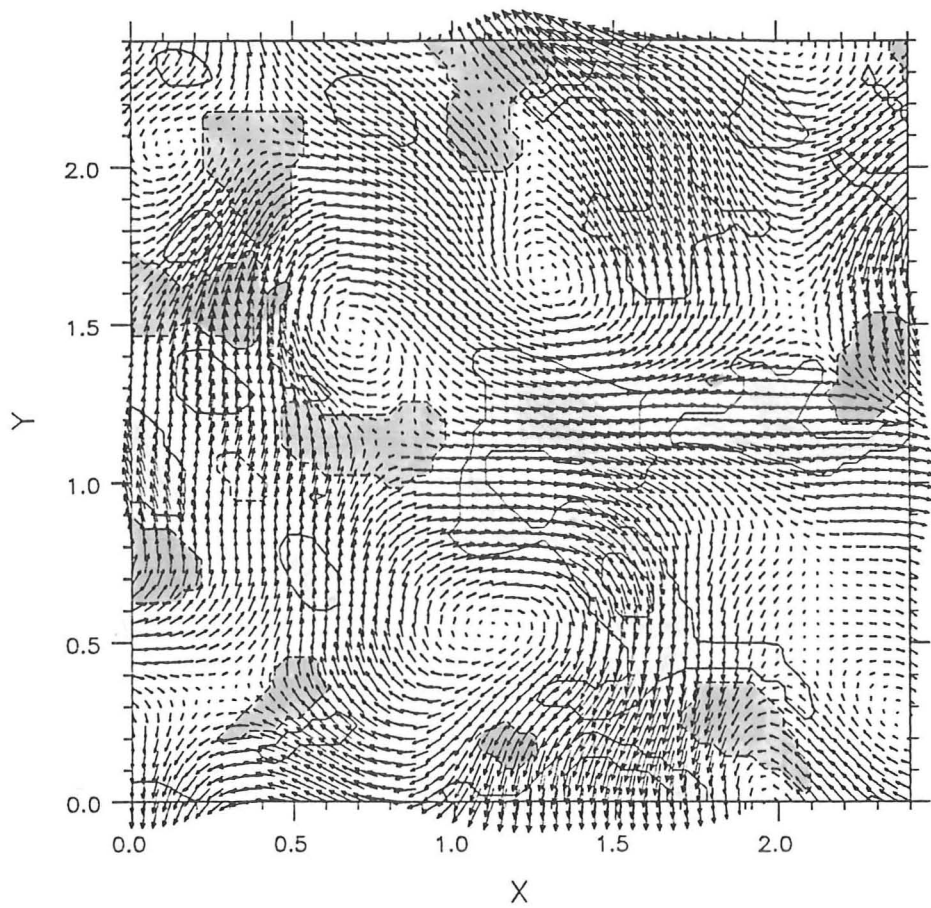
Fig. 2.17 Stream and convergence zones together with the velocity vectors of exponential energy spectrum. Green: Stream zones ($\Pi < -\Pi_S$; $u^2 > u^2_{\mathrm{rms}}$); Blue: Convergence zones ($\Pi > \Pi_C$; $p > -p_C$).

(a)

Fig. 2.18 The velocity vectors in $x - y$ plane shown together with the vorticity contours, ω_3.
Green: weak vorticity; Orange: strong vorticity. At time (a) $t = 0.0$; (b) $t \approx T_L$.
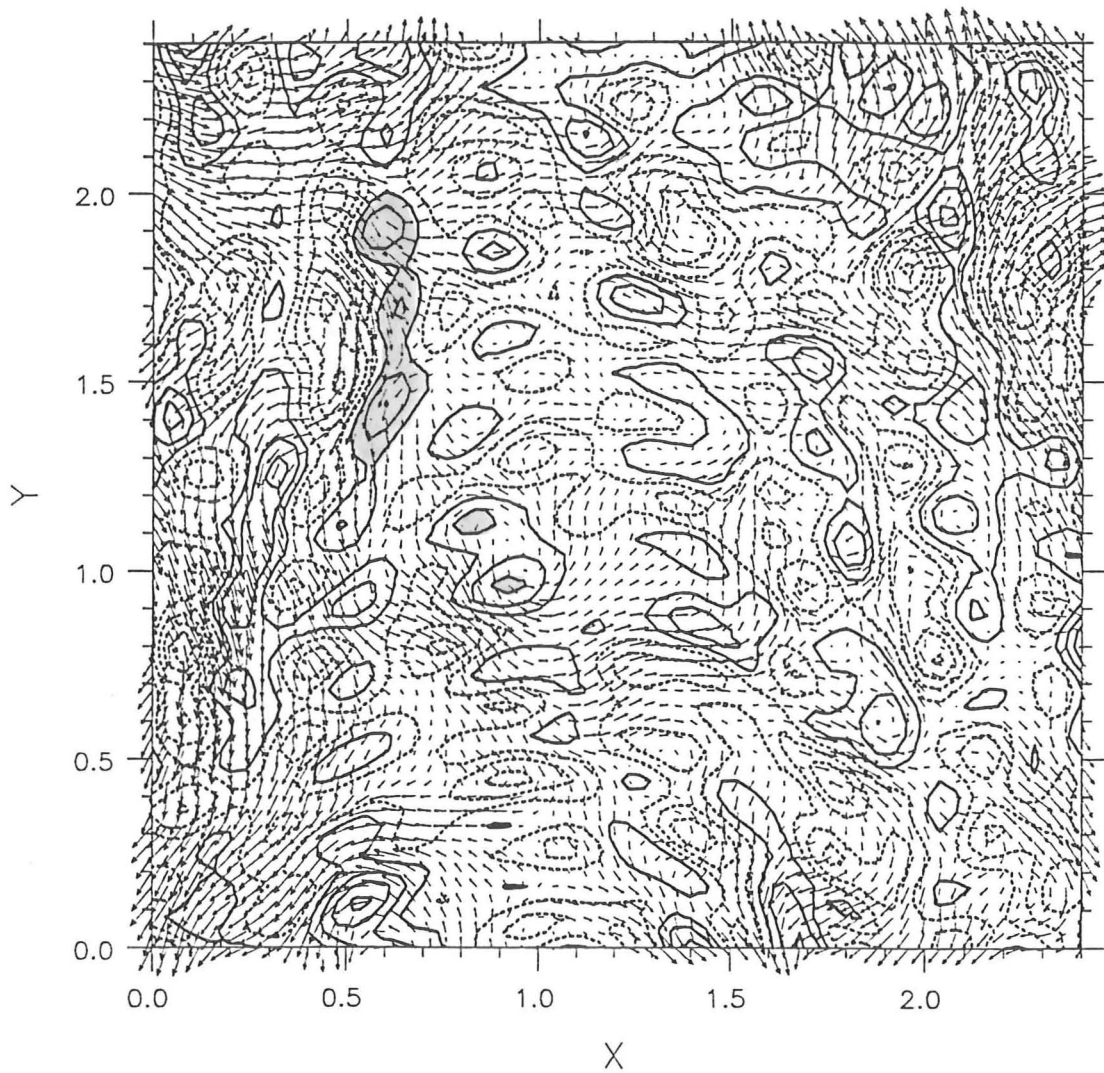
(b)
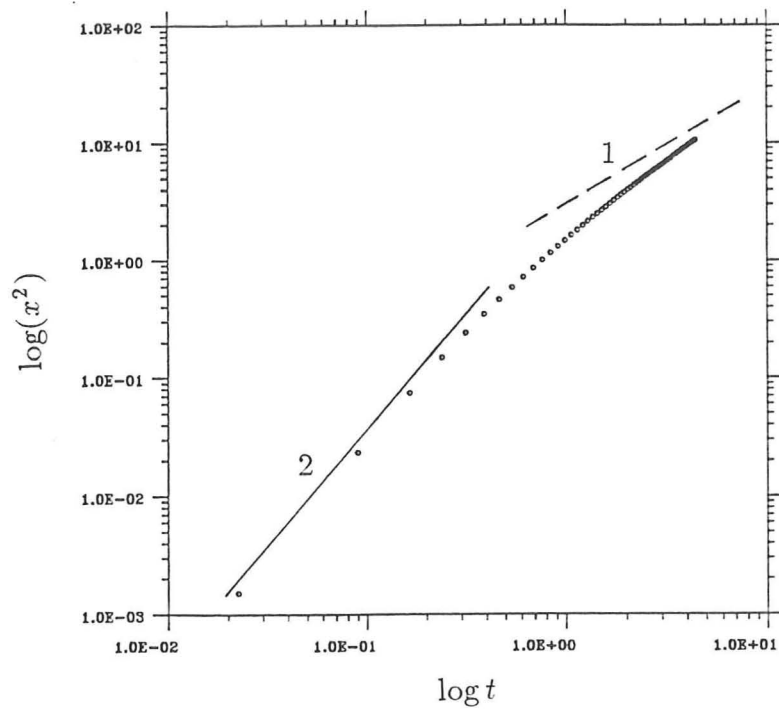
Fig. 2.19   The mean square displacement of fluid element from a fixed point in an isotropic, stationary and homogeneous turbulence. ——— $\langle \mathbf{x}^2 \rangle = \langle \mathbf{u}^2 \rangle t^2$; $---$ $\langle \mathbf{x}^2 \rangle \propto t$.
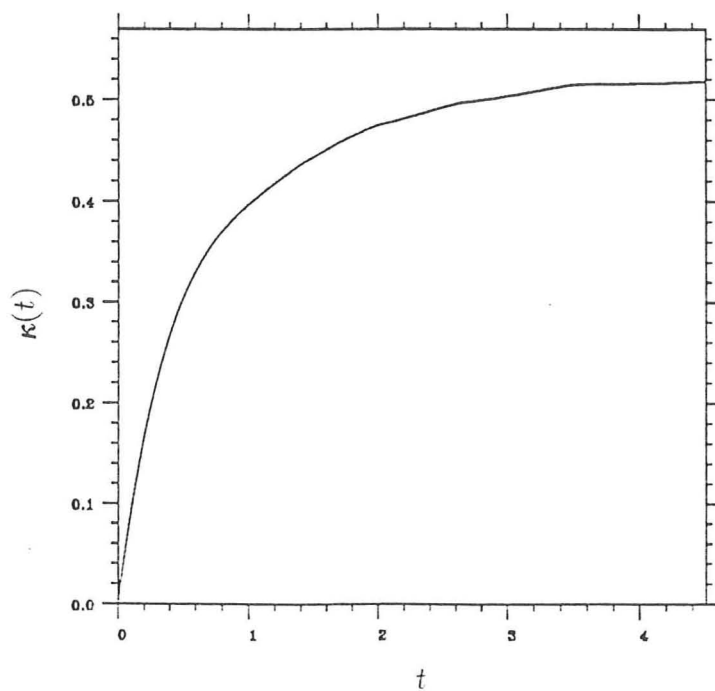
Fig. 2.20   The eddy diffusivity $\kappa(t) = \frac{1}{3} \langle \mathbf{x}(t).\mathbf{u}(\mathbf{x}(t),t) \rangle$ vs. time.
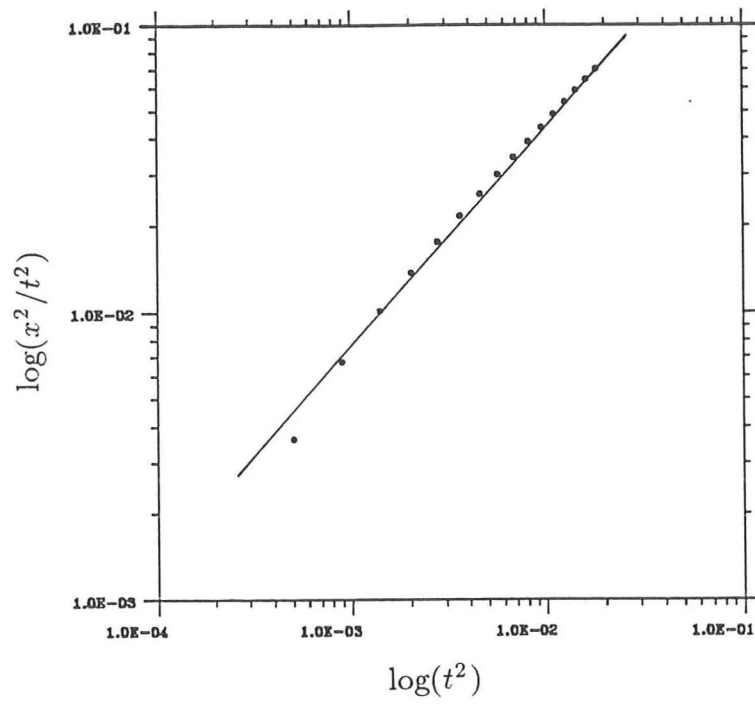
Fig. 2.21　The Lagrangian microscale $\tau_L \approx 0.41$.
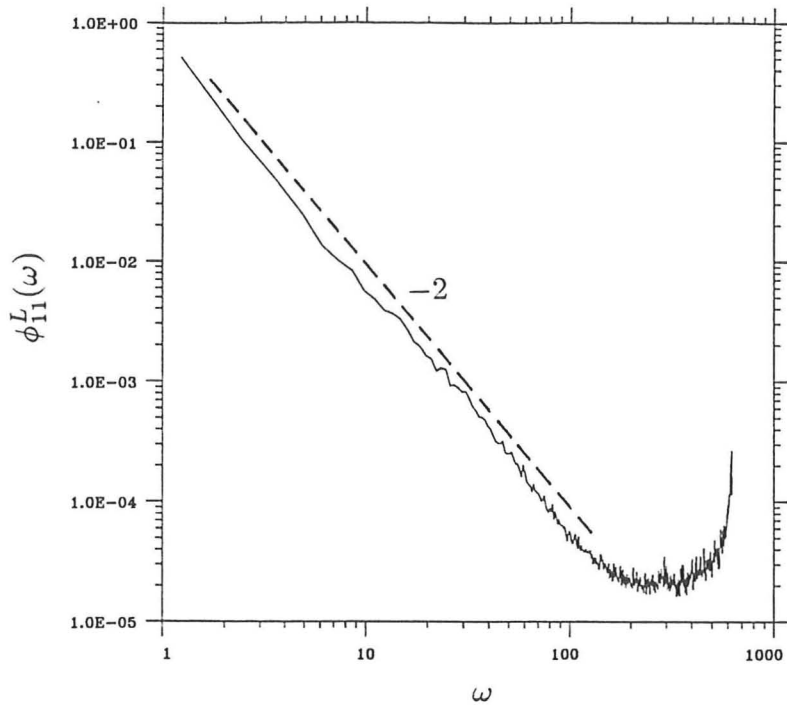
Fig. 2.22   Average Lagrangian spectrum $\phi_{11}^L(\omega)$ with a -2 -slope.

	k_c	k_η	No. of modes
——————	5.00	50.00	32
··············	5.00	100.00	64
– – – – –	5.00	200.00	128
– · – · –	5.00	300.00	256
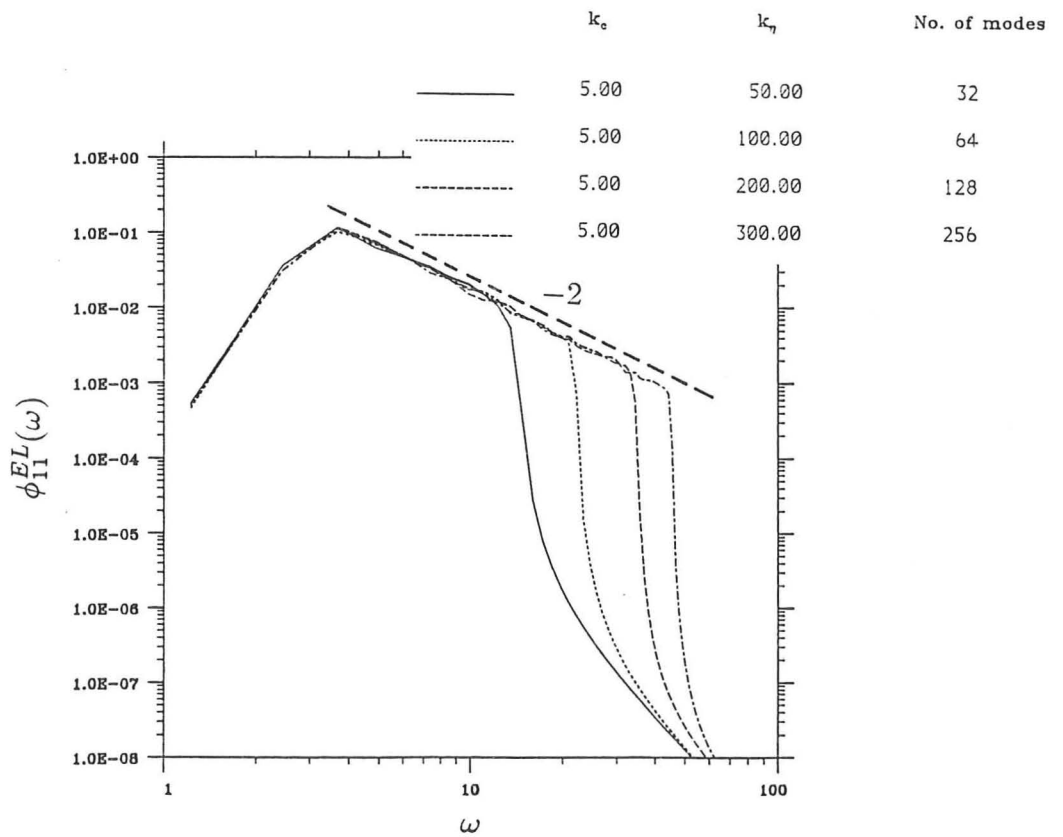
Fig. 2.23   Average 'Eulerian-Lagrangian' spectrum $\phi_{11}^{EL}(\omega)$ with a -2 -slope.
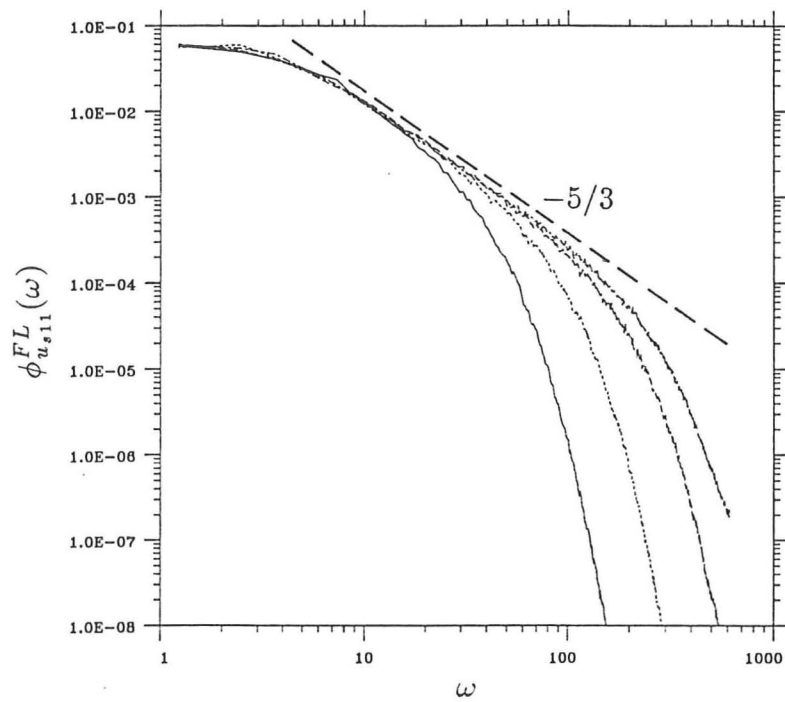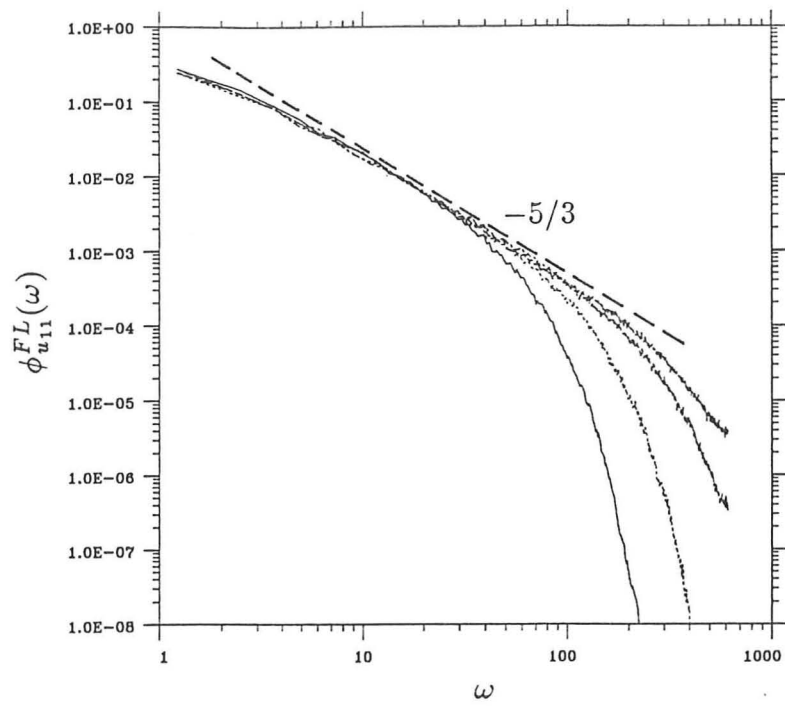
	k_c	k_η	No. of modes
———	5.00	50.00	32
············	5.00	100.00	64
- - - - -	5.00	200.00	128
– – – –	5.00	300.00	256

Fig. 2.24   Average Frozen Lagrangian spectra. (a) $\phi_{u_{11}}^{FL}(\omega)$;   (b) $\phi_{u_{s11}}^{FL}(\omega)$ both with a $-5/3$ -slope.
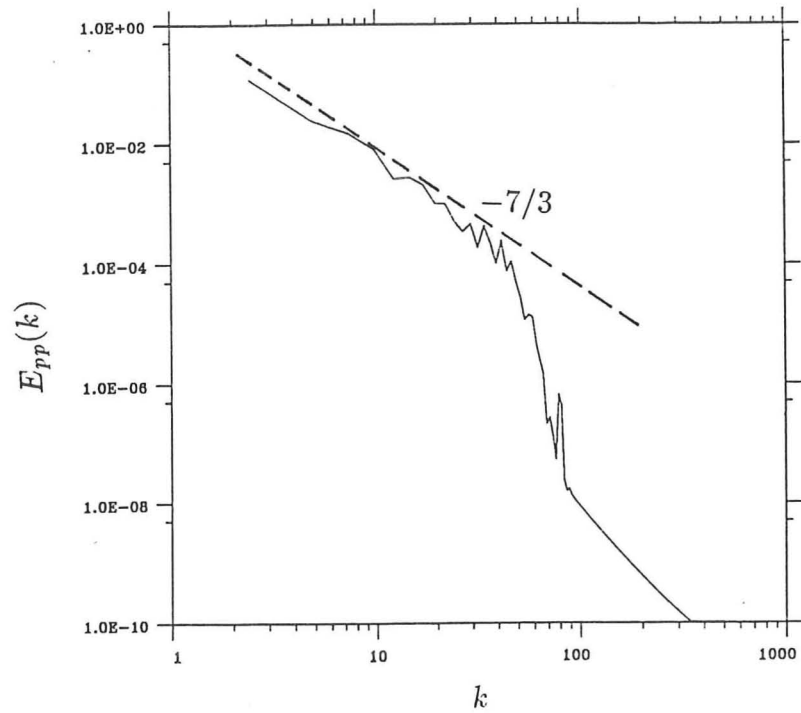
Fig. 2.25   Average pressure spectrum in wavenumber space $E_{pp}(k)$ with a $-7/3$ -slope.
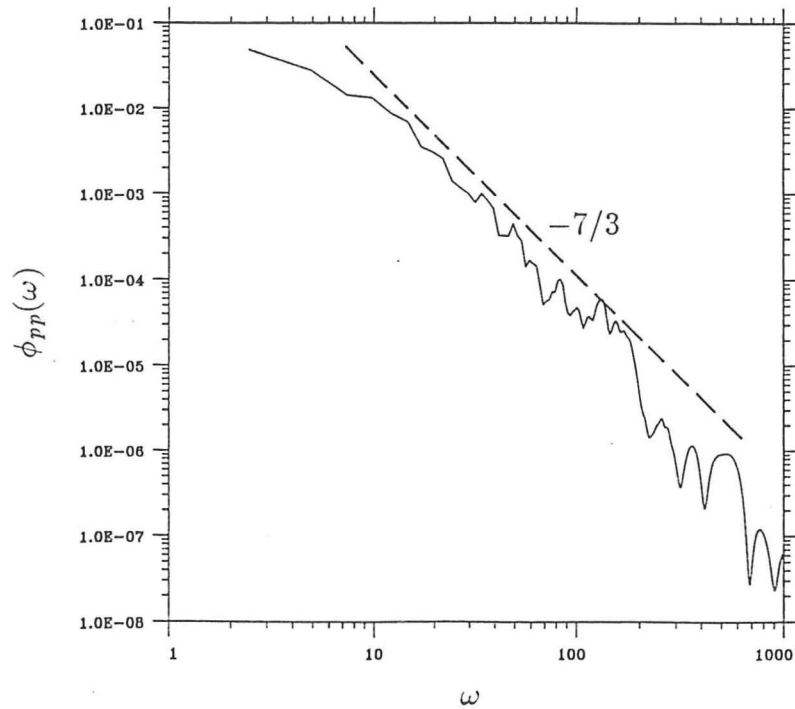
Fig. 2.26   Average pressure spectrum in frequency space $\phi_{pp}(\omega)$ with a $-7/3$ -slope.

CHAPTER THREE

Particle Motion

3.1 Introduction

The purpose of this study is to consider the motion of a small, spherical particle moving in fluid and to examine whether this type of motion persists in a more general context. The interaction of the turbulence with the particle cannot properly be taken into account through mean value computations. The non-linearity of the equation of motion for the particle gives rise to a highly complex problem to which there is no simple answer. Looking for numerical tools, the Direct Numerical Simulation or the Large Eddy Simulation appear to be the good candidates to analyse the effect of these interactions since they are based on a numerical integration of Navier-Stokes and the equation of motion for the particle without any closure assumptions. No such simulations have been reported because they are prohibitively expansive, and limited to *low* Reynolds numbers in the case of DNS. Our aims are take account of the requirements of models of practical interest (*high* Reynolds number flows). The following was taken as the definition of the problem, given the random Eulerian velocity field $\mathbf{u}(\mathbf{x}, t)$ defined in some statistical sense which is *similar* to turbulence but does not satisfy the Navier-Stokes equation. Attention will be focused on the statistics (e.g. u_{fp}, R_{fp}^L, ϕ_{fp} and T_{L_p}, etc ...) which relate to the velocity of the fluid u_{fp} along the particle trajectories, in particular to investigate the role played by particle inertia and fall velocity. Because once u_{fp} is known, it is straight forward to compute the velocity and the displacement of the particle and their statistics.

In Chapter one, different approaches of modelling, representing and understanding of u_{fp} has been presented. In §3.2 the equation of motion in *high* Reynolds number is derived, then in §3.3 the problem is formulated more precisely and one-dimensional model problems are studied. These solutions help in deriving estimates for three-dimensional case. From §3.4 to 3.8, *new* results are presented and as following:

(i)   spectra of ϕ_{fp}, ϕ_{v_R} and ϕ_{pp} can be related as function of relaxation time τ_p of the particle;

(ii)   the results are given from numerical simulations of particle motion in a random velocity field generated by Random Fourier Modes. These results are then considered in terms of

the asymptotic limits of either zero fall velocity or very large inertia;

(iii) simulated results of KS are compared with different models (simulation of random flight by Nalpanis and Hunt (1985), experimental results of Snyder and Lumley (1971));

(iv) the influence of flow structure on the settling or rising velocity of particles or bubbles in turbulent flows.

3.2 Aerosol-particle motion

3.2.1 Equation of Motion

In general, the equation of motion of a particle is extremely complicated and therefore several simplifying assumptions must be made:

(1) The concentration of particles is small (say, the volume fraction less than 0.003) enough so that the interaction between the particles can be neglected. The effect of the particle on the flow, which are caused by the inviscid displacement of fluid by the particle, by the increased turbulence in the wake (e.g. Lance *et al.* 1980), and by the increase in dissipation around the particle produced by its relative motion. The latter is dominant for small particles whose Reynolds number is small. Thus only motions of single particles will be considered. The particle is assumed to be sufficiently large for Brownian motion to be neglected in comparison with the transport originating in the interaction of the particle with the turbulent velocity field. Therefore, the particle-fluid interaction is play a dominant role. Since the equation governing Brownian motion is by Langevin's equation $du/dt = -\beta_b u + A(t)$. In this equation the coefficient of the viscous term β_b may for a spherical particle be calculated from Stoke's Law, $\beta_b = 6\pi a\mu/m$, where a is the radius of the particle, μ viscosity of the fluid, and m the mass of the particle. The reciprocal of β_b is a kind of 'relaxation time' of the viscous effects. To gain an idea of its order of magnitude, consider a spherical particle of density $\rho \simeq 1 \times 10^{-6}$ gm^{-3}, floating in air, $\mu = 1.6 \times 10^{-4}$gs^{-1}m^{-1}. If the radius of the particle is $a = 10^{-6}$m (limit of visibility) we have $\beta_b^{-1} = 1.4 \times 10^{-8}$s, so that the viscous relaxation time, even for such a relatively large particle is only of order of 0.01μs. The time-scale of diffusion phenomena normally concerning us is very much larger than this.

(2) The fluid has a constant mean flow (for simplicity, taken to be zero), the turbulent fluctuations superimposed upon this flow being consider isotropic, stationary and homogeneous throughout a frame of reference moving with the mean velocity. Many of the results presented are valid if this condition is relaxed.

(3) The domain of turbulence is infinite in extent, which removes the need for considering the interaction with a solid wall.

We have to distinguish two cases as to whether the characteristic size of that particle is larger or smaller than that the smallest spatial scale of turbulence that can influence its movement. If the particle is large compared to the scale of turbulence, the main effect of the turbulence will be on the drag coefficient and the particle will follow the slower large-scale turbulent motion of the fluid. If the particle is small compared to the smallest scale of turbulence, it will respond to all the turbulence components of the fluid. Under the latter circumstance, the flow resistance of the particle will be viscous with respect to the ambient fluid. We will only consider this case.

Let $\mathbf{x}_p(t)$ be the position of the particle at time t and $\mathbf{v}(t)$ and $\mathbf{u}(\mathbf{x}_p, t)$ be the velocities of the particle and the fluid element at the position $\mathbf{x}_p$ and time t. Then a solid particle suspended in turbulent flow fluctuates by responding to fluctuation in the velocity of the surrounding fluid. This response is governed by the equation of motion

$$m_p \frac{d\mathbf{v}}{dt} = \mathbf{F}(\mathbf{u}, \mathbf{v}, t) \,. \tag{3.2.1}$$

The force $\mathbf{F}$ on the particle is made up of many different contributions (Basset (1888), Boussinesq (1903) and Oseen (1927)). Tchen extended this work first to a sphere settling under gravity in a fluid with an unsteady but uniform flow and secondly to an unsteady and non-uniform flow, with a view to application to turbulent flows. Unfortunately Tchen's second extension was somewhat *ad hoc* and contained several errors. Since then, several papers have appeared correcting or modifying terms in the equation.

For high particle Reynolds number the equation of motion has been obtained by Auton *et al.* (1988) and we shall review it in the following:

(a) *Acceleration force*

By analysing inviscid flow around a sphere in rotational straining flow. Thomas *et al.* (1983) and Auton *et al.* (1988); Auton 1987), under the assumption of local homogeneity (or a small particle), showed that the interfacial force on a sphere in 3-dimension with volume $\mathbf{V}$ moving in an inviscid fluid with density ρ, is small compared with the length over which the velocity gradients vary can be expressed wholly in term of $\dfrac{D\mathbf{u}}{Dt}$, and in terms of $\dfrac{d\mathbf{v}}{dt}$, the rate of change of the velocity of body, i.e.

$$\mathbf{F}_A = \rho \mathbf{V} \left[(1 + C_M) \frac{D\mathbf{u}}{Dt} - C_M \frac{d\mathbf{v}}{dt} \right], \tag{3.2.2a}$$

where $\dfrac{D\mathbf{u}}{Dt}$ is the acceleration of the undisturbed flow at the location $(\mathbf{x}_p)$ of the particle and is defined by

$$\frac{D\mathbf{u}}{Dt} = \left[\frac{\partial \mathbf{u}}{\partial t} + \mathbf{u}.\nabla\mathbf{u} \right]_{\mathbf{x}=\mathbf{x}_p} \,. \tag{3.2.2b}$$

C_M is the added mass coefficient which ranges from ∞ for discs or plates normal to the flow (although $C_M \mathbf{V}$ is finite and is of order d^3, where d is a length scale), to zero for long shapes parallel to the flow. For a circular cylinder in two-dimensional flow $C_M = 1$ and for a sphere $C_M = 1/2$ (Batchelor 1967). If the particle is not spherical, the force $\mathbf{F}_A$ is not parallel to $D\mathbf{u}/Dt$ or $\mathbf{v}$ (Batchelor 1967, Chap. 7), and the above formulae are not correct.

Many alternative suggestions have been made for the term $C_M D\mathbf{u}/Dt$ in (3.2.2a). Regrettably very many have been wrong, particularly in text books on two phase flows. The errors and controversy have centered on the definition of the correct acceleration for the fluid, for this non-uniform unsteady flow. Corrsin and Lumley (1965), for example, point out the restriction in Tchen's analysis, and, in particular, emphasized the role of the pressure gradient of the basis flow in contributing also to the net fluid force on the particle though they themselves were wrong. See also Riley (1971) on the contribution of the viscous stresses to this term from external flow. Other papers have appeared on the subject of Tchen's equation, e.g. Hinze (1975), Soo (1967), giving different modifications. However, all these subsequent modifications were introduced in an *ad hoc* manner. Only until recently has the correct equation for *low* particle Reynolds number been obtained, from first principles by Maxey and Riley (1983) (but they introduced *term* that are wrong at high Reynolds number). The difference between Tchen's equation and Maxey and Riley equation is in the form of the fluid driving force. The particle velocity and acceleration terms are identical in either case to those in the BBO equation.

The usual error has been to assume that the added mass acceleration terms should be proportional to the acceleration of the fluid as seen by the volume $\mathbf{V}$, not by the acceleration of a fluid element passing $\mathbf{V}$, so the incorrect result of (3.2.2) has the form

$$\mathbf{F}_A = \rho \mathbf{V} \left[\frac{D\mathbf{u}}{dt} - C_M \left(\frac{d\mathbf{v}}{dt} - \left[\frac{d\mathbf{u}}{bt} \right]_{\mathbf{x}=\mathbf{R}(t)} \right) \right], \tag{3.2.3a}$$

where

$$\left[\frac{d\mathbf{u}}{dt} \right]_{\mathbf{x}=\mathbf{R}(t)} = \left[\frac{\partial \mathbf{u}}{\partial t} + (\mathbf{v}.\nabla)\mathbf{u} \right]_{\mathbf{x}=\mathbf{R}(t)} \tag{3.2.3b}$$

is the change of fluid velocity following the position of the body.

Expression (3.2.2) has also been derived by a number of authors (Tollmein 1938, Yakimov 1973) for *irrotational* flows; these are reviewed by Thomas *et al.* (1983).

(b) *Lift force*

If the ambient flow is rotational (e.g. a shear flow) there is an additional vorticity lift force $\mathbf{F}_L$ is caused by the interaction between the vorticity and the relative velocity of the body with

respect to the undisturbed flow, which may be written:

$$\mathbf{F}_L = \rho \mathbf{V} C_L (\mathbf{u} - \mathbf{v}) \wedge \boldsymbol{\omega}. \tag{3.2.4}$$

Here $\boldsymbol{\omega}$ is the fluid vorticity in the absence of the particle. For inviscid flow the particle lift coefficient C_L is 0.5 for spherical particle and for circular cylinder $C_L = 2$ (Batchelor 1967, p.543). The value of C_L shown here is for weak shear (an assumption has to be made that the vorticity is weak enough that $|\boldsymbol{\omega}|a \ll |\mathbf{v} - \mathbf{u}|$), consistent with local homogeneity; Auton (1983) described in detail how the calculation can be performed using a 'Drift-function method' due to Lighthill (1957), which evaluates the vorticity change ω_1 due to the stretching of a uniform upstream vorticity $\boldsymbol{\omega}$ around an obstacle in an uniform flow. Note that $\mathbf{F}_L$ is orthogonal to both the relative velocity and the liquid vorticity and in a sense which tends to increase the relative vorticity, i.e. it is towards the high speed side if the particle move against the flow or more slowly than the flow but it is towards the low speed side if the particle moves with the flow and faster than the flow. This force is often neglected in force descriptions, even when the flow field is strongly rotational. For example it is neglected by Nielsen (1979) in his analysis of sand particle motion in Rankine vortices. Also see Hinze 1975, Soo 1967. Bayerlein (1981) included the lift force and was able to show that it is important mechanism for non-uniform distribution of bubbles in a vertical pipe flow.

This is not a Magnus effect as it is not caused by rotation of the body but by the displacement and distortion of the vorticity of the ambient flow. Even in inviscid flow the spinning of particles (if they are non-spherical) can affect the lift force and hence Magnus effect exists. For spherical particles the Magnus force will usually be negligible when the particle is free to rotate with the ambient fluid. It is possible that non-spherical particle or at high Reynolds number (based on v_R), the spherical particle is spinning due to the local velocity shear, it will experience significant lift force. Physically this is one possible reason for the migration of particles from regions of high shear near the wall towards the centre line of the pipe as experienced in coal dust when transport through water pipe. White (1982) suggested that inclusion of Magnus and lift forces is essential to obtain accurate predictions of the trajectories of saltating solid particles in a wind tunnel but his results did not conclusively show this. White's expression for the Magnus lift force is

$$\mathbf{F}_{LM} = \frac{3}{2}\rho(\mathbf{u} - \mathbf{v}) \wedge (2\,\boldsymbol{\Omega} - \boldsymbol{\omega}),$$

where $\boldsymbol{\Omega}$ is the angular velocity of the particle, vanishes when the particle rotates with the same angular velocity as the ambient fluid.

(c) *Body force due to gravity*

The body force on the particle due to gravity

$$\mathbf{F}_B = \rho_p \mathbf{V} \mathbf{g},$$

(3.2.5)

where $\mathbf{g}$ is the gravitational vector.

(d) *The drag force*

When the particle moves steadily in a viscous fluid in steady uniform motion the expression for a drag force $\mathbf{F}_D$ produced by the pressure distribution and the surface viscous stress, which is a function of the particle radius a, the density, viscosity of the fluid and the relative velocity $(\mathbf{u} - \mathbf{v})$ between the fluid and the particle. For a spherical particle $\mathbf{F}_D$ is parallel to $(\mathbf{u} - \mathbf{v})$. The usual dimensional scaling for a spherical particle, leads to

$$\mathbf{F}_D = \frac{1}{2} C_D \rho \, |\mathbf{u} - \mathbf{v}|(\mathbf{u} - \mathbf{v}) \pi a^2,$$

(3.2.6a)

where a is the radius of the particle and C_D is the drag coefficient and it is an empirically known function of particle Reynolds number (Morsi and Alexander 1971, Clift *et al.* 1978) of the relative velocity

$$\mathrm{Re}_p = |\mathbf{u} - \mathbf{v}| a / \nu,$$

(3.2.6b)

where ν is the kinematic viscosity. At high Reynolds number, C_D is approximately equal to constant, and at low Reynolds number (Stokes flow) $C_D \propto 1/\mathrm{Re}$ (see Table 3.1).

For typical conditions of small particle where the terminal fall velocity V_T does not vary much with particle radius a (about 3mm in diameter), then it is convenient to define $\mathbf{F}_D$ in terms of V_T rather than the unknown drag coefficient C_D since V_T is better known. From (3.2.6a), we have

$$\frac{1}{2} \rho C_D V_T^2 \pi a^2 = |\Delta \rho| V g,$$

(3.2.7)

where $\Delta \rho = \rho_p - \rho_g$. Substituting (3.2.7) back into (3.2.6a), we obtain

$$\mathbf{F}_D = \rho \mathbf{V} g \frac{|\Delta \rho|}{\rho} \frac{|\mathbf{u} - \mathbf{v}|(\mathbf{u} - \mathbf{v})}{V_T^{*2}},$$

(3.2.8)

where V_T^* is that value of the terminal velocity in still fluid for the same value of C_D as the particle fall through the flow. For a particle in a pure liquid, whether at high or low Reynolds number, $C_D \propto 1/\mathrm{Re}$. Thus from (3.2.6a) and (3.2.7), we have

$$\mathbf{F}_D = \rho \mathbf{V} g \frac{|\Delta \rho|}{\rho} \frac{(\mathbf{u} - \mathbf{v})}{V_T^*},$$

(3.2.9)

where V_T is the *actual* fall velocity of that particular particle.

For a high Reynolds number particle in dirty liquid, premature separation of the boundary layers occur and formation of a broad fluctuating wake. Then form drag, not viscous drag, predominates and is proportional to the square of relative velocity, also C_D is approximately constant at high Reynolds number, so we have

$$\mathbf{F}_D = \rho \mathbf{V} g \frac{|\Delta\rho|}{\rho} \frac{|\mathbf{u} - \mathbf{v}|(\mathbf{u} - \mathbf{v})}{V_T^2} , \qquad (3.2.10)$$

where V_T is the *actual* fall velocity.

To cover the most common situations (3.2.9) and (3.2.10), we write

$$\mathbf{F}_D = \rho \mathbf{V} g \frac{|\Delta\rho|}{\rho} \frac{\mathbf{u} - \mathbf{v}}{V_T} f\left(\frac{|\mathbf{u} - \mathbf{v}|}{V_T}\right) , \qquad (3.2.11)$$

where $f = 1.0$ or $f = |\mathbf{u} - \mathbf{v}|/V_T$. The function $f\left(\dfrac{|\mathbf{u} - \mathbf{v}|}{V_T}\right)$ is need to accommodate the effect of surface tension non-uniformities arising from accumulation of contaminants on the particle.

(e) *Drag force is unsteady non-uniform (Basset history term)*

If a particle experiences a drag force associated with viscous forces, then vorticity is shed into its wake. When the particle is moving unsteadily (by a change of velocity Δu_p over a time t_p) or the flow is unsteady especially if the flow reverses, the rate at which vorticity is shed into the wake changes and the distribution of previously shed vorticity in the wake relative to the body has to be considered.

At low Reynolds number, the criteria for these effects to be negligible that

$$\frac{a^2}{t_p \mu} \lesssim 1 \qquad \text{and} \qquad \frac{t_p (\Delta u_p)^2}{\ell_w u_p} \lesssim 1 ,$$

where ℓ_w is the relevant scale of the wake $\sim (a + \nu t_p)$. A formula has been developed for this case (Basset history term).

In general, the instantaneous drag depends not only on the instantaneous velocities and accelerations, but also on conditions which prevailed during development of the flow. The Basset history term in which past acceleration is included, weighted as $(t - \tau)^{1/2}$, where $(t - \tau)$ is the time elapse since the past acceleration. The form of the history integral results from diffusion of vorticity from the particle. This force is expressed by

$$\mathbf{F}_{BH} = 6a^2 \rho \sqrt{\pi \nu} \int_0^t \frac{\dfrac{d\mathbf{u}}{d\tau} - \dfrac{d\mathbf{v}}{d\tau}}{\sqrt{t - \tau}} \, d\tau. \qquad (3.2.12a)$$

By integrating (3.2.12a) by parts a more suitable expression for use in the computation may be obtained as follows:

$$\mathbf{F}_{BH} = 12a^2\rho\sqrt{\pi\nu}\left\{\sqrt{t}\left[\frac{d\mathbf{u}}{d\tau} - \frac{d\mathbf{v}}{d\tau}\right]_{t=0} + \int_0^t \sqrt{t-\tau}\left(\frac{d^2\mathbf{u}}{d\tau^2} - \frac{d^2\mathbf{v}}{d\tau^2}\right)d\tau\right\}. \qquad (3.2.12b)$$

Lumley (1957, chapter 2, §4) has shown that the Basset history term can be neglected provided that $\left(a_p^2\omega_m/\mu\right)^{1/2} \ll 1$, where ω_m is a characteristic high frequency of the Eulerian velocity field. For more details concerning the Basset history term see Soo (1967).

For the calculation presented here, it is assumed that the particles are small enough that their Reynolds number is of order 1 and that the Basset history term can be omitted.

At high Reynolds number the criterion (Graham 1980) is

$$\frac{t_p\Delta u_p^2}{au_p} \lesssim 1 \qquad \text{if} \qquad \Delta u_p \lesssim u_p;$$

$$\frac{t_p\Delta u_p}{a} \gtrsim 1 \qquad \text{if} \qquad \Delta u_p \gtrsim u_p.$$

Once the interfacial force $\mathbf{F}$ is determined, the motion of the particle is related to $\mathbf{F}$ by Newton's second law

$$\mathbf{F} = \rho_p\mathsf{V}\left(\frac{d\mathbf{v}}{dt} - \mathbf{g}\right). \qquad (3.2.13)$$

In deriving the following equation of motion for spherical particle in a turbulent flow, the various effects which contribute to the overall particle motion are assumed to be separable and independent and that the particle radius is much smaller than the length scale of the inhomogeneity of the liquid. These equations may be combined to yield

$$\frac{d\mathbf{v}}{dt} = \frac{|\gamma-1|}{\gamma+C_M}\,g\,\frac{\mathbf{u}-\mathbf{v}}{V_T}\,f\left(\frac{\mathbf{u}-\mathbf{v}}{V_T}\right) + \frac{\gamma-1}{\gamma+C_M}\,\mathbf{g}$$

$$+ \frac{1+C_M}{\gamma+C_M}\frac{D\mathbf{u}}{Dt} + \frac{C_L}{\gamma+C_M}(\mathbf{u}-\mathbf{v})\wedge\boldsymbol{\omega} + \frac{6a^2\sqrt{\pi\nu}}{\gamma+C_M}\int_0^t \frac{\dfrac{d\mathbf{u}}{d\tau} - \dfrac{d\mathbf{v}}{d\tau}}{\sqrt{t-\tau}}\,d\tau, \qquad (3.2.14)$$

where $\gamma = \rho_p/\rho$ is the density ratio between the particle and its surrounding fluid.

Parenthetically it should be noted that for a heavy particle $\gamma \gg 1$ and for small relative particle Reynolds number $\mathrm{Re}_p \ll 1$ (based on terminal velocity and particle size), the last three terms in the equation (3.2.14) can be neglected and the drag force is linear (Stokes flow), thus the limiting equation (3.2.14) can be written as:

$$\frac{V_T}{g}\frac{d\mathbf{v}}{dt} = \mathbf{u} - \mathbf{v} + V_T\widehat{\mathbf{g}}, \qquad (3.2.15)$$

where $\widehat{\mathbf{g}} = \mathbf{g}/|\mathbf{g}|$.

3.3 Model problems

3.3.1 *Simplified equation of motion for the particle*

Our eventual aim was to use (3.2.14) in our simulation. However, due to computational expense, we use (3.2.15) instead, i.e. we are ignoring the added mass term, the lift force and Basset history term. Supposing that the relative Reynolds number (based on terminal velocity and particle size) is less than 1 and the particles are small relative to the smallest length in the turbulence (the Kolmogorov length scale $\eta = (\nu^3/\varepsilon)^{1/4} \simeq 1\text{mm}$ in the lower atmosphere) so that the flow about a particle is nearly a simple shear and have time constants short relative to the shortest time scales ($\tau = (\nu/\varepsilon)^{1/2} \simeq 0.08\text{s}$ in the atmosphere) then it follows from (3.2.15) that the equation of motion has the form

$$\tau_{p_o}\frac{d\mathbf{v}}{dt} = \mathbf{u}(\mathbf{x}_p, t) - \mathbf{v}(t) + \mathbf{w}_o\,, \qquad (3.3.1)$$

where $\mathbf{v}$ is the particle velocity, τ_{p_o} ($= V_T/g = m_p/6\pi a\mu$) is an inertia parameter (according to Stokes flow) and $\mathbf{w}_o$ ($= m_p\mathbf{g}/6\pi a\mu$) is the Stokes settling velocity for still fluid (the time scale restriction is satisfied for $\mathbf{w}_o \ll 0.78\text{m/s}$ in the atmosphere). The equation represents a balance of the particle inertia and acceleration, with the fluid drag force produced by the motion of the particle relative to the surrounding fluid and the force due to gravity. In writing the above equation, we have also make the following assumptions that all particles are rigid spheres; particle-particle interactions are neglected and the effect of the particle on the flow is neglected. Despite the restriction that have been imposed, (3.3.1) is applicable to many different aerosol problems: in air flow under most atmospheric conditions (3.3.1) would apply for instance to aerosol particles or cloud drops in the range $2\mu\text{m} < a_p < 30\mu\text{m}$.

The equation of motion is scaled by u', the variance of the fluctuating velocity in the flow field and by L the integral length scale as given by (2.2.23). Non-dimensional variables are introduced as follows:

$$\mathbf{x}^* = \frac{\mathbf{x}}{L}, \quad \mathbf{x}_p^* = \frac{\mathbf{x}_p}{L}, \quad t^* = \frac{tu'}{L}, \quad \mathbf{v}^* = \frac{\mathbf{v}}{u'}, \quad \mathbf{u}^* = \frac{\mathbf{u}}{u'} \quad \text{and} \quad \mathbf{w}^* = \frac{\mathbf{w}}{u'}. \qquad (3.3.2)$$

Also normalise $\varepsilon^* = \varepsilon u^3/L$. The scaled form (3.3.1), with the asterisks suppressed, is

$$\tau_p\frac{d\mathbf{v}}{dt} = \mathbf{u}(\mathbf{x}_p(t), t) - \mathbf{v}(t) + \mathbf{w}\,, \qquad (3.3.3a)$$

where

$$\frac{d\mathbf{x}_p}{dt} = \mathbf{v}(t)\,. \qquad (3.3.3b)$$

The particle motion can be characterised by two dimensionless parameters. The inertia parameter (Stokes number), τ_p, is defined as
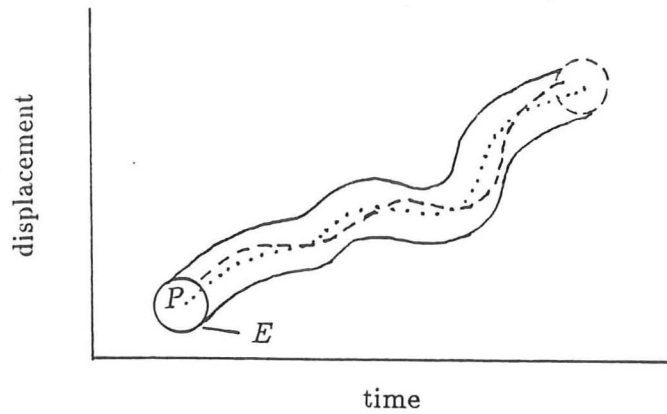
$$\tau_p = \tau_{p_o}u'/L, \qquad (3.3.4)$$

Fig. 3.1 Displacement of a particle P and that of a spherical fluid element

E. ———— path of centroid of E; $---$ path of P.

with inertia more significant the larger the value of τ_p. The scaled particle settling velocity for still-fluid $\mathbf{w}$ defined as

$$\mathbf{w} = \mathbf{w}_o / u'. \tag{3.3.5}$$

Equations (3.3.3a, b) are a pair of coupled ordinary differential equations whose right-hand side is a stationary random function of space and time. Formally, the analytical solution of $\mathbf{v}(t)$ is

$$\mathbf{v}(t) = \mathbf{v}(0)e^{-t/\tau_p} + \frac{e^{-t/\tau_p}}{\tau_p} \int_0^t e^{t'/\tau_p}(\mathbf{u} + \mathbf{w}) \, dt'. \tag{3.3.6}$$

In general the integral equation (3.3.6) does not exist explicit solution for arbitrary $\mathbf{u}(\mathbf{x}_p, t)$, it nonetheless provides a relationship between the velocity $\mathbf{v}(t)$ and $\mathbf{u}(\mathbf{x}_p, t)$, but the foregoing are random variable in which statistics can assumed to be known. Therefore, it is necessary to approach the problem of the motion of the particle in a turbulent flow and consequently also the phenomena related to it in a statistical manner.

In fact (3.3.3) is a stochastic nonlinear equation and a solution would consists of finding the complete probability density function, $P[\mathbf{u}(\mathbf{x}_p, t)]$. Complete knowledge of this would imply a solution to the closure problem of turbulence. Therefore a theoretical attack on this highly non-linear problem if far from clear. However, Phythian (1975) by making the assumption that the Eulerian velocity field $\mathbf{u}(\mathbf{x}, t)$, has a Gaussian probability distribution and calculations based on this compare well with Kraichnan's (1970) solution for model turbulent spectra. Nevertheless, theoretical attempts are mostly limited to the investigation of results of *ad hoc* hypotheses. An experimental approach to the problem is extremely difficult because of the absence of reliable methods for measuring the Lagrangian statistical characteristics of the turbulence and therefore few reliable results exist.

Tchen (1947) and Hinze (1975) assume that during the motion of the particle, the neighbourhood will be formed by the same fluid (Fig. 3.1), and making the assumption that the Lagrangian correlation of the fluid along the particle trajectory,

$$R^L_{fp_{ij}}(\tau) = \frac{\langle u_i(\mathbf{x}_p(t), t) u_j(\mathbf{x}_p(t+\tau), t+\tau)\rangle}{\sqrt{\langle u_i^2(\mathbf{x}_p(t), t)\rangle}\sqrt{\langle u_j^2(\mathbf{x}_p(t+\tau), t+\tau)\rangle}} \tag{3.3.7}$$

was the same as the Lagrangian velocity correlation of the flow,

$$R^L_{ff_{ij}}(\tau) = \frac{\langle u_i(\mathbf{x}_f(t), t) u_j(\mathbf{x}_f(t+\tau), t+\tau)\rangle}{\sqrt{\langle u_i^2(\mathbf{x}_f(t), t)\rangle}\sqrt{\langle u_j^2(\mathbf{x}_f(t+\tau), t+\tau)\rangle}}, \tag{3.3.8}$$

and concluded that the long time particle and fluid point diffusivities were equal. The problem of finding the particle diffusivity is to determine $R^L_{fp_{ij}}$. Pismen and Nir (1979) using the 'independence approximation' (expressing the Lagrangian correlation tensor as the average of the Eulerian correlation function taken with respect to the uncertain position of the particle) and the characteristic function of the velocity field is Gaussian while Reeks (1977) used an iterative approximation for $\mathbf{x}_p(t)$ based on some initial position $x_p(0)$ of the particle, they both used Kraichnan (1970) model spectrum

$$\Phi_{ii}(k, t) = (2\pi)^{-1} k^{-2} E(k) \exp\left[-\frac{1}{2}(u_o k_o t)^2\right],$$

where

$$E(k) = 16(2/\pi)^{1/2} u_o^2 k^4 k_o^{-5} \exp(-2k^2/k_o^2)$$

and obtained approximation to the velocity correlation along the particle trajectory, R^L_{fp}. Reeks (1980) compared these approximations with another approximation based on Kraichnan's Direct Interaction Procedure with value of the diffusivity of the particle motion in a statistical simulation of particle motion in a random flow field and good agreement was found with value of diffusivity from each approximation.

3.3.2 Solution in one-dimensional case with arbitrary velocity

The major difficulty in solving (3.3.3) is the random variable $\mathbf{u}(\mathbf{x}_p, t)$; no previous studies have satisfactorily solved this without making *ac hoc* hypotheses or developing concepts. So we study certain model problems. Although the differential equations (3.3.3a, b) and the integral (3.3.6) cannot be solved for any arbitrary velocity fields $\mathbf{u}(\mathbf{x}, t)$, (3.3.3a, b) can be solved in the one-dimensional case. This solution helps in deriving estimates for the three-dimensional case.

Case of zero settling velocity $W_g = 0$

In the limit of $\omega_T \tau_p \ll 1$, where $\omega_T (\sim u_o/L)$ is the typical circular frequency of the fluid velocity fluctuations, the relative velocity of fluid and particle is small, thus the primary motion of the

particle is to follow the trajectory, $\mathbf{x}^{(0)}(t)$, of the fluid element. However, due to the inertia of the particle, the particle does not completely follow the fluid element. Therefore, the particle inertia produce perturbations to this basic motion, $\mathbf{x}^{(0)}(t)$. The equation (3.3.3a) for the particle motion may be solved in terms of a perturbation expansion based on powers of $\epsilon = \tau_p$, i.e.

$$\mathbf{x}_p(t) = \mathbf{x}^{(0)}(t) + \epsilon \mathbf{x}^{(1)}(t) + \epsilon^2 \mathbf{x}^{(2)}(t) + \dots \tag{3.3.9}$$

Then by the Taylor expansion, we have

$$\mathbf{u}(\mathbf{x}_p(t), t) = \mathbf{u}(\mathbf{x}^{(0)}(t), t) + \epsilon \mathbf{x}^{(0)}(t).\nabla \mathbf{u}(\mathbf{x}^{(0)}(t), t) + \dots \tag{3.3.10}$$

The Taylor expansion allows the perturbation to be found explicitly and expressed eventually in terms of Eulerian data. The expansion is valid if $|\mathbf{x}'_p|$, the departure of $\mathbf{x}_p(t)$ from $\mathbf{x}^{(0)}$, is small compared to the lengthscale L_x of the flow field. Substituting (3.3.9) into (3.3.3), we have

$$\frac{d\mathbf{x}^{(0)}(t)}{dt} + \epsilon \frac{d\mathbf{x}^{(1)}(t)}{dt} + \dots \approx \mathbf{u}(\mathbf{x}^{(0)}(t), t) + \epsilon \mathbf{x}^{(1)}(t).\nabla \mathbf{u}(\mathbf{x}^{(0)}(t), t) + \dots$$

$$- \epsilon \left(\frac{d^2 \mathbf{x}^{(0)}(t)}{dt^2} + \dots \right).$$

For simplicity, consider the one dimension case only, i.e. the x-direction, the above equation becomes

$$\frac{dx^{(0)}(t)}{dt} + \epsilon \frac{dx^{(1)}(t)}{dt} + \dots = u(\mathbf{x}^{(0)}(t), t) + \epsilon x^{(1)}(t) \frac{\partial u(\mathbf{x}^{(0)}(t), t)}{\partial x} - \epsilon \left(\frac{d^2 x^{(0)}(t)}{dt^2} + \dots \right).$$

Equate power of ϵ, for ϵ^0 and ϵ^1, we have

$$\frac{dx^{(0)}(t)}{dt} = u(\mathbf{x}^{(0)}(t), t) , \tag{3.3.11}$$

and

$$\frac{dx^{(1)}(t)}{dt} = x^{(1)}(t) \frac{\partial u(\mathbf{x}^{(0)}, t)}{\partial x} - \frac{d^2 x^{(0)}(t)}{dt^2}$$

$$= x^{(1)} \frac{\partial u}{\partial x} - \frac{du}{dt}, \tag{3.3.12}$$

where $u = u(\mathbf{x}^{(0)}(t), t)$ and $x^{(1)}(t) = x^{(1)}$.

Let the function at the position of the particle at time t be

$$\zeta(t) = \exp \int_0^t -\frac{\partial u(t')}{\partial x} \, dt' , \tag{3.3.13}$$

this is a random function if $\frac{\partial u}{\partial x}$ varies along the x-direction (since u is random), then

$$x^{(1)} = -\zeta^{-1} \int_0^t \zeta(t') \dot{u}(t') \, dt',$$

(3.3.14)

where dot means d/dt and assuming $x^{(1)}(0) = 0$.

The dispersion rate in the x-direction $\frac{1}{2} \left\langle \frac{dx_p^2}{dt} \right\rangle$ may be written as

$$\frac{1}{2} \left\langle \frac{dx_p^2}{dt} \right\rangle = \left\langle x_p \frac{dx_p}{dt} \right\rangle$$

$$= \left\langle x^{(0)} \frac{dx^{(0)}}{dt} \right\rangle + \epsilon \left\langle \left(x^{(1)} \frac{dx^{(0)}}{dt} + x^{(0)} \frac{dx^{(1)}}{dt} \right) \right\rangle + \dots ,$$

(3.3.15)

Integrating the first term w.r.t. t, it can be easily shown that

$$\left\langle x^{(0)^2} \right\rangle = \left\langle u^2 \right\rangle t^2 , \qquad\qquad t \ll T_L ,$$

and

$$\left\langle x^{(0)^2} \right\rangle = 2 \left\langle u^2 \right\rangle T_L t , \qquad\qquad t \gg T_L ,$$

where T_L is the Lagrangian integral time scale. These results are consistent with Taylor's (1921) kinematics predictions for the fluid particle diffusion.

Now let us consider the correction term E

$$\mathsf{E} = x^{(1)} \frac{dx^{(0)}}{dt} + x^{(0)} \frac{dx^{(1)}}{dt}$$

$$= - \left(u + \int_0^t \frac{\partial u(t')}{\partial x} u(t') \, dt' \right) \zeta^{-1}(t) \int_0^t \zeta(t') \dot{u}(t') \, dt' - \int_0^t \frac{du(t')}{dt'} u(t') \, dt' .$$

(3.3.16)

For small value of t,

$$\zeta(t) = \exp \int_0^t -\frac{\partial u(t')}{\partial x} \, dt' \approx \exp \left(-t \left[\frac{\partial u}{\partial x} \right]_{t=0} \right) \approx 1 - t \left[\frac{\partial u}{\partial x} \right]_{t=0} + \dots .$$

Therefore

$$\zeta(t)^{-1} \approx 1 + t \left[\frac{\partial u}{\partial x} \right]_{t=0} + \dots .$$

Substituting this into (3.3.16) and neglecting the t^2 and any other higher order term, we have

$$\mathsf{E} \approx - \left\{ [u]_{t=0} + t \left[u \frac{\partial u}{\partial x} \right]_{t=0} + \dots \right\} \left\{ 1 + t \left[\frac{\partial u}{\partial x} \right]_{t=0} + \dots \right\} t \, [\zeta \dot{u}]_{t=0} - t \, [\dot{u} u]_{t=0}$$

$$= -2t \, [\dot{u} u]_{t=0} - t^2 \left[\dot{u} \frac{\partial u^2}{\partial x} \right]_{t=0}$$

$$= -2t^2 \left[u \frac{\partial u}{\partial x} u \frac{\partial u}{\partial x} \right]_{t=0} .$$

(3.3.17)

This analysis implies the correction must be negative and proportional to t^2. At this stage it is necessary to make some approximation about the fourth-order velocity and velocity-gradient product mean value. Many experiments have shown that the velocity statistics are approximately jointly Gaussian, so that the fourth-order velocity correlation tensor (Batchelor 1953), which can be written in terms of the second-order velocity correlations. i.e.

$$
\langle u_i(\mathbf{x}, t) u_j(\mathbf{x}', t') u_k(\mathbf{x}'', t'') u_l(\mathbf{x}''', t''') \rangle = \langle u_i(\mathbf{x}, t) u_j(\mathbf{x}', t') \rangle \cdot \langle u_k(\mathbf{x}'', t'') u_l(\mathbf{x}''', t''') \rangle
$$
$$
+ \langle u_i(\mathbf{x}, t) u_k(\mathbf{x}'', t'') \rangle \cdot \langle u_j(\mathbf{x}', t') u_l(\mathbf{x}''', t''') \rangle
$$
$$
+ \langle u_i(\mathbf{x}, t) u_l(\mathbf{x}''', t''') \rangle \cdot \langle u_j(\mathbf{x}', t') u_k(\mathbf{x}'', t'') \rangle. \quad (3.3.18)
$$

When (3.3.18) is used in (3.3.17), a number of terms cancel because of the homogeneity, we obtain

$$
\langle \mathsf{E} \rangle = -2t^2 \left[\langle u^2 \rangle \left\langle \left(\frac{\partial u}{\partial x} \right)^2 \right\rangle \right]_{t=0}.
$$

Therefore, for a small time t, from (3.3.16) we have

$$
\frac{1}{2} \left\langle \frac{dx_p^2}{dt} \right\rangle = \langle u^2 \rangle t - 2\epsilon t^2 \left[\langle u^2 \rangle \left\langle \left(\frac{\partial u}{\partial x} \right)^2 \right\rangle \right]_{t=0}. \quad (3.3.19)
$$

Since u, $\dfrac{\partial u}{\partial x}$ are stationary random functions, therefore $\langle u^2 \rangle$ and $\left\langle \left(\dfrac{\partial u}{\partial x} \right)^2 \right\rangle$ are independent of time, therefore (3.3.19) becomes

$$
\langle x_p^2 \rangle = \langle u^2 \rangle t^2 - \frac{1}{3} \epsilon t^3 \langle u^2 \rangle \left\langle \left(\frac{\partial u}{\partial x} \right)^2 \right\rangle \qquad \text{for} \qquad t \ll T_L, \quad (3.3.20)
$$

For $t \gg T_L$, let $\vartheta = \displaystyle\int_0^t \frac{\partial u}{\partial x}(t') \, dt'$, it can be shown that the variance of ϑ is

$$
\sigma_\vartheta^2 = 2 \left\langle \left(\frac{\partial u}{\partial x} \right)^2 \right\rangle \tau_L t \qquad \text{for} \qquad t \gg \tau_L,
$$

where τ_L is the integral time scale for the velocity gradient of the fluid, then from (3.3.13), the mean value of $\zeta(t)$ is

$$
\langle \zeta(t) \rangle = \exp \left\{ \left\langle \left(\frac{\partial u}{\partial x} \right)^2 \right\rangle \tau_L t \right\}.
$$

Also, making the assumption that both of the autocorrelation functions of u and $\dfrac{\partial u}{\partial x}$ have the form

$$
R_u(t) = \exp \left(-\frac{t}{T_L} \right), \qquad \text{and} \qquad R_{\frac{\partial u}{\partial x}}(t) = \exp \left(-\frac{t}{\tau_L} \right),
$$

we obtain the asymptotic result for t is large comparing with T_L and the result is summarised below

$$\langle x_p^2 \rangle = \left[2 \langle u^2 \rangle T_L - \frac{\epsilon \langle u^2 \rangle \left\langle \left(\frac{\partial u}{\partial x}\right)^2 \right\rangle \tau_L (T_L + 2)}{1 + \left\langle \left(\frac{\partial u}{\partial x}\right)^2 \right\rangle \tau_L^2} \right] t \qquad \text{for} \qquad t \gg T_L, \qquad (3.3.21)$$

It has been show that perturbation methods can be formulated the problem of dispersion in a one-dimensional random velocity field and these methods can be used to obtain asymptotic approximation both for time less or greater than T_L. The results have shown that both for 'short' and 'long' times, the mean square displacement of the particle is less than that of the fluid element in the case of zero fall velocity, i.e. the diffusivity of the particle is less than that of the fluid element. We will show that the 'long' time result is consistent with the results presented in the next section with the velocity represented as a series of 'jumps'. The question arises of whether one can extend this method for three-dimensional flow field. An attempt has been made to extend this into 3-D, but because of the nonlinearity, the equation cannot be solved analytically. Thus from either the Lagrangian or Eulerian point of view, theoretical analysis of the problem is mostly limited to investigation of results of *ad hoc* hypotheses and to compute 'short' time and 'long' time results.

3.3.3 *One-dimensional model problem*

Since the simplified equation of motion (3.3.3a) is linear, we can thus represent the response of a particle to a flow of arbitrary velocity $\mathbf{u}(t)$ as linearly superposition of the response to the spectral components of $\mathbf{u}(t)$. By expressing $u_{fp}(t)$ and $\mathbf{v}(t)$ as Fourier integrals, we have

$$\mathbf{v}(t) = \int_{-\infty}^{\infty} \widetilde{\mathbf{v}}(\omega) e^{i\omega t} \, d\omega \qquad \text{and} \qquad \mathbf{u}_{fp}(t) = \int_{-\infty}^{\infty} \widetilde{\mathbf{u}}_{fp}(\omega) e^{i\omega t} \, d\omega, \qquad (3.3.22)$$

where ω is the circular frequency. Using standard techniques of Fourier analysis, it follows from equation (3.3.3a), we have $\widetilde{\mathbf{v}}(\omega) = \dfrac{\widetilde{\mathbf{u}}_{fp}(\omega)}{(1 + i\tau_p \omega)}$. Thus, the particle's energy spectrum can be expressed as a function of the fluid's velocity spectrum along the particle trajectory through a 'particle response function' χ, which is a measure of a particle's response to accelerations or frequency spectrum ϕ_{fp} of the fluid velocity seen by the particle, i.e.

$$\phi_{pp}(\omega) = \frac{\phi_{fp}(\omega)}{1 + \tau_p^2 \omega^2} = \chi^2(\omega) \phi_{fp}(\omega) \,, \qquad (3.3.23)$$

where the spectra are normalised so that

$$\langle u_{fp}^2 \rangle = \int_0^{\infty} \phi_{fp}(\omega) \, d\omega \qquad \text{and} \qquad \langle v^2 \rangle = \int_0^{\infty} \phi_{pp}(\omega) \, d\omega \,.$$

The effect of $\chi^2(\omega)$ is roughly equivalent to applying a low-pass cutoff to the turbulent velocity spectrum at $\omega \sim 1/\tau_p$ (to be precise this would correspond to a 50% reduction in spectral density).

A brief calculation also shows that the spectrum of the mean-square relative velocity $v_R = v - u_{fp}$ is:

$$\phi_{v_R}(\omega) = \frac{\tau_p^2 \omega^2}{1 + \tau_p^2 \omega^2} \phi_{fp}(\omega) \qquad (3.3.24a)$$

$$= \tau_p^2 \omega^2 \phi_{pp}(\omega). \qquad (3.3.24b)$$

The early investigators of Soo (1967) and Hinze (1975) assumed that $\langle \mathbf{u}(\mathbf{x}_p(0), 0)\mathbf{u}(\mathbf{x}_p(t), t)\rangle$ was the same as the Lagrangian velocity correlation of the flow, $\langle \mathbf{u}(\mathbf{x}_f(0), 0)\mathbf{u}(\mathbf{x}_f(t), t)\rangle$ (particle constrained to move with a single correlated region of fluid). This assumption leads to the diffusion coefficients of particles and fluid elements being equal which is not true even for quite small light particles. However $\langle \mathbf{u}(\mathbf{x}_p(0), 0)\mathbf{u}(\mathbf{x}_p(t), t)\rangle$ depends on the particle motion itself and the particle motion can only be understood in terms of statistics of the velocity of the fluid along the particle trajectories $\mathbf{u}_{fp}(t)$.

(a) *A simple one-dimensional problem*

Consider a stationary velocity consists of a series of 'jumps' with zero mean and frequency ω (Fig. 3.2) in which only exists one length scale L_n and has the form

$$u_n(x) = U_o + U_n H(x - x_n), \qquad (3.3.25)$$

where $u_n^2 = u_o^2$ and

$$H(x - x_n) = \begin{cases} 1, & \text{if } x_n < x < x_n + L_n \text{ ;} \\ 0, & \text{otherwise.} \end{cases}$$

Here $x_n = nL_n$, $n = 0, 1, 2, \ldots$.

fluid velocity
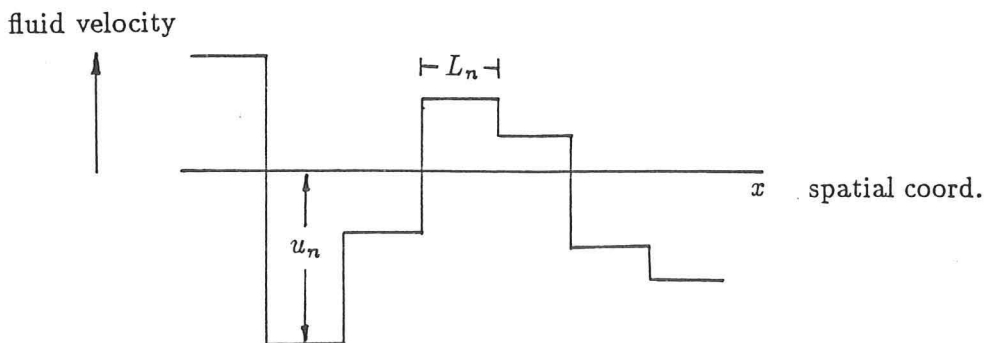
Fig. 3.2 The form of the velocity field for $u_n(x)$.

We recall that the one-dimensional equation of motion for the particle is

$$\tau_p \frac{dv}{dt} = u - v \qquad (3.3.26)$$

and together with initial conditions $v = 0$, $x_o = 0$ at $t = 0$, then the velocity of the particle for the first 'jump' is given by

$$v = U_o \left(1 - e^{-t/\tau_p}\right). \tag{3.3.27}$$

For the second 'jump', i.e. when the particle is at $x = x_1$, with $\tau_p dv/dt = U_1 - U_o$, we have

$$v = U_o + (U_1 - U_o)\left(1 - e^{-(t-t_1)/\tau_p}\right). \tag{3.3.28}$$

So the error in v is $\mathcal{O}\left(\Delta t_n/\tau_p\right)$, where Δt is the time taken for each 'jump'. However the relative velocity between the fluid and the particle is negligible provided that $\omega\tau_p \ll 1$, i.e. $\langle v^2 \rangle$ is not affected. Hence the velocity of the particle will only be affected for $\omega > \tau_p^{-1}$ (or time scale $\lesssim \tau_p$). But the mean time ΔT_p for particle to travel between 'jumps' *decrease* by $\mathcal{O}(\tau_p/\Delta T_o)$, where ΔT_o is the time for the fluid element to travel between the 'jumps'.

This can also be seen easily by considering

$$\Delta T_p = \frac{L_n}{U_o + U_n + \Delta v_n},$$

where Δv_n is the error in v between 'jumps'. Taking the ensemble average, we have

$$\langle \Delta T_p \rangle = \frac{L_n}{U_o} \left[1 - \frac{\langle U_n + \Delta v_n \rangle}{U_o} + \frac{\langle U_n^2 + 2U_n\Delta v_n + \Delta v^2 \rangle}{U_o^2} + \cdots\right]$$

$$= \Delta T_o \left[1 + \frac{2\langle U_n\Delta v_n \rangle}{U_o^2} + \cdots\right], \tag{3.3.29}$$

since $U_n^2 \gg \Delta v_n^2$ if $\tau_p \ll 1$. Therefore, owing to the inertia effect, we have

$$\langle U_n\Delta v_n \rangle < 0, \tag{3.3.30}$$

i.e.   if $U_n < 0$, $\Delta v_n > 0$ $\Rightarrow$ faster $\Rightarrow$ shorter time (on long time steps)

and   if $U_n > 0$, $\Delta v_n < 0$ $\Rightarrow$ slower $\Rightarrow$ longer time (on short time steps).

A simple explanation for this phenomenon is that a particle will in general interact with an eddy going in the same direction for a long time and with an eddy going in the opposite direction for a short time (Fig. 3.3).

Alternatively, by considering the mean square displacement x_p of the particle, i.e.

$$\langle x_p^2 \rangle + \langle \Delta x^2 \rangle = \langle U_n^2 \rangle T_{L_p} t \qquad \text{for} \qquad t \gg \tau_p, \tag{3.3.31}$$

where Δx the change in x_p caused by each 'jump'. For a particular n, we have

$$\Delta x_n = \int \Delta v_n \, dt = \tau_p U_n,$$

therefore
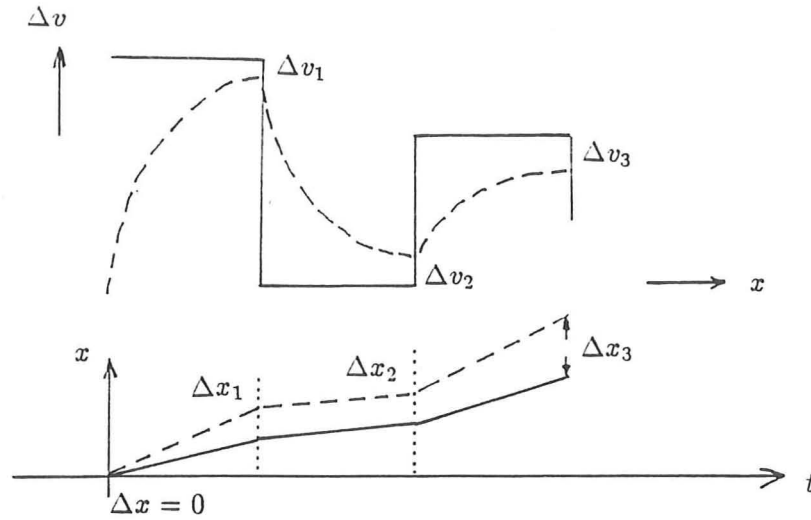
Fig. 3.3 The respond of the particle to the velocity $u_n(x)$.

$$\left\langle \sum_1^N (\Delta x_n)^2 \right\rangle = N\tau_p \left\langle U_n^2 \right\rangle .$$

But the number of 'jumps' (to first order) $N = t/\Delta T_o = x/L_n$. The implies

$$\text{changes in } \left\langle (\Delta x)^2 \right\rangle = \frac{t}{\Delta T_o}\tau_p^2 \left\langle U_n^2 \right\rangle = \frac{u_o^2 \tau_p^2 t}{T_L}, \tag{3.3.32}$$

i.e. change in $\left\langle (\Delta x)^2 \right\rangle$ is proportional to the square of τ_p. This result is valid in one-dimensional 'turbulent flow' with one length scale. Since as $t \to \infty$,

$$\left\langle x_p^2 \right\rangle = 2 \left\langle v^2 \right\rangle T_{L_p} t = 2t\phi_{pp}(\omega \to 0) , \tag{3.3.33}$$

so we see that

$$\phi_{pp}(\omega \to 0) = \phi_{pp}(\tau_p \to 0; \omega \to 0) \left[1 - \mathcal{O}(\tau_p^2)\right] .$$

The above analysis clearly shows that Soo's analysis is wrong; he incorrectly assumed that $\phi_{fp}(\omega) = \phi_{ff}(\omega)$, and therefore he obtained

$$\phi_{pp}(\omega \to 0) \sim \phi_{ff}(\omega \to 0), \tag{3.3.34}$$

which leads to the experimentally incorrect result that

$$\left\langle x_p^2(t \to \infty) \right\rangle = \left\langle x_f^2(t \to \infty) \right\rangle , \tag{3.3.35}$$

i.e. the long time particle and fluid element diffusion coefficients were equal.

What the analysis has shown that the differences between the particle and fluid element on the *small scale* lead to *large scale* changes in the mean square displacement.

This analysis also suggest that the spatial structure of the velocity field affects the correction Δx. Hence the need to *model* the actual space-time structure of turbulence.

(b) *What happens if 'jumps' or 'eddies' change over at different length scale ℓ_e?*
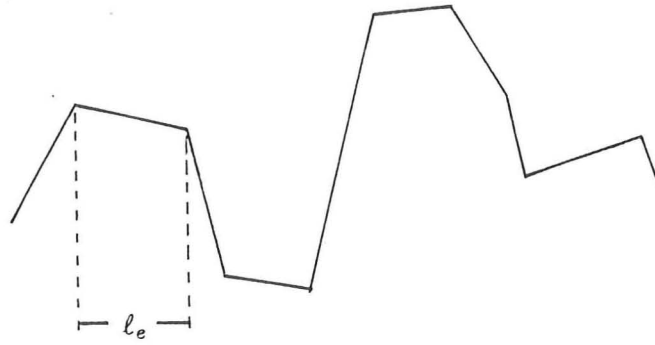
Fig. 3.4 The form of the velocity field for $u_n(x)$ with different length scales.

Let the typical time for 'eddy' velocity to change is $\tau_e \sim \ell_e/U_n = \ell_e/\Delta u_e$ (Fig. 3.4). By doing the one-dimensional analysis in the previous section, it is clear that ΔT_p or Δx^2, the average time taken to cross each 'eddy' or mean square displacement is also reduced by $\mathcal{O}(\tau_p^2)$, i.e.

$$\Delta T_p = \Delta T_o \left[1 - \beta \left(\frac{\tau_p}{T_o} \right)^2 \right], \tag{3.3.36a}$$

$$\langle x^2 \rangle = \langle x_o^2 \rangle \left[1 - \beta \left(\frac{\tau_p}{T_o} \right)^2 \right]. \tag{3.3.36b}$$

β is much smaller if $\tau_e \gg \tau_p$ (in fact $\mathcal{O}(\tau_p/\tau_e)$). Hence, ΔT_p is only affected by these eddies that change on a time scale $\mathcal{O}(\tau_p)$ or less.

(c) *Estimate of inertia correction for mean square dispersion*

From the previous discussion (b), it follows that the main difference in displacement Δx occurs for eddies with time scale τ_p or less. Hence, if $\Delta T_o \sim \tau_p$ and in the inertia subrange, change in fluid velocity in time τ_p is $\Delta u \sim \sqrt{\varepsilon \tau_p}$, so change in $(\Delta x)^2$ for each 'eddy' $\sim (\Delta u)^2 \tau_p^2 \sim \varepsilon \tau_p^3$. Taking the ensemble average, we have

$$\langle (\Delta x)^2 \rangle \sim \frac{t}{\tau_p} \varepsilon \tau_p^3 \sim t \varepsilon \tau_p^2 . \tag{3.3.37}$$

Since $\varkappa_p(t \to \infty) = (\pi/2)\phi_{pp}(\omega = 0)$, so the diffusivity of particle

$$\varkappa_p = \varkappa_f - \widehat{\beta}_i \varepsilon \tau_p^2 , \tag{3.3.38}$$

where $\widehat{\beta}_i$ depends on the type of 'turbulence' – especially the 'sharpness' of the eddies. Therefore the change of $\varkappa_p$ due to inertia is proportional to the square of τ_p.

(d) *What about fall velocity V_T?*

V_T changes the relative speed of particle across the eddies. If the fall velocity $V_T \gg \Delta u \sim \sqrt{\varepsilon \tau_p}$, in the inertia subrange, then critial eddies have length scale $\tau_p V_T$ rather than $\sqrt{\varepsilon \tau_p^3}$. Hence

$$\text{Velocity of eddy} \ = (\varepsilon \tau_p V_T)^{1/3},$$

$$\text{Change in } x_p \text{ for each 'jump'} \ = \tau_p (\varepsilon \tau_p V_T)^{1/3}.$$

No. of critical eddies cut in time t is equal to t/τ_p, thus

$$(\Delta x)^2 = \frac{t}{\tau_p}(\varepsilon \tau_p V_T)^{2/3}\tau_p^2 = \varepsilon^{2/3}\tau_p^{5/3}V_T^{2/3}t \ , \tag{3.3.39}$$

thus

$$\varkappa_p = \varkappa_f - \widehat{\beta}_t \varepsilon^{2/3}\tau_p^{5/3}V_T^{2/3} \ , \tag{3.3.40}$$

where $\widehat{\beta}_t$ is a proportional constant. Therefore, we conclude that change of diffusivity of the particle due to fall velocity is proportional to $\tau_p^{5/3}$. Comparing (3.3.40) shows that the fall velocity effect is larger if $\varepsilon \tau_p^2 \ll \varepsilon^{2/3}\tau_p^{5/3}V_T^{2/3}$ or $\varepsilon \tau_p \ll V_T^2$ or $\tau_p/T_L \ll (V_T/u_o)^2$.

Using a simple, phenomenological model of turbulence, we have shown that particle diffusivity is less than that of fluid.

3.4 New scaling analysis for spectra ϕ_{fp}, ϕ_{v_R}, ϕ_{pp}

In order to distinguish ϕ_{fp}, ϕ_{v_R} and ϕ_{pp}, the following observations are made:

(a) Velocity spectrum of fluid along particle trajectories $\phi_{fp}(\omega)$

(i) when the particle is light enough to follow the fluid motion then

$$\mathbf{u}_{fp}(\mathbf{x}, t) \rightarrow \mathbf{u}_f(\mathbf{x}, t) \qquad \Rightarrow \qquad \phi_{fp}(\omega) \rightarrow \phi_{ff}(\omega) \ , \tag{3.4.1a}$$

also if $\tau_p \omega_c \ll 1$, then $\phi_{fp}(\omega) \simeq \phi_{ff}(\omega)$ for $\omega \lesssim \omega_c$.

(ii) however, for the heavy particle with significant inertia (only response to low frequency of the flow) and hence there exists a relative velocity $\mathbf{v}_R$ between the particle and the fluid element, so

$$\mathbf{u}_{fp}(\mathbf{x}, t) \rightarrow \mathbf{u}_f(\mathbf{x} + \mathbf{v}_R t, t). \tag{3.4.1b}$$

If $\left\langle u_f^2 \right\rangle \gtrsim \left\langle u_p^2 \right\rangle$, then the particle cutting through small eddies corresponding to large frequencies such that for $\omega \geqslant \varepsilon/V_T^2$, we have

$$\phi_{fp}(\omega) \sim \phi^E(\omega) = \beta_{fp}\varepsilon^{2/3}v_R^{2/3}\omega^{-5/3}, \tag{3.4.2}$$

where β_{fp} is a proportional constant. By virtue of (i) and (ii), the spectrum $\phi_{fp}(\omega)$ must have the form as shown in figure 3.5.
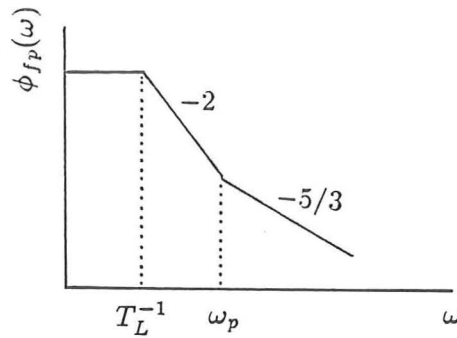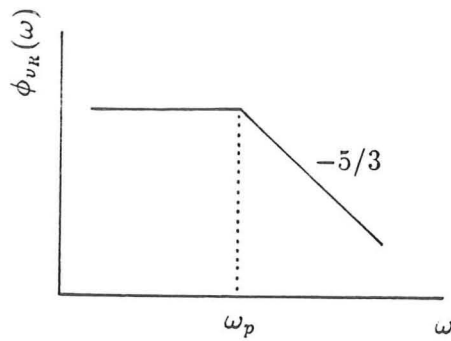

Fig. 3.5 The form of the velocity spectrum for $\phi_{fp}(\omega)$.

Also, if the particle has terminal velocity, i.e. $\mathbf{v} = \mathbf{u}(\mathbf{x}, t) + V_T$ and $V_T \ll u_o$, then for high frequency ($\gtrsim \omega_p$) particles cut through eddies, we have $\phi_{fp}(\omega) = \varepsilon^{2/3} V_T^{2/3} \omega^{-5/3}$ for $\omega > \varepsilon/V_T^2$. Therefore the combined effects are

$$\phi_{fp}(\omega) \sim \varepsilon^{2/3} \left(V_T^2 + v_R^2 \right)^{1/3} \omega^{-5/3} \qquad \text{for} \qquad \omega > \varepsilon/V_T^2, \tag{3.4.3}$$

i.e. with the $-5/3$ spectrum.

(b) Relative velocity spectrum $\phi_{v_R}(\omega)$

(i) At the cut-off frequency $\omega \sim 1/\tau_p$, we have $v_R \sim u_o$. If $1/\tau_p \ll u_o/L \sim \omega_T$, then

$$\phi_{v_R}(\omega) \sim \tau_p^2 \omega^2 \phi_{fp}(\omega) \sim \varepsilon \tau_p^2 \qquad \text{for} \qquad \omega \ll \omega_T. \tag{3.4.4}$$

(ii) For the frequency range of $\omega \gg \omega_p$, particles cut through small eddies with scale V_R/ω, so that

$$\phi_{v_R}(\omega) \sim \phi_{fp}(\omega) \sim \varepsilon^{2/3} v_R^{2/3} \omega^{-5/3}. \tag{3.4.5}$$

Note that

$$v_R^2 \sim \int_{\omega_p}^{\infty} \phi_{ff}(\omega) \, d\omega \sim \varepsilon \omega_p^{-1} = \varepsilon \tau_p.$$

Substituting this into (3.4.5), we have

$$\phi_{v_R}(\omega) = \beta_{v_R} \varepsilon \tau_p^{1/3} \omega^{-5/3}, \tag{3.4.6}$$

where β_{v_R} is a proportional constant. By virtue of (i) and (ii), the spectrum $\phi_{v_R}(\omega)$ must have the form as shown in Figure 3.6.

Fig. 3.6 The form of the velocity spectrum for $\phi_{v_R}(\omega)$.

(c) Particle velocity spectrum $\phi_{pp}(\omega)$

Note from (3.3.24b), we have $\phi_{pp}(\omega) \ll \phi_{v_R}(\omega)$ for $\omega^2 \gg 1/\tau_p^2$ and $\phi_{pp}(\omega) \ll \phi_{ff}(\omega)$ for $1/\tau_p \gg \omega$.

(i) Since the particle responds to all frequencies below $\omega_c \sim 1/\tau_p$, hence

$$\phi_{pp} \sim \phi_{fp} \sim \varepsilon\omega^{-2} \qquad \text{for} \qquad 1/T_L \ll \omega \lesssim \omega_c. \tag{3.4.7}$$

(ii) Also for high frequencies $\omega \gtrsim 1/\tau_p$ and the inertia of the particle is small, we have

$$\phi_{pp}(\omega) = \frac{\phi_{fp}(\omega)}{1 + \tau_p^2\omega^2} \sim \frac{1}{\tau_p^2\omega^2}\phi_{fp}(\omega) \sim \varepsilon\tau_p^{-2}\omega^{-4}. \tag{3.4.8}$$

On the other hand, if the particle has high inertia, in the limit of $\tau_p \gg 1$, this is equivalent to a stationary observer watching the flow passed by, (i.e. Eulerian frame of reference) hence, the spectrum should have the form $\phi_{fp} \propto \omega^{-5/3}$. Therefore ,we have

$$\phi_{pp}(\omega) = \frac{\phi_{fp}(\omega)}{1 + \tau_p^2\omega^2} \sim \frac{1}{\tau_p^2\omega^2}\varepsilon\tau_p^{1/3}\omega^{-5/3} \sim \varepsilon\tau_p^{-5/3}\omega^{-11/3}. \tag{3.4.9}$$

In the intermediate range, we should expect $\phi_{pp} \propto \omega^p$, where $-4 < p < -11/3$ for large ω. Thus, the spectrum of ϕ_{pp} has the form as shown in figure 3.7.
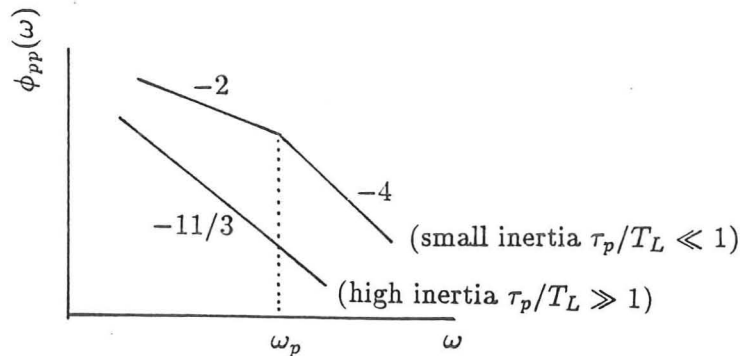
Fig. 3.7 The form of the velocity spectrum for $\phi_{pp}(\omega)$.

We have computed the spectra of $\phi_{fp}(\omega)$ and $\phi_{pp}(\omega)$ with different values of τ_p by tracking individual particle trajectories in turbulent flow generated by Random Fourier Modes and taking the FFT of the velocities to obtain the spectra. Figure 3.8 shows that $\phi_{fp}(\omega)$ has a slope of -2 for the whole inertial range of ω when $\tau_p = 0.2$ (i.e. low inertia). As τ_p increases from 0.2 to 3.0, $\phi_{fp}(\omega)$ has a slope of -2 when $\omega \lesssim 30.0$ and $-5/3$ when $\omega \gtrsim 30.0$, as predicted from the scaling argument.

We have also tested the validity of the formula (3.3.23a) and figure 3.9a, b show the two spectra for different values of τ_p. Fig. 3.9a shows that (3.3.23a) is indeed valid for small values of τ_p (i.e. low inertia), the computed spectrum $\phi_{pp}(\omega)$ coincides with $\phi_{pp}(\omega)$ obtained from the formula (3.3.23a). However, as τ_p increase to 3.0, the computed spectrum $\phi_{pp}(\omega)$ has higher values than $\phi_{pp}(\omega)$ obtained from formula (3.3.23a) at the low frequency end, i.e. the inertia seems to have amplified the fluctuation of the velocity of the particle.

The spectrum $\phi_{pp}(\omega)$ has been investigated further so as to verify the results obtained in §3.4(c). Figure 3.10 shows that for low inertia, the slope of $\phi_{pp}(\omega)$ is indeed -2 for $\omega \lesssim 10$ and -4 for $\omega \gtrsim 50$. For high inertia, as expected the slope of $\phi_{pp}(\omega)$ is $-11/3$ for the whole inertial range of frequency.

3.5 Numerical method for particle motion with Stoke's Law

The problem of following a solid particle path in a velocity field $\mathbf{u}(\mathbf{x}, t)$ is solved by integrating, to sufficient accuracy, the differential equation (3.3.3), given values $\mathbf{x}(t = t_o) = \mathbf{x}_o$, and $\mathbf{x}'(t = t_o) = \mathbf{x}'_o$.

The differential equation (3.3.3), for the particle trajectories was integrated numerically using a "Predictor-Corrector" method. It was chosen because (i) it only requires the evaluation of the R.H.S. once per step, (as opposed to other methods of the same order of accuracy, especially a Runge-Kutta method, which requires the evaluation four times per step), and (ii) it is a relatively stable method provided the time step is small.

The method we use is described in the following:

At $t = t_o$, compute $\mathbf{x}''_o$ from (3.3.3). Take fixed steps $h = t_n - t_{n-1}$. After the first step, we have $\mathbf{x}''_{n-1}$ from the previous step, so we do not need to compute it from (3.3.3). A step consists of the following sequence:

(i) Predictor: predict $\mathbf{x}_n^{(p)}$ and compute $\mathbf{u}_n^{(p)}$ from it,

$$\mathbf{x}_n^{(p)} = \mathbf{x}_{n-1} + h\mathbf{x}'_{n-1} + \frac{1}{2}h^2\mathbf{x}''_{n-1}, \qquad (3.5.1a)$$

and

$$\mathbf{u}_n^{(p)} = \mathbf{u}(\mathbf{x}_n^{(p)}, t_n). \qquad (3.5.1b)$$

this is the only evaluation of $\mathbf{u}(\mathbf{x}, t)$, in steps after the first.

(ii) Evaluate

$$\mathbf{x}_n'' = \left(\tau_p + \frac{1}{2}h\right)^{-1}\left[\mathbf{u}_n^{(p)} + \mathbf{w} - \mathbf{x}_{n-1}' - \frac{1}{2}h\mathbf{x}_{n-1}''\right], \tag{3.5.2a}$$

and

$$\mathbf{x}_n' = \left(\tau_p + \frac{1}{2}h\right)^{-1}\left[\frac{1}{2}h\left(\mathbf{u}_n^{(p)} + \mathbf{w}\right) + \mu\left(\mathbf{x}_{n-1}' + \frac{1}{2}h\mathbf{x}_{n-1}''\right)\right]. \tag{3.5.2b}$$

(iii) Corrector: then either

$$\mathbf{x}_n = \mathbf{x}_{n-1} + \frac{1}{2}h\left(\mathbf{x}_n' + \mathbf{x}_{n-1}'\right), \tag{3.5.3a}$$

or

$$\mathbf{x}_n = \mathbf{x}_{n-1} + \frac{1}{2}h\left(\mathbf{x}_n' + \mathbf{x}_{n-1}'\right) - \frac{h^2}{12}\left(\mathbf{x}_n'' - \mathbf{x}_{n-1}''\right). \tag{3.5.3b}$$

Equations (3.5.2) and (3.5.3) arise from solving

$$\tau_p\mathbf{x}_n'' + \mathbf{x}_n' - \mathbf{u}_n^{(p)} - \mathbf{w} = 0, \tag{3.5.4a}$$

and

$$\mathbf{x}'_n - \mathbf{x}'_{n-1} - \frac{1}{2}h\left(\mathbf{x}_n'' + \mathbf{x}_{n-1}''\right) = 0, \tag{3.5.4b}$$

for $\mathbf{x}_n'$ and $\mathbf{x}_n''$. (3.5.4b) is the trapezoidal rule for integration $\mathbf{x}''$; (3.5.3a) is the same rule for integrating $\mathbf{x}'$, while (3.5.3b) contains also an approximation to the error term $-h^3\mathbf{x}'''/12$.

We could re-compute $\mathbf{u}_n(\mathbf{x}, t)$ and iterate equations (3.5.1) to (3.5.3), but we do not do this because of the expense. The convergence rate would be $|\theta/4|$ for case (3.5.3a) and $|\theta/6|$ for case (3.5.3b) (see Appendix D), so this must be small to justify not iterating. (Even if one had a perfect predictor, the step would still be accurate only to the finite order of the corrector. This incurable error term is on the same order as that which our iteration is supposed to cure, so we are at best only changing the coefficient in front of the error term by a fractional amount. So dubious an improvement is certainly not worth the effort. Our extra effort would be better spent in reducing the stepsize.) The stability and the error estimation of the PC method are given in the Appendix D.

Trial runs of particle trajectories method

In order to have confidence in the results of the simulation and the integration procedure, we used a different numerical method, the expensive but reliable Harwell Subroutine DC03AD, also known as Gear's method, of order 1 to 5. The method automatically chooses stepsize and order of the integration formula. The results of the two, using different time steps for

$- 83 -$

PC method have been compared in order to check the sensitivity of the method to different time steps. All the comparisons were towards the end of the integration where any divergence between methods would most likely be maximised (Table 3.2).

The first test used a time step $\Delta t = 0.01$. The velocity and the position of the particle were compared with those calculated using DC03AD, and whilst there was reasonably good agreement between the positions, the particle velocities differed substantially.

The second test was made with the time-step reduced from 0.01 to 0.005. The results of this test are shown in column two of table 3.2. The comparison with DC03AD is favourable. This was taken as evidence that the chosen time step of 0.005 was small enough not to influence the evaluation of the quantities of interest.

The velocity statistics of particles are not stationary even if the turbulence is homogeneous and stationary and that, for the motion of particles, one must prescribe not only the initial position but also the initial particle velocity. This is quite true, but in this study we basically work in the framework of the so-called stationary case, as is done by Hinze (1975). Namely, it is assumed that the velocity statistics of the particles does not depend on the time. In particular, we wish to compute statistics for the inertial particle after they have reached a statistical state which is independent of the initial conditions, the difference between the fluid point and particle paths results from two effects; one is the difference in initial conditions, the other the difference in dynamic response. For small time, launching the particle with local fluid velocity will cause it to follow the fluid point path much better, however for large time the influence of initial condition is less and less important, and the difference in dynamic response dominates. Therefore, we want to choose $\mathbf{v}(t = 0)$ so as to minimise the length of initial period of adjustment. We make the assumption that, at least at large Reynolds numbers, the Lagrangian velocity time correlation function of the fluid may be represented by an exponential form

$$R_{ff}^L(\tau) = \exp\left(-\tau/T_L\right), \tag{3.5.5}$$

where T_L is the Lagrangian integral time scale of the fluid point. Then (3.3.3) is a straightforward, linear, first order stochastic differential equation. After some labor, the mean square velocity of the particle is given explicitly by

$$\left\langle \mathbf{v}^2(t) \right\rangle = \frac{T_L}{T_L + \tau_p} \left\langle \mathbf{u}^2 \right\rangle + \frac{2\tau_p T_L}{T_L^2 - \tau_p^2} \left\langle \mathbf{u}^2 \right\rangle e^{-(1/\tau_p + 1/T_L)t}$$

$$- \frac{\tau_p}{T_L - \tau_p} \left\langle \mathbf{u}^2 \right\rangle e^{-2t/\tau_p}. \tag{3.5.6}$$

We are interested in $\mathbf{v}(t)$ at large t. Thus at time $t \gg \tau_p$, when $e^{-t/\tau_p} \approx 0$, the particle has 'forgotten' its initial velocity $\mathbf{u}(0)$, in the sense that the contribution that depends on

$\mathbf{u}(0)$ has decayed to zero, i.e. reach to an equilibrium state. For $t \to \infty$, we have $\langle \mathbf{v}^2 \rangle \to \langle \mathbf{u}^2 \rangle T_L/(T_L + \tau_p)$, i.e. $\langle \mathbf{v}^2 \rangle \propto 1/\tau_p$ for large τ (see also Hinze 1975, p467), therefore we chose $\mathbf{v}(t = 0) = \mathbf{u}(t = 0)\sqrt{T_L/(T_L + \tau_p)}$, as the initial condition.

One measure of the independence of the statistical state is that the mean square velocity of the particle relative to the fluid, $\{\mathbf{v}(\mathbf{a}, t) - \mathbf{u}[\mathbf{x}_p(\mathbf{a}, t), t]\}$. We denote this mean square difference velocity by $\langle \Delta u_{\text{Rel}}^2 \rangle$. In all cases, $\langle \Delta u_{\text{Rel}}^2 \rangle$ rises initially but then settles down to a constant value after approximately a time equal to the particle time constant τ_p (see Fig. 3.11). It is obvious that during this time, the particle is under the influence of its initial condition. Thus, all the particle statistics are calculated after at least one τ_p from the starting time.

Figure 3.12 is a typical plot of the cross-correlation function between the particle and fluid velocities,

$$R_{uv}^L(\tau) = \frac{\langle u[\mathbf{x}(t), t].v[(\mathbf{x}(t + \tau), t + \tau]\rangle}{\langle u[\mathbf{x}(t), t].v[(\mathbf{x}(t), t]\rangle} \tag{3.5.7}$$

(in this case, $\tau_p = 0.4$, $W_g = 0$.) Notice that the correlation has a maximum value not at the origin ($\tau = 0$) but at a positive value of τ, approximately τ_p. This peak shift is due to the fact whenever a velocity difference exists between the particle and surrounding fluid, it takes the particle a finite amount of time (approximately τ_p) to respond to this difference.

3.5.1 *Results of simulation*

It is seen that very little is know about the R_{pf}^L and R_{pp}^L (the particle velocity autocorrelation function as in (3.3.8) but with u being replaced by v). No completely satisfactory theory exist as yet. The specific aim of this work was to generate the data via computing simulation — this involves following individual particle trajectories in the generated fluid velocity field by Random Fourier modes and computing a sufficiently large number of particle trajectories to form statistically significant averages. Finally, after appropriate processing of the data and calculations, information on the Lagrangian statistics of the particle are obtained in the form of numerical values and graphic curves. There are two limiting cases which are a little easier to handle. The first is $W_g \to 0.0$, in which case $\mathbf{u}$ is the Lagrangian velocity seen by the wandering fluid point. The second is $W_g \to \infty$, in which case the falling particle cuts rapidly through the frozen turbulence, so that $\mathbf{u}$ is the Eulerian velocity sampled along a vertical line. A range of particle inertia parameters and fall velocities were used: six values of $\tau_p = 0.0075, 0.5, 1.0, 1.5$ and 2.0 with $W_g = 0.0$ were simulated. The first one is light enough to behave like a fluid point and the last one is heavy enough to have significant inertia and "crossing-trajectories" effects. Also, six values of $W_g = 0.0, -0.5, -0.8, -2.0, -5.0$, and -20.0 with $\tau_p = 0.2$ were simulated so as to see the 'crossing-trajectories' effects.

(a) *The effect of varying the particle inertia parameter*

The simplest and most interesting case, considered first, is that of particle dispersion in an isotropic turbulent fluid where the effect of gravity can be ignored ($W_g = 0$), all results obtained are due entirely to the inertial effects, without interference of the "crossing-trajectories" effect. In this instance, the dispersion is totally isotropic, so that the subscripts on the velocity vectors can be dropped. As particle inertia increases the particle becomes less and less sensitive to fluctuations in the fluid velocity, and the Lagrangian autocorrelation of the fluid velocity experienced by the particle, $R_{fp}^L(\tau)$, tends towards the Eulerian autocorrelation of the fluid velocity, $R_f^E(\tau)$. Conversely, as the particle inertia decreases, the particle behaves more and more as a fluid element, and $R_{fp}^L(\tau)$ tends towards the Lagrangian autocorrelation of the fluid velocity $R_{ff}^L(\tau)$. It is known (Shlien and Corrsin 1973) that these two curves – $R_f^E(\tau)$ and $R_{ff}^L(\tau)$ – intersect, with $R_f^E(\tau) < R_{ff}^L(\tau)$ for small τ and $R_f^E(\tau) > R_{ff}^L(\tau)$ for large τ, so we would expect the curves of $R_{fp}^L(\tau)$ for different values of particle inertia also to intersect. This is shown in figure 3.13. (The crossover between curves cannot be seen in the results of Reeks 1977.) Note that the intersection point between the curves $R_{fp}^L(\tau; \tau_p = 2.0)$ and $R_{ff}^L(\tau)$ is approximately at $\tau = 0.25$ which is consistent with the intersection point between the curves $R_f^E(\tau)$ and $R_{ff}^L(\tau)$ in figure 2.8. It is expected that the more sluggish particles follow the fluid particle paths less accurately (even with small particle time constant of $\tau_p = 0.075$), and they cross the trajectories of fluid particles more often and more rapidly. This suggests that the record of the fluid velocity surrounding the more sluggish particles should show more high frequency content than the fluid velocity surrounding the less sluggish particles. This would imply that the correlations would fall off more rapidly as τ_p is increased. For the τ_p-range studied, they do fully exhibit this fall off.

The curves of the particle correlation function $R_{pp}(\tau)$ (Fig. 3.14a) for various particle inertia parameters are consistent with the notion of the persistence of the particle velocity with increasing inertia parameter τ_p. All curves appear to be similarly shaped. The minor distinctions in shape become evident when the curves are superimposed by scaling the abscissa with the integral time scale of the particle $T_L^p(\tau_p)$, (Fig. 3.14b). Particle inertia effect decreased the particle r.m.s. fluctuating velocity from $\langle u_1^2 \rangle$ at $\tau_p = 0$ to zero at $\tau_p \to \infty$ (Fig. 3.15). The particle with $\tau_p = 2.0$ had a mean-squared velocity of approximately 80% less than that of the fluid, while the particle with $\tau_p = 0.075$, had a mean-squared velocity of approximately 20% less than that of the fluid. This can be explained that the particle can gain their fluctuation velocity only from the fluid turbulence, obviously this fluctuation velocity should depend on the interaction time between the particle and the eddies. As the inertia of the particle increases, the

particle cuts through the eddies hence the interaction time decreases, consequently the particle fluctuation velocity decreases. This can also be seen in (3.5.6); the fluctuation velocity of the particle $\langle \mathbf{v}^2(t) \rangle$ is inversely proportional to the inertia parameter τ_p.

The dispersion of the particle from a fixed point is represented by the mean square displacement $\langle \mathbf{x}_{ij}^2 \rangle$ and the particle diffusivity $\varkappa_{ij}^p$ which is defined as

$$\varkappa_{ij}^p(\tau) = \frac{1}{2}\frac{d}{dt}\langle x_{p_i}.x_{p_j} \rangle = \langle x_{p_i}.v_j \rangle = \langle v_p^2 \rangle \int_0^\tau R_{pp_{ij}}^L(t)\, dt\,. \tag{3.5.8}$$

This is a function of time, except at large diffusion times, when they tend to $\langle v'^2 \rangle T_L^p$ for isotropic turbulence. Because this apparent eddy diffusivity can thus be determined from turbulent properties, we may be tempted to regard it as simply a more complicated counterpart of molecular diffusivities. As mentioned previously, the inertia effect is mainly represented by the particle time constant. Csanady (1963) showed that the asymptotic particle diffusivity is independent of the particle time constant. Wells and Stock's (1983) experiments also show that there is not a large difference of diffusivity between light particles and heavy particles, although there is an indication that the diffusivity of heavy particles is a little larger than of the light ones. Reeks (1977) and Pismen & Nir (1978) also indicated that in the absence of gravity, the asymptotic particle diffusivity is in general greater than that for the fluid. Our model simulations are shown in figure 3.16, it can be seen that, for small values of the particle diffusivity, $\tau_p \lesssim 0.5$, $\varkappa^p$ rises from zero, eventually reaches a value which is *less* than the equivalent long-time fluid point diffusivity $\varkappa^f(\infty) \approx 0.52$. This is consistent with the one-dimensional analysis of the velocity field consisting of a series 'jumps' in the previous section (see (3.3.38)).

For larger values of τ_p (> 0.5), $\varkappa^p$ rises and has not reached the asymptotic form because we have not taken a sufficiently large dispersion time. Increasing dispersion time has an escalating increase in computation time because of the backward Lagrangian integration (2.2.19). Clearly a compromise had to be set for a given computing time (40 mins of Cray-2 CPU). It is necessary that we take a sufficient large number of realisations to reduce statistical errors. This has to be offset by carrying the simulation time only up to approximately $10T_L$. Although the asymptotic form of $\varkappa^p$ has not been reached for $\tau_p > 0.5$, it seems that $\varkappa^p$ will settle down to a value which is *larger* than $\varkappa^f(\infty)$. Moreover, if $\tau_p/T_L \gg 1$, one might expect the particles, since they will not have sufficient time to respond to the flow structures and to move in nearly rectilinear path, and then to stop ultimately due to friction (no matter what is the initial velocity), i.e. $\langle v^2 \rangle \to 0$. Hence $\varkappa^p = \langle v^2 \rangle T_L^p \to 0$. This can also be seen in the one-dimensional case with $u \gg v$ and $\tau_p \gg T_L$, because the time for the particle to be displaced is so long that it is better to write

(3.3.26) as

$$v\frac{dv}{dx} = \frac{1}{\tau_p}u(x), \qquad \text{then} \qquad v^2 = \frac{2}{\tau_p}\int_0^x u(x')\,dx'.$$

Therefore, $\langle v^2 \rangle \sim u'L/\tau_p$, this is consistent with (3.5.6). For a particle with fluctuating velocity v' and with significant inertia, i.e. only response to the energy containing eddies with length scale L, then one would expect the time scale $T_p \sim L/v$ for the velocity of the particle to change as it passes the eddies. Therefore, we have $\varkappa^p \sim u'^{1/2}L^{3/2}/\tau_p^{1/2}$, i.e. as $\tau_p \to \infty$, $\varkappa^p \to 0$.

Figure 3.17 shows the variations in the asymptotic particle diffusivity $\varkappa^p$ (obtained from Fig. 3.16) for different values of particle time constant τ_p. These results demonstrate that the extent of particle dispersion in the absence of gravity depends strongly on the particle time constant τ_p $(= \tau_{p_o}u'/L)$, the ratio of particle response time to the characteristic time of the flow. Particle with relatively small τ_p values (~ 0.5) are dispersed less than the fluid, probably due to the fact that the particles are trapped by vortices. Particles at intermediate values of $\tau_p(\sim \mathcal{O}(1))$ are dispersed faster than the fluid, i.e., they may move at the edges of vortices which may have the ability to fling the particles outside them and hence disperse more effectively. As $\tau_p \to \infty$, the dispersion tends to zero. This result is in agreement with the previous experimental observations by Yule (1980) and computing simulation of particle dispersion in an axisymmetric jet by Chung & Troutt (1988).

Figure 3.18 shows the pdf of the curvature of the trajectories of the particles. It can be seen that for the case of fluid element, $\tau_p = 0.0$, the distribution of the pdf is quite even through out the values between 0.0 to 20.0, and has a maximum at about 1.5, but as τ_p increases, the maximum of pdf becomes more and more predominant and the values of the curvature where the maximum occurs decreases (less curved).

The correlation functions of the relative fluid-particle velocity at different, τ_p, (Fig. 3.19) do not resemble each other as closely as the particle velocity correlation function. All curves display a characteristic range of negative correlations. An explanation of this feature is obtained by recalling that, according to (3.3.3), the relative velocity correlation functions are proportional to the correlation functions of particle acceleration, and a positive acceleration of a particle at any moment make this negative acceleration at some future moment more probable. The curves in figure 3.19, show an increase in the characteristic correlation time with increasing τ_p.

We now address the following question: Is the pdf of the fluid velocity seen by the particle independent of the particle inertia parameter, τ_p? And if so, is the pdf Gaussian? Intuitively, one expects that a point moving with the fluid and a particle cutting through the eddies, in a large number of trials, would not be subject to the same kind of velocity fluctuations, would statistically speaking not sample the same velocity population. However, figure 3.20 shows the

normalised pdf for different τ_p, it may be seen that there is fairly close agreement between the pdf's, although some differences are noticeable around the peak. The corresponding normalised pdfs of the particle velocity are shown in figure 3.21, again they are Gaussian (since the $\mathbf{u}(\mathbf{x}_p, t)$ is Gaussian) and they all have zero mean and the variances decrease as τ_p increase.

Finally, we would also like to find out how do particles with different values of τ_p move through eddies. One measure of this is the pdf of the angle between the velocities of the particle and that of the fluid element as the particle moves through the flow. It can be seen (Fig. 3.22) that as τ_p increases, the peak of the pdf decreases, i.e. the particle is cutting through the eddy more and more.

(b) *The effect of varying the fall velocity*

In a lot of practical situations, the gravitational settling cannot be ignored and often plays a decisive role in determining the particle dispersion. So we consider a non-zero W_g and analyse the influence of the deterministic motion due to gravity on the Lagrangian statistics of a suspended particle. It is useful to separate the deterministic and random parts of the particle velocity $v_i(t)$:

$$v_i(t) = \tilde{v}_i + \bar{v}_i, \qquad \langle \tilde{v}_i \rangle = 0, \tag{3.5.9}$$

since we assume that the only external force acting on the particle is gravity, so we chose $\bar{v}_3 = W_g$ and $\bar{v}_1 = \bar{v}_2 = 0$. Separating also the random part of the particle displacement, the fluctuations about the mean values are given by

$$x_i(t) = \tilde{x}_i(t) - \bar{x}_i, \qquad i = 1, 2; \tag{3.5.10a}$$

$$x_3(t) = \tilde{x}_i(t) - \bar{x}_3 = \tilde{x}_3(t) - x_{3_o} - W_g t, \tag{3.5.10b}$$

in which x_{3_o} is the initial vertical position, $x_i(t)$ are the instantaneous positions and $\bar{x}_i$ are the average position. Henceforth, all the Lagrangian statistics are calculated in a frame of reference moving with the fall velocity. For a particle suspended in isotropic turbulence yet having a steady fall velocity due to gravity, the system retain axial symmetry in the x- and y-directions. So we will only consider the statistics in the direction perpendicular (11-direction) to W_g and in the direction parallel (33-direction) to W_g.

The effect of increasing W_g on R_{fp}^L is to decrease slightly both $R_{fp_{33}}^L$ and $R_{fp_{11}}^L$ (Fig. 3.23). This is simply due to the fact that, as the fall velocity increases, the particles fall through the fluid faster, and thus "see" higher frequency fluctuations. It can be noted that if the turbulent intensity is less than, or of the same order, as the fall velocity (i.e. $W_g \leq 1$) then both $R_{fp_{33}}^L$ and $R_{fp_{11}}^L$ exhibit only slight dependence on W_g because the velocity fluctuation are mainly caused by eddy decay. However, $R_{fp_{33}}^L$ decreases mildly with increasing W_g. It is

interesting to note that as $W_g \to \infty$, the particle cut through the spatial structure of turbulence, a negative region appears in R^L_{fp11}. In this case, the turbulent eddies passing through the particles are the same as if they were advected past a fix point of observation by the mean flow; then the eddies do not change substantially during their time of passage (Taylor's "frozen flow field hypothesis"). For the purpose of calculation, the fluid velocity correlations R_{fp} can be approximated as Eulerian space-time correlation $R^E_{ij}(\mathbf{x}, t)$ of the velocity $u_i(0,0)$ with the velocity $u_i(x_3 = W_g\tau, \tau)$, i.e. $R^L_{fp}(\tau) \to R^E(W_g\tau, 0)$. The reason for the existence of the negative region is that Eulerian fluid velocity spatial cross-correlations are negative over certain separations in order to satisfy continuity.

The particle velocity correlations R^L_{pp11} and R^L_{pp33} are shown in figure 3.24. It can be seen that as W_g increases, both R^L_{pp11} and R^L_{pp33} decreases because the particle crosses the fluid turbulence eddies and loses velocity correlation more rapidly than a fluid element. This result has been predicted by various authors (e.g. Yudine 1959, Csanady 1963) Note that the R^L_{pp11} is always greater than R^L_{pp33}.

Figure 3.25 illustrates the particle diffusivity, $\varkappa^p_{ij}$, on the parameter, W_g. Clearly the effect of increasing the fall velocity is to reduce the particle diffusivity both normal to, and parallel to, W_g compared with the isotropic case. For $W_g \leq \mathcal{O}(1)$, the differences between diffusivity parallel to and perpendicular to W_g are small. However, when $W_g > \mathcal{O}(1)$, the vertical drift has a significant effect, so that the mean velocity component, W_g, draws the particle out of the strongly correlated fluid element. This reduces the diffusivity markedly, and in the limit $W_g \to \infty$, the integral time scale for $R^L_{pp}(\tau)$ approaches L/V_T. However, the magnitude of L depends on the direction of the separation vector, $V_T\tau$. From (3.5.8), we have

$$\varkappa^p_{11} = \varkappa^p_{22} = v'^2 L_{11}/V_T, \qquad \varkappa^p_{33} = v'^2 L_{33}/V_T, \qquad \text{for} \qquad V_T \gg u', \qquad (3.5.11)$$

where L_{11} and L_{33} are the longitudinal and lateral integral scales respectively (Batchelor 1953). Since in isotropic turbulence $L_{33} = 2L_{11}$, (3.5.11) implies that the asymptotic diffusivity $\varkappa^p_{33} = 2\varkappa^p_{11}$. This is known as the continuity effect (Csanady 1963). Figure 3.25 shows that the ratio of the particle diffusivity normal to W_g to parallel to W_g tends to its ultimate value of 2 as expected. (The increase in $\varkappa^p_{ij}(\infty)$ with increasing τ_p is observable only for small values of W_g, and the coefficient finally declines as W_g becomes dominant.)

The simulations show that the crossing-trajectories effect indeed dominates the particle dispersion and is to decrease the particle dispersion as shown in figure 3.26.

Both of the $\langle \tilde{v}_3^2 \rangle$, and the $\langle \tilde{v}_1^2 \rangle$, of mean square velocities of the particle parallel to and perpendicular to W_g are showed in figure 3.27 for the same choice of the fall velocity. It can be

seen that $\langle \tilde{v}_3^2 \rangle$ is always greater that $\langle \tilde{v}_1^2 \rangle$. It can be seen that in the limit as $W_g \to \infty$,

$$\frac{\varkappa_{33}^p(\infty)}{\varkappa_{11}^p(\infty)} = \frac{\langle \tilde{v}_3^2 \rangle}{\langle \tilde{v}_1^2 \rangle} \to 2 \,, \tag{3.5.12}$$

again in agreement with that of Csanady (1963).

The correlation functions of relative fluid-particle fluctuating velocity depend strongly on W_g, there is a slight decrease of correlation time as W_g increases from 0 to 20 (Fig. 3.28).

3.5.2 Particle trajectories with different inertia and fall velocity

The particle trajectory is calculated by integrating (3.3.3) through a simulated velocity field, using a Predictor-Corrector Method. Figures 3.29 and 3.30 show typical trajectories for a single particle with a range of fall velocities and inertia parameters. In figure 3.29 the fall velocity has been set equal to zero and the inertia parameter ranges from 0.0 (low inertia) to 2.0 (high inertia). Particles with low inertia appear to become trapped, briefly, in eddies and move from eddy to eddy, whilst particles with high inertia pass through the eddies. It is interesting to note that the greatest trapping effect appears to occur at some intermediate value of the inertia parameter ($0.05 < \tau_p < 0.5$). We learn from these trajectories that particles with smaller inertia parameter tend to follow the streamlines, while those with larger inertia parameters tend to follow an almost straight path propelled by their large initial inertia. Intermediate particles will be entrained by the flow initially, but they will be flung out of the looping flow field at some point, depending on their inertia/drag ratio. Also it seems reasonable to conclude that the flow field at some range of inertia parameter is capable of producing large particle dispersion, as a result of the strong entrainment power which induces the particles into vortical motion and then flings them out of the vortex structures (e.g. Yule 1980, Chung and Troutt 1988).

In figure 3.30 the inertia parameter has been held constant and the fall velocity varied. It appears that for fall velocities less than a critical value ($W_g \sim 2.0$) the particles remain suspended, whilst for fall velocities greater than the critical value, they settle out. The critical fall velocity may also depend on the inertia parameter, and this effect therefore requires further investigation (see §3.8).

3.6 Comparison with the experiments of Snyder and Lumley

Snyder & Lumley (1971) (henceforth referred to as SL) used four different particles with properties listed in Table 3.3., where τ_p is the particle inertial parameter and W_g is the terminal velocity, i.e. the Stokes velocity corrected by a method recommended by Fuchs (1964). The particles are injected on the centreline of the wind-tunnel, 51cm after the grid with a mean velocity equal to the mean velocity of the flow. Measurements of the mean square displacements $\langle x^2 \rangle$

were made by taking photographs at ten stations spaced logarithmically along the wind tunnel in a grid decaying turbulence. The flow is oriented vertically upwards, to avoid gravitational vertical drift of the particles with respect to the mean horizontal streamlines which would be encountered for a horizontal windtunnel. The turbulence is produced by a grid located in a 40cm-square section, with a 5m-tunnel section. In this section, the particles remain reasonably far from the walls so that these influences can be neglected. The mean velocity of the flow is $\overline{U}_z = 6.5$m/s (the direction z being the mean flow direction). The grid mesh dimension is $M = 2.54$cm corresponding to a Reynolds number equal to 10,000. Turbulence measurements were made and energy decay laws on the centerline of the test section established. The longitudinal and transverse variance σ_u^2 and σ_w^2 decreasing according to the decay laws,

$$\sigma_u = \overline{U}_z \bigg/ \left[42.4 \left(\frac{\ell}{M} - 16\right)\right]^{1/2}, \tag{3.6.1a}$$

$$\sigma_w = \overline{U}_z \bigg/ \left[39.4 \left(\frac{\ell}{M} - 12\right)\right]^{1/2}, \tag{3.6.1b}$$

where ℓ is the distance from the grid.

	Hollow glass	Solid glass	Corn	Copper
τ_p (msec)	1.70	45.0	20.0	49.0
w (cm/sec)	1.67	44.2	19.8	48.3
Reynolds number Re_p	0.05	2.48	1.10	1.45

Table 3.3. Particle properties in Snyder & Lumley's experiments.

These experimental results provide a good baseline against which to test our model. To reproduce the velocity field we follow Pismen & Nir (1979) and Helland et al. (1977), and assume that the energy spectrum for grid-generated turbulence has the von Kármán-Pao form (Pao 1965)

$$E(k, L, \eta) = E_o \frac{(kL)^4}{(1 + (kL)^2)^{17/6}} \exp\left[-\gamma(k\eta)^{4/3}\right], \tag{3.6.2}$$

where E_o and γ are constant, η is the Kolmogorov length scale and L is an 'energy scale'. This formula is chosen to have $E \sim k^{5/3}$ for large k and $E \sim k^4$ for small k. Also, for large value of k have the exponential-like cut-off of the energy spectrum at dissipation-scale wavenumber $(k\eta = \mathcal{O}(1)$, say), depending on a particular case. The empirical spectrum was fitted by Helland et al.(1977) successfully to two independent grid turbulent experiments data by suitable choice of the parameters γ and scale ratio L/η. SL measured the wavenumber spectrum $\phi_{11}(k_1)$ rather than the energy spectrum $E(k)$, since this is impossible to measure as pointed out in §2.2. We require $E(k)$ as input for this simulation, but the two are related (e.g. Batchelor 1953) by:

$$\phi_{11}(k_1) = \frac{1}{2} \int_{k_1}^{\infty} \left(1 - \frac{k_1^2}{k^2}\right) \frac{E(k)}{k} \, dk. \tag{3.6.3}$$

Values for η, L, γ and E_o were obtained by substituting (3.6.2) into (3.6.3) and then minimising the mean square deviation between the calculated spectrum $\phi_{11}(k_1)$ and that measured by SL. The three-dimensional spectrum is depicted in figure 3.31.

In the experiments the turbulence decayed with distance, although the spectra were self-preserving (quasi-stationarity). SL corrected for this using the method of Batchelor (1952), but this is only valid if the energy spectrum is self-preserving, especially over the relatively small diffusion times using in the experiments. So it will be assumed that the fluid velocity fluctuations are stationary and homogeneous, by taking the average turbulent intensity, i.e., at $\ell/M = 73$. As pointed out by Pismen and Nir (1979), the assumption of quasi-stationarity is valid if the particle time constant τ_p is small compared with the timescale for the decay of the turbulence.

Snyder and Lumley give the integral scales L_{11} at several points of the flow and the scale L_{33} is then estimated by $L_{33} = L_{11}/2.58$ which is experimentally satisfied at $\ell/M = 73$ and corresponds to a slight non-isotropy. The Lagrangian time scale is estimated according to Corrsin's relation

$$T_L \approx L_{33} \Big/ \sqrt{\langle u_1^2 \rangle}, \qquad (3.6.4)$$

which is approximately equal to 90ms at $\ell/M = 73$, so the time step Δt is chosen to be $T_L/10$. The particles were released with an initial velocity equal to the mean fluid velocity, and their trajectories calculated by integrating (3.3.3). Statistical results were obtained from an ensemble of 2700 trajectories. To remove the influence of the release conditions the particles were allowed to disperse somewhat before the statistics were calculated; tests showed that the results were then independent of the initial conditions.

SL hoped that the hollow glass spheres would be small and light enough to behave as a fluid elements whilst the copper spheres would show significant inertial effects. Figures (3.32a, b) show sample computed trajectories for these two particle types. As expected, the hollow glass spheres disperse more quickly and widely than the copper spheres, and the individual trajectories fluctuate more rapidly.

Figure 3.33 shows the autocorrelation curve $R_{fp}(\tau)$ for the transverse *fluid velocities* sampled by the different particles. The most interesting point is that the autocorrelation decays fastest for the the particles with highest inertia. This is the 'crossing trajectories' effect (Yudine 1959, Csanady 1963) – particles with high inertia tend to cut through eddies, whilst particles with low inertia remain 'trapped', so $R_{fp}(\tau)$ decays more rapidly for particles with high inertia. It has been argued (Csanady 1963) that the autocorrelation of the transverse *particle velocity*, $R_{pp}(\tau)$ should also decay faster for particles with higher inertia.

The autocorrelations for the copper and glass spheres are identical, showing that particle inertia is the dominant influence. Because these particles have high inertia and fall velocity, their autocorrelations will be similar to the Eulerian spatial autocorrelation $R^E_{ff}(r)$, $r = \overline{U}\tau$. It follows from continuity (Hinze 1975) that the curve $R^E_{ff}(r)$ must contain a region of negative correlation, and this can be seen for the copper and glass spheres for $0.02 < \tau < 0.06$. This region vanishes for the lighter particles.

Figure 3.34 shows the autocorrelation function $R_{pp}(\tau)$ for the particle velocities, together with the experimental results. The most obvious feature of this comparison is that the experiments suggest that $R_{pp}(\tau)$ *decreases* with increasing inertia, whilst the computations suggest that it *increases* with increasing inertia. Although it might seem more likely that an increase in particle inertia should cause an increase in $R_{pp}(\tau)$, because the particle does not respond to all the higher frequency oscillations of the fluid (i.e. it acts like a "low pass" filter), so its correlation $R_{pp}(\tau)$, drops off slower than that of the surrounding fluid, $R_{ff}(\tau)$, however, the 'crossing trajectories' effect has been used to suggest that the opposite trend should occur. These experimental results support the existence of such an effect, although we have never observed it in our simulations. Pismen & Nir (1979) simulated the dispersion of copper spheres and also found that the computed $R_{pp}(\tau)$ decayed more slowly than that measured by SL. They argued that the correction for decaying turbulence, whilst being appropriate for fluid elements, could not be applied to particles with significant inertia. This cannot explain, however, why the experimental curve for the hollow glass spheres decays more slowly than the computed curve.

In both the experiments and the computations $R_{pp}(\tau)$ is almost identical for the copper and solid glass spheres, with the copper decaying slightly more slowly than solid glass; this is probably due to the slightly higher inertia of the copper spheres.

SL found that all the autocorrelation functions could be collapsed onto one curve by a suitable choice of timescale for each particle. However the curves in Figure 34 have different forms and cannot be condensed into one.

Yudine (1959) and Csanady (1963) both predict that for heavy particles the particle autocorrelation function $R_{pp}(\tau)$ should have the same *form* as the Eulerian spatial autocorrelation $R^E_{ff}(r)$. SL found that, within the limits of experimental accuracy, their results agreed with this. If we assume that $R^E_{ff}(r)$ is similar to $R_{fp}(\tau)$ for dense particles, then we can test this by comparing $R_{fp}(\tau)$ with $R_{pp}(\tau)$ for the copper. The two computed curves do not appear to have the same form at all, and the general trend of the $R_{pp}(\tau)$ curves suggests that the similarity will decrease further with increasing inertia. The point to be made is that there is no basic reason to expect the Lagrangian correlation in time to be directly related to the Eulerian correlation in space. By dimensional reasoning, SL pointed out that the correlations cannot be similar in

shape. Kolmogorov's theory shows that $\phi_{11}(k) \propto \varepsilon^{2/3} k^{-5/3}$ and that $\phi_{11}(\omega) \propto \varepsilon \omega^{-2}$, so that the spectra, and hence the correlations, cannot have the sameshape. However, Pasquill (1974 pp. 131–132) has shown that, if the Lagrangian integral timescales are fixed, the dispersion is relatively insensitive to the shape of R^L.

Figure 3.35 shows the computed and measured mean square dispersion $\langle x^2 \rangle$. In general the agreement is very good for all four particle types, especially when it is considered that there has been no empirical adjustment of the parameters. This agreement might seem a bit surprising, given the apparent disagreement between the measured and calculated autocorrelation functions, because the dispersion can also be calculated (Taylor 1921) from the autocorrelation function :

$$\langle x^2 \rangle = 2 \langle v^2 \rangle \int_0^T \int_0^t R_{pp}(\tau) \, d\tau dt. \tag{3.6.5}$$

For the copper, the computed $R_{pp}(\tau)$ exceeds the experimental, but the computed dispersion is less than that measured in the experiments. We therefore conclude that the computed value for $\langle v^2 \rangle$ must be *less* than that measured by SL. Conversely, the hollow glass experimental curve for $R_{pp}(\tau)$ exceeds that for the simulation, but the measured dispersion is less than that predicted by the simulation. In this instance, therefore, the computed value for $\langle v^2 \rangle$ must be *greater* than that measured by SL.

There is a possible explanation for this. SL estimate that as much as 40% of the turbulent energy associated with the hollow glass spheres could have been lost, due to undersampling. They also suggest that noise due to measurement errors would be much more significant for the heavy particles, and this could have lead to an overestimate of their turbulent energy.

It is possible that the disagreements between the simulations and the experiments may be due to the decaying turbulence in the experiments. To investigate this we hope in the near future to use Kinematic Simulations to model particle dispersion in decaying turbulence.

3.7 Particles/bubbles gravitational settling/rising

3.7.1 *Introduction*

Suspended particles occur in many natural turbulent flows, in the atmosphere terminal velocity governs the residence times of various aerosols, such as soil duct from wind erosion, man-made pollutants, and the growth rate of water droplets falling under gravity. In civil engineering, particle settling is important to sediment fallout in estuaries, as well as in many other industrial process. While much is now known about the terminal fall or rise velocities in still fluid of various particles and bubbles (Clift *et al.* 1978), relatively little is known about the influence of fluid flows, especially turbulent flows, on the average terminal velocity of such particle.

In the absence of mean vertical mean flow, the random fluid motion produce fluctuating drag on a particle and tends to move it upwards and downwards with equal probability. On the other hand, gravity acts downwards constantly and hence the net effect ought to be a downwards motion of the particle at some fall velocity. It is not clear what the effect of these fluctuating forces will be on the average fall velocity and whether or not in homogeneous turbulence, the particles will settle asymptotically at the same rate as they would in still fluid.

The numerical simulations of random Fourier modes was carried out by Riley (1971) in a homogeneous, isotropic and stationary flow. By solving the equation of motion with linear drag law to obtain particle trajectories, he found no difference between the average particle fall velocity in the random flow field and in still fluid. Reeks (1977) using an iterative solution to the equation of motion for the particle and has argued that in homogeneous turbulence, there would be no net effect on the average fall velocity. Also Nielsen (1984) showed that in a pure wave motion, such effects are all purely oscillatory and therefore does not cause a net reduction of fall velocity. However, Manton (1974), in a study of particles in various vortex flow fields, noted that a particle may follow an approximately closed trajectory in an axisymmetric flow about a horizontal axis. Thus it is argued that turbulence should cause particles to fall at a much slower rate than their terminal velocity, even in the absence of a mean updraft. On the other hand, recent studies, by Maxey and Corrsin (1986) of a two-dimensional, incompressible cellular flow field and Maxey (1987) of homogeneous turbulence generated by random Fourier modes, have shown that owing to the influence of particle inertia, and the bias this produces in the particle trajectories towards regions of high strain rate and/or low vorticity, the increase in fall velocity was most pronounced for $V_T/\sigma_u \leqslant 1$ but was negligible for $V_T/\sigma_u > 2$. At this stage, however, it is still not possible to draw any overall conclusions about average particle fall velocity from these investigations.

In the next two sections, we investigate whether in general particle fall or bubble rise velocities in homogeneous, stationary turbulence differ from those in still fluid, in particular to investigate the role played by the structures of the flow field. In the following section, we study particle or bubble trajectories in a simple flow structures, then in §3.7.3 results are given from numerical simulations of particle and bubble motion in a homogeneous, stationary and isotropic, random velocity flow field. These results are then related in terms of the structure of the flow field.

3.7.2 *Motions of particles and bubbles in some simple vortex flows*

A turbulent flow is not completely incoherent, i.e., consisting only of white noise. Thus somewhat coherent motion, eddies or vortices exists in the turbulent flow. The most important

flow structure in connection with suspended particle is that of a vortex (Yule 1980, Chung & Troutt 1988) because such vortices are able to trap particles or bubbles temporarily and carry them along over considerable distances and eventually fling them out of the vortex as it starts to decay.

In the following we shall see how by solving the equation of motion in approximate form can easily provide approximate particle or bubble trajectories in simple flow structures and how the structure of these trajectories can provided important information on the terminal velocity in turbulent flows.

Consider a particle with density ratio $\gamma = \rho_p/\rho$ in a forced vortex whose axis is horizontal where

$$\mathbf{u} = \left(-\frac{\Omega}{2}x_2, \ \frac{\Omega}{2}x_1, \ 0\right), \qquad \boldsymbol{\omega} = (0, \ 0, \ \Omega), \qquad \mathbf{g} = (0, \ g, \ , 0).$$

In this case

$$\frac{D\mathbf{u}}{Dt} = \left(-\frac{1}{4}\Omega^2 x_1, \ -\frac{1}{4}\Omega^2 x_2, \ 0\right)$$

and

$$(\mathbf{u} - \mathbf{v}) \wedge \boldsymbol{\omega} = \left(-v_2 + \frac{\omega}{2}x_1, \ v_1 + \frac{\Omega}{2}x_2, \ 0\right)\Omega.$$

Substituting these into equation (3.2.14) and by assuming a linear drag law and neglecting the Basset history term, we have

$$\frac{dv_1}{dt} = -c_1 v_2 - c_2 x_1 - c_3 v_1 - c_4 x_2, \tag{3.7.1a}$$

$$\frac{dv_2}{dt} = c_1 v_1 - c_2 x_2 - c_3 v_2 - c_4 x_1 + c_5, \tag{3.7.1b}$$

where

$$c_1 = \frac{C_L}{\gamma + C_M}, \qquad c_2 = \left(\frac{1}{4}\frac{1 + C_M}{\gamma + C_M} - \frac{1}{2}\frac{C_L}{\gamma + C_M}\right)\Omega^2,$$

$$c_3 = \frac{|\gamma - 1|}{\gamma + C_M}\frac{g}{v_T}, \qquad c_4 = \frac{\Omega}{2}c_3 \qquad \text{and} \qquad c_5 = \frac{\gamma - 1}{\gamma + C_M}g.$$

The equations have solution for $\mathbf{x}_p$ which is proportional to $\exp(\theta t)$ and the possible value of θ are the roots of the quartic polynomial

$$\theta^4 + 2c_3\theta^3 + b_1\theta^2 + b_2\theta + b_3 = 0, \tag{3.7.2}$$

where

$$b_1 = c_1^2 + 2c_2 + c_3^2, \qquad b_2 = 2c_2 c_3 + 2c_1 c_4 \qquad \text{and} \qquad b_3 = c_2^2 + c_4^2.$$

In general the roots of the polynomial (3.7.2) must be found numerically, but some special results may be deduced.

(a) *Drag can be neglected* i.e. $\mathbf{F}_A/\mathbf{F}_D \rightarrow \infty$, $\mathbf{F}_L/\mathbf{F}_D \rightarrow \infty$

In this case, we have $c_3 = c_4 = 0$, then (3.7.2) simplifies considerably and an explicit expression for θ can be found, i.e.

$$\theta^4 + (c_1^2 + 2c_2)\theta^2 + c_2^2 = 0.$$

Then the particle displacement $\mathbf{x}_p$ is given by (Hunt *et al.* 1988)

$$\mathbf{x}_p = \mathbf{A} \exp(i\theta_1 t) + \mathbf{B} \exp(i\theta_2 t) - 2\mathbf{g}/c_2, \tag{3.7.3}$$

where $\mathbf{A} = a(1, i)$, $\mathbf{B} = b(1, i)$ and the two frequencies of oscillation are the roots θ_1, $\theta_2 = c_1(2c_6 + 1)/\sqrt{2} \pm \sqrt{1 + 4c_6}$ for a sphere, where $c_6 = c_2/c_1^2 - 1/4$.

Thus the bubbles ($\gamma = 0.0$) can move in circles around a point $8g/\Omega^2$ *above* the centerline (and for particles around a point below $8g/\Omega^2$ and above the centerline), with two possible frequencies.

(b) *Drag is very large* i.e. $\mathbf{F}_A/\mathbf{F}_D \rightarrow 0$, $\mathbf{F}_L/\mathbf{F}_D \rightarrow 0$

In this limiting case, inertia forces can be neglected, i.e., $c_1 = c_2 = c_3 = 0$, then (3.7.2) reduces to

$$\theta^4 + 2c_3\theta^2 + c_4^2 = 0.$$

The solution for $\mathbf{x}_p$ of this is well known (e.g. Tooby *et al.* 1977) and leads to bubbles and particles moving in circular orbits:

$$x_1 = A \cos(\Omega t/2 + \phi) - 2V_T/\Omega \qquad \text{and} \qquad x_2 = A \sin(\Omega t/2 + \phi), \tag{3.7.4}$$

where the amplitude A and phase ϕ of the orbits depend on the initial conditions. The orbits of bubbles are centred about a position $2V_T/\Omega$ on the *downflow* side of the centre of the vortex (*upflow* side for particles).

In general, the bubble or particle will circulate around a fixed point, which lies between $x_1 = 0$, $x_2 \simeq 8g/\Omega^2$ and $x_1 = \pm 2V_T/\Omega$, $x_2 = 0$.

(c) *Very heavy particles* i.e. $\gamma \rightarrow \infty$

In this case, we have $c_1 = c_2 = 0$ since γ is large, so (3.7.2) reduces to

$$\theta^4 + 2c_3\theta^3 + c_3^2\theta^2 + c_4^2 = 0,$$

then the roots form two complex conjugate pairs

$$\theta = r \pm iq, \qquad \theta = s \pm iq, \tag{3.7.5}$$

where

$$rs = -q^2, \qquad r + s = -c_3 \qquad (3.7.6)$$

and $q^2 = (-c_3^2 \pm \sqrt{c_3^4 + 16c_4^2})/8$.

At least one or the other of r and s must be positive in order to satisfy (3.7.6), and so this point is unstable. This is consistent with the finding by Manton (1974) and Nielsen (1984) that the equilibrium points become unstable as the density of the particle become greater than that of surrounding flow. Moreover, at small values of V_T the growth rates of these instabilities are small. A particle passing close to such a point may appear to be temporarily suspended or trapped in the flow, and spiral slowly out of the vortex as found in the simulation result of Perkins and Hunt (1986).

The next question to be asked is whether this trapping is a feature only of the rather unnatural, forced vortex. The answer is no, Nielsen (1984), Perkins and Hunt (1986) considered the more realistic model of a Rankine vortex in which the velocity field is given by

$$\mathbf{u}(x, y) = \frac{\Omega}{1 + \left(\frac{x}{R}\right)^2 + \left(\frac{y}{R}\right)^2}(-y, x). \qquad (3.7.7)$$

It is characteristic for this vortex model that the core rotates as a rigid body, with the velocity being proportional to the distance from the centre, which $\mathbf{u}$ becomes inversely proportional to this distance further away.

By considering the simplified case in which inertia and lift forces are neglected, the only forces then acting are buoyancy and drag, i.e.

$$\mathbf{v} = \mathbf{u} + V_T. \qquad (3.7.8)$$

Perkins and Hunt (1986) was able to show that there are two stagnation points and their coordinates are $\left(R\Omega/2V_T \pm \sqrt{(R\Omega/2V_T)^2 - 1}, \, 0\right)$. Also, the particle trajectories through (x_o, y_o) are

$$\frac{x}{R} = \frac{x_o}{R} + \frac{\Omega R}{2V_T} \ln \left[\frac{1 + \left(\frac{x_o}{R}\right)^2 + \left(\frac{y_o}{R}\right)^2}{1 + \left(\frac{x}{R}\right)^2 + \left(\frac{y}{R}\right)^2} \right]$$

as shown in figure 3.36. Some of these are closed and could thus keep the particle trapped. Trapping is only possible if the settling velocity is less than the maximum upward velocity, that is, if $V_T < \Omega R/2$.

Furthermore, by solving the full equation of motion (3.2.14) numerically (neglecting the Basset force) in an irrotational vortex (Auton 1983) and in an Rankine vortex (Perkins and Hunt 1986), they were able to show that bubbles released beneath an vortex could be trapped

within the vortex, eventually spiralling into the centre. The trajectory of the bubble was dependent on the circulation of the vortex and the initial position of bubble relative to the centre of the vortex. A convenient measure of the trapping power of a vortex is the width A_t, parallel to the horizontal y-direction of the initial position of trapping particles. Auton showed that the non-dimensional trapping width, may be expressed as a function, A_t^*, of the density ratio and the non-dimensional circulation $C^* = \Omega g / V_T^3$ and $A_t^* = A_t g / V_T^2 = A_t^*(\gamma, C^*)$. And numerical prediction of A_t^* is given by Auton (1983), essentially as V_T increases, A_t^* decreases monotonically for bubbles, i.e., it is unlikely being trapped.

(d) *Particles and bubbles in convergence regions*

In the case of particles or bubbles in irrotational solenoidal flow near a stagnation point, the velocity field is given by

$$\mathbf{u} = (\alpha x_1, \ -\alpha x_2, \ 0),$$

hence

$$\frac{D\mathbf{u}}{Dt} = (\alpha x_1, \ -\alpha x_2, \ 0), \qquad \mathbf{g} = (0, \ g, \ 0).$$

Substituting these into equation (3.2.14), assuming a linear drag law and neglecting the Basset history term, we have

$$\frac{dv_1}{dt} = c_1(\alpha x_1 - v_1) + c_2(\alpha x_1),$$

$$\frac{dv_2}{dt} = c_1(-\alpha x_2 - v_2) + c_2(-\alpha x_2) + c_3,$$

where

$$c_1 = \frac{\gamma - 1}{\gamma + C_M} \frac{g}{V_T}, \qquad c_2 = \frac{1 + C_M}{\gamma + C_M} \qquad \text{and} \qquad c_3 = \frac{\gamma - 1}{\gamma + C_M} g.$$

If the initial conditions are $x_2 = 0$ and $dx_2/dt = V_T$ at $t = 0$, then the equation has solution of the form

$$x_2 = A_o \exp(\theta_1 t) + B_o \exp(\theta_2 t) + \frac{c_2}{\alpha(c_2 + c_3)},$$

where θ_1, θ_2 are equal to $-c_1 \pm \sqrt{c_1^2 - 4(c_1 + c_3)}/2$, also $A_o + B_o = -c_2/\alpha(c_1 + c_2)$ and $A_o \theta_1 + B_o \theta_2 = V_T$. If the residence time of the particle or bubble in the convergence regions is small, then by series expansion of $\exp(\theta_i t)$, we have

$$x_2 = V_T t.$$

Thus, the convergence region has no effect on the average settling velocity if the residence time in C-region is small.

3.7.3 Results of simulation

For each realisation of the simulation, a random flow field is generated as described in chapter 2 and 16 particles are released at random positions in the Eulerian field (at least three integral length scales apart) at time $t = 0$ with the initial conditions:

$$\mathbf{x}_p(t = 0) = \mathbf{x}_0, \qquad \mathbf{v}(t = 0) = \mathbf{u}(\mathbf{x}_0, t = 0) + V_T. \qquad (3.7.9)$$

The motion of the particle is not sensitive to the choice of the initial velocity, especially if attention is found on the asymptotic states.

The motion of a particle or a bubble is found by numerically solving the full equation of motion (3.2.14), using the Predictor-Corrector method with a square drag law. By neglecting the Basset history force, the scaled form of (3.7.9) can be rewritten as

$$\frac{d\mathbf{v}}{dt} = \frac{|\gamma - 1|}{\gamma + C_M} \frac{g}{V_T^2} |\mathbf{u} - \mathbf{v}| (\mathbf{u} - \mathbf{v}) + \frac{\gamma - 1}{\gamma + C_M} \mathbf{g}$$

$$+ \frac{1 + C_M}{\gamma + C_M} \frac{D\mathbf{u}}{Dt} + \frac{C_L}{\gamma + C_M} (\mathbf{u} - \mathbf{v}) \wedge (\nabla \wedge \mathbf{u}), \qquad (3.7.10)$$

where we have introduced the non-dimensional variables as in equation (3.3.2), i.e., the non-dimensionalised settling velocity V_T $(= V_T/u')$; the time t $(= tu'/L)$ and the gravitational constant g $(= gL/u'^2)$.

At each advancing time step, the fluid velocity $\mathbf{u}(\mathbf{x}_p, t)$ along the particle or bubble trajectories are computed by (2.2.5). The procedure is repeated so that each run contains 100 realisations. The ensemble approach is used to compute particle and fluid statistics. The simulation were carried on at least $t = 13\,T_L$ and the asymptotic, steady-state statistics were estimated by further time-averaging the values between $t = 7\,T_L$ and $13\,T_L$. In all the simulations the still-fluid terminal fall or rise velocity V_T was taken to be in the x_3 direction.

In order to cut down the computational cost, the flow field is static in time which implies an infinite Eulerian integral timescale T_E. As we have shown in Chapter 2 that the Lagrangian integral time scale T_L does not vary much as compared with the frozen Lagrangian case and the spatial structure of the flow is a dominant process for the particle dispersion. One might say that the time dependence only affects dispersion phenomena appreciably if it affects the spatial structure strongly and with some persistence.

As long as the particle is moving, the time scale on which the flow field around the particle changes is too short for there to be much effect. Indeed, as indicated in the frozen Lagrangian time scale T_L. In view of this, static simulation of KS has been adopted for the subsequence runs in this section.

I. *Particles with no inertia*

In the complete absence of particle and fluid inertia, the fluid drag force on the particle balances the force due to gravity at every instant, i.e. the net force on the particle is zero. This allows one to defined a 'particle velocity field' $v(\mathbf{x}, t)$ as

$$v(\mathbf{x}, t) = \mathbf{u}(\mathbf{x}, t) + V_T, \tag{3.7.11a}$$

so that for a given particle

$$\frac{d\mathbf{x}_p}{dt} = \mathbf{v}(t) = v(\mathbf{x}_p, t), \tag{3.7.11b}$$

i.e. particle velocity is equal to sum of the still-fluid terminal velocity and the instantaneous velocity of the surrounding fluid.

In statistically homogeneous and stationary turbulence the ensemble average of $\langle \mathbf{v}(t) \rangle$ will reach some asymptotic stationary value, long after the particle release. Taking ensemble average of (3.7.11a) as $t \gg T_L$, we have

$$\langle \mathbf{v}(t) \rangle = \langle \mathbf{u}(\mathbf{x}_p, t) \rangle + V_T. \tag{3.7.12}$$

The ensemble average of the fluid velocity along the particle trajectories $\langle \mathbf{u}(\mathbf{x}_p, t) \rangle$ differs from both a Eulerian, fixed-point average and a Lagrangian average following a fluid element. Whether or not the turbulence has any net effect on the terminal velocity depends on whether or not $\langle \mathbf{u}(\mathbf{x}_p, t) \rangle = 0$.

This no inertia limited case has been studies by Maxey & Corrsin (1986) and Maxey (1987). They have pointed out that since V_T is a constant and the fluid flow field is incompressible it follows that $v(\mathbf{x}, t)$ is also incompressible, i.e. an initially uniform distribution of particles will remain statistically uniform with no tendency to accumulate. The average particle velocity then is the same as when the particles were released which is just V_T, because the Eulerian (spatial) average $\langle \mathbf{u}(\mathbf{x}, t) \rangle$ is zero. This can also be seen by note that the equation of motion for particle (3.7.11a) has the same form as a Lagrangian material element moving in the 'particle velocity field', $v(\mathbf{x}, t)$. Lumley (1962) has shown that for homogeneous and stationary turbulence, in an incompressible flow, one point average statistics are equal in spatial (Eulerian) and material (Lagrangian) coordinates of the flow field. This lead to $\langle \mathbf{v}(t) \rangle$ equal to the Eulerian mean value of $v(\mathbf{x}, t)$, i.e.

$$\langle \mathbf{v}(t) \rangle = V_T. \tag{3.7.13}$$

Therefore the turbulent has no net effect on the terminal velocity if there is no inertia, any effect necessarily requires the influence of particle inertia.

The average particle terminal velocity have been computed for particle with different V_T in this no inertia limited case to obtain the asymptotic values, long after the particle release (Figure 3.37). As expected, the turbulent have no net effect on the terminal velocity of the particles and the average velocity of the particle $\langle v_1 \rangle$, $\langle v_2 \rangle$ were found to be zero and $\langle v_3 \rangle = V_T$ to within statistical error limits.

II. *Particle with inertia*

When the inertia of the particle is finite, the motion of the particle is determined by the full equation (3.2.14) with the initial condition as in (3.7.9). In this section, we will consider the effect of (1) varying the terminal velocity (changing the drag) while keeping density ratio γ, g constant; (2) varying the gravity term g while keeping γ and the drag force constant; (3) Also by varying the density ratio γ, the effect of added mass and lift force can be investigated.

The particles and bubbles terminal velocity $\langle v_3 \rangle$ has been computed for different value of V_T to obtain the asymptotic values, long after the particle release (Fig 3.38a, b and c). The most obvious feature is that both for the bubbles and the particles, the average rise and fall terminal velocities are always less than that of still fluid.

As shown in figure 3.38a, for the bubbles with $V_T \lesssim 1.5$, the average rise velocity $\langle v_3 \rangle$ is about 60% less than that in still fluid. This is consistent with Thomas's description of bubble detrainment in the plunging jet flow use an effective rise speed which is only one quarter of the bubble rise speed in still water. The differences decrease as V_T increasing from 1.5 and vanish eventually as V_T tends to infinity. For a particle with the density ratio of $\gamma = 2.65$, which corresponds to the sand particle in water, the influence of turbulence is less, from figure 3.38b, for the particles with terminal velocity $V_T \lesssim 4$, the computed fall terminal velocity $\langle v_3 \rangle$ is about 10% less than that of fluid and the differences disappear as $V_T \to \infty$. By increasing further of the density ratio, say, $\gamma = 833.0$, which corresponds to coal particles in air, the influence of turbulence is even less as compared to the two previous cases (Fig. 3.38c), apart for $V_T \lesssim 1$, the average terminal velocity $\langle v_3 \rangle$ is about 10% less than that of still fluid. For particle with larger fall velocity, there is only very slight reduction in the average terminal velocity, being negligible for $V_T \gtrsim 5$.

Figures 3.39a, b and c show that the influence of gravity g on the terminal velocity for a fixed value of drag force with $g/V_T^2 = 1.0$ by varying V_T. Yet again, the computed terminal velocity $\langle v_3 \rangle$ is less than V_T is the obvious feature, and $\langle v_3 \rangle \to V_T$ as $V_T \to \infty$.

The reason of the differences of the average terminal velocity between the computed and the still fluid velocity can be provided by examining on the average velocity $\langle \mathbf{u}(\mathbf{x}_p, t) \rangle$ and the average square velocity $\langle \mathbf{u}^2(\mathbf{x}_p, t) \rangle$ of the fluid along the particle trajectories. In the case of

bubbles, figure 3.40a shows that indeed $\langle u_1(\mathbf{x}_p, t)\rangle$ and $\langle u_2(\mathbf{x}_p, t)\rangle$ were found to be zero to within statistical error limits. However $\langle u_3(\mathbf{x}_p, t)\rangle$ is always negative. i.e. the bubble spends most of its time in the 'downward moving' region of the flow. Also $\langle u_3(\mathbf{x}_p, t)\rangle$ decreases approximately linearly from 0.0 to -1.0 and reaches its minimum value of -1.0 at $V_T \approx 1.5$, further increasing V_T in results of increasing $\langle u_3(\mathbf{x}_p, t)\rangle$, as V_T tends to infinity, then the bubble average flow velocity $\langle u_3(\mathbf{x}_p, t)\rangle$ tends to the Eulerian average value of zero and this corresponds to the computed average rise velocity tends backs to the rise velocity in the still fluid.

By coupling this with $\langle \mathbf{u}^2(\mathbf{x}_p, t)\rangle$, we conclude that there are two possible mechanisms responsible for this effect of $\langle v_3 \rangle \lesssim V_T$. Let us concentrate on the bubble case for the moment, in this case when $V_T \lesssim 1.0$, as mentioned previously, $\langle v_3 \rangle$ is about 60% less than that of V_T. Also, in the figure 3.40a shows that the mean square velocity fluctuations $\langle u_i^2(\mathbf{x}_p, t)\rangle$ is always less than the turbulent intensity $u'^2 \ (= 1)$, From the simulation of Auton (1983) in a line vortex, bubbles within the trapped width are spiral in towards a stable point (the lift force on the bubble exactly balances the buoyancy force) which would lie on the negative x-axis if the centre of the vortex is at the origin and rotate anti-clockwise. And from chapter 2, we show that in the eddy regions of the flow, $\langle u_E^2 \rangle < u'^2$, therefore the bubbles must be trapped by eddies in the 'downward-moving' side of the eddies.

Secondly, if $V_T \gtrsim 1.0$, the mean square velocity fluctuation $\langle u_3^2(\mathbf{x}_p, t)\rangle$ is always greater than 1, reaches to its maximum value of 1.8 at $V_T \approx 2$, and finally tending back to 1 as $V_T \to \infty$ for qualitative reasons mentioned in the last but one paragraph. This means that the bubbles cannot be trapped by eddies and they must tend to spend more time in the downward moving parts of the streaming since in the streaming regions $\langle u_S^2 \rangle \gtrsim u'^2$. (note that even though $\langle u_{3E}(\mathbf{x}_p, t)\rangle > \langle u_{3S}(\mathbf{x}_p, t)\rangle$ because the velocity of the fluid sample by the particle are not vertically downward on average but inclined at some angle, θ say, to the horizontal which is more than $\pi/4$ since $\theta = \tan^{-1}\sqrt{\langle u_{3S}^2 \rangle / \langle u_{1S}^2 \rangle} \approx \sqrt{1.6/1.2} \gtrsim \pi/4$.)

The above argument can be further supported by plotting the total amount of time when bubbles spend in different regions of the flows against V_T (Following Hunt et al. 1988b, only dividing the flow into four zones). Note that as $V_T \to \infty$, the total time for bubbles or particles spending in different regions of the flow is equal to the total volume occupied by different regions of the flow (Eulerian sampling) or this is equivalent (Lumley 1962) to that of a fluid element spending different time in different regions of the flow (Lagrangian sampling). In our simulation with the von Kárman energy spectrum, the flow consists of 7%, 32%, 5% and 56% of eddy, streaming, convergence and undefined regions respectively. Figure 3.41 shows that the time spent by the bubbles in eddy, streaming and convergence regions are 15%, 29% and 3% of its total time at $V_T \approx 1$ respectively, which corresponds to spending more time in eddy

regions and less time in streaming and convergence regions as compared to that of a fluid element. However, by further increasing V_T, the bubble tends to spend more time (36%) in the streaming regions as suggested above and further increasing V_T still, the time spent for bubbles in the eddy, streaming and convergence regions tend back to that of a fluid element. Furthermore by looking at the resident time of the bubbles at different regions of the flow (Fig. 3.42), at $V_T \simeq 1$, the resident time normalised by T_L of eddy, τ_E, is greater than that of streaming τ_S, and as $V_T \to \infty$, $\tau_S > \tau_E$ since the typical diameter of these zones is about $L/4$ in the eddy regions and L in length and $L/2$ in width in streaming regions.

The reason for the bubble spending more time in the downwards moving part of the streaming regions in the case of $V_T \gtrsim 1$ is due to the lift force $\mathbf{F}_L$. When the bubble is moving against and at the edges the streaming as show in figure 3.43a, the lift force tends to draw the bubble into the centre of the streaming regions where the speed of the flow is fastest. However, if the bubble is moving with and at the edges the streaming (figure 3.43b), the lift force tends to push the bubble away from the centre of streaming where the flow is slower or entering different regions of the flow. By neglecting the lift force in the full equation, V_T is only slightly reduced as compared to V_T, and being negligible as $V_T \gtrsim 20$, also the bubbles do not tend to spend more time in streaming regions.

In the case of a particle with $\gamma = 2.65$ and 833.0, $\langle u_1(\mathbf{x}_p, t) \rangle = \langle u_2(\mathbf{x}_p, t) \rangle = 0$ (Fig. 3.40b, c) as in the bubble case. However, the mean fluctuating value of $\langle u_3(\mathbf{x}_p, t) \rangle \gtrsim 0$ and reaches its maximum value at $V_T \simeq 3$, also $\langle u_1^2(\mathbf{x}_p, t) \rangle = \langle u_2^2(\mathbf{x}_p, t) \rangle \simeq 1$ and $\langle u_3^2(\mathbf{x}_p, t) \rangle \gtrsim 1$ and has a maximum value of around $V_T \simeq 3$. This means that the particles tend to spend more of its time in the upward-moving part of the flow and hence $\langle V_T \rangle \lesssim V_T$. However, $\langle u_3^2(\mathbf{x}_p, t) \rangle$ is only sightly greater than u'^2, this implies that the particle must spend either more of its time in the upward-moving part of the streaming or at the very edges of upward-moving part of eddy regions in which $\langle u_E^2 \rangle \simeq u'^2$. In order to distinguish the two, we can examine the graphs of where is the particle spending its time in different regions of the flow. As can be seen in figure 3.44, the particles with $\gamma = 2.65$ spend 9% and 35% (with $\gamma = 833.$ spend 8% and 34% in figure 3.45) of its time in eddy and streaming regions, this corresponds to spend more time both in eddy and streaming regions than of a fluid element at $V_T \approx 2$ respectively. This means that the particle are still being trapped by eddies. However, the residence time $\tau_E < \tau_S$. And by increasing V_T still, the time spent for particles in the eddy, streaming and convergence regions tend back to that of a fluid element (Figs. 3.46 and 3.47).

3.8 Summary and some conclusions

The present study was undertaken to investigate the feasibility and the results of numerically simulating turbulent dispersion without prohabitive cost in computer time.

The accurate measurement of the particle motion and velocity is especially difficult, even in more or less homogeneous flows. Experiments such as those of Snyder and Lumley (1971) or Wells and Stock (1983) have been directed towards measurements of the particle dispersion rather than individual trajectories. By contrast, in our numerical simulation of the particle motion in a flow field it is relatively easy to trace the motion of the individual particles – the particle position $\mathbf{x}_p$, velocity $\mathbf{v}$, acceleration $d\mathbf{v}/dt$, the velocity of the fluid in the vicinity of the particles $\mathbf{u}(\mathbf{x}_p, t)$, the relative velocity $\mathbf{v}_R$ of the fluid and particle – can be easily computed, and their statistical properties can then be found. Thus in-depth study of an individual process can be made. Furthermore, the various parameters involved in the full equation of motion of the particle can be investigated in great detail.

This method of investigation appears to be useful when qualitative kinematic effect are sought. The method of solutions was to first set up a mathematical model of the random velocity field. Then an "ensemble" of realisations of this field was generated digitally. In each realisation, the governing equations were integrated numerically for various values of the particle time constant τ_p and its fall velocity W_g, the output was stored. After a large enough number of realisations had been completed that meaningful statistical results could be obtained, various statistical quantities of interest were computed. In this manner a solution to the problem was obtained.

The results are

(i) The long time particle and fluid element coefficients is not equal because the effect of small scale leads to large scales changes in the mean square displacement and hence the diffusivity of the particle.

(ii) Setting the fall velocity of the particle $W_g = 0$ and increasing the particle time constant τ_p tended to increase the solid particle velocity time correlation.

(iii) The extent of particle dispersion in the absence of gravity depends strongly on the particle time constant τ_p $(= \tau_{p_o} u'/L)$, the ratio of particle response time to the characteristic time of the flow. Particle with relatively small τ_p values (~ 0.5) are dispersed less than the fluid. Particles at intermediate values of τ_p ($\sim \mathcal{O}(1)$) are dispersed faster than the fluid. And as $\tau_p \to \infty$, the dispersion tends to zero.

(iv) With τ_p constant, increasing W_g tended to decrease the solid particle dispersion.

(v) The method of investigation appears reliable when the Eulerian spatial field is the de-

termining factor in the process (e.g., in "rapid" fallout problem), since the Eulerian spatial statistics can be modelled very precisely, hence the hypothesis of frozen turbulence (Csanady 1963) gave accurate estimates of the autocorrelation of the velocity of the fluid along the particle trajectories and hence give a good estimate of particle dispersion.

(vi) The terminal velocity V_T of the particles (or bubbles) in a turbulent flow is less than that of still fluid, when the terminal velocity of the particle is less than that of the turbulent intensity u'. The decrease in fall velocity is most pronounced for $V_T \lesssim 1$ but was negligible for $V_T/u' > 2$.

We have shown that the necessity for understanding the structures of the flow if satisfactory models are to be developed for turbulent dispersion. Small particles closely follow the fluid particle trajectories. However, larger particle with significant inertia or fall velocity, are shown to cut through eddies. Realistic modelling of particle dispersion requires modelling of the eddies and their interactions with the particles. One can envisage flows in which individual eddies may be considered as 'reactors' which are continually entraining and interacting with the particles (Brown and Hutchinson 1979). Current modelling approaches, based on time average flux equations, should preferably be adapted to include information of the spatial structure of the velocity fields with these eddies and their interaction with the particles.

Particle density ρ_p kg/m^3	Fluid density ρ_f kg/m^3	Ratio of densities γ	Kinematic viscosity ν m^2/sec	Particle diameter d_p μ	Terminal velocity V_T m/sec	Drag coefficient C_D	Particle Reynolds no. Re$_p$	Particle time constant T_p msec	Situation
2.65×10^3	1.0×10^3	2.65×10^0	1.0×10^{-6}	50 – 500	2.9×10^{-3} – 7.9×10^{-2}	1.3×10^2 – 1.7×10^0	1.9×10^{-1} – 3.9×10^1	2.9×10^{-1} – 8.1×10^0	sand in water
2.65×10^3	1.2×10^0	2.21×10^3	1.5×10^{-5}	50 – 500	1.9×10^{-1} – 3.9×10^0	3.9×10^1 – 9.6×10^{-1}	6.4×10^{-1} – 1.3×10^2	1.9×10^1 – 4.0×10^2	sand in air
1.20×10^0	1.0×10^3	1.20×10^{-3}	1.0×10^{-6}	500 – 5000	5.0×10^{-2} – 2.7×10^{-1}	3.2×10^2 – 3.0×10^0	7.3×10^{-2} – 1.9×10^3	5.1×10^0 – 2.8×10^1	bubbles in water
1.00×10^3	1.2×10^0	8.33×10^2	1.5×10^{-5}	10 – 500	3.7×10^{-3} – 2.1×10^0	8.1×10^3 – 1.3×10^0	3.0×10^{-3} – 7.0×10^1	3.7×10^{-1} – 2.1×10^2	droplet in air
7.00×10^3	1.2×10^0	5.83×10^3	1.5×10^{-5}	10 – 10000	2.2×10^{-2} – 4.1×10^1	1.6×10^3 – 4.7×10^{-1}	1.5×10^{-2} – 2.7×10^4	2.3×10^0 – 4.2×10^3	Iron Ore in air

Table 3.1

The definition of the particle time constant is not identical to $T_p = d_p^2[1 + (2\rho_p/\rho_f)]/36\nu$, which conforms to the definition $T_p = V_T/g$ if the particle obeys Stokes flow. As can be seen from table 3.1, only a few particles had a Reynolds number less than one and hence obeyed Stokes flow. The definition used here is a better physical measure of the particle time constant, i.e. the time required for a particle subjected to a step change in velocity to reach 64% of its final velocity. The terminal velocities, drag coefficients and the particle Reynolds numbers were estimated by the drag coefficient equations by Morsi and Alexander (1972).

DC03AD $\Delta t = 0.005$ $\Delta t = 0.01$

```
DC03AD                                                          Δt = 0.005                                                    Δt = 0.01

THE NTH TIME STEP =  580   THE CURRENT TIME = 0.290000E+01    =  580                                                    =  290
CURRENT  POSITION = 0.107314E+01 0.364568E+01 0.146529E+01    = 0.107737E+01 0.361798E+01 0.146549E+01                 = 0.107890E+01 0.360016E+01 0.147649E+01
CURRENT  VELOCITY = -.198057E+00 0.643472E-01 -.217875E-01    = -.216608E+00 0.575462E-01 -.125997E-01                = -.216428E+00 0.580626E-01 0.743507E-03
THE NTH TIME STEP =  581   THE CURRENT TIME = 0.290500E+01    =  581
CURRENT  POSITION = 0.107217E+01 0.364600E+01 0.146517E+01    = 0.107630E+01 0.361827E+01 0.146543E+01
CURRENT  VELOCITY = -.191123E+00 0.622006E-01 -.242838E-01    = -.211165E+00 0.567421E-01 -.137186E-01
THE NTH TIME STEP =  582   THE CURRENT TIME = 0.291000E+01    =  582                                                    =  291
CURRENT  POSITION = 0.107123E+01 0.364630E+01 0.146504E+01    = 0.107526E+01 0.361855E+01 0.146536E+01                 = 0.107678E+01 0.360073E+01 0.147648E+01
CURRENT  VELOCITY = -.184335E+00 0.601191E-01 -.268550E-01    = -.205714E+00 0.559940E-01 -.148505E-01                = -.207631E+00 0.553669E-01 -.190443E-02
THE NTH TIME STEP =  583   THE CURRENT TIME = 0.291500E+01    =  583
CURRENT  POSITION = 0.107032E+01 0.364659E+01 0.146492E+01    = 0.107424E+01 0.361882E+01 0.146528E+01
CURRENT  VELOCITY = -.180354E+00 0.553451E-01 -.239014E-01    = -.201294E+00 0.536510E-01 -.149334E-01
THE NTH TIME STEP =  584   THE CURRENT TIME = 0.292000E+01    =  584                                                    =  292
CURRENT  POSITION = 0.106942E+01 0.364686E+01 0.146480E+01    = 0.107324E+01 0.361905E+01 0.146521E+01                 = 0.107474E+01 0.360125E+01 0.147646E+01
CURRENT  VELOCITY = -.176553E+00 0.509244E-01 -.210666E-01    = -.196023E+00 0.498573E-01 -.140118E-01                = -.200408E+00 0.497810E-01 -.266431E-02
THE NTH TIME STEP =  585   THE CURRENT TIME = 0.292500E+01    =  585
CURRENT  POSITION = 0.106855E+01 0.364710E+01 0.146470E+01    = 0.107226E+01 0.361932E+01 0.146514E+01
CURRENT  VELOCITY = -.172820E+00 0.468802E-01 -.185083E-01    = -.194910E+00 0.463936E-01 -.131431E-01
THE NTH TIME STEP =  586   THE CURRENT TIME = 0.293000E+01    =  586                                                    =  293
CURRENT  POSITION = 0.106770E+01 0.364733E+01 0.146462E+01    = 0.107130E+01 0.361955E+01 0.146508E+01                 = 0.107276E+01 0.360171E+01 0.147644E+01
CURRENT  VELOCITY = -.169018E+00 0.431811E-01 -.162345E-01    = -.191811E+00 0.432252E-01 -.122331E-01                = -.195543E+00 0.417134E-01 -.113685E-02
THE NTH TIME STEP =  587   THE CURRENT TIME = 0.293500E+01    =  587
CURRENT  POSITION = 0.106686E+01 0.364753E+01 0.146454E+01    = 0.107034E+01 0.361975E+01 0.146502E+01
CURRENT  VELOCITY = -.165048E+00 0.397454E-01 -.143012E-01    = -.188593E+00 0.402950E-01 -.112113E-01
THE NTH TIME STEP =  588   THE CURRENT TIME = 0.294000E+01    =  588                                                    =  294
CURRENT  POSITION = 0.106605E+01 0.364773E+01 0.146447E+01    = 0.106941E+01 0.361995E+01 0.146496E+01                 = 0.107052E+01 0.360209E+01 0.147644E+01
CURRENT  VELOCITY = -.160836E+00 0.364586E-01 -.127158E-01    = -.185152E+00 0.375342E-01 -.100410E-01                = -.191862E+00 0.350818E-01 0.137164E-02
THE NTH TIME STEP =  589   THE CURRENT TIME = 0.294500E+01    =  589
CURRENT  POSITION = 0.106524E+01 0.364791E+01 0.146442E+01    = 0.106849E+01 0.362014E+01 0.146492E+01
CURRENT  VELOCITY = -.161428E+00 0.375321E-01 -.990534E-02    = -.182924E+00 0.364987E-01 -.892074E-02
THE NTH TIME STEP =  590   THE CURRENT TIME = 0.295000E+01    =  590                                                    =  295
CURRENT  POSITION = 0.106443E+01 0.364810E+01 0.146437E+01    = 0.106758E+01 0.362032E+01 0.146487E+01                 = 0.106890E+01 0.360244E+01 0.147646E+01
CURRENT  VELOCITY = -.161474E+00 0.387822E-01 -.751158E-02    = -.182003E+00 0.374305E-01 -.841512E-02                = -.190793E+00 0.335646E-01 0.197474E-02
THE NTH TIME STEP =  591   THE CURRENT TIME = 0.295500E+01    =  591
CURRENT  POSITION = 0.106363E+01 0.364830E+01 0.146434E+01    = 0.106667E+01 0.362051E+01 0.146483E+01
CURRENT  VELOCITY = -.160795E+00 0.404724E-01 -.565404E-02    = -.161023E+00 0.391022E-01 -.675311E-02
THE NTH TIME STEP =  592   THE CURRENT TIME = 0.296000E+01    =  592                                                    =  296
CURRENT  POSITION = 0.106282E+01 0.364851E+01 0.146432E+01    = 0.106577E+01 0.362071E+01 0.146478E+01                 = 0.106698E+01 0.360280E+01 0.147647E+01
CURRENT  VELOCITY = -.159510E+00 0.427843E-01 -.450383E-02    = -.180026E+00 0.415929E-01 -.957548E-02                = -.192812E+00 0.372964E-01 -.496555E-05
THE NTH TIME STEP =  593   THE CURRENT TIME = 0.296500E+01    =  593
CURRENT  POSITION = 0.106203E+01 0.364873E+01 0.146430E+01    = 0.106487E+01 0.362093E+01 0.146473E+01
CURRENT  VELOCITY = -.158007E+00 0.457021E-01 -.419415E-02    = -.179052E+00 0.446554E-01 -.103808E-01
THE NTH TIME STEP =  594   THE CURRENT TIME = 0.297000E+01    =  594                                                    =  297
CURRENT  POSITION = 0.106124E+01 0.364896E+01 0.146427E+01    = 0.106398E+01 0.362116E+01 0.146468E+01                 = 0.106505E+01 0.360320E+01 0.147647E+01
CURRENT  VELOCITY = -.156805E+00 0.490055E-01 -.470950E-02    = -.178165E+00 0.478066E-01 -.106717E-01                = -.194931E+00 0.420921E-01 -.471856E-03
THE NTH TIME STEP =  595   THE CURRENT TIME = 0.297500E+01    =  595
CURRENT  POSITION = 0.106047E+01 0.364921E+01 0.146424E+01    = 0.106309E+01 0.362140E+01 0.146463E+01
CURRENT  VELOCITY = -.154582E+00 0.484798E-01 -.708729E-02    = -.176392E+00 0.487538E-01 -.993091E-02
THE NTH TIME STEP =  596   THE CURRENT TIME = 0.298000E+01    =  596                                                    =  298
CURRENT  POSITION = 0.105970E+01 0.364945E+01 0.146420E+01    = 0.106222E+01 0.362164E+01 0.146458E+01                 = 0.106312E+01 0.360362E+01 0.147647E+01
CURRENT  VELOCITY = -.151887E+00 0.477815E-01 -.855773E-02    = -.173456E+00 0.476264E-01 -.837895E-02                = -.191750E+00 0.442380E-01 0.964733E-03
THE NTH TIME STEP =  597   THE CURRENT TIME = 0.298500E+01    =  597
CURRENT  POSITION = 0.105895E+01 0.364969E+01 0.146416E+01    = 0.106136E+01 0.362188E+01 0.146455E+01
CURRENT  VELOCITY = -.148673E+00 0.469696E-01 -.910196E-02    = -.170063E+00 0.466340E-01 -.661616E-02
THE NTH TIME STEP =  598   THE CURRENT TIME = 0.299000E+01    =  598                                                    =  299
CURRENT  POSITION = 0.105821E+01 0.364992E+01 0.146411E+01    = 0.106052E+01 0.362211E+01 0.146452E+01                 = 0.106124E+01 0.360406E+01 0.147648E+01
CURRENT  VELOCITY = -.144983E+00 0.461332E-01 -.879263E-02    = -.166215E+00 0.458641E-01 -.482417E-02                = -.183926E+00 0.436696E-01 0.184062E-02
THE NTH TIME STEP =  599   THE CURRENT TIME = 0.299500E+01    =  599
CURRENT  POSITION = 0.105750E+01 0.365015E+01 0.146407E+01    = 0.105970E+01 0.362234E+01 0.146450E+01
CURRENT  VELOCITY = -.140945E+00 0.452003E-01 -.778928E-02    = -.161950E+00 0.453175E-01 -.318225E-02
THE NTH TIME STEP =  600   THE CURRENT TIME = 0.300000E+01    =  600                                                    =  300
CURRENT  POSITION = 0.105680E+01 0.365037E+01 0.146404E+01    = 0.105890E+01 0.362256E+01 0.146448E+01                 = 0.105945E+01 0.360451E+01 0.147650E+01
CURRENT  VELOCITY = -.136754E+00 0.441644E-01 -.631635E-02    = -.157367E+00 0.449269E-01 -.185035E-02                = -.175405E+00 0.443394E-01 0.136786E-02
```

Table 3.2 shows a comparison of the different numerical schemes between Predictor-Corrector method and Gear's method (DC03AD).
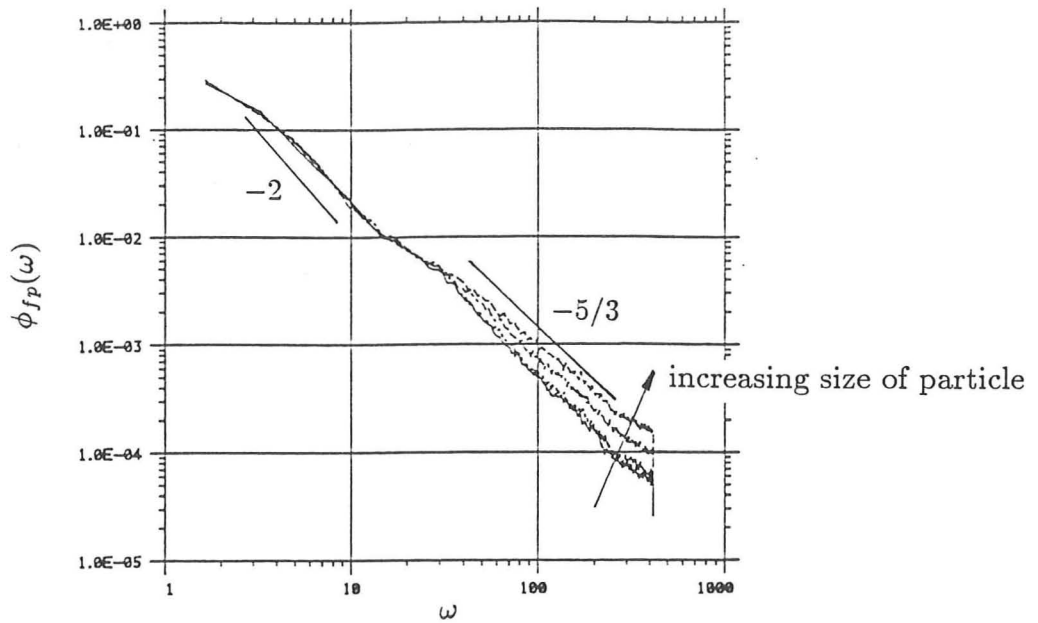
Fig. 3.8 Average Lagrangian velocity spectra of the fluid velocity at the location of a particle with relaxation time τ_p, $\phi_{fp}(\omega)$ with -2-slope if $\omega < \tau_p^{-1}$, and $-5/3$-slope if $\omega > \tau_p^{-1}$. For $\omega \ll \tau_p^{-1}$ this is the same as the Lagrangian spectrum.

$u_3(\mathbf{x}_p, t)$

$u_1(\mathbf{x}_p, t)$

(a)

(b)
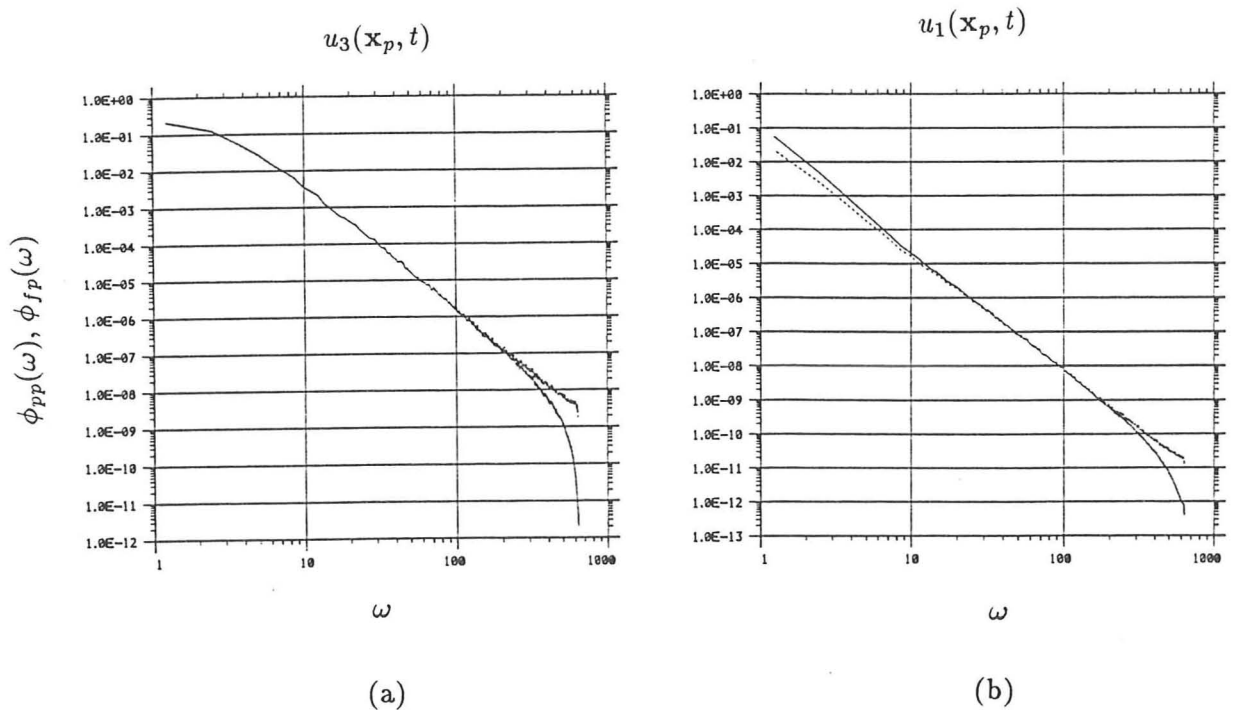
Fig. 3.9 Test the validity of the formula (3.3.23). —— is computed spectrum $\phi_{pp}(\omega)$ from the simulation of KS; $---$ spectrum of ϕ_{pp} obtained from the (3.3.23). (a) $W_g = 0.0$ and $\tau_p = 0.2$; (b) $W_g = 0.0$ and $\tau_p = 3.0$.
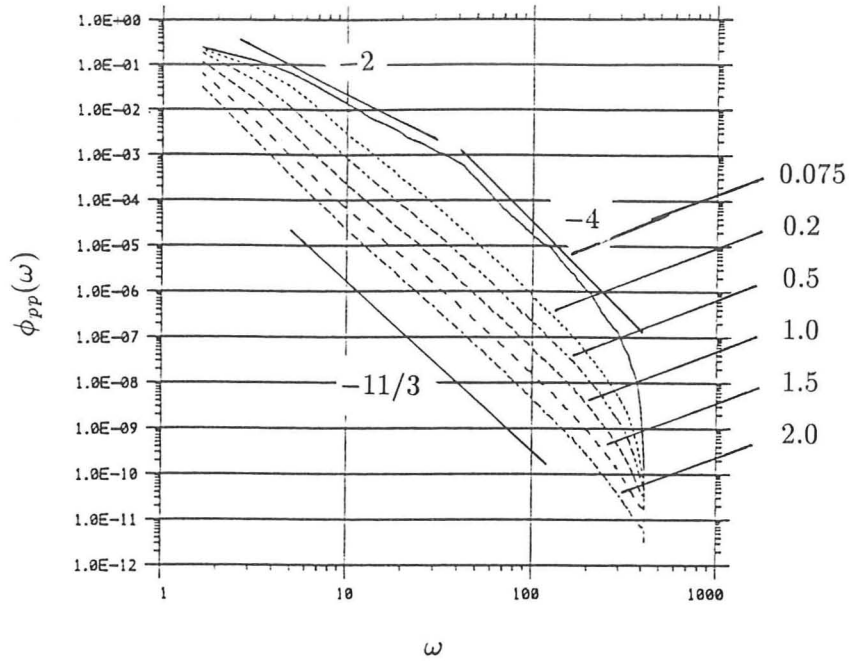
Fig. 3.10 Graphs show the spectra of $\phi_{pp}(\omega)$ with different particle time constants τ_p.
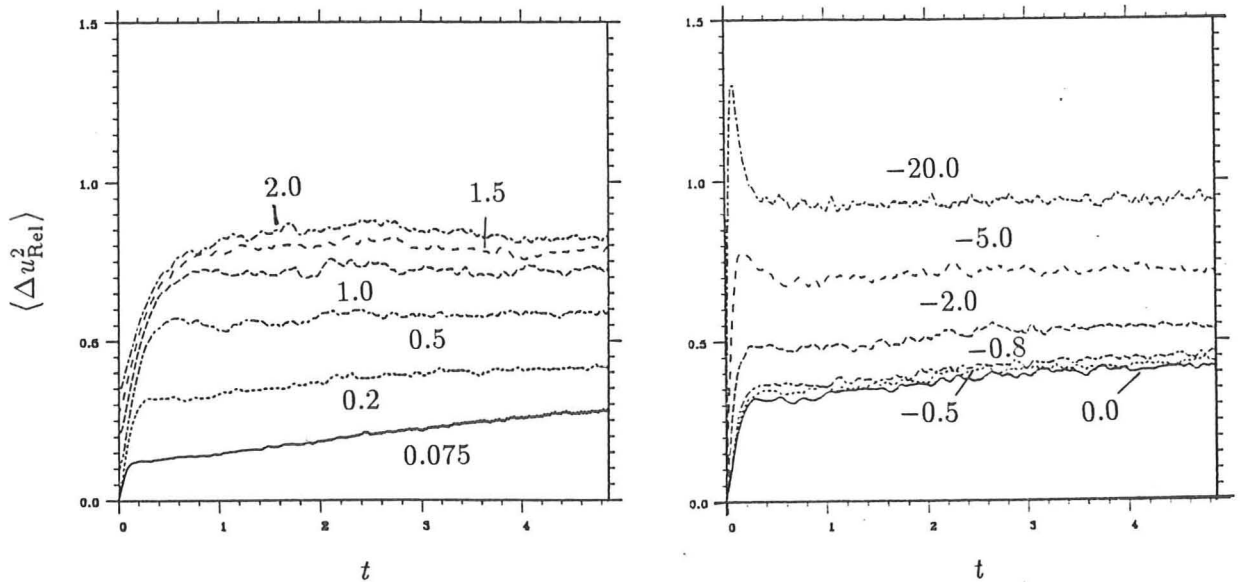
Fig. 3.11 The mean-square relative velocity $\langle \Delta u_{\text{Rel}}^2 \rangle$ are plotted against time t. (a) The settling time increases with increasing inertia parameter. Numbers indicate values of τ_p, $W_g = 0$. (b) The settling time does not depend on W_g. Numbers indicate values of W_g, $\tau_p = 0.2$.
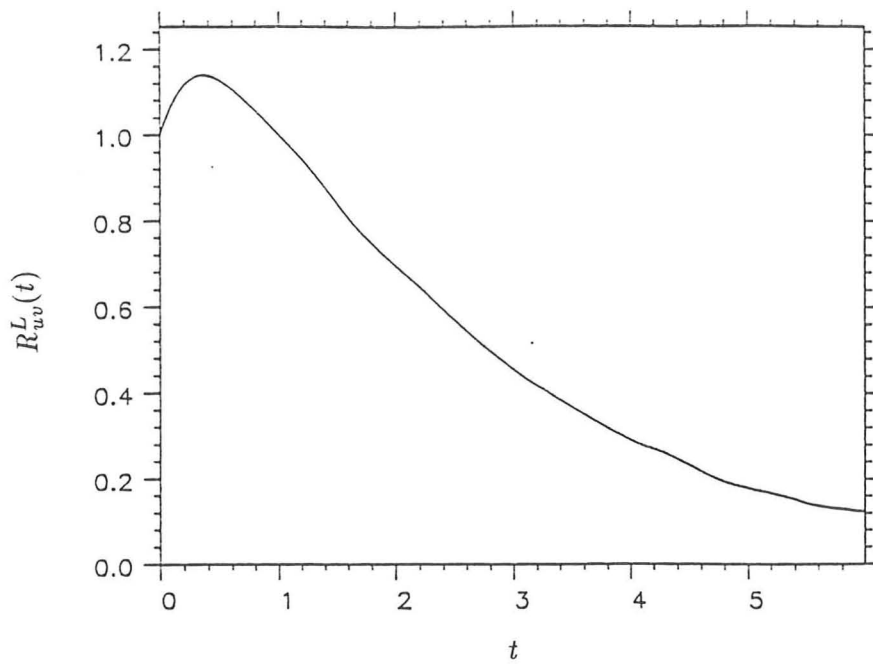
Fig. 3.12   Graphs show a typical plot of the velocity cross-correlation function $R_{uv}^L(t)$ between the particle and fluid element with $\tau_p = 0.4$ and $W_g = 0.0$.
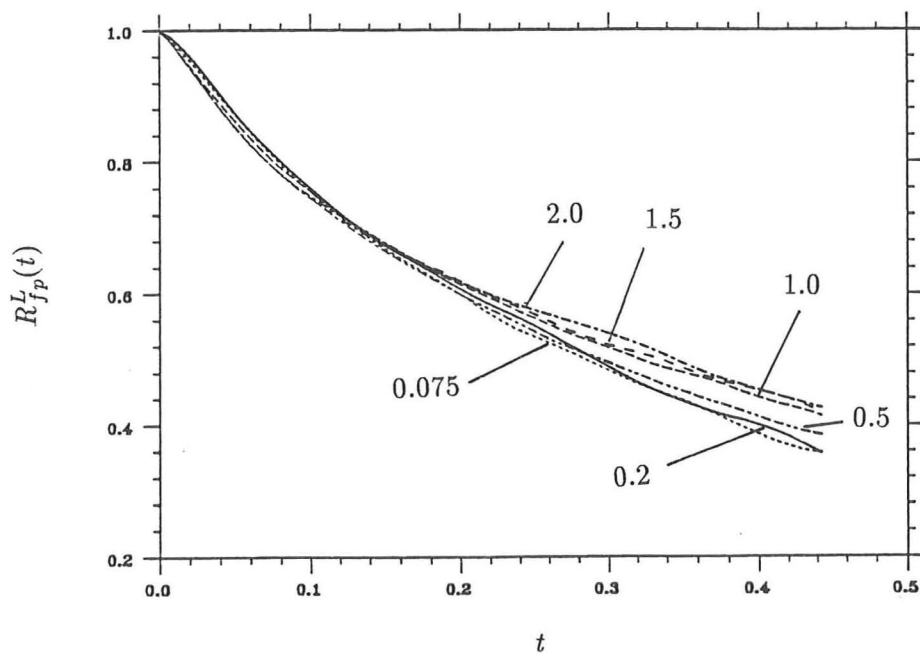
Fig. 3.13   Graphs show a comparison of the auto-correlation functions of the fluid velocity along the particle trajectories $R_{pf}^L(t)$. Numbers indicate values of τ_p with $W_g = 0.0$.
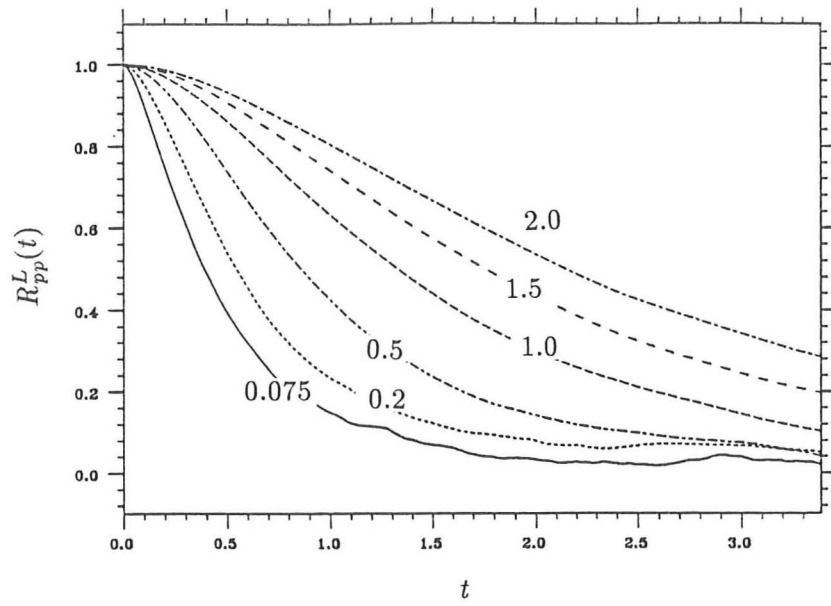
(a)
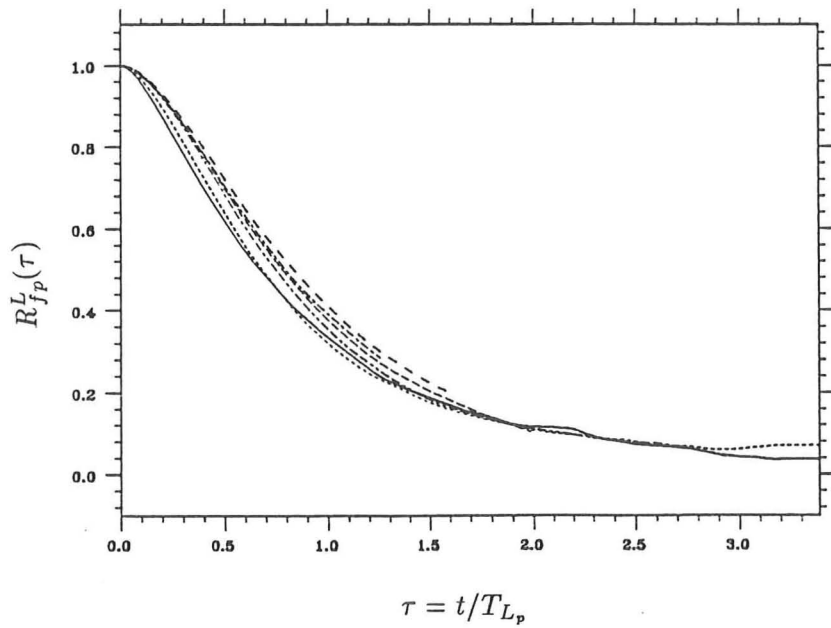
(b)

Fig. 3.14 (a) Graphs show the Lagrangian auto-correlation functions of the particle $R_{pp}^L(t)$. (b) The Lagrangian auto-correlation functions of the particle $R_{pp}^L(t)$ normalised by their integral time scales of the particle. Numbers indicate values of τ_p with $W_g = 0.0$.
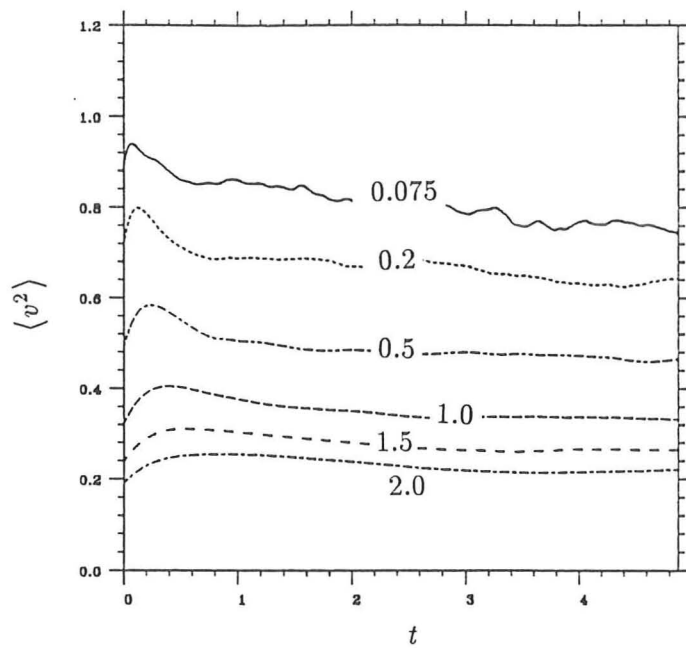
Fig. 3.15 Graphs show the mean-square fluctuating velocities of the particle. Numbers indicate values of τ_p with $W_g = 0.0$.
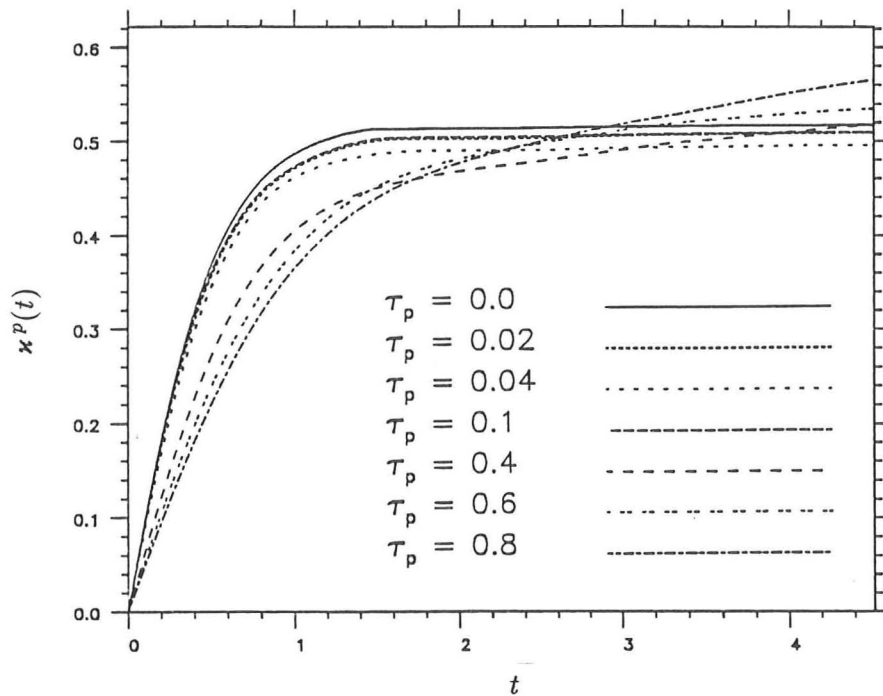
Fig. 3.16 Particle diffusivities $\varkappa_{ij}^p$ are plotted against time t. All curves rise from zero and eventually settle down to a fixed values.
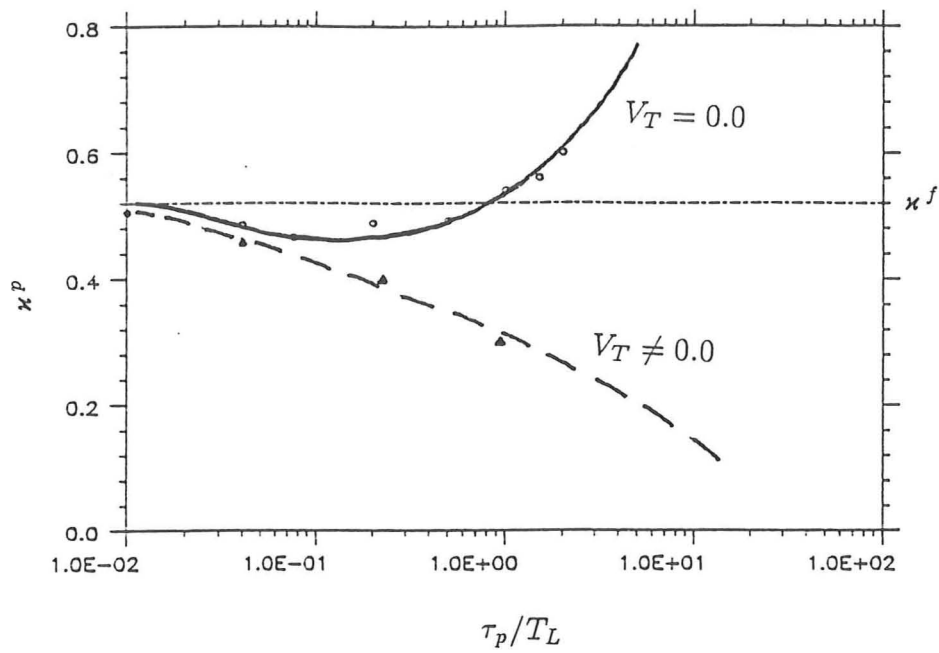
Fig. 3.17   Particle diffusivities $\varkappa_{ij}^p$ are plotted against particle time constant τ_p.
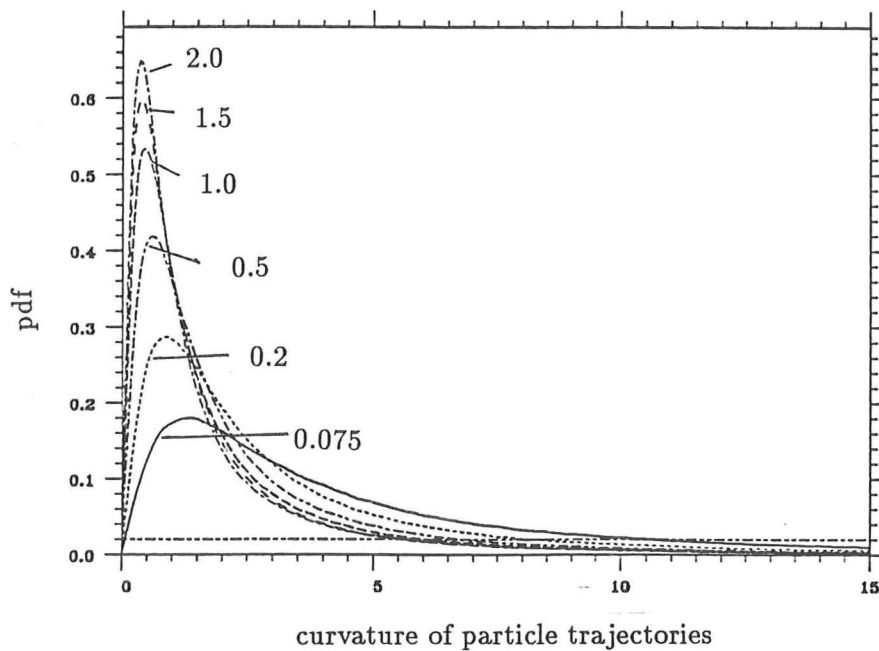
Fig. 3.18   Graphs show the pdf's of the curvature of the particle trajectories. Numbers indicate values of τ_p with $W_g = 0.0$.
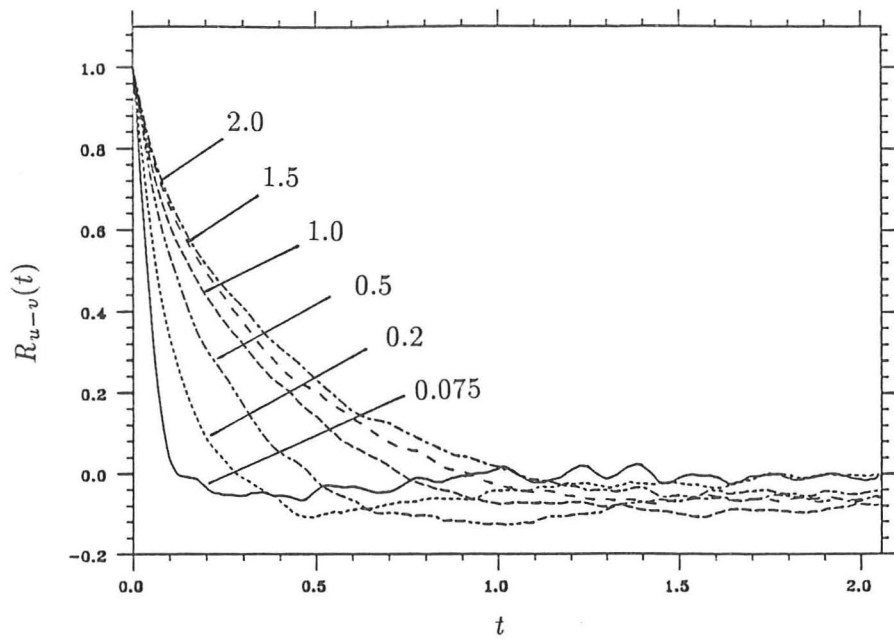
Fig. 3.19   Graphs show the auto-correlation functions of fluid-particle relative velocity. Numbers indicate values of τ_p with $W_g = 0.0$.
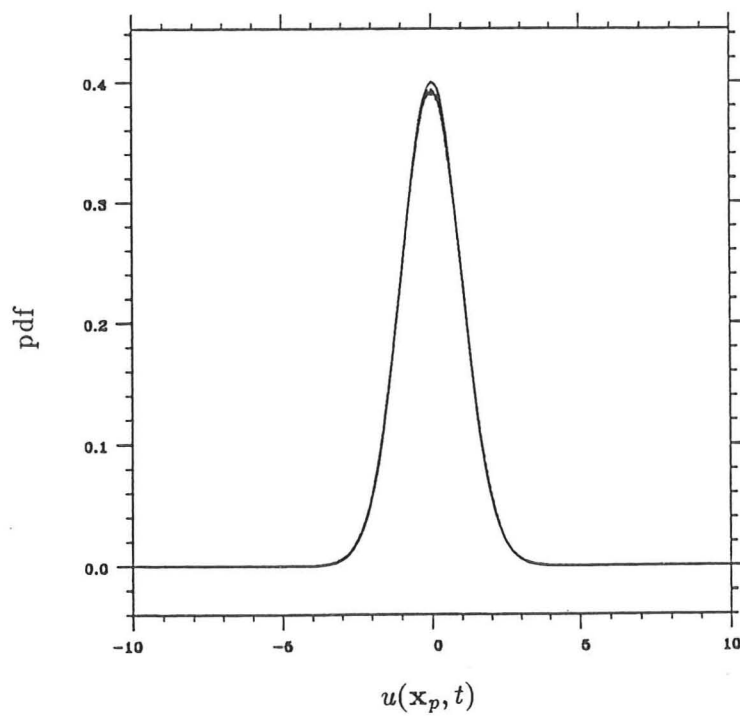
Fig. 3.20   Graphs show the pdf's of the velocity of the fluid as seen by the particle.
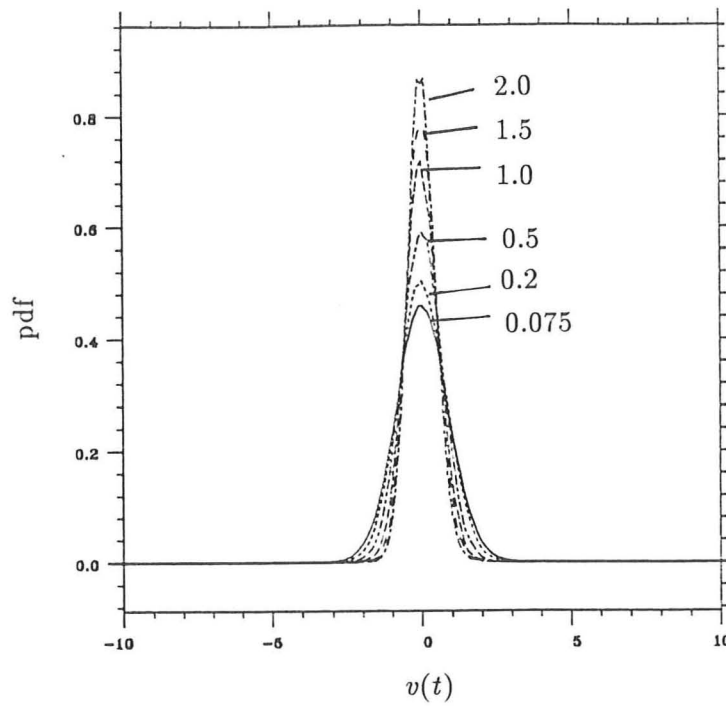
Fig. 3.21   Graphs show the pdf's of the velocity of the particle. Numbers indicate values of τ_p with $W_g = 0.0$.
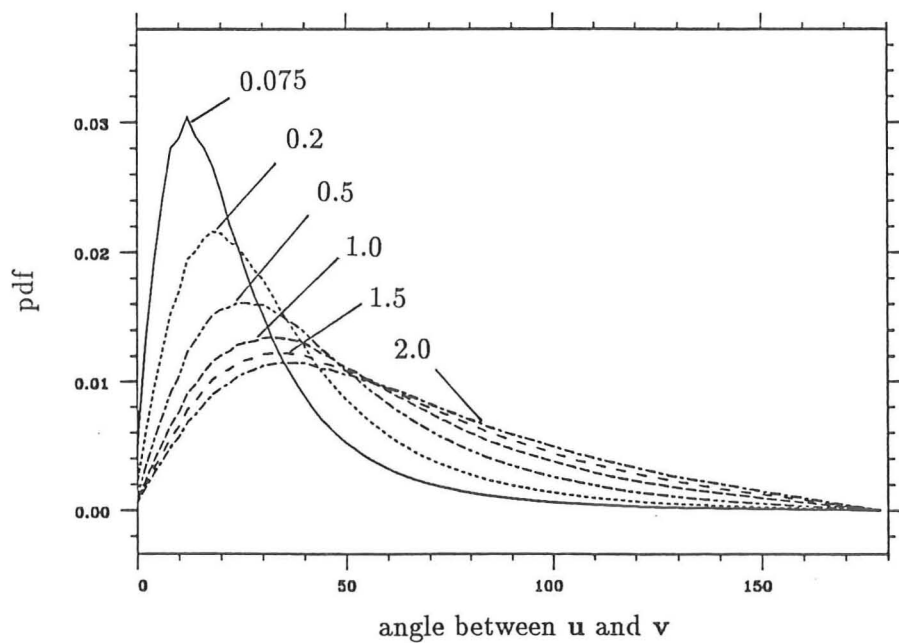
Fig. 3.22   Graphs show the pdf's of the angles between the velocity of the particle and that of fluid. Numbers indicate values of τ_p with $W_g = 0.0$.
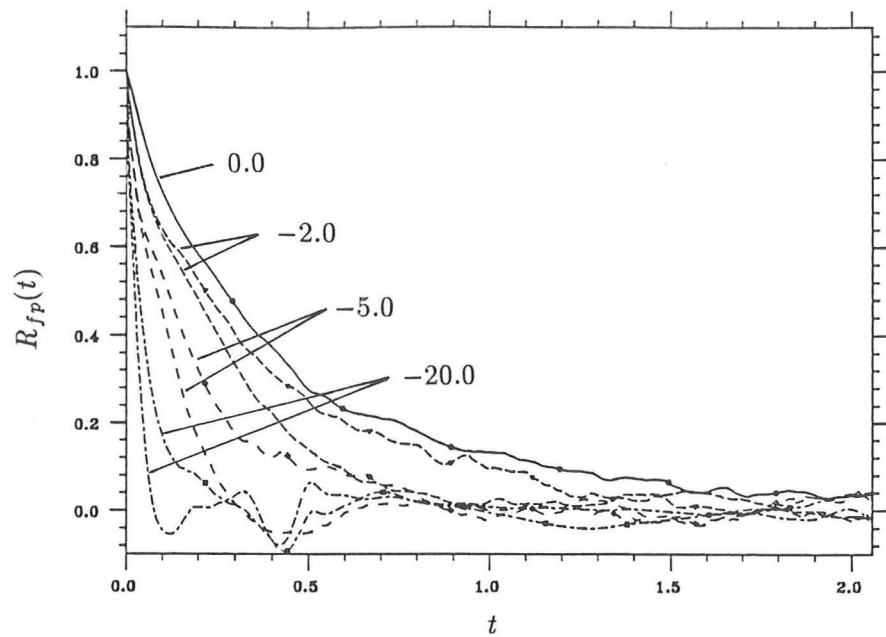
Fig. 3.23   Graphs show the auto-correlation functions of fluid velocity as seen by the particle. Numbers indicate different values of W_g with fixed value of $\tau_p = 0.2$. Lines without and with symbols correspond to parallel and perpendicular correlations to the direction of W_g respectively.
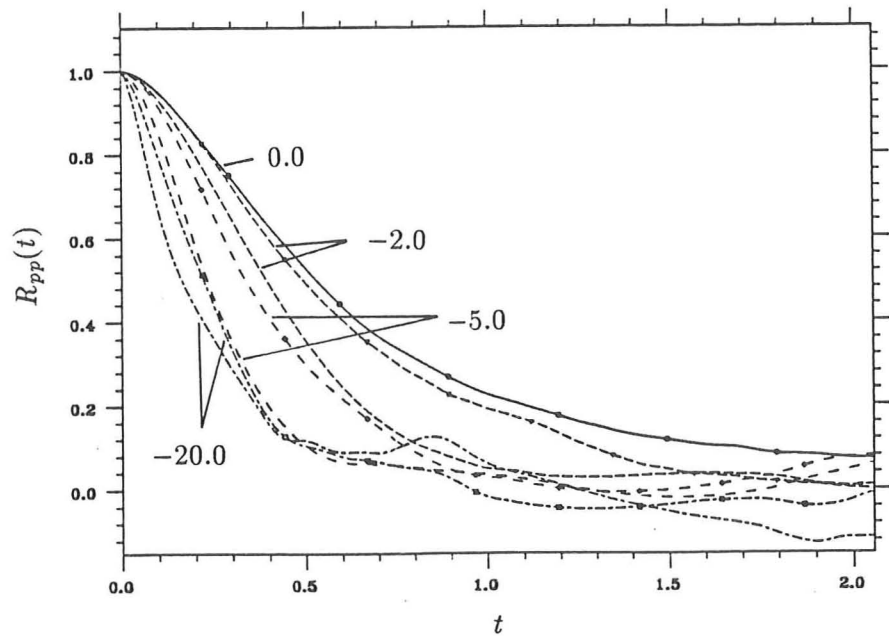
Fig. 3.24   The velocity auto-correlation functions of the particle are plotted with fixed value of $\tau_p = 0.2$. R^L_{pp} decreases as W_g increases and numbers indicate different values of W_g.
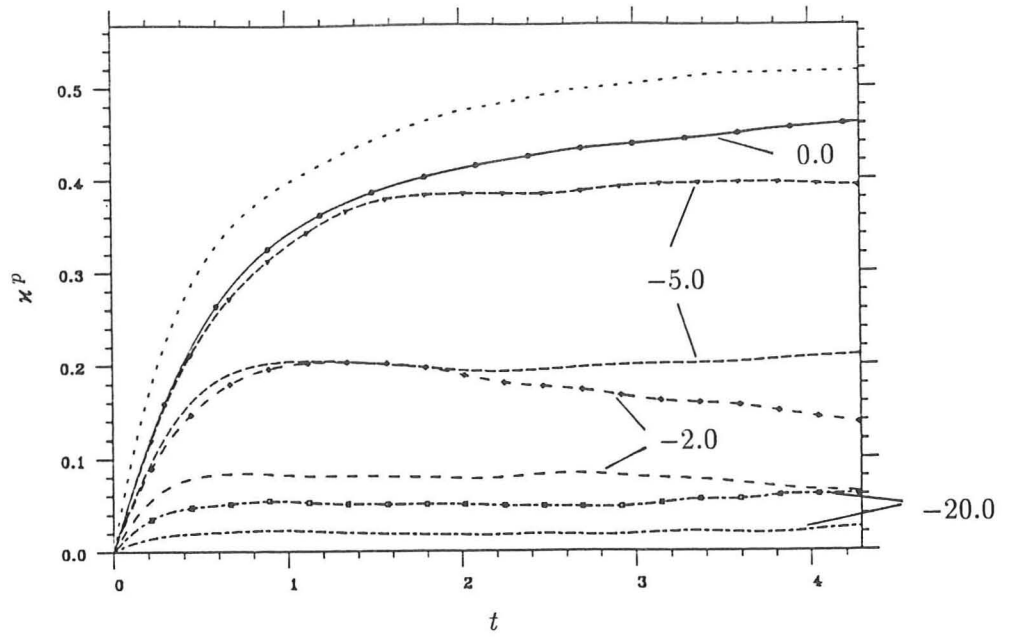
Fig. 3.25 The particle diffusivities are plotted with fixed value of $\tau_p = 0.2$. $\varkappa^p(\infty)$ decreases as W_g increases and numbers indicate different values of W_g. Lines without symbols parallel and lines with symbols perpendicular to the direction of W_g and numbers indicate different values of W_g.
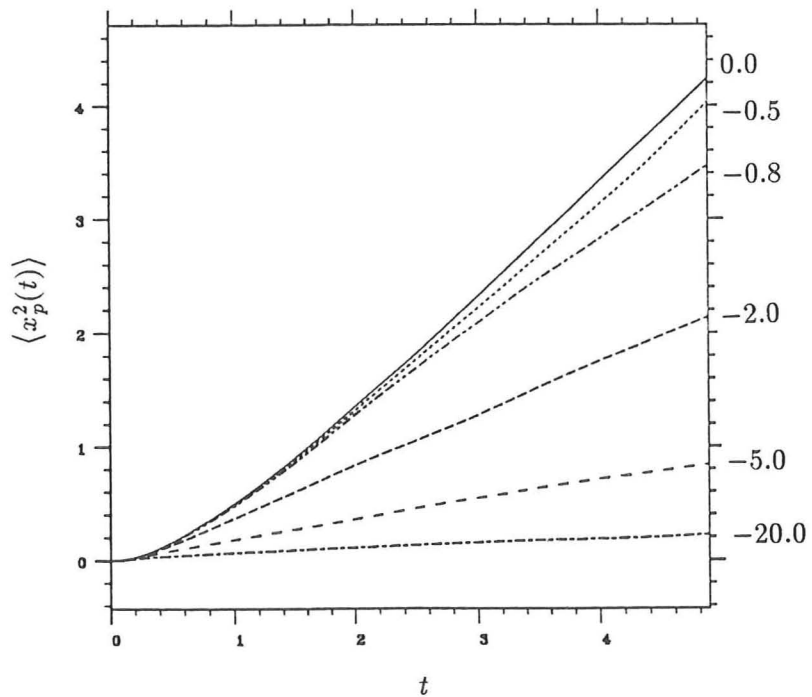
Fig. 3.26 Graphs show the mean square displacements of the particle with fixed value of $\tau_p = 0.2$. $\langle x_p^2 \rangle$ decreases as W_g increases and numbers indicate different values of W_g.
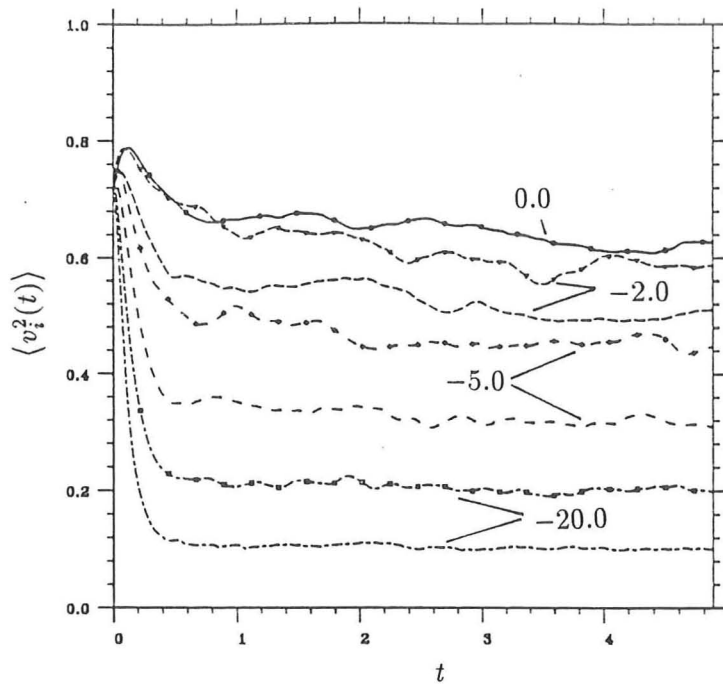
Fig. 3.27 Graphs show the mean-square fluctuating velocities of the particle with fixed value of $\tau_p = 0.2$, lines without symbols parallel and lines with symbols perpendicular to the direction of W_g and numbers indicate different values of W_g.
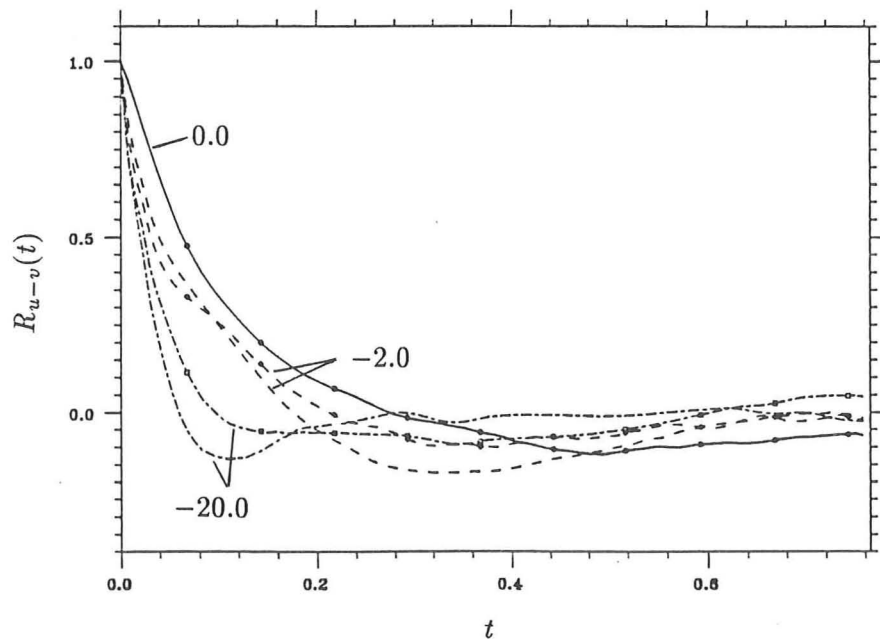
Fig. 3.28 Graphs show the correlation functions of relative fluid-particle fluctuating velocity with fixed value of τ_p, lines without symbols parallel and lines with symbols perpendicular to the direction of W_g and numbers indicate different values of W_g.
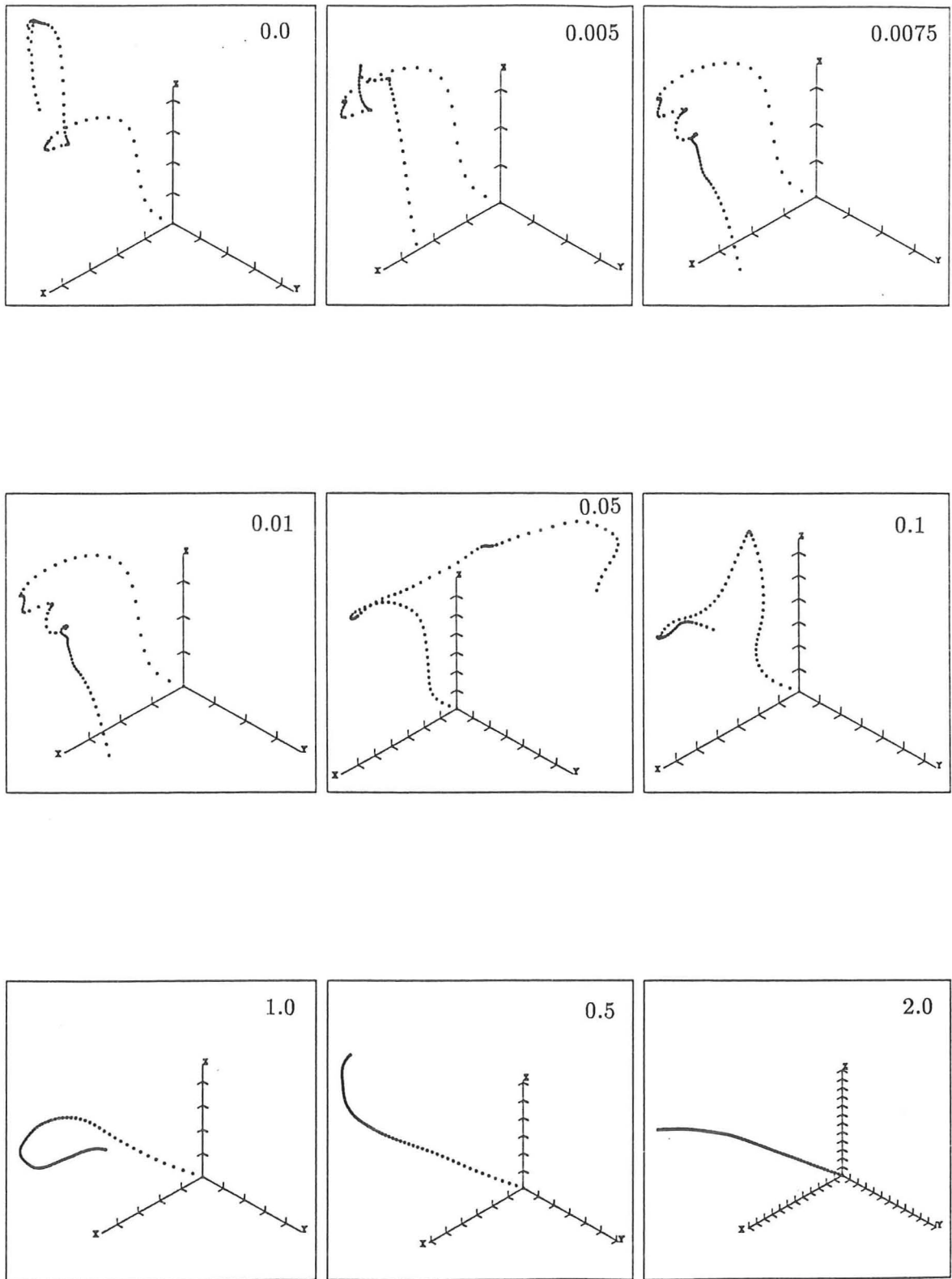
Fig. 3.29   Graphs shows the particle trajectories with the fixed value of $W_g = 0.0$ and different value of τ_p.
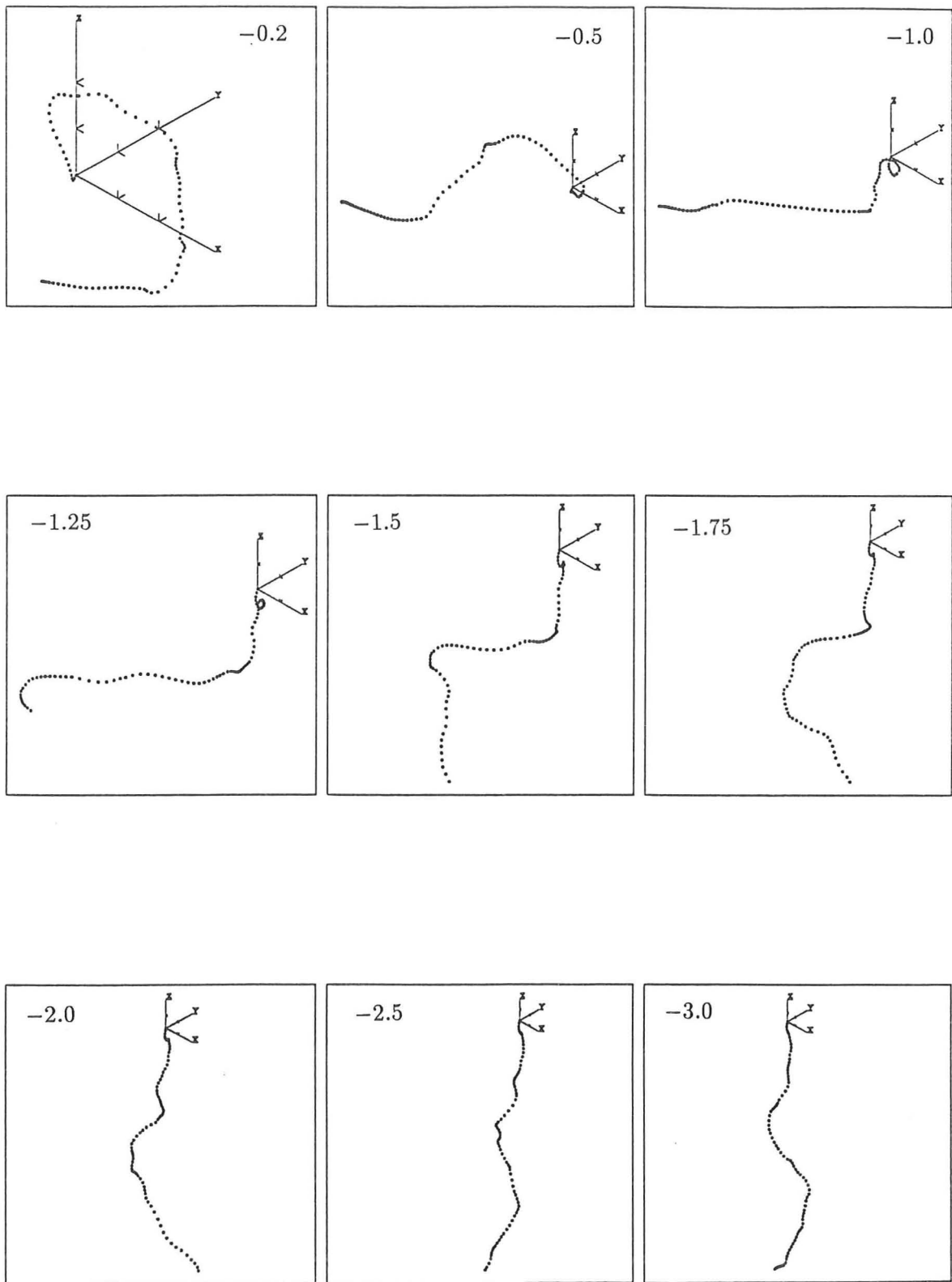
Fig. 3.30 Graphs shows the particle trajectories with the fixed value of $\tau = 0.01$ and different value of W_g.
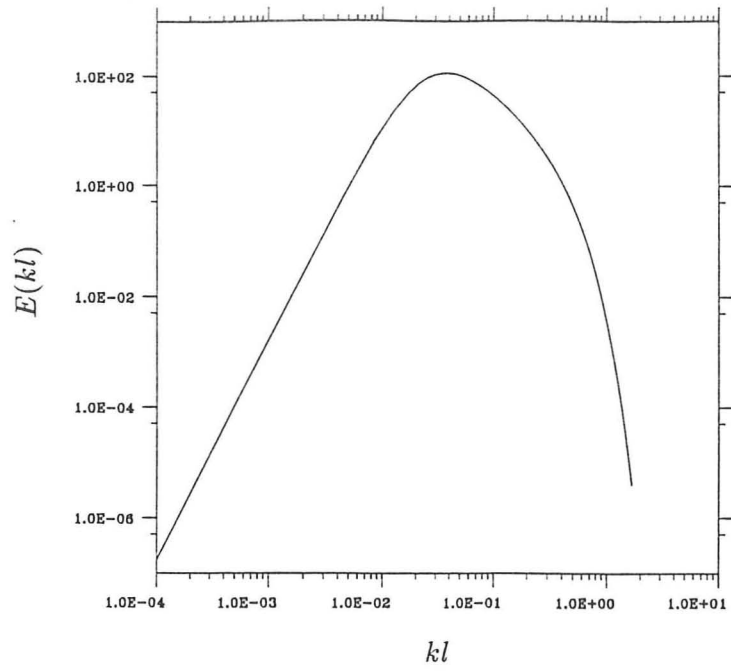
Fig. 3.31 Three-dimensional normalised turbulence energy spectrum for Snyder and Lumley's experiment.

(a)

(b)
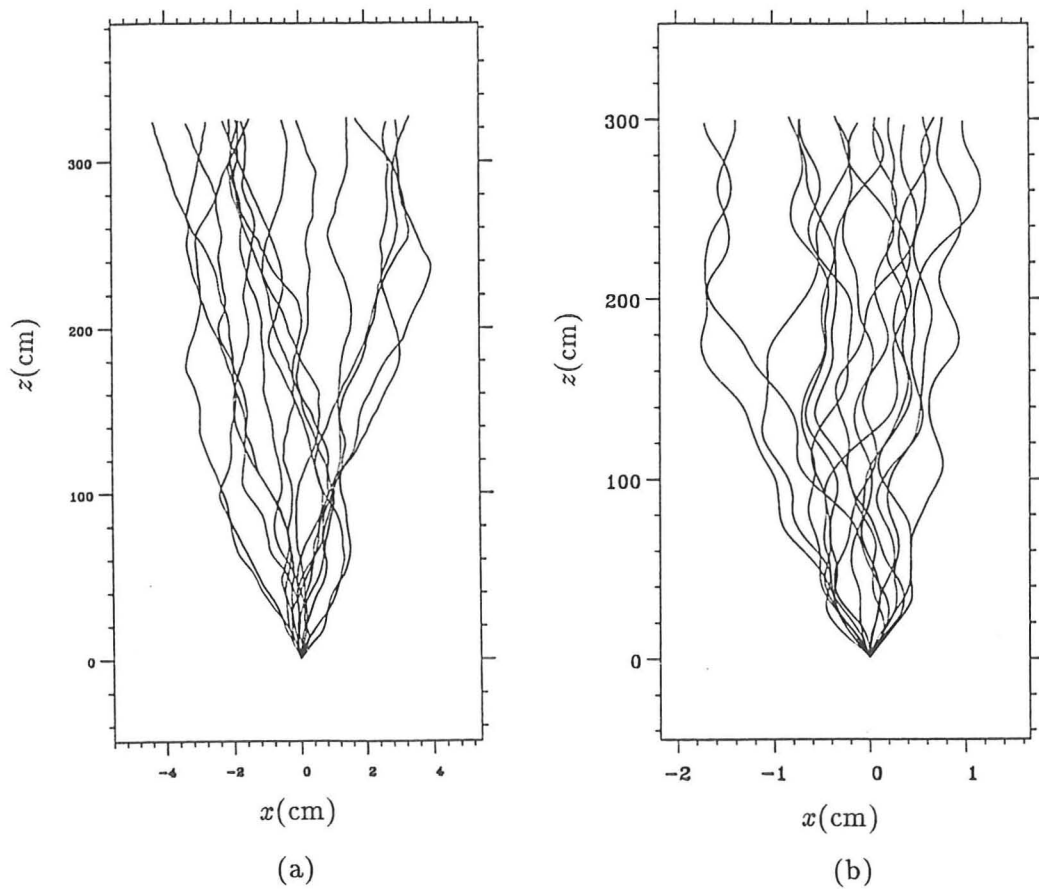
Fig. 3.32 Typical particle trajectories of Snyder and Lumley's experiment simulated by Kinematics simulation. (a) Hollow glass spheres; (b) Copper spheres.
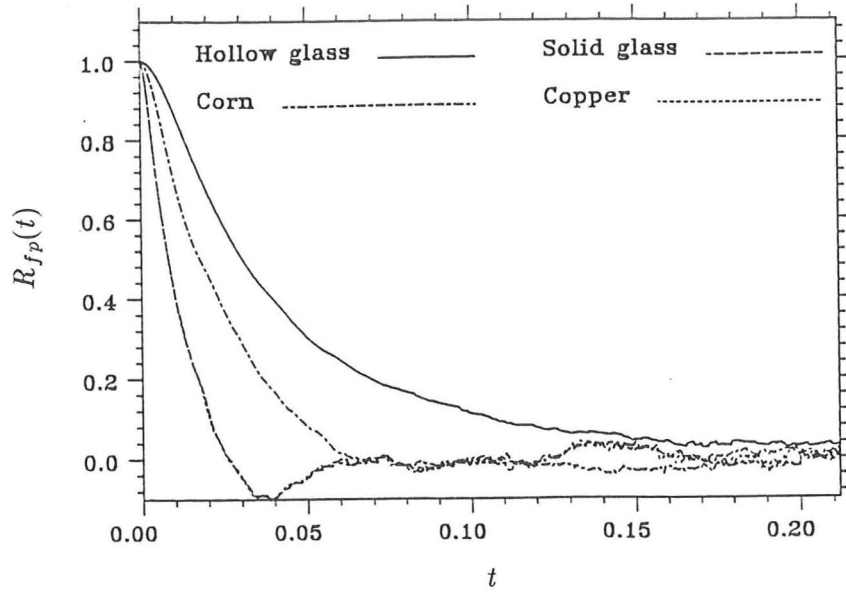
Fig. 3.33   Graphs shows the autocorrelation functions of the fluid velocities sampled by different type of particles of Snyder and Lumley's experiment simulated by Kinematics simulation.
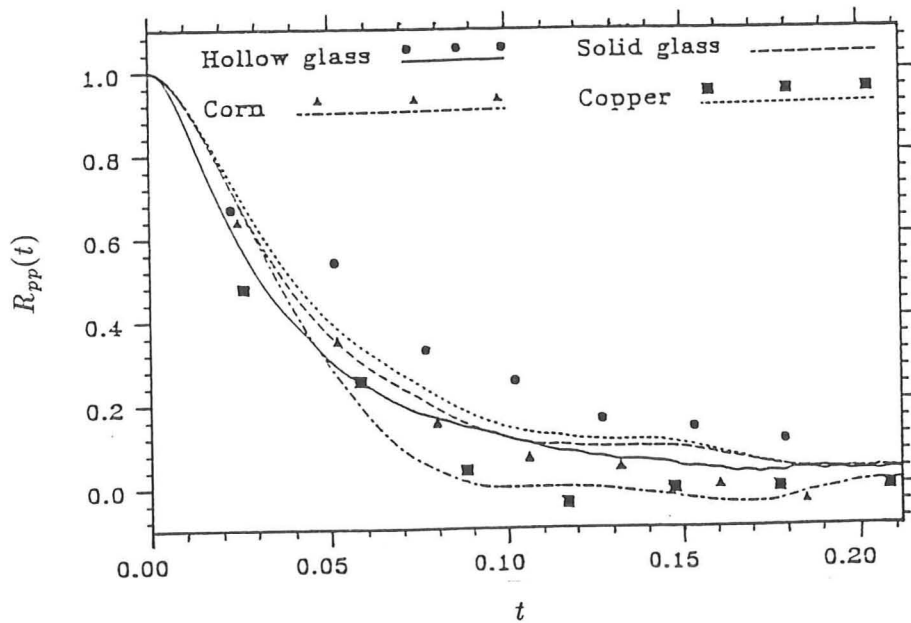
Fig. 3.34   Graphs shows the auto-correlation functions of the particle velocities of Snyder and Lumley's experiment (Symbols for experments and lines for simulations).
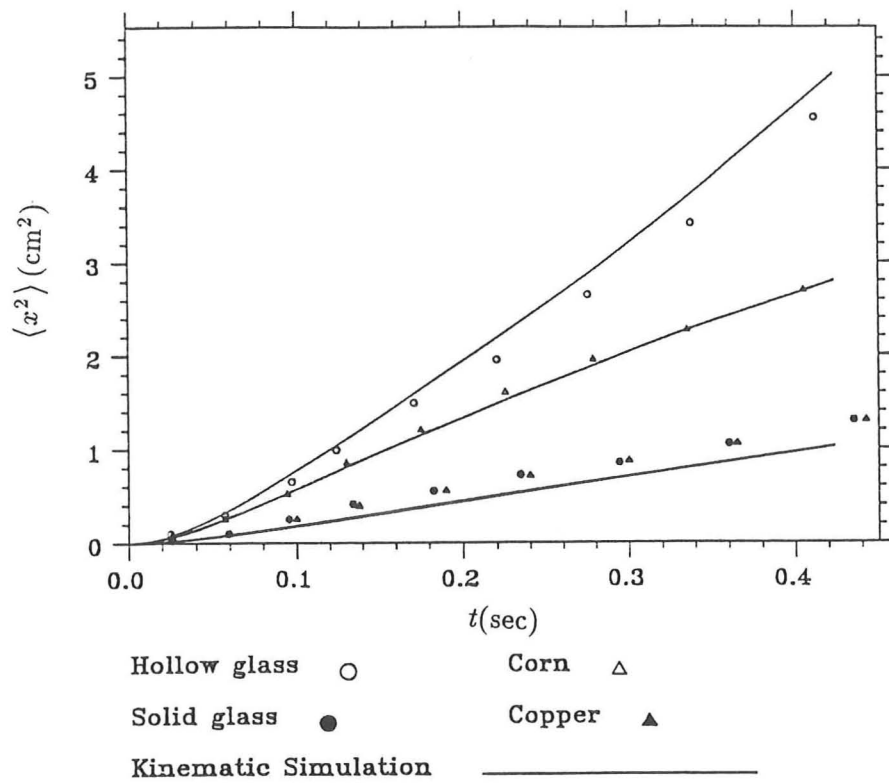
Fig. 3.35   Graphs shows the mean square displacements of the particle of Snyder and Lumley's experiment (Symbols for experments and lines for simulations).
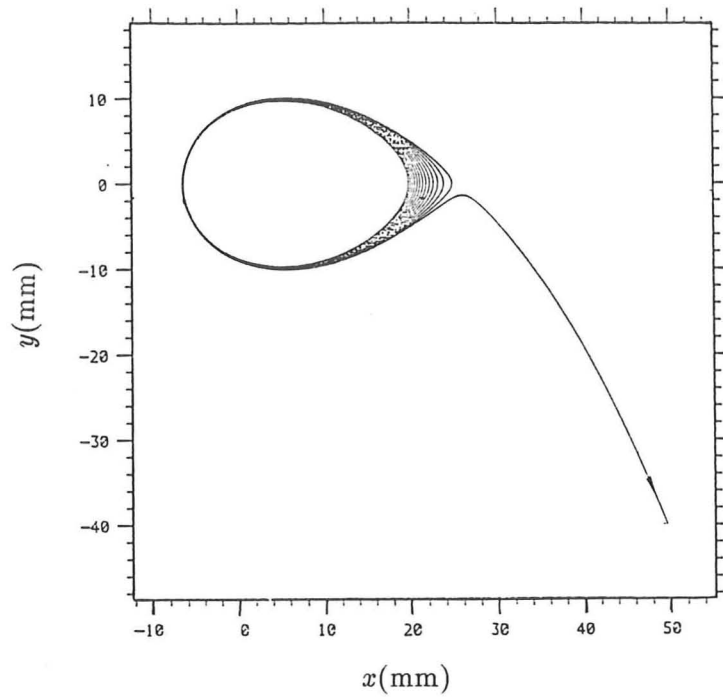
Fig. 3.36 Graph shows a typical dense particle trajectory in a Rankine vortex by Perkins and Hunt (1986).
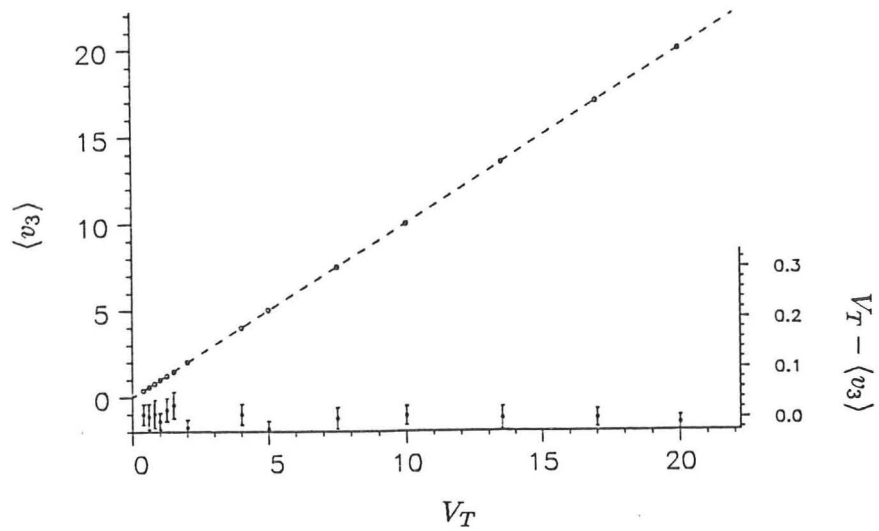
Fig. 3.37 Simulation results for asymptotic average settling velocity $\langle v_3 \rangle$ against still-fluid settling velocity V_T; particle time constant $\tau_p = 0.0$: ○ ○, $\langle v_3 \rangle$; ◊ ◊, different in settling velocity $V_T - \langle v_3 \rangle$. Error bars show possible statistical error with one standard error of the mean.
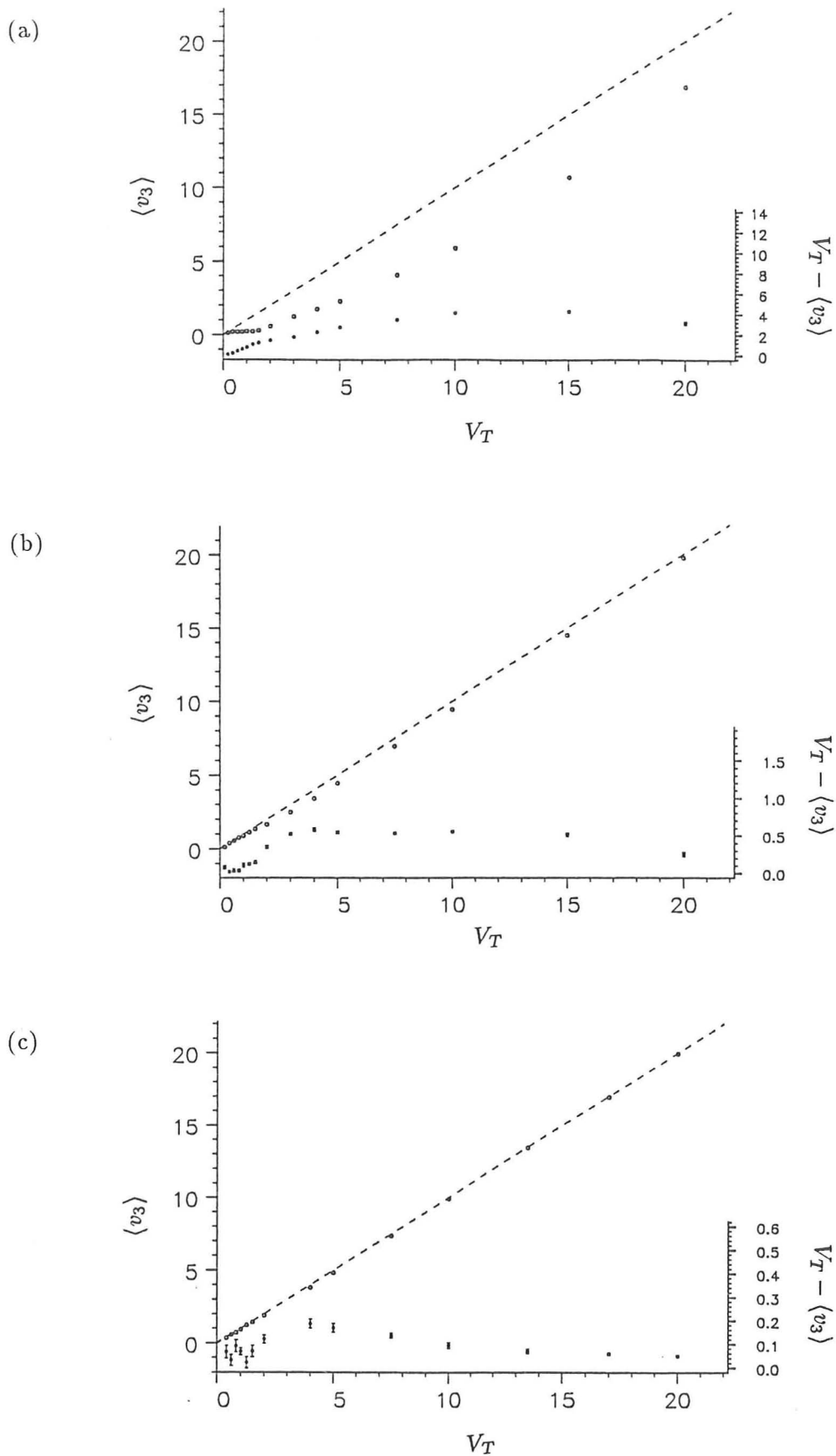
Fig. 3.38 Simulation results for asymptotic average settling velocity $\langle v_3 \rangle$ against still-fluid settling velocity V_T. (a) $\gamma = 0.0$; (b) $\gamma = 2.65$; (c) $\gamma = 833.0$, all with gravity $g = 0.0$: ∘ ∘, $\langle v_3 \rangle$; ◊ ◊, different in settling velocity $V_T - \langle v_3 \rangle$. Error bars show possible statistical error with one standard error of the mean.
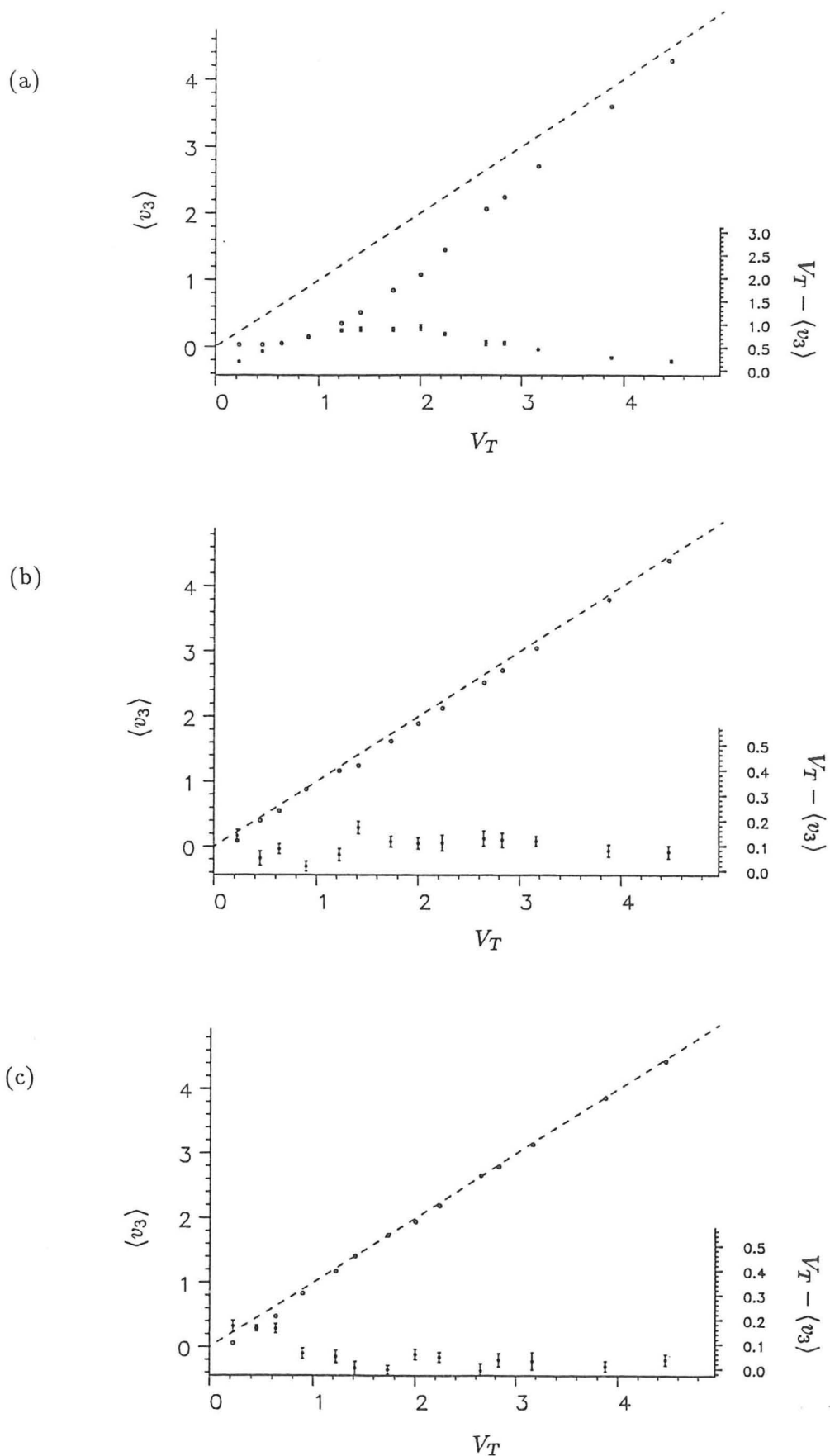
Fig. 3.39 Simulation results for asymptotic average settling velocity $\langle v_3 \rangle$ against still-fluid settling velocity V_T. (a) $\gamma = 0.0$; (b) $\gamma = 2.65$; (c) $\gamma = 833.0$, all with drag coefficients equal to constant $g/V_T^2 = 10.0$: ○ ○, $\langle v_3 \rangle$; ◊ ◊, different in settling velocity $V_T - \langle v_3 \rangle$. Error bars show possible statistical error with one standard error of the mean.
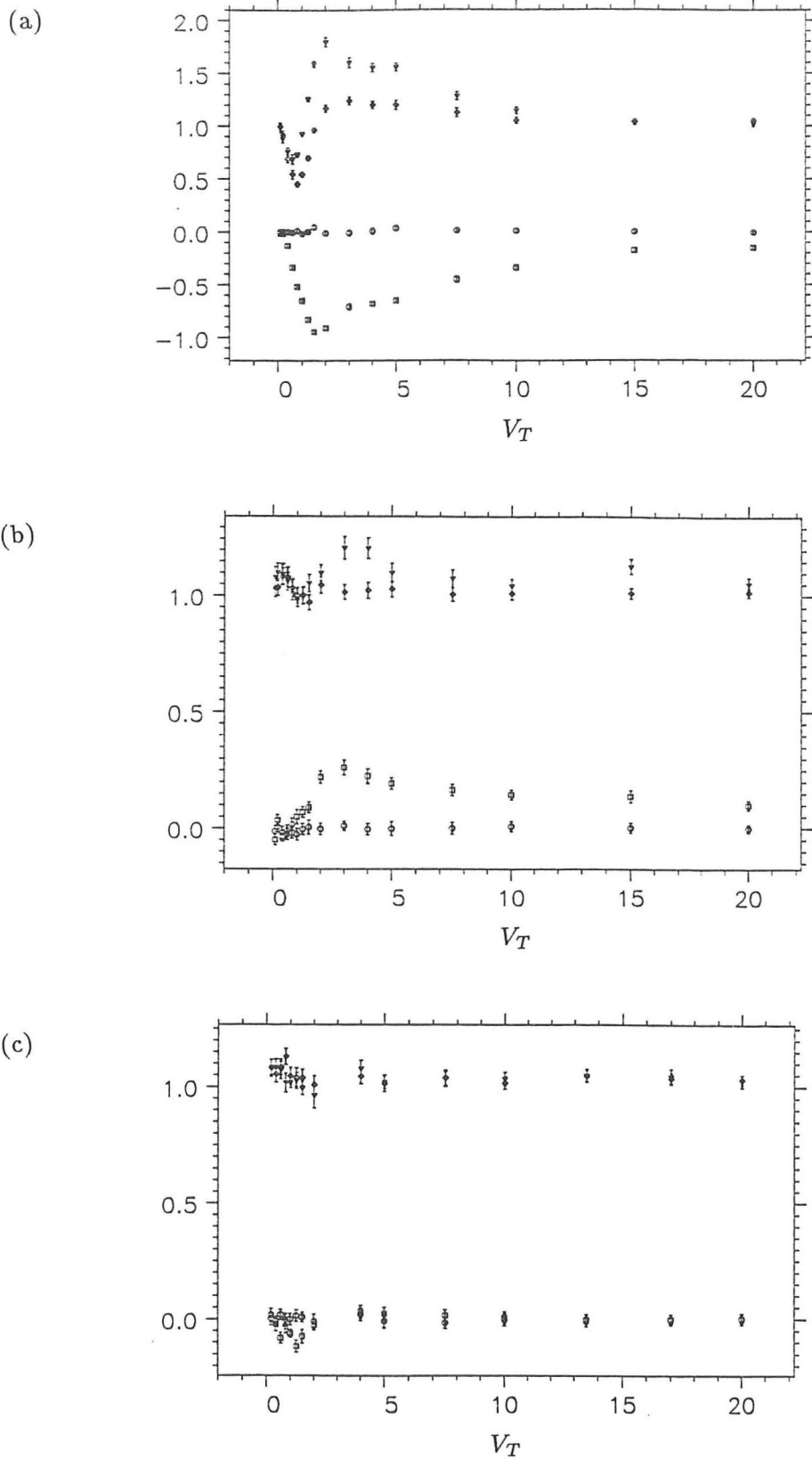
Fig. 3.40 Simulation results for asymptotic mean and mean square velocity fluctuations along the particle trajectories against still-fluid settling velocity V_T. (a) $\gamma = 0.0$; (b) $\gamma = 2.65$; (c) $\gamma = 833.0$, all with $g = 10.0$. $\circ$ $\circ$, $\langle u_1(\mathbf{x}_p) \rangle = \langle u_2(\mathbf{x}_p) \rangle$; $\square$ $\square$, $\langle u_3(\mathbf{x}_p) \rangle$; $\Diamond$ $\Diamond$, $\langle u_1^2(\mathbf{x}_p) \rangle = \langle u_2^2(\mathbf{x}_p) \rangle$; ∇ ∇, $\langle u_3^2(\mathbf{x}_p) \rangle$. Error bars show possible statistical error with one standard error of the mean.
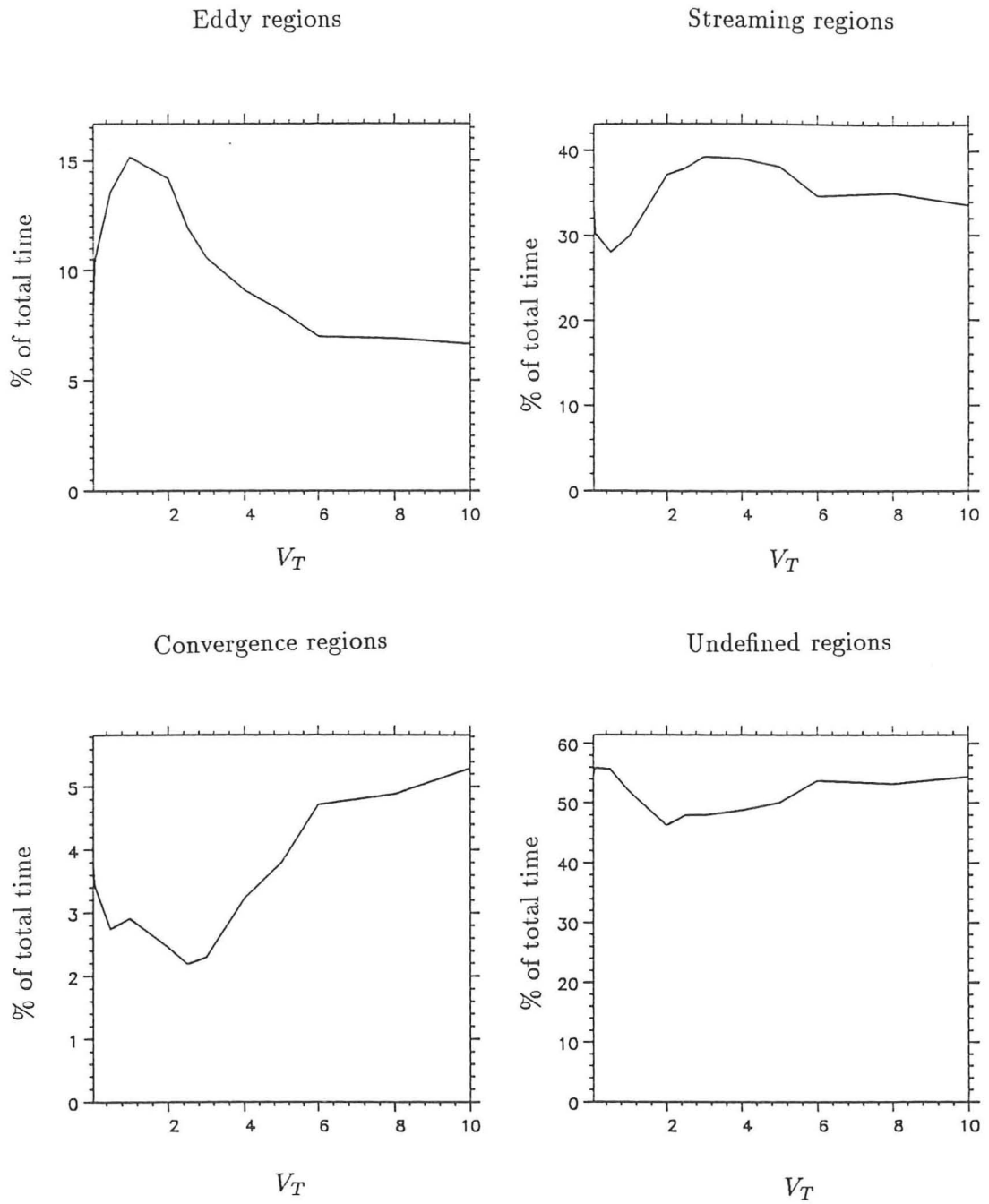
Fig. 3.41   The percentage of the total time spent by the bubble ($\gamma = 0.0$) at different regions of the flows plotted against settling velocity V_T with $g = 10.0$.
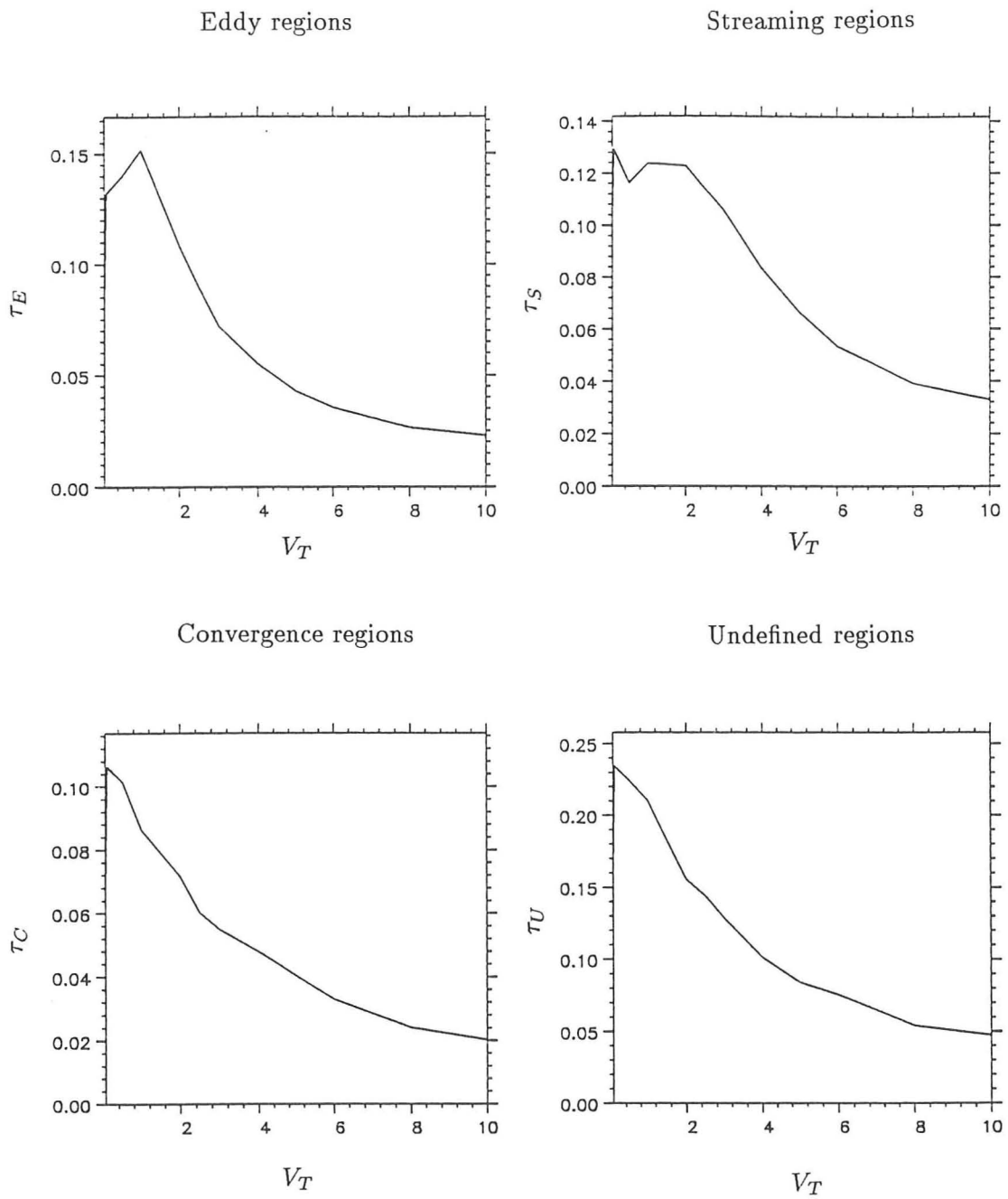
Fig. 3.42   The resident time of the bubble ($\gamma = 0.0$) at different regions of the flows plotted against settling velocity V_T with $g = 10.0$.
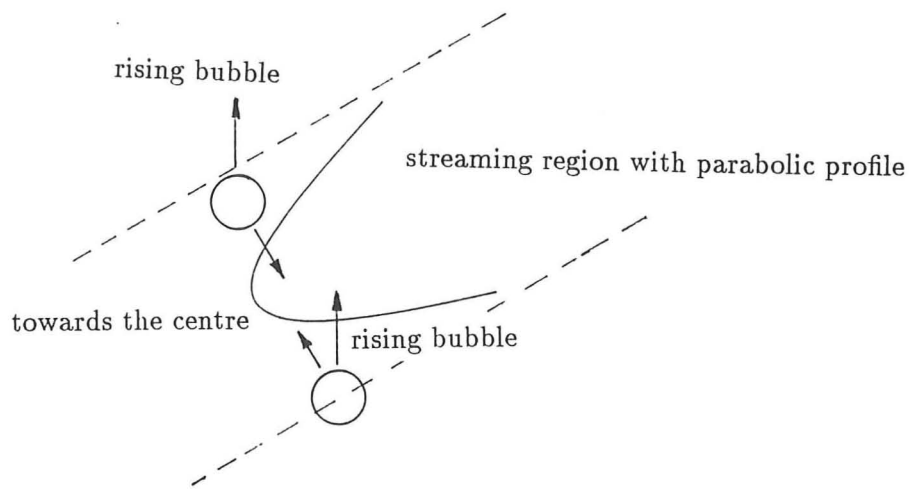
(a)
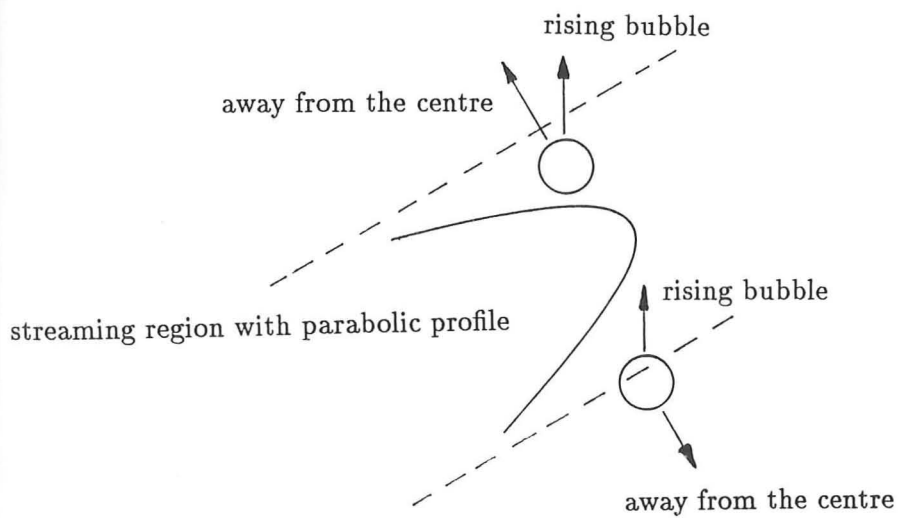
(b)

Fig. 3.43   The trajectories of the bubble move in a streaming region with parabolic profile.
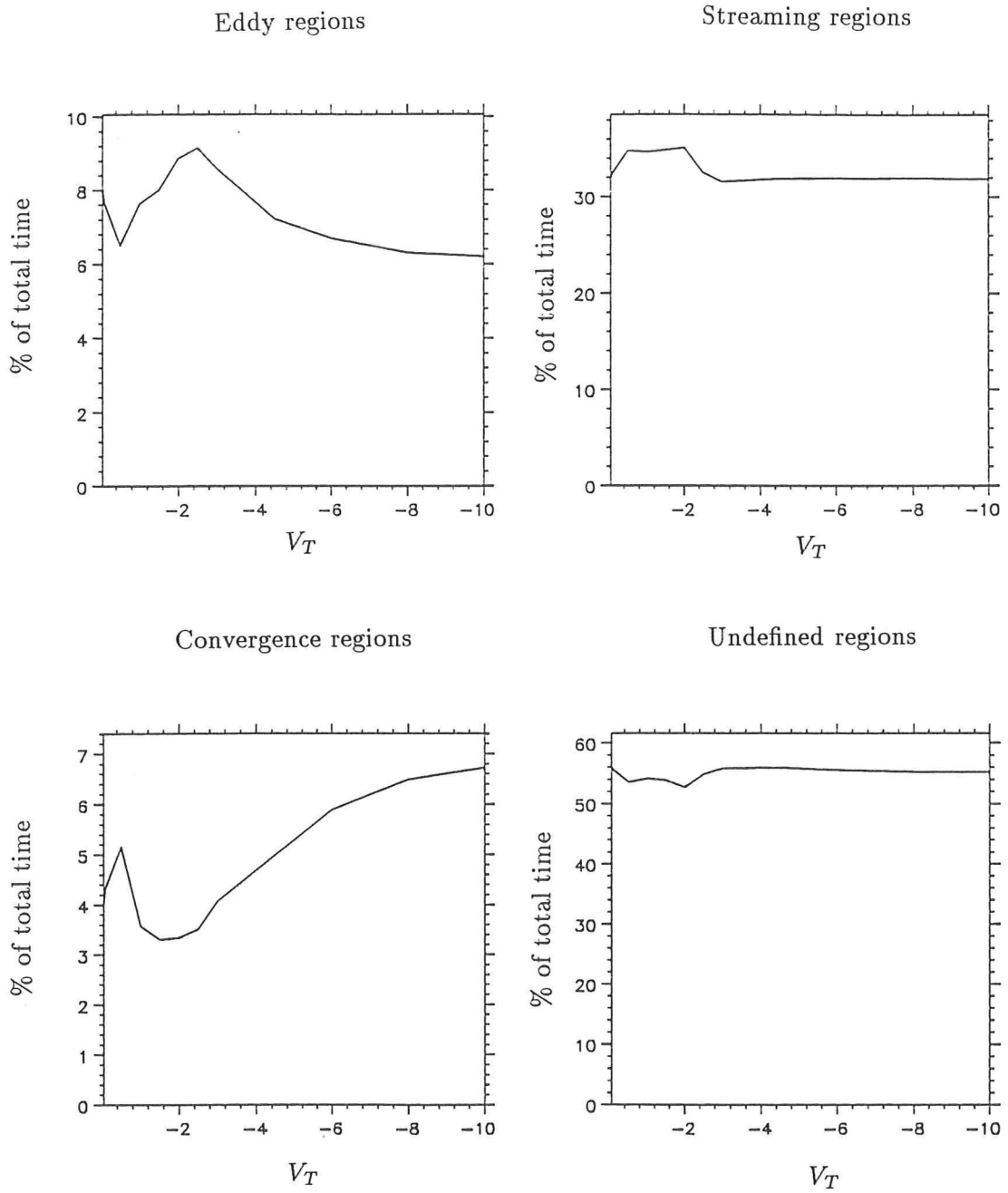
Fig. 3.44 The percentage of the total time spent by the particle ($\gamma = 2.65$) at different regions of the flows plotted against settling velocity V_T with $g = 10.0$.
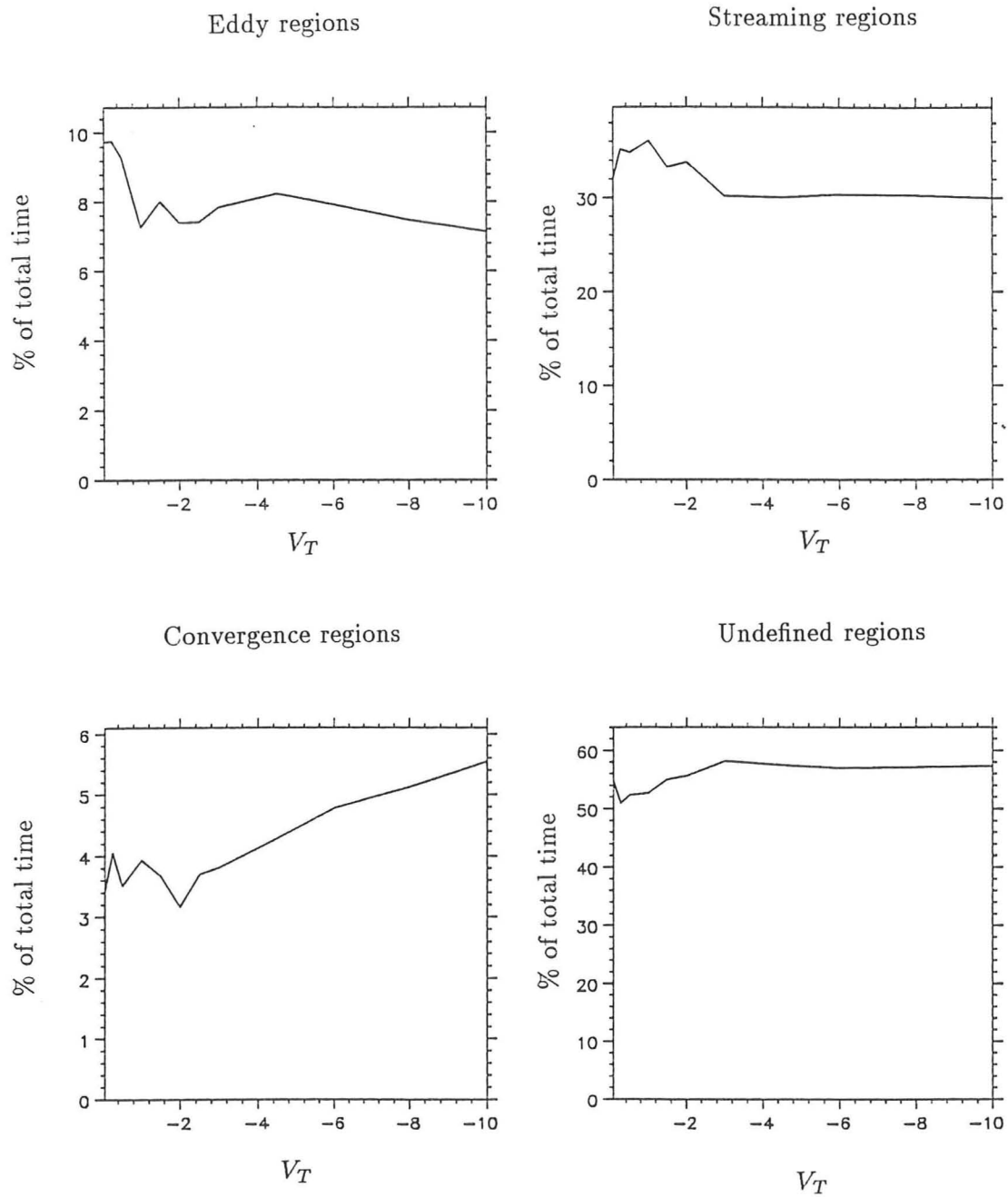
Fig. 3.45 The percentage of the total time spent by the dense particle ($\gamma = 833.0$) at different regions of the flows plotted against settling velocity V_T with $g = 10.0$.
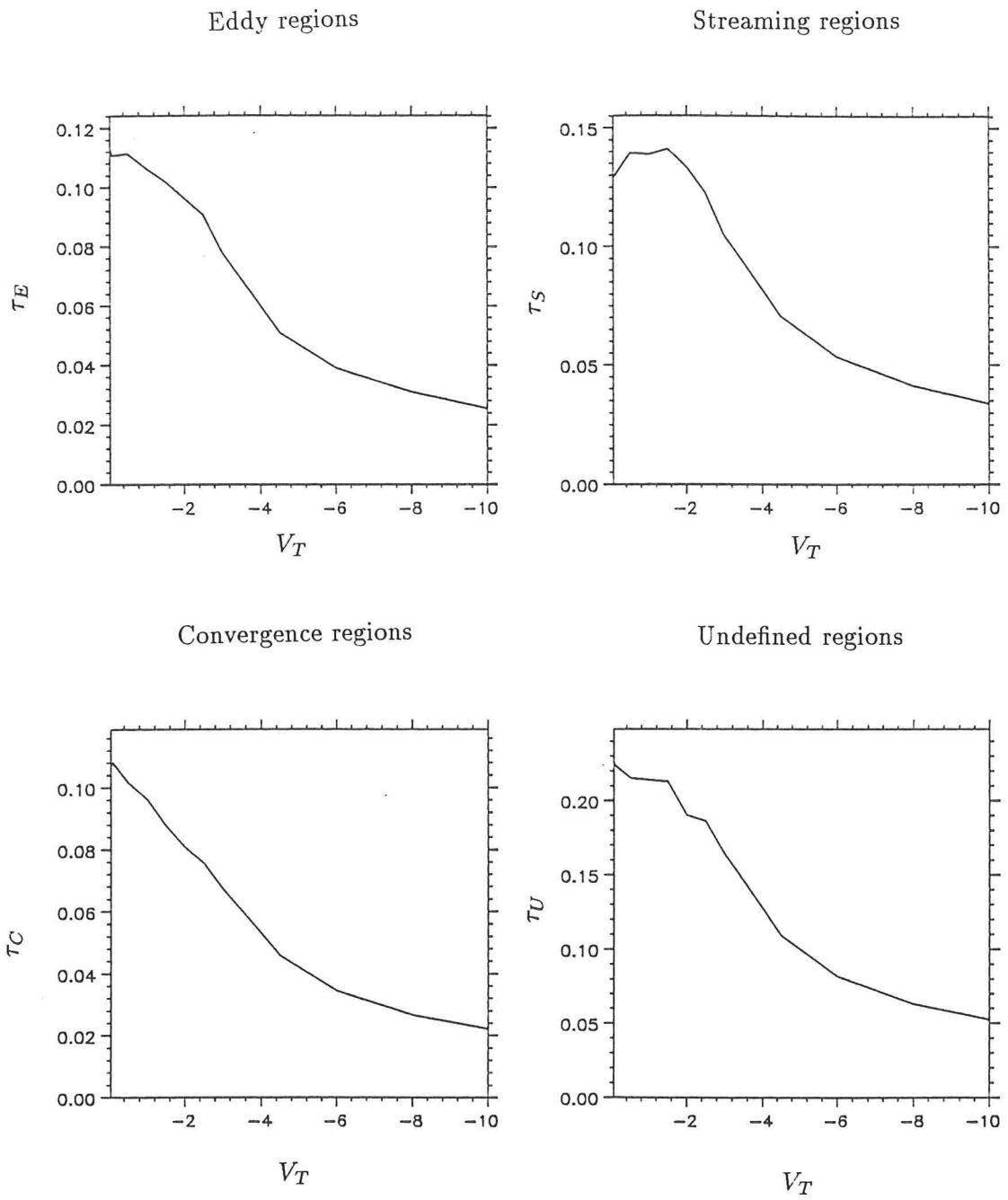
Fig. 3.46 The resident time of the particle ($\gamma = 2.65$) at different regions of the flows plotted against settling velocity V_T with $g = 10.0$.
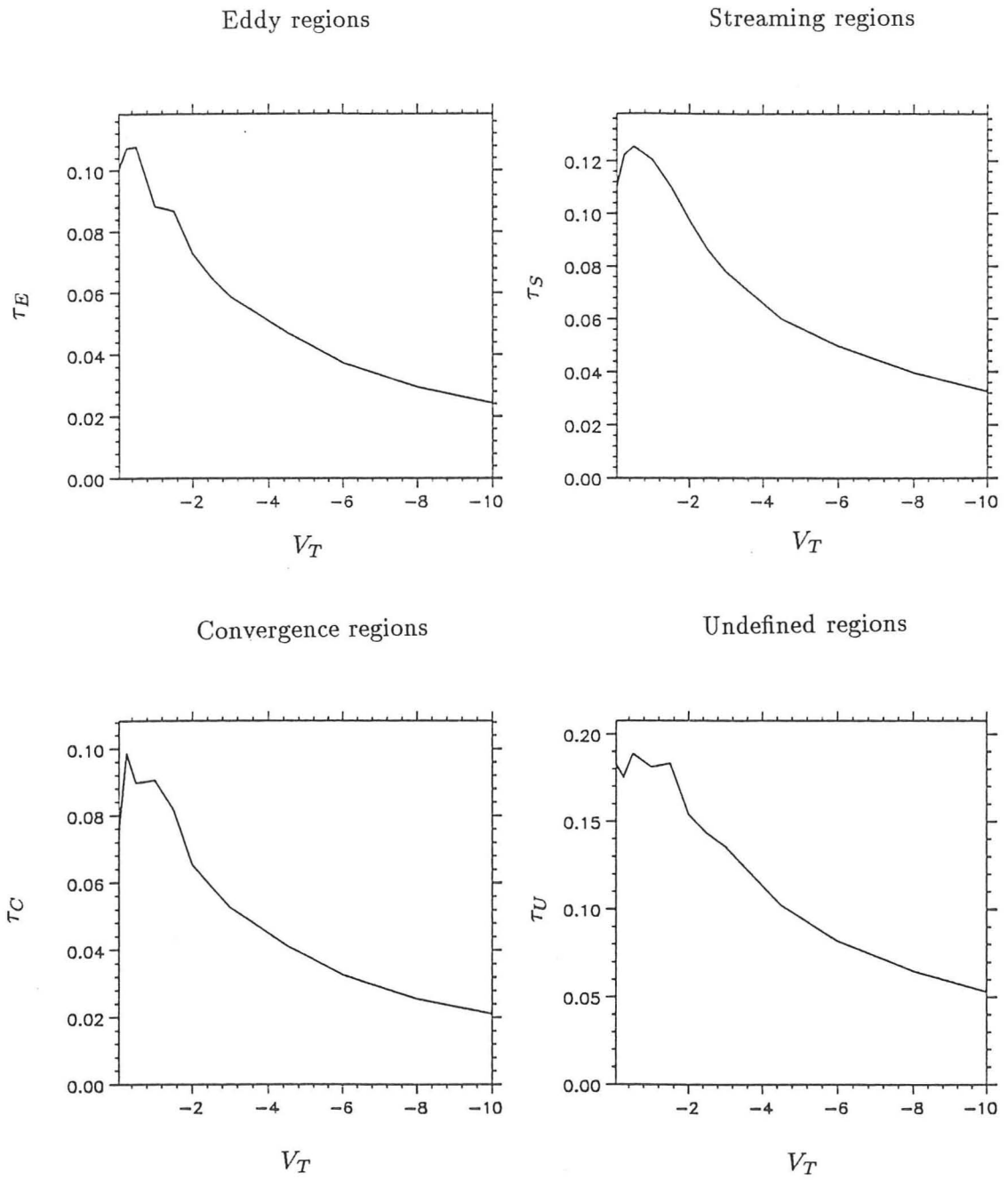
Fig. 3.47   The resident time of the dense particle ($\gamma = 833.0$) at different regions of the flows plotted against settling velocity V_T with $g = 10.0$.

Shear Flow Turbulence Structure by Rapid Distortion Theory

The aim of this chapter is to produce an *simulation* and a *conceptional picture* of shear flow in order to predict and explain how fluid and (eventually) solid particles *move*.

4.1 Introduction

The structure of shear flow turbulence has been the subject of intense, mostly experimental, studies over many years. The major experimental tools have been the hot-wire anemometer and flow visualization techniques, but even with statistical sampling methods; experimentally these techniques cannot give detailed enough information to describe the wide range of temporal and spatial scales of the three-dimensional turbulent eddies present in the flow. Inevitably, interpretation of the limited data is uncertain, and there are substantial differences of opinion as to what are the essential features.

The problem of homogeneous turbulent shear flow has been examined analytically by several investigators. Several of these (e.g. Pearson 1959, Townsend 1956) have explained the generation of Reynolds stress in turbulence in terms of a theory based largely on the idea that a parcel of turbulent fluid whose scale is small compared with the shear zone width is subjected to a local uniform mean strain rate. Townsend (1956) conjectured that (a) a state of structural equilibrium of the turbulence would be attained under the action of an irrotational, constant mean strain rate, and that (b) this state is approximately the same as that produced by a uniform plane (rotational) shearing motion with equal strain rate. Moffatt (1967) suggested that this neglect of the rigid body rotation may be unjustifiable if the process of vortex line stretching is less efficient when the rigid body rotation is present. Several authors developed a 'weak turbulence' analysis (Rapid Distortion Theory) for shear flow in which the self-interaction of the turbulent field was neglected, and computed the linearized response of an initially isotropic turbulence subjected to a sudden uniform gross shear. The results show qualitative features of turbulence strikingly like those observed in real shear flow (as shown later).

Beginning with Theodorsen (1952), a number of investigators, have proposed that turbulent

boundary layers are largely composed of horseshoe vortices (hairpins). These structure are thought to originate at the wall and to extend to the outer layers with the inclination angle of about 45° to the flow direction. But the crucial role in the near-wall region plays in the turbulence dynamics was first conclusively demonstrated by Kline *et al.* (1967). They used hydrogen bubbles generated by an electric wire to visualize the flow in a low-speed water channel. The technique revealed the presence of low-speed streaks (Figure 4.1) of fairly regular spanwise spacing. Intermittently, the streaks begin to oscillate and then break up in a fairly violent motion, a "burst" (Figure 4.2). Kline *et al.* (1967) proposed a conceptual model for bursting. In this model the fundamental dynamical mechanisms sorted out are the life-up of low-speed streak and stretching of spanwise vorticity producing a thin shear layer that is inflectionally unstable.

Townsend (1970) shows that an eddy model consisting of a pair of roller eddies inclined at about 30° to the flow direction is generally consistent with two-point correlation functions calculated from the rapid-distortion theory. He suggests the double-roller eddies as the dominant structures in turbulent shear flows. In the recent study of a fully developed turbulent channel flow which is conducted using a database generated by the Large-Eddy simulation by Moin and Kim (1985). It is shown that away from the wall the distortion of the inclination angle of vortical structures inclined at 45° to the wall. Similar hairpins have been found in *homogeneous* turbulent shear using Direct Numerical simulation flow by Rogers and Moin (1987), and from the observations of hairpin eddies with and without the wall, they concluded that hairpin structure are a prevalent, if not universal aspect of an turbulent shear flow. Hence, these study indicate that deformation of sheets of spanwise vorticity by random velocity fluctuations and stretching by the mean rate of strain are sufficient ingredients for the generation of the hairpins. Also the study of homogeneous shear flow by Lee *et al.* (1987) showed that high shear rate alone is sufficient for generation of the streaky structures similar to those in the wall region of turbulent channel flow and presence of a solid boundary is not necessary.

The shear flow chosen to be modelled is the homogeneous, turbulent shear flow. This flow contains the complicated coupling of turbulent and mean velocity fields which is characteristics of most natural and engineering turbulent flows, but it has a simplicity of statistical homogeneity. Furthermore, a considerable amount of experimental data describing the field was available (Champagne *et al.* 1970, Harris *et al.* 1977), which can be used for comparison.

The objective of this study is to use rapid distortion theory together with Kinematic Simulation to examine the response of homogeneous turbulence to suddenly imposed mean shear and to determine if their organized structure, is similar to those found in turbulent boundary layers (Moin and Kim 1985, Lee *et al.* 1987). These findings should reaffirm the relevance of

homogeneous "building-block flows" and of their detailed study en route to understand more complex flows. In §4.2, the mathematical development of RDT is briefly summarised. In §4.3 a brief description of the method of simulation for KS in shear flow is presented; the results of the simulation (spectra, turbulent intensities, length scales ... etc.) have been compared to that of RDT. In §4.4, we computed instantaneous turbulence fields based on the result of Linear Rapid Distortion theory has shown how a velocity field of random Fourier components undergoing mean shear produce many of the characteristics structure in the flow that are observed in experiments and direct numerical simulation at moderate Reynolds number. A summary is provided in §4.5.

4.2 Analysis

4.2.1 *General*

Rapid Distortion Theory (RDT hereafter) is useful for understanding the structure of turbulence subjected to a suddenly imposed mean deformation. When the mean deformation is very rapid compared to the turbulent time scale (for a limited time T_D (or time of travel $T_D \sim L/U_0$) distortion by mean flow gradient $\partial U_i/\partial x_j$, or other disturbance much larger than the distortion by turbulence acting on itself), the governing equation can be linearized by neglecting the nonlinear (turbulent inertial) terms. In homogeneous turbulence, analytic solutions for the Fourier components of the turbulent velocity can be obtained as functions of total strain (Moffatt 1965, Townsend 1970), and hence statistical quantities may be obtained directly.

We consider the uniform strain to be caused by a mean motion

$$U_i = C_{ij} x_j, \tag{4.2.1}$$

where C_{ij} are constants independent of position (It can be a function of the gradient-direction distance in inhomogeneous flow, e.g. turbulent channel flow.). For simplicity we shall take them to be independent of time also, though this is not essential; the analysis can be carried out equally well for the case $C_{ij} = C_{ij}(t)$.

We consider a *weak* homogeneous turbulent velocity u_i to be superposed on the mean strain U_i such that the velocity becomes the sum

$$\widetilde{u}_i = U_i + u_i \tag{4.2.2}$$

and its corresponding vorticity and pressure are given by

$$\widetilde{\omega}_i = \Omega_i + \omega_i, \qquad \widetilde{P}_i/\rho = P + p, \tag{4.2.3}$$

where ρ being the uniform density, Ω and P are the mean component and ω and p are the fluctuating component of the vorticity and reduced pressure. The Navier-Stokes and the vorticity

equations are:

$$\frac{\partial \tilde{u}_i}{\partial t} + \tilde{u}_j \frac{\partial \tilde{u}_i}{\partial x_j} = -\frac{1}{\rho} \frac{\partial \tilde{p}}{\partial x_i} + \nu \frac{\partial^2 \tilde{u}_i}{\partial x_i \partial x_j} \qquad (4.2.4)$$

and

$$\frac{\partial \tilde{\omega}_i}{\partial t} + \tilde{u}_j \frac{\partial \tilde{\omega}_i}{\partial x_j} = \tilde{\omega}_j \frac{\partial \tilde{u}_i}{\partial x_i} + \nu \frac{\partial^2 \tilde{u}_i}{\partial x_i \partial x_j}, \qquad (4.2.5)$$

where $\frac{\partial u_i}{\partial x_i} = 0$, $\omega_i = \epsilon_{ijk} \frac{\partial u_k}{\partial x_j}$ so that $\frac{\partial \omega_k}{\partial x_k} = 0$ and ν is the kinematics viscosity. The pressure term may be eliminated by the standard procedure of taking the divergence of (4.2.4) using the continuity condition, which gives

$$\frac{1}{\rho} \frac{\partial^2}{\partial x_i^2} \tilde{p} = -\frac{\partial^2 \tilde{u}_i \tilde{u}_j}{\partial x_i \partial x_j} = 2 \frac{\partial U_i}{\partial x_j} \frac{\partial u_j}{\partial x_i} + \frac{\partial u_i}{\partial x_j} \frac{\partial u_j}{\partial x_i}, \qquad (4.2.6)$$

so that the pressure field may be regarded as consisting of a nonlinear component and a linear component with respect to the velocity fluctuations.

In homogeneous turbulence, the equations for the turbulent components, u_i, become

$$\frac{\partial u_i}{\partial t} + U_j \frac{\partial u_i}{\partial x_j} + u_j \frac{\partial U_i}{\partial x_j} + u_j \frac{\partial u_i}{\partial x_j} = -\frac{\partial p}{\partial x_i} + \nu \frac{\partial^2 u_i}{\partial x_j \partial x_j}. \qquad (4.2.7)$$

For a mean flow of magnitude U_o, varying on a length scale D, and for turbulent velocity fluctuations of order u', with an associated integral length scale L, the relative magnitude of the terms in equation (4.2.7) may be estimated.

$$u_j \frac{\partial U_i}{\partial x_j} \sim \frac{u' U_o}{D}, \qquad \frac{\partial^2 u_i}{\partial x_j \partial x_j} \sim \frac{u'}{L^2}. \qquad (4.2.8)$$

So if $U_o/D \gg u'/L$ and the Reynolds number $u'L/\nu \gg 1$, (4.2.7) may be approximated by,

$$\frac{\partial u_i}{\partial t} + U_j \frac{\partial u_i}{\partial x_j} + u_j \frac{\partial U_i}{\partial x_j} = -\frac{\partial p}{\partial x_i} + \mathcal{O}\left(\frac{u'^2}{L}\right). \qquad (4.2.9)$$

Since the turbulence is assumed to be weak, i.e. $u'/U_o \ll 1$, we are justified in neglecting the term $u_j(\partial u_i/\partial x_j)$ and hence (4.2.7) can be linearized to give (4.2.9). In a similar fashion, its corresponding linear vorticity equation is

$$\frac{\partial \omega_i}{\partial t} + U_j \frac{\partial \omega_i}{\partial x_j} + u_j \frac{\partial \Omega_i}{\partial x_j} - \omega_j \frac{\partial U_i}{\partial x_j} - \Omega_j \frac{\partial u_i}{\partial x_j} = 0 + \mathcal{O}\left(\frac{u'^2}{L^2}\right), \qquad (4.2.10)$$

where the neglected nonlinear terms of (4.2.9) and (4.2.10) are

$$-\frac{\partial u_i u_j}{\partial x_j} + \frac{\partial \langle u_i u_j \rangle}{\partial x_j}$$

and

$$\nu \nabla^2 \omega_i - u_j \frac{\partial \omega_i}{\partial x_j} + \omega_j \frac{\partial u_i}{\partial x_j} + \left\langle u_j \frac{\partial \omega_i}{\partial x_j} \right\rangle - \left\langle \omega_j \frac{\partial u_i}{\partial x_j} \right\rangle.$$

The condition that $U_o/D \gg u'/L$ implies that the mean shear is strong and that during the life-time of an eddy the dynamics are controlled by mean shear rather than 'self-modulation' and inertial decay to smaller scales. This is the essential condition of Rapid Distortion theory, and ensures a substantial distortion of the large scale turbulence may be imposed before an eddy decays. In terms of Fourier components, it means that interactions between pair of Fourier components are negligible. The condition that $u'L/\nu \gg 1$, ensure that the turbulence is of high Reynolds number and that the direct viscous decay of the large eddy scales or wavelength of Fourier components) of the order of L_o is not significant. The general condition of RDT have been reviewed by Hunt (1978) and Carruthers and Hunt (1990).

4.2.2 The structure of shear flows from RDT

If the flow undergoes plane shear by the mean flow, this case can be represented by $C_{13} = \alpha$ (constant), all other $C_{ij} = 0$, namely,

$$U_1 = \alpha x_3, \qquad U_2 = 0 \qquad \text{and} \qquad U_3 = 0. \tag{4.2.11}$$

Consideration of the equation for turbulent vorticity in presence of uniform mean shear indicates that this has two effects on a vortex element: since the mean velocity profile is $(\alpha x_3, 0, 0)$, therefore the mean vorticity is $\langle \Omega \rangle = (0, \alpha, 0)$. The vorticity equation from (4.2.5) is

$$\frac{\partial \omega_i}{\partial t} + \alpha x_3 \frac{\partial \omega_i}{\partial x_1} = \omega_3 \alpha \delta_{i1} + \alpha \frac{\partial u_i}{\partial x_2}. \tag{4.2.12}$$

By looking at each individual component, we have

$$\frac{d\omega_1}{dt} = \omega_3 \frac{\partial U_1}{\partial x_3} + \Omega_2 \frac{\partial u_1}{\partial x_2}, \tag{4.2.13a}$$

$$\frac{d\omega_2}{dt} = \Omega_2 \frac{\partial u_2}{\partial x_2}, \tag{4.2.13b}$$

$$\frac{d\omega_3}{dt} = \Omega_2 \frac{\partial u_3}{\partial x_2}, \tag{4.2.13c}$$

(4.2.13b) shows that a mean vortex line can be stretched along its length, generating vorticity fluctuations (lifting the vortex line of mean). Looking at the streamwise component, ω_1, the first term on the right of (4.2.13a) represents the rotation of a fluctuating vorticity line element ω_3 in the direction of shear. Since the principal axes of the mean-strain rate tensor are inclined

at 45° to x_1. Therefore, the stretching of vorticity by the mean differential motion is highest along the lines inclined at 45° to x, and the second term is the rotation of Ω_2 by u_1. (4.2.13c) shows that the generation of spanwise component, ω_3 is stretching Ω_3 by u_3.

Note also that the dominant fluctuating velocity is streamwise, $u_1 \sim -\dfrac{\partial U}{\partial z}u_3 t$ and fluctuating vorticity is spanwise $\omega_3 \sim \dfrac{\partial u_1}{\partial z}$. A combination of lifting, shearing, and stretching thus produces a horseshoe vortex loop (Figure 4.3), exactly the type of structure observed in the boundary layer. If the double-roller eddies are regarded as just one part of these structures (the 'legs'), then it would appear RDT can indeed describe the formation of such structures.

4.2.3 Evolution of the Fourier coefficients

The equation (4.2.9) is now linear and may be analysed in terms of Fourier components, for a given initial disturbance. Following Townsend (1976), the standard resolution of the turbulent velocity distribution into its Fourier wavenumber components were employed, assuming local homogeneity. We write the turbulent velocity distribution at time t as

$$u_i(\mathbf{x},t) = \sum a_i(\boldsymbol{\kappa},t)e^{i\boldsymbol{\kappa}(t)\cdot\mathbf{x}}. \tag{4.2.14}$$

The simplified equations for the amplitude of one Fourier component of the velocity fluctuation, which shall be referred to as the 'rapid-strain' equations (Townsend 1976) follows as

$$\frac{da_1(\boldsymbol{\kappa})}{dt} = \alpha\left(2\frac{k_1^2}{k^2} - 1\right)a_3(\boldsymbol{\kappa}), \tag{4.2.15a}$$

$$\frac{da_2(\boldsymbol{\kappa})}{dt} = 2\alpha\frac{k_1 k_2}{k^2}a_3(\boldsymbol{\kappa}), \tag{4.2.15b}$$

$$\frac{da_3(\boldsymbol{\kappa})}{dt} = 2\alpha\frac{k_1 k_3}{k^2}a_3(\boldsymbol{\kappa}), \tag{4.2.15c}$$

with

$$\frac{dk_1}{dt} = \frac{dk_2}{dt} = 0, \qquad \frac{dk_3}{dt} = -\alpha k_1. \tag{4.2.16}$$

To summarize, the 'rapid strain' equations are expected to be valid description of distortion of the larger scales of high Reynolds number, low intensity turbulence, and for distortion time small in comparison with a typical decay time for the energetic eddies (the distortion time is far less than the Lagrangian scale of the turbulence, $t_d \ll T_L \sim L/u'$).

The solutions (Townsend 1976) to the rapid strain equations may be expressed in terms of initial conditions as (in vector form):

$$a_i(\boldsymbol{\kappa},t) = A_{ij}(\boldsymbol{\kappa},t)a_j(\boldsymbol{\kappa},0), \tag{4.2.17}$$

i.e. the changes are linear in the amplitudes and

$$[A_{ij}] = \begin{bmatrix} 1 & 0 & A_1 \\ 0 & 1 & A_2 \\ 0 & 0 & A_3 \end{bmatrix},$$

(4.2.18)

where

$$A_1 = \frac{k_0^2}{k_1^2 + k_2^2} Q_1 a_3(\boldsymbol{\kappa}_0, 0) + a_1(\boldsymbol{\kappa}_0, 0),$$

(4.2.19a)

$$A_2 = \frac{k_1 k_2}{k_1^2 + k_2^2} Q_2 a_3(\boldsymbol{\kappa}_0, 0) + a_2(\boldsymbol{\kappa}_0, 0),$$

(4.2.19b)

$$A_3 = \frac{k_0^2}{k_0^2 - 2\beta k_1 k_{30} + \beta^2 k_1^2} a_3(\boldsymbol{\kappa}_0, 0),$$

(4.2.19c)

and

$$Q_1 = -\frac{k_2^2}{k_1(k_1^2 + k_2^2)^{1/2}} \arctan\left[\frac{\beta k_1(k_1^2 + k_2^2)^{1/2}}{k_0^2 - \beta k_1 k_{30}}\right] + \frac{\beta k_1^2(k_0^2 - 2k_{30}^2 + \beta k_1 k_{30})}{k_0^2(k_0^2 - 2\beta k_1 k_{30} + \beta^2 k_1^2)},$$

(4.2.20a)

$$Q_2 = \frac{k_0^2}{k_1(k_1^2 + k_2^2)^{1/2}} \arctan\left[\frac{\beta k_1(k_1^2 + k_2^2)^{1/2}}{k_0^2 - \beta k_1 k_{30}}\right] + \frac{\beta(k_0^2 - 2k_{30}^2 + \beta k_1 k_{30})}{(k_0^2 - 2\beta k_1 k_{30} + \beta^2 k_1^2)}.$$

(4.2.20b)

The wavenumber vector $\boldsymbol{\kappa}$ is the vector in a frame moving with the local mean flow, and coincident with the fixed frame initially; being related to $\boldsymbol{\kappa}_0 = (k_{10}, k_{20}, k_{30})$, the initial wavenumber by

$$\boldsymbol{\kappa} = (k_{10}, k_{20}, k_{30} - \beta k_{10}).$$

(4.2.21)

In these equations, and in what follows, the suffix 0 refers to conditions at $t = 0$, and the suffices 1, 2 and 3 refer to components in the x, y and z directions.

As pointed out by Moffatt (1965), (4.2.21) shows that wavenumber components are rotated and stretched by the mean shear, and that for large strains most of the energy comes from components with lower k, corresponding to eddies elongated in the direction of the mean flow. An example of the straining of two modes in this manner in physical space is shown in figure 4.4a and in wavenumber space in figure 4.4b.

Turbulence statistics in homogeneous turbulent flow evolve in time and the total shear

$$\beta = \alpha t$$

(4.2.22)

is chosen as the dimensionless time parameter.

As in most computations of rapid distortion theory, it has been assumed that the initial turbulence was isotropic (and incompressible), so that $\Phi_{ij}(\boldsymbol{\kappa}, 0)$ could be expressed simply and uniquely as

$$\Phi_{ij}(\boldsymbol{\kappa}_0, 0) = \frac{E(k)}{4\pi k^4}(k^2 \delta_{ij} - k_i k_j),$$

(4.2.23)

where $k^2 = k_i k_i$ and $E(k)$ is the energy spectrum.

The solutions for the Fourier components of the velocity may be used to obtain spectra. The solution for the form of velocity spectra at times $t > 0$ may be expressed in terms of the initial conditions as

$$\Phi_{ij}(\boldsymbol{\kappa}) = A_{ip} A_{jq} \Phi_{pq}(\boldsymbol{\kappa}_0, 0)$$

$$= \frac{E(k)}{4\pi k^4} \left[A_{ip} A_{jq}(k^2 \delta_{pq} - k_p k_q) \right], \tag{4.2.24}$$

from which relevant statistics may be obtained by integration over all wave-numbers. For example

$$\langle u_i(\mathbf{x}) u_j(\mathbf{x} + \mathbf{r}) \rangle = \int_{\boldsymbol{\kappa}} \Phi_{ij}(\boldsymbol{\kappa}, t) e^{i\boldsymbol{\kappa}.\mathbf{r}} \, d^3\boldsymbol{\kappa}. \tag{4.2.25}$$

The behaviour of the turbulence and its development are determined by the strain parameter, α, which is the time integral of the mean shear. Notice that the quantity inside the square brackets of (4.2.24) depends only on the direction of the wavenumber vector and on α, not their magnitude, so that the shear distortion does not discriminate between *high* and *low* wavenumbers.

An important controlling parameter in the study of turbulence structure is the shear-rate parameter

$$\alpha^* = \alpha L / u', \tag{4.2.26}$$

which represents the ratio of the turbulence and mean field time-scales.

If $\alpha^* \gg 1$, this means that the mean deformation is very rapid compared to the turbulence time scale. If $\alpha^* \sim 1$, this relaxation time t_r is of order L/u', so the criterion for the importance of nonlinear terms is that $t > t_r \sim L/u'$ ('turnover time' or the Lagrangian time scale). But if α^* is large, the rate at which the anisotropy is growing by linear processes is so much greater than by nonlinear processes that, as Lee *et al.* (1987) have shown, the nonlinear redistributive processes are negligible even when $t > t_r$ (For spectra with a rapid cut-off at large wavenumbers k, e.g. the exponential decay).

It is worth pointing out here that as shown in chapter 2, the one-dimensional functions are related to $E(k)$ by

$$\phi_{11}(k_1) = \frac{1}{2} \int_{k_1}^{\infty} E(k) \left(1 - \frac{k_1^2}{k^2} \right) \frac{dk}{k} \tag{4.2.27a}$$

and

$$\phi_{22}(k_1) = \frac{1}{2} \left[\phi_{11}(k_1) + k_1 \frac{d\phi_{11}(k_1)}{dk_1} \right]. \tag{4.2.27b}$$

Substituting $E(k)$ into (4.2.27a), we obtain

$$\phi_{11}(k_1) = \frac{g_2}{(g_1 + k_1^2)^{5/6}}, \tag{4.2.28a}$$

$$\phi_{22}(k_1) = \phi_{33}(k_1) = \frac{g_2}{2(g_1 + k_1^2)^{5/6}} \left[1 + \frac{2k_1^2}{g_1 + k_1^2} \right], \tag{4.2.28b}$$

which of course show that

$$\phi_{22}(0) = \phi_{33}(0) = \frac{1}{2}\phi_{11}(0) \qquad \text{when} \qquad k = 0 \tag{4.2.29a}$$

and

$$\phi_{22}(k_1) = \phi_{33}(k_1) = \frac{4}{3}\phi_{11}(k_1) \qquad \text{when} \qquad k \to \infty. \tag{4.2.29b}$$

4.3 Results of Simulation

4.3.1 *Method of simulation*

The numerical method of the Kinematic simulation of turbulence with mean shear distortion is essentially the same as in the case of homogeneous, isotropic turbulence simulation as described in chapter 2, i.e. the technique of KS is to superpose linearly space-time Fourier modes with random coefficients and so the simulation was started from an initially-random velocity field with a prescribed Eulerian energy spectrum. However, because of distortion of the velocity field by the mean shear, the wave-vectors $\boldsymbol{\kappa}$ and the Fourier coefficients $\mathbf{a}_n(\boldsymbol{\kappa})$ and $\mathbf{b}_n(\boldsymbol{\kappa})$ are varied with time as given by (4.2.17– 4.2.21). Therefore, during the unsteady simulation of turbulent shear flow, at each advancing time step Δt, the wave-vectors and the Fourier coefficients are updated and hence, the required computing time is about three to four times more expensive than the equivalent homogeneous case. Typically the CPU time required in the University main frame (IBM 3080) for the computations with grid points 7200 (120×60, in x, y) for a range $0 < k \le 50$ is about 60s per time step. The computations was carried out for about one integral time scale of the turbulence using approximately 5 CPU hours.

4.3.2 *Evolution of turbulence statistics*

(i) Intensity of turbulence

To calculate the changes of intensities the appropriate spectrum function must be integrated over all wavenumbers, because the form of A_i ($i = 1, 2, 3$) turn out to be independent of the choice of $E(k)$ and may be evaluated from the surface integral

$$\langle u_i^2 \rangle = \frac{3}{8\pi} \langle u_{10}^2 \rangle \int_0^{2\pi} \int_0^\pi A_{ip}(\theta, \phi, \alpha) A_{iq}(\theta, \phi, \alpha) \left(\delta_{pq} - \frac{k_p k_q}{k^2} \right) \sin\theta \; d\theta d\phi, \tag{4.3.1}$$

where $k_1 = k \sin\theta \cos\phi$, $k_2 = k \sin\theta \sin\phi$ and $k_3 = k\cos\theta$.

The intensity has been computed and are shown in figure 4.5, scaled by the initial turbulent intensity $\langle u_{i0}^2 \rangle$. As can be seen on the graphs, $\langle u_1^2 \rangle$ and $\langle u_2^2 \rangle$ increase progressively by the mean shear, and indeed the production of turbulent energy is supply directly to $\langle u_1^2 \rangle$, and other components receive energy through the effects of pressure and the pressure-strain rate correlation. The correlation $\langle u_3^2 \rangle$ decreases, with increasing shear β. By comparing these profiles, we note that the turbulent r.m.s. velocity $(\langle u_1^2 \rangle, \langle u_2^2 \rangle)$ is larger at the larger strain rate; also $\langle u_1^2 \rangle > \langle u_2^2 \rangle > \langle u_3^2 \rangle$, but the latter inequality is stronger at the larger strain rate. When $\beta \gg 1$, $\langle u_1^2 \rangle \propto \beta$ and $\langle u_3^2 \rangle \propto \beta^{-1}$. The computation of $\langle u_i^2 \rangle$ from KS compared well with RDT as shown on figure 4.5.

(ii) One-dimensional spectra of the turbulence

To investigate how the spatial structure of the turbulence changes with shear, 'two-point' spectra $\phi_{ij}(\boldsymbol{\kappa})$ can be calculated using (4.2.19) and (4.2.24), and the solution is given by Townsend (1976). One-dimensional spectrum function is obtained by integrating

$$
\phi_{ij}(k_1) = \int_{-\infty}^{\infty} \int_{-\infty}^{\infty} \Phi_{ij}(k_1, k_2, k_3) \, dk_2 dk_3
$$

$$
= \frac{3}{8\pi} \langle u_{10}^2 \rangle \int_0^{\infty} \int_0^{2\pi} A_{ip}(r, \theta, \alpha) A_{jq}(r, \theta, \alpha) \left(\delta_{pq} - \frac{k_p k_q}{k^2} \right) r \, d\theta dr, \qquad (4.3.2)
$$

where $k_1 = k$, $k_2 = rk\cos\theta$ and $k_3 = rk\sin\theta$.

Graphs of the one-dimensional energy spectra $\phi_{ij}(k_1, \beta)$ derived from RDT are plotted for different values of β in figures 4.6a, b and c. Figure 4.6a shows that the shape of the spectrum $\phi_{11}(k_1)$ of the streamwise velocity is unchanged as β increases but that if k_1 is $\mathcal{O}(1)$, then the spectrum is very much more amplified than in the region where k_1 is greater than $\mathcal{O}(1)$. Clearly, the shape of the $\phi_{22}(k_1)$, $\phi_{33}(k_1)$ spectra are significantly changed as β increases. Both spectra have a peak as β increases, however, when $k_1 = 0$, the spectra are not affected by shear. For large k_1, $\phi_{22}(k_1)$ increases whilst $\phi_{33}(k_1)$ decreases.

It is of fundamental important to observe the peaks in the streamwise spectra $\phi_{22}(k_1; \beta)$ and $\phi_{33}(k_1; \beta)$ of the spanwise velocities (figure 4.6b, c), which imply the existence of eddies of the corresponding streamwise scales. The peaks shift to lower value of k_1 as β increases implying that the length of the 'streaks' increase.

The simulated results of $\phi_{ii}(k_1)$ at $\beta = 1.5$ are shown in figure 4.7. These values are to be compared with the analytical values of RDT. This is an interesting comparison since for each realisation, we compute the velocity field at a given shear β by the distortion matrix A_{ip}, i.e.,

$$
u_i(\mathbf{x}, \beta) = A_{ip} u_p(\mathbf{x}, 0) = \sum A_{ip} a_p(0) e^{\{i(\boldsymbol{\kappa}_n(t).\mathbf{x} - \omega_n t)\}}. \qquad (4.3.3)
$$

The spectra ϕ_{ij} is obtained after the average of 100 realisations of the computed velocity field, i.e.,

$$\phi_{ij}(k_1) = \sum\sum A_{ip}A_{jq}\langle a_p(0)a_q(0)\rangle e^{ik_1 x_1}. \tag{4.3.4}$$

The agreement between the simulated and RDT results is good (as it should be). These results justify the confidence we place in our model and the numerical procedures.

The simulated spectra drop off at $k_1 = 75.0$ which is the cut-off wavenumber. Note that the slope of all three spectra $\phi_{11}(k_1)$ remain $-5/3$ and are not affected by shear, which has been well established in many field experiments (Monin and Yaglom 1971).

(iii) Local isotropy

The ubiquitous strain-rate of shear flow acts upon "eddies" of all sizes, tending to make the turbulence anisotropic at all wavenumbers. In shear flow the situation is complicated by the fact that energy is received by the turbulence from the mean flow in a highly anisotropic condition, as can be seen from component energy equations (Tennekes & Lumley 1972). In plane turbulent channel flow, for example,

$$\rho\langle uw\rangle\frac{dU}{dz} + \frac{\rho}{2}\frac{d}{dz}\langle u^2 w\rangle + \left\langle u\frac{\partial p}{\partial x}\right\rangle = 0,$$

$$\frac{\rho}{2}\frac{d}{dz}\langle v^2 w\rangle + \left\langle v\frac{\partial p}{\partial y}\right\rangle = 0,$$

$$\frac{\rho}{2}\frac{d}{dz}\langle w^3\rangle + \left\langle w\frac{\partial p}{\partial z}\right\rangle = 0,$$

which shows that *all* turbulent energy appears first as $\langle u^2\rangle$. The expectation of local isotropy is based on the idea that the non-linear spectral energy cascade is an orientation-losing process, primarily through the cross-spectrum of pressure-velocity covariance at all numbers.

A necessary condition for local isotropy is that the eddies with time scales, small compared to the time scales of shear $\tau_s = (dU/dz)^{-1} = \alpha^{-1}$. A suitable eddy time scale is

$$\tau_e = (k^3 E)^{-1/2}, \tag{4.3.5}$$

where E is the three-dimensional spectrum. We expect the onset of isotropic to occur in the inertial subrange of E, i.e. $k^{-5/3}$ range, so (4.3.5) may be expressed as

$$\tau_e = \alpha_k^{-1/2}\varepsilon^{-1/3}k^{-2/3}, \tag{4.3.6}$$

where α_k is a constant. As expected this time scale decreases with eddy size, hence the effect of the shear also decreases, since the mean velocity has less time to strain the eddy. This

isotropy at large k values has been confirmed by experiment (Kaimal *et al.* 1972). The behaviour of $\phi_{22}(k_1, \beta)/\phi_{11}(k_1, \beta)$ and $\phi_{33}(k_1, \beta)/\phi_{11}(k_1, \beta)$ obtained by RDT as a function of k_1 is particularly revealing (see figures 4.8a, b) since it identifies the onset of the isotropic ratio. Note that when $\beta = 0$, as $k_1 \to 0$, $\phi_{22}(k_1) = \phi_{33}(k_1) = \phi_{22}(k_1)/2$ and as $k_1 \to \infty$, $\phi_{22}(k_1) = \phi_{33}(k_1) = 4\phi_{22}(k_1)/3$, in agreement of (4.2.29). However, by increasing β up to 1.5, $\phi_{22}(k_1)/\phi_{11}(k_1) \approx 4/3$, increasing β further still, $\phi_{22}(k_1)/\phi_{11}(k_1)$ drops lower than 1 and similarly $\phi_{33}(k_1)/\phi_{11}(k_1)$ drops. The discrepancy of anisotropy in high wave-number range is that RDT applies the same shear rate to *all* wavenumber k and during this distortion, individual eddies are extended in directions of positive rate of strain and compressed in the directions of negative rate of strain. Hence $\phi_{11}(k_1)$ is overpredicted at large k because the effective shear experienced by small eddies would be considerably less than that experienced by the large eddies as a result of the shorter lifetimes of the scales.

It is also instructive to compute the ratio of ϕ_{22}/ϕ_{11} and ϕ_{33}/ϕ_{11} as a function of k to show the anisotropy of the turbulent structure in our model. The computed results of $\phi_{22}(k_1)/\phi_{11}(k_1)$ and $\phi_{33}(k_1)/\phi_{11}(k_1)$ are plotted in figures 4.9a, b at $\beta = 0.0$ and 1.5. The sudden increase at the high wavenumber end is due to the finite cut-off of wavenumber. By looking at ratio $\phi_{22}(k_1)/\phi_{11}(k_1)$ and using the fact that $E(k) \propto k^{-5/3}$, we have

$$
\frac{\phi_{22}(k_1)}{\phi_{11}(k_1)} = \frac{\dfrac{1}{2}\displaystyle\int_{k_1}^{k_\eta} \left(1 - \frac{k_1^2}{k^2}\right) \frac{E(k)}{k}\, dk}{\dfrac{1}{4}\displaystyle\int_{k_1}^{k_\eta} \left(1 + \frac{k_1^2}{k^2}\right) \frac{E(k)}{k}\, dk}
$$

$$
= \frac{16 k_1^{-5/3} + \left(-11 k_\eta^{-5/3} - 5 k_1^2 k_\eta^{-11/3}\right)}{12 k_1^{-5/3} + 2\left(-11 k_\eta^{-5/3} + 5 k_1^2 k_\eta^{-11/3}\right)}. \tag{4.3.7}
$$

And if $k_\eta \to \infty$, $\phi_{22}(k_1)/\phi_{11}(k_1) \to 4/3$ but if k_η is finite, then $\phi_{11}(k_1, 0, 0) \to 0$ faster than $\phi_{11}(k_1, 0, 0)$ as $k_1 \to k_\eta$. So the ratios $\phi_{22}(k_1)/\phi_{11}(k_1)$ and similarly $\phi_{33}(k_1)/\phi_{11}(k_1)$ tends to increase drastically as $k \to k_\eta$.

However, comparison between the computed results and the experimental data show that the large eddies (low wavenumber), processing most but not all the energy, usually play a significant role in transport of scalars, or particles. They are persistent and coherent structures which interact with the mean flow in the 'rapid-distortion' manner and hence the larger eddies of the turbulence have very nearly the structure predicted by the rapid-distortion theory. So the subsequent sections of this chapter, we focus on the large scale eddies motion that are determined by the shear. Our aim is to explore further the concepts of a generic or common structure in the *energy-containing range* of shear flow turbulence.

(iv) Two-point correlations function and integral length scales

Two-point correlation function is useful method to extract information on the spatial structure of the flow. Grant (1958) and Townsend (1976) examined two-point-correlation profiles for their consistency with a *proposed* model. If the flow contains a *dominant* structure, distributed stochastically in space, its presence should clearly be marked in the two-point correlation function. The two-point correlation is defined as

$$R_{pq}(\mathbf{r}, \beta) = \frac{\langle u_p(\mathbf{x}, \beta) u_q(\mathbf{x} + \mathbf{r}, \beta) \rangle}{\sqrt{\langle u_p^2(\mathbf{x}, \beta) \rangle \langle u_q^2(\mathbf{x} + \mathbf{r}, \beta) \rangle}}, \tag{4.3.8}$$

where $\mathbf{x}$ is the position of each point and $\mathbf{r}$ is the separation vector. We will only consider the 'principal' correlation functions,

$$R_{ii}(r, 0, 0), \qquad R_{ii}(0, r, 0), \qquad R_{ii}(0, 0, r),$$

where $i = 1$, 2, 3, i.e. those with separation parallel to the conventional axes of reference. However, for homogeneous shear flow, (a) it is statistically invariance of rotations of 180° about y-axis and (b) invariance for reflection on the (x, z)-plane. From these conditions, it is noteworthy that:

$$R_{12}(0, r_2, 0) = R_{23}(0, r_2, 0) = 0,$$

$$R_{12}(r_1, r_2, r_3) = -R_{12}(r_1, -r_2, r_3),$$

$$R_{13}(r_1, r_2, r_3) = R_{13}(r_1, -r_2, r_3),$$

$$R_{23}(r_1, r_2, r_3) = -R_{23}(r_1, -r_2, r_3),$$

and

$$R_{ii}(r_1, r_2, r_3) = R_{ii}(r_1, -r_2, r_3),$$

where $i = 1$, 2, 3. This can be seen that by considering the correlation

$$R_{12}(0, r, 0) = \langle u_1(0, 0, 0) u_2(0, r_2, 0) \rangle$$

computed in the coordinate system F (see figure 4.10). In the coordinate system F^*, obtained from F by a rotation of 180° about the y-axis, we have

$$R_{12}^*(0, r_2, 0) = \langle u_1^*(0, 0, 0) u_2^*(0, r_2, 0) \rangle.$$

Now $u_2^*(0, r_2, 0) = u_2(0, r_2, 0)$ and $u_1^*(0, 0, 0) = -u_1(0, 0, 0)$, so $R_{12}^*(0, r_2, 0) = -R_{12}(0, r_2, 0)$. However, condition (a) requires that $R_{12}^*(0, r_2, 0) = R_{12}(0, r_2, 0)$. So we conclude that condition (a) implies $R_{12}(0, r_2, 0) = 0$; similarly $R_{23}(0, r_2, 0) = 0$. A similar argument with condition (b) leads to the remaining relationships between the correlation functions.

The average in the equation (4.3.8) is taken over all three space dimensions, homogeneity implies that this is equivalent to an ensemble average over many flow fields (typically, the ensemble is taken from 100 realisations and each realisation has 10 samples). The separation distance has been non-dimensionalised by the integral lengthscale.

The simulation of shear flow by Rapid Distortion theory changes the forms of the correlation functions as shown in figures 4.11 to 4.13. These profiles show that, in general, for small separation distances, the correlation for the velocity in the direction of the displacement is larger than the corresponding transverse correlations. This is the effect of the continuity equation. In addition, the longitudinal correlation in the streamwise direction extends over longer distance than do all other correlations for β up to 3.0. This result was also obtained by Deardorff (1970) using LES in turbulent channel flow..

After some distortion time later at $\beta = 3.0$, it can be seen (figure 4.11c) that the streamwise velocity correlation $R_{11}(r, 0, 0)$ shows significant elongation, consistent with the existence of streaks.

Figure 4.12c shows the spanwise two-point correlations at $\beta = 3.0$. It can be seen that the longitudinal correlation $R_{22}(0, r, 0)$ assumes the 'transverse' form and develops negative values for large values of r, indicating that convergence or divergence of flow in the Oy direction is common.

In figure 4.13c, the two-point velocity correlation with the direction of separation along the z-axis is shown. As in figure 4.12c, $R_{22}(0, 0, r)$ profiles turn negative, but with smaller values. In addition, a notable contrast with isotropic turbulence is that lateral correlation $R_{11}(0, 0, r)$ does not become negative and assume the 'longitudinal' form. Of course, continuity requires 'back flow' in terms of a negative transverse correlation region for R_{11} somewhere in the $(0, r_2, r_3)$-plane.

All these velocity correlations function are consistent with the RDT correlations obtained by Townsend (1970).

Integral length scales of stationary random variables can be inferred from energy spectra simply from Fourier transform relation between the auto-correlation and the spectrum. Hence, the integral length scales in the x_p-direction of the correlations between the velocity components u_i and u_j at different shear rate β are

$$L_{ij}^{x_p}(\beta) = \int_0^\infty R_{ij}(x_p; \beta) \, dx_p \qquad (4.3.9a)$$

$$= \frac{\pi \phi_{ij}(k_p = 0; \beta)}{2 \langle u_i u_j(\beta) \rangle}, \qquad \text{(no sum on } i \text{ and } j\text{)}. \qquad (4.3.9b)$$

Thus the $L_{ij}^{xp}(\beta)$ measurements contains the chance of consistency check between the RDT and the simulation of KS.

The streamwise integral scales L_{ii}^x in uniform shear as a function of total shear are shown in figure 4.14. The effect of shear is to increase the streamwise scales of the streamwise and vertical velocity fluctuations L_{uu}^x, L_{ww}^x and to reduce the scale of the spanwise fluctuation, L_{vv}^x, for all shear rate. The increase of L_{uu}^x indicates elongation with shear of the streamwise streaks.

Figure 4.15 shows the spanwise integral scales L_{ii}^y as a function of total shear. The scales of the streamwise velocity fluctuation L_{uu}^y and the spanwise fluctuation L_{vv}^y, are markedly decreased with increasing total shear whilst the scale of the vertical motion L_{ww}^y, is increased. Since L_{uu}^y may be interpreted as the characteristic scale for the spanwise extent of the streamwise eddies (streaks), as the total shear increases, the spanwise extent of the streaky eddies decreases. Note that L_{uu}^y decreases faster than L_{vv}^y.

Similarly, figure 4.16 shows the vertical integral scales L_{ii}^z as a function of total shear. The scale of the streamwise velocity fluctuation L_{uu}^z and the vertical fluctuation L_{ww}^z, are increased with increasing total strain whilst the scale of spanwise fluctuation L_{vv}^z, is decreased.

Note that L_{uu}^y seems to be the smallest of all the integral scales at $\beta = 3.0$.

(v) The Lagrangian velocity correlations and its integral time scales

A critical parameter in understanding dispersion processes is the Lagrangian time scale which determines the time for which a particle 'remember' the velocity it processed at time of release. For a turbulence at high Reynolds number, in the absence of any boundaries in homogeneous turbulence, the *time scale T_L* for the variation of the velocity of any fluid element is of order of L/u', sometimes known as the 'turnover time', or the Lagrangian time scale (Corrsin 1963), i.e.,

$$T_L \simeq L/u'. \tag{4.3.10}$$

This estimate has been justified by several laboratory experiments for *homogeneous* grid turbulence (e.g. Snyder and Lumley 1971). In chapter 2, from the simulation of KS we obtained $T_L \simeq 0.52$. This can be compared with the measured value by Snyder and Lumley (1971) of $T_L^w \simeq L_{ww}^x/\sigma_w = 0.5$, in our normalisation. The agreement is good. However it is also widely used without much justification in *inhomogeneous* turbulence. If the variance of velocity components and length scales are proportional to each other throughout a flow, then (4.3.10) appears to be an adequate estimate. But in homogeneous turbulent shear flow, the length scales L_{uu}^x, L_{ww}^z increase and L_{vv}^y decreases as β increases, whilst, the velocity fluctuations σ_u, σ_v increase, and σ_w decreases as β increases. If one tries to make an estimates of T_L^{ii} in terms of Eulerian

velocity and length scales, the choice of one or other component in (4.3.10) has an important effect on the estimation of T_L^{ii}. In this section, we investigate that how the Lagrangian integral time scales change by total shear β and from the simulations presented we suggest which is the correct choice and what the physical reasons are.

The Eulerian fluctuation velocity is given by

$$\widetilde{\mathbf{u}}(\mathbf{x}, t) = \left(\frac{dU_1}{dx_3}\right) x_3 \mathbf{e}_1 + \mathbf{u}(\mathbf{x}, t)$$

$$= \alpha x_3 \mathbf{e}_1 + \mathbf{u}(\mathbf{x}, t), \qquad (4.3.11)$$

where $\mathbf{e}_i$ is a unit vector in the i direction. The Lagrangian velocity $\widetilde{\mathbf{V}}(\mathbf{a}, t)$ can be decomposed in the contribution from Eulerian mean velocity with Eulerian turbulence, both are random, i.e.

$$\widetilde{\mathbf{V}}(\mathbf{a}, t) = \widetilde{\mathbf{u}}[\mathbf{X}(\mathbf{a}, t), t] = \alpha X_3(\mathbf{a}, t)\mathbf{e}_1 + \mathbf{V}(\mathbf{a}, t), \qquad (4.3.12)$$

where $\mathbf{V}(\mathbf{a}, t) = \mathbf{u}(\mathbf{X}, t)$; since $\mathbf{X}_3$ is the random vertical displacement, hence the first component is also random, where $\mathbf{X}(\mathbf{a}, 0) = \mathbf{a}$. The auto-correlation function $R_{ij}^L(\tau)$ of the fluctuating velocity of fluid particle is

$$\widetilde{R}_{ij}^L(\tau) = \frac{\left\langle \widetilde{V}_i(\mathbf{a}, t)\widetilde{V}_j(\mathbf{a}, t + \tau) \right\rangle}{\sqrt{\widetilde{V}_i^2(\mathbf{a}, t)}\sqrt{\widetilde{V}_j^2(\mathbf{a}, t + \tau)}}, \qquad (4.3.13a)$$

the auto-correlation function of just the component $\mathbf{V}$ is

$$R_{ij}^L(\tau) = \frac{\langle V_i(\mathbf{a}, t)V_j(\mathbf{a}, t + \tau) \rangle}{\sqrt{V_i^2(\mathbf{a}, t)}\sqrt{V_j^2(\mathbf{a}, t + \tau)}}. \qquad (4.3.13b)$$

Since $\mathbf{V}$ is not the only component of the Lagrangian fluctuation velocity. The auto-correlation introduced by (4.3.13a) is the "effective" Lagrangian velocity auto-correlation which determines diffusion. The contribution by (4.3.13b) is academic.

Computing or measuring the Lagrangian features of a turbulent shear flow requires an excessive length of time to follow a marked fluid element in order to obtain complete Lagrangian statistics, and also the turbulence of the simulated shear flow changes with time (i.e., the flow is non-stationary). In order to make the situation slightly tractable in this respect and recalled that in chapter 2, we have found that the Lagrangian integral time scale in the time dependence case is approximately equal to that of in the frozen case. Therefore, for given total shear β, the turbulent shear flow simulated by KS is kept frozen so as to track the fluid particles to obtain 'frozen' Lagrangian statistics.

The Lagrangian integral time scale is defined as $T_{ij}^L = \int_0^\infty \widetilde{R}_{ij}^L(\tau)\, d\tau$. The ensemble average of $\widetilde{R}_{ij}^L(\tau)$ are taken over 3200 particles (400 realisations and 8 particles are tracked at each realisation) so as to minimise the statistical errors. Figure 4.17 shows the computed fluid particle velocity auto-correlation functions $\widetilde{R}_{11}^L(\tau)$, $\widetilde{R}_{22}^L(\tau)$ and $\widetilde{R}_{33}^L(\tau)$ at $\beta = 0.75$, 1.5 and 3.0. The changes of the shape of the correlation functions between different components increase as the total shear β increases. The changes of the Lagrangian integral time scales T_{ii}^L with β are plotted in figure 4.18. It can be seen that T_{11}^L and T_{22}^L decrease whilst T_{33}^L increases with increasing total shear β.

The usual concept of particle motion in eddies is that the particles move around *within* an eddy with a velocity of the order of σ_u and over a scale L_{ww}^x, therefore the time scale for moving around in the eddy is of order L_{ww}^x/σ_w. But is this a good estimate of the Lagrangian time scale? We note that the variance of the fluid particle displacement along the $0x_1$ axis in the direction of the mean flow for large time τ is asymptotically proportional to τ^3 (Monin and Yaglom 1971), that is, it increases with time significantly more rapidly than the variance of the transverse displacements, asymptotically proportional to τ. Therefore fluid particles move in the direction of shear much faster with a maximum velocity component σ_u (Turfus and Hunt 1986), so the Lagrangian integral time scale should be of order

$$T_L^{ii} = L_{uu}^i/\sigma_u, \qquad (4.3.14)$$

i.e. time to travel for fluid particle between eddy regions along stream regions.

In figure 4.18, we have plotted $L_{uu}^i(\beta)/\sigma_u(\beta)$ to test the hypothesis of (4.14) normalised on its homogeneous value, where $\sigma_u(\beta)$ is the maximum velocity component. Comparison is good except for large value of β where σ_u is overestimated by RDT for large value of β because there is no non-linear energy transfer between different components.

To gain a better understanding into the structure of the flow and how fluid particle moves within it, a computer motion picture simulating flow-visualization experiments was made. Several sequences of picture were generated. At regular intervals in each sequence ($\Delta T = 0.05 \approx 0.1 T_L$), 100 particles were released along a line either parallel or normal to the z-axis. These particles were followed until the particles were completely decorrelated with their initial positions, i.e. $t \simeq 2T_L$.

Figure 4.19 shows the fluid particles released along a line parallel to the z-axis. It can be seen that the fluid particles moved much faster in the direction of shear and was slowly carried upwards in the z-direction as they were advected by the mean flow. This picture is very similar to the one obtained by Moin and Kim (1982) in their numerical investigation of turbulent channel flow.

Figure 4.20 shows the particle released along a line parallel to the y-axis and located above the x-axis ($x = 0.1$). It can be seen that some of the fluid particles were ejected upwards away for the xOy-plane. The resulting pattern illustrates the foundation of low and high-speed streaks on the $x0y$-plane.

However, figure 4.21 is obtained by tracking particles initially distributed on a plane parallel to the xOy-plane at $Z = 0.1L$. The initial sheet of particles is distorted by the instantaneous velocity field. Figures 4.20 and 4.21 illustrate how different aspects of flow characteristics are emphasized by different visualization methods.

4.3.3 *Structure of the vorticity field*

The computed flow field by KS together with RDT were analysed in a manner similar to the channel-flow study of Moin and Kim (1985).

(i) Distribution of inclination angle of the vorticity vector field

Measurement of the inclination angle of the vorticity vector which is the relevant quantity for determination of the orientation of hairpin vortices.

At each grid point, the inclination angle of the vorticity vector to the mean flow direction

$$\theta = \arctan\left(\omega_z/\omega_x\right), \tag{4.3.15}$$

is calculated. Here ω_x and ω_z are the components of the vorticity vector in the directions streamwise, x, and normal to the mean flow, z, respectively. In this study, the structure of the spanwise component of vorticity vector is not included. The sign convention for the angle θ and the coordinate system are shown in figure 4.22.

Figure 4.23 shows the distribution of the angles θ for the initial flow field (i.e. $\beta = 0$). The initial vorticity field exhibits no directional preference as expected for an isotropic field. In figure 4.24, histograms describing the distribution of the angle θ at several shear rate $\beta = \alpha t = 2.0, 4.0$, and 6.0. The contribution of each grid point is weighted with the magnitude of the projected vorticity vector, $\omega_{xz} = \sqrt{\omega_x^2 + \omega_z^2}$. The distribution attains rather sharp maxima at $45°$ and $-135°$ (the direction of principal elongation of the mean strain), also a maximum-to-minimum ratio increases as β increases and with ratio of about $10:1$ when $\beta = 6.0$. Figure 4.25 shows the histogram at $\beta = 6.0$ that was constructed without consideration of the magnitude of the vorticity vector at each grid point. The maxima still occurs at $45°$. However, the maximum-to-minimum ratio decreases to approximately $4:1$.

The fact that the weighted histogram has a substantially higher maximum-to-minimum ratio than the unweighted histogram indicates that not only are the vorticity vectors predominantly oriented at $45°$ or $-135°$, but also that such orientation is accompanied by increased

vorticity magnitude. This is as expected because the production (stretching) of vorticity due to mean motion is highest along the lines inclined at 45° (or −135°) to the mean-flow direction, x. On the other hand, vorticity oriented at a 135° (or −45°) angle from the mean-flow direction is destroyed (compressed) most rapidly. If turbulent vorticity were only generated (destroyed) by the stretching (compression) of vorticity fluctuations due to mean rate of strain, then at any instant the probability of finding vortex lines inclined at 45° (135°) to the x-axis would be higher (lower) than at other angles.

The above statistical study clearly shows the preferential alignment of the vorticity vectors in planes inclined at 45° to the flow direction. However, the information about the structure of the flow that can be extracted from this study is limited. In particular, the correction between vorticity vectors and hairpin vortices cannot be solely established from the above histograms. This leads us to examine the two-point velocity correlation function.

(ii) Two-point correlations of velocity

In 4.3.3(i), it was shown that in a large portion of the flow the vorticity exhibits a preferred inclination of about 45° to the flow direction, i.e. planes inclined near 45° to the flow direction are likely to contain strong vortical structures, so it is much more informative to obtain two-point correlation functions with the direction of 'probe' separation along the eddy axis rather than along the Cartesian coordinate axes.

Figures 4.26a, and b show the two-point correlations of the three velocity components (at $\beta = 3.0$) with separations along x-, s- and n- directions (see figure 4.22). The striking difference between the correlations is the behaviour of R_{ww}, the correlation between spanwise velocity components separated along $\mathbf{r}_s$ and $\mathbf{r}_n$. In particular, $R_{ww}(\mathbf{r}_s)$ (figure 4.26a) does not become negative (i.e. the two-point correlation profiles show a relatively large distance over which the eddies are correlated), whereas the $R_{ww}(\mathbf{r}_n)$ (figure 4.26b) correlation turn negative. This is consistent with a vortex tube inclined at 45° to the flow direction (see figure 4.27). Along the structure (s-direction) w-velocity maintains the same sign, whereas crossing through the vortex tube it changes sign.

(iii) Structure of the instantaneous vorticity field

In addition to the above statistical analysis, we examine the vorticity vectors of instantaneous three-dimensional vorticity field for direct evidence of the presence of hairpin vortices.

Following the experimental analysis of Head and Bandyopadhyay (1981). Let us consider a hairpin vortex projected on a plane inclined (a) at an angle of 45° and (b) at an angle of 135° to the flow direction respectively, as indicated in the sketch, figure 4.28.

With the plane inclined 45° to the flow direction as the hairpin, we should expect to see only a brief glimpse of the hairpin with the tip disappearing from the picture if it is curled over into the flow as shown. We should expect vortex pairs to appear with structures consisting of two adjacent regions with opposite vorticity signs (up or down arrows), which may be attributed to the two legs of a hairpin. Or sometimes the picture should show Ω or U-shape structures if the hairpin lie entirely on the 45° plane.

On the other hand, with the plane inclined at 135° to the flow so that cross-sections of the hairpins can be seen, we might expected to find that vortex pairs of different sizes and orientations (circular shapes) should dominate the picture.

Of course, the real situation is unlikely to be as simple and clear-cut as the sketches might suggest. It should be pointed out that our view is limited to a two-dimensional plane, and we are identifying only those hairpin with legs in approximately the same (y, r_s)-plane.

Figures 4.29a and b show the projection of vorticity vectors (at $\beta = 7.2$) on a randomly selected plane inclined at 45° and 135° to the mean flow direction. Figure 4.29 shows the vorticities have stronger up or down motions (arrows) whilst figure 4.29b shows that the vorticities have circular shapes. Noted that, while the figures are presented in pairs to emphasize the contrast between the 45o and 135° views, the combinations are arbitrary and the pairs do not represent simultaneous pictures.

4.4 Detailed flow structures

In this section we shall investigate the detail structure of the computed flow field in uniform shear. This will be done by examining contour plots of instantaneous velocity and vorticity field. Also, to see how the structures changes with different initial spectra.

In order to examine the effect of low shear rate on the turbulence structure, contours of streamwise turbulent velocity u from a homogeneous shear flow simulation with small $\alpha = 20.0$ and at $\beta = 9.4$ are plotted on a horizontal (x, y)-plane in figure 4.30 which indicates that at low shear rate structure are not highly elongated in the streamwise direction.

In figures 4.31a and b, similar u-contour plots in homogeneous turbulent shear flow field at high shear rate ($\alpha = 43.2$) are shown at different time $\beta = 4.7$ and 9.4 respectively. At the earlier time ($\beta = 4.7$), figure 4.31a shows structures somewhat elongated in the streamwise direction. The contour plot at a later time ($\beta = 9.4$) clearly shows the flow patterns in figure 4.31b is the existence of highly elongated high- and low-speed streaks structures alternating in the spanwise direction similar to the streaks observed in the near-wall region of turbulent boundary layers (Kline *et al.* 1967). In contrast, the normal and spanwise velocity components do not exhibit streaky structures. This means that, as shear is prolonged, the lateral extent of the streaks are

mainly controlled by the effect of shear and the presence of a solid boundary is not necessary, also that the essential mechanism responsible for the formation of the streak is contained in the linear theory (Lee *et al.* 1987).

Figure 4.32 shows the contour plot of spanwise vorticity fluctuation, ω_y in the same (x, y)-plane as in figure 4.31b.

Streamwise streak pattern of z-vorticity can also be seen in figure 4.33. Condition are identical to those of figure 4.32, and careful comparison with that figure shows that the vorticity spots resides in the relatively quiescent corridors between the high velocity streak.

This is consistence with the picture in figure 4.3, i.e. the vortex line ('head') are lifted by velocity fluctuations. Since the vortex line cannot end in the middle of the flow, they are linked to the 'leg' of the vortex lines which correspond to the regions of high z-vorticity observed in figure 4.33. It is easy to see that, if the 'head' of the vortex line are constrained to be in between the streaks, the picture becomes something like the one in figure 4.3, and the induced longitudinal velocity fluctuations should consist of high velocity narrow streaks, bounding wider bands of lower velocity.

In order to focus on the change of flow with different spectra, two other forms of initial spectra

$$E_1(k) = A_1 k^2 e^{-A_2 k^2} \tag{4.4.1a}$$

and

$$E_2(k) = A_3 k^4 e^{-A_4 k^2} \tag{4.4.1b}$$

have been used for our KS simulations together with RDT, where A_1, A_2, A_3 and A_4 are constants. Figures 4.34 and 4.35 show the contours of streamwise velocity components (with $\alpha = 40.0$ and $\beta = 23.7$) from the same homogeneous shear flow simulation with the above spectra. One can distinguish several localized regions of very high-speed fluid (large concentration of solid lines) that are located on the high-speed streak. It is apparent that the gross feature of the degree of streaky structures in figures 4.34 and 4.35 are higher than that of the von Kármán spectrum's simulation. This is consistent with the results of RDT obtained by Hunt & Carruthers (1989) – when the Reynolds number is small so that the energy spectrum $E(k)$ has no inertial subrange and for large enough strain, over an increasing range of wavenumber, their calculations show that the small-scale spectrum obtains to the form $E(k) \propto k^{-2}$ whatever the initial energy spectrum, provided it decreases faster than k^{-2}, a feature of many observations and computations (Champagne *et al.* 1970, Rogallo 1981).

The similarity of these spectra at low Reynolds numbers can be explained that the effect of the shear is to produce high localised gradient $\partial u_1 / \partial x_2$ and $\partial u_1 / \partial x_3$, or vortex sheet surrounding long, narrow region or 'streak', where the streamwise fluctuations are positive or negative,

rather than being characteristic of any cascade process, which is only found at high Reynolds numbers.

However, if the initial spectrum decreases slower than k^{-2}, for instance, for turbulence at very high Reynolds number, such as in atmospheric or oceanic turbulent flows ($R_\lambda \gtrsim 10^4$), where there is a $-5/3$ spectrum (von Kárman spectrum), the effect of shear is to maintain a $-5/3$ spectrum, which has been well established in many experiments (e.g. Wyngaard & Cote 1972) and also can be seen in our simulations.

The results above imply that the essential mechanism responsible for the formation of the streaks in most turbulent shear flows is contained in the *linear* theory rather than the effects of non-linear interactions. The algebraic form of the spectra is consistent with the existence of discontinuities in velocity or velocity gradients on the scale of k^{-1}.

Linear rapid distortion theory has shown how a velocity field of random Fourier components undergoing mean shear produces many of the characteristic structures in the flow that are observed in experiments and DNS at moderate Reynolds number. In the remaining part of this section, following the work in Chapter 2, we objectively characterise the flow structure into three regions (Eddy, streaming and convergence zones). Using the criteria of Hunt, Wray and Moin (1988), we show how the shape and distribution of the (E), (S) and (C) regions change when shear is applied.

Figure 4.36a shows the streaming regions of an initially isotropic velocity field distributed on the surfaces of the cuboid. They seem to be connected, their shapes somewhat elongated with no preferred directions and they are uniformly distributed. However, after shear is applied at $\beta = 5.0$ (Fig. 4.36b), the distributions of streaming regions seem to be rather discrete and much more elongated in the direction of shear.

Figures 4.37a and 4.38a show the eddy and convergence regions of an initially isotropic velocity field. It can be seen that both regions are distributed uniformly in space with some of the eddy regions connected and elongated, whilst the convergence regions are of round shapes. After shear is applied at $\beta = 5.0$, figure 4.37b and 4.38b show that both regions are elongated in the direction of shear. In order to find out the angle of inclination after distortion, we assume that individual eddy or convergence regions have elliptical shapes, and ellipses have been fitted to these regions, according to the following criteria: (i) equal position of centroid of area; (ii) equal area; (iii) equal 2nd moments of area. The results are shown in figure 4.39 and the average angle of inclination to the direction of the flow after average of 10 realisations (of volume $(2L)^3$) is 9° for streaming regions, 12° for eddy regions and 13° for convergence regions. This is surprising since vorticity at 45° to the flow direction.

4.5 Summary and conclusions

The evolution of turbulence statistics and instantaneous turbulence structures in homogeneous shear at high shear rate are studied by using Kinematic Simulation with Rapid Distortion Theory.

The results has been shown that applying the linear (RDT) distortion to an actual realisation of initially homogeneous isotropic velocity fields leads to velocity field that contain many major large-scale coherent structures. These structures appear very *similar* in shape and distribution to structures that have been found in the direct simulation of homogeneous uniform shear flows. This similarity implies that RDT is a useful tool of computing the structure in shear flows. Among the results were the following:

(i)   It is found that higher shear rate alone (without the wall) can produce the streaky structures similar to the structure observed in the viscous sublayer of turbulent boundary layers (Lee *et al.* 1988).

(ii)   There is a large portion of the flow the distribution of inclination angle of vorticity vector attains its maximum at 45° (and −135°) to the flow direction. This is expected because the production (stretching) of vorticity due to mean motion is *highest* along the lines inclined at 45° (or 135°) to the mean flow direction. However, streaming and eddy regions was found at lower angle to the mean flow.

(iii) A Lagrangian integral time scale is found by statistically averaging over a large number of numerically-simulated trajectories in a frozen field at a given shear β. The computations indicate that the Lagrangian time scale T_L^{ii} is proportional to L_{uu}^i/σ_u, where σ_u is the maximum r.m.s. velocity component.

(iv)   High shear rate applied to initial spectra of the form of E_1 and E_2 which have faster fall-offs than k^{-2}, the resulted spectra have a form of k^{-2} which is a characteristic of a spectrum of vortex sheets, such as are observed on the sides of high-speed streaks in these flows.
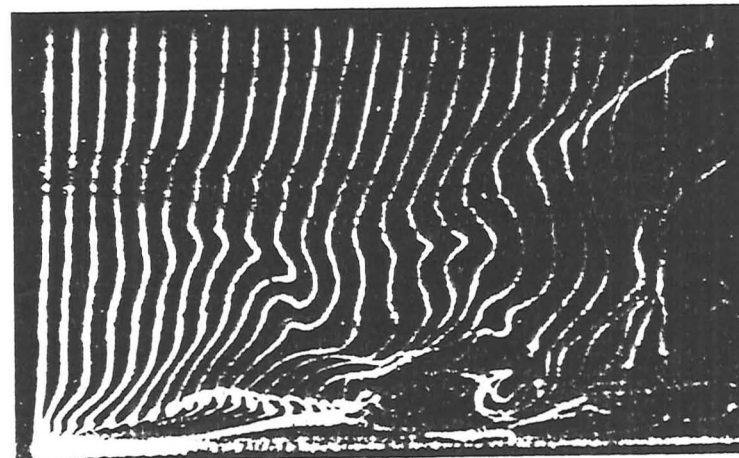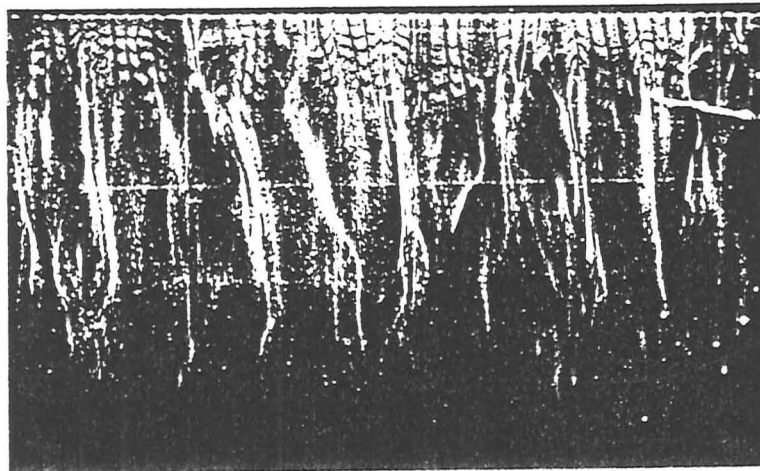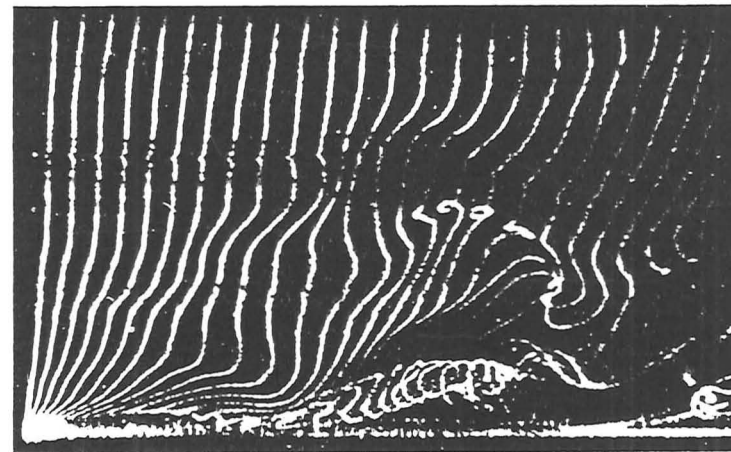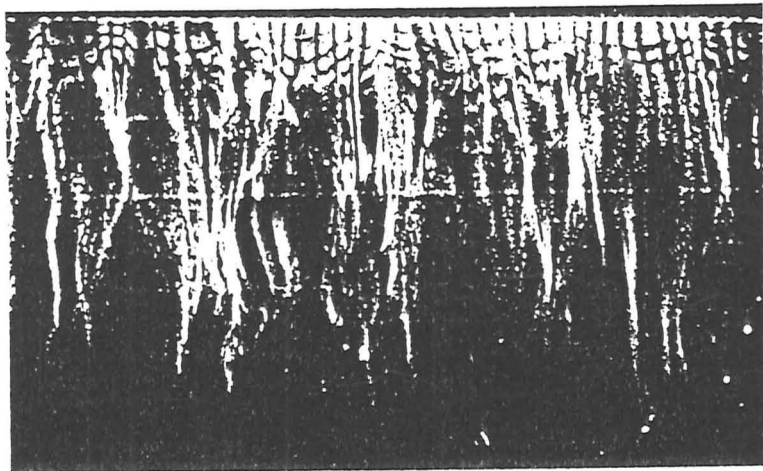
Fig. 4.1   Near-wall structure of a turbulent flat-plate boundary layer (top view) visualized with hydrogen bubbles (from Kline *et al.* 1967).

Fig. 4.2   Near-wall structure of a turbulent flat-plate boundary layer (side view). Sequence showing formation of streamwise vortex during second stage of bursting. Lower photograph shows 0.5s after upper one (from Kline *et al.* 1967).
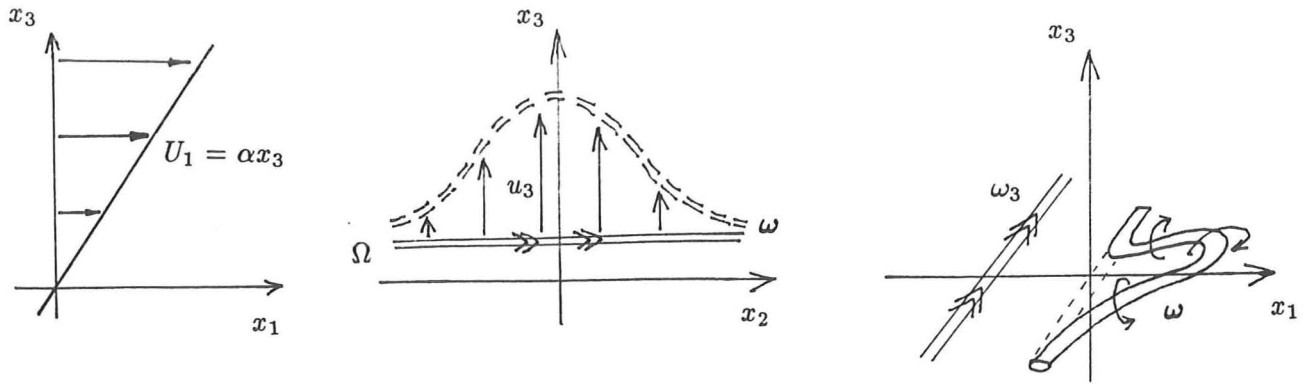
Fig. 4.3   (a) The uniform shear velocity profile. (b) Generation of ω_3 from the spanwise variation of a fluctuating u_3 motion. (c) Rotation and stretching of ω_3 by the mean shear to give ω_1 and the horse-shoe vortex.
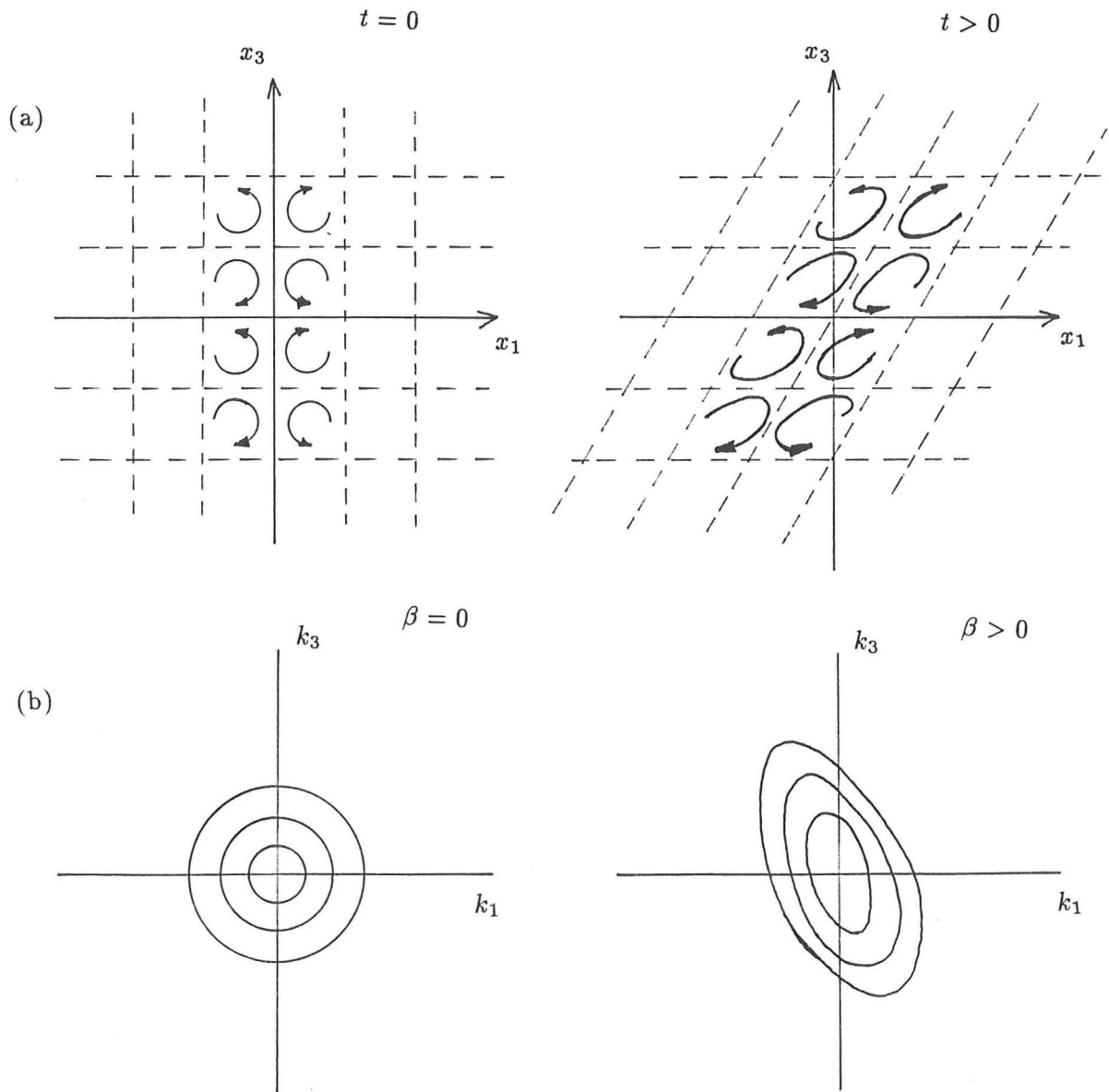
Fig. 4.4   (a) Straining of two modes by mean shear. (b) The constant probability contours for κ_n at $\beta = 0.0$ and the effect of shear quantatively is to tilt the ovals for $\beta > 0.0$.
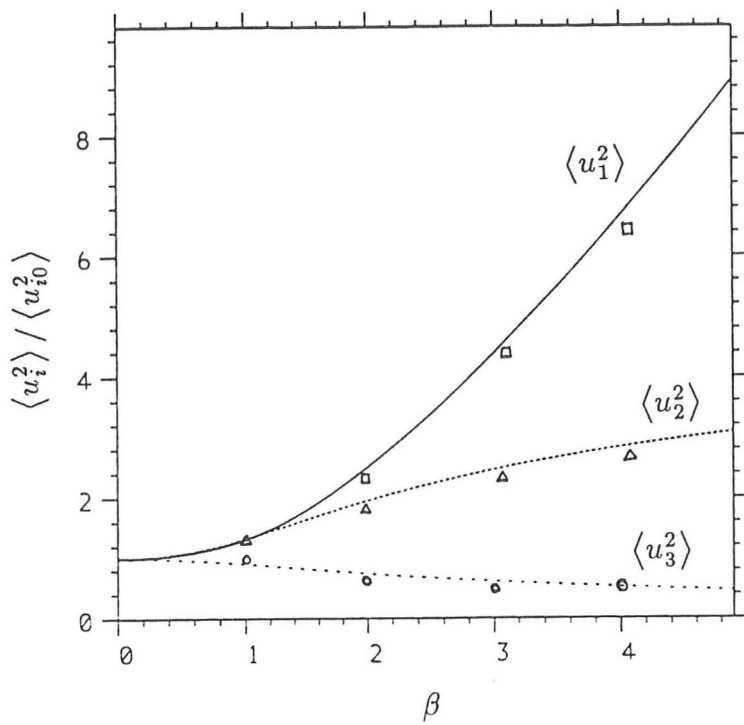
Fig. 4.5 Calculated dependence of the intensities of velocity components on total shear β. Lines represents the rapid-distortion approximation and symbols represent the KS simulation. Results scaled by $\langle u_{01}^2 \rangle$.
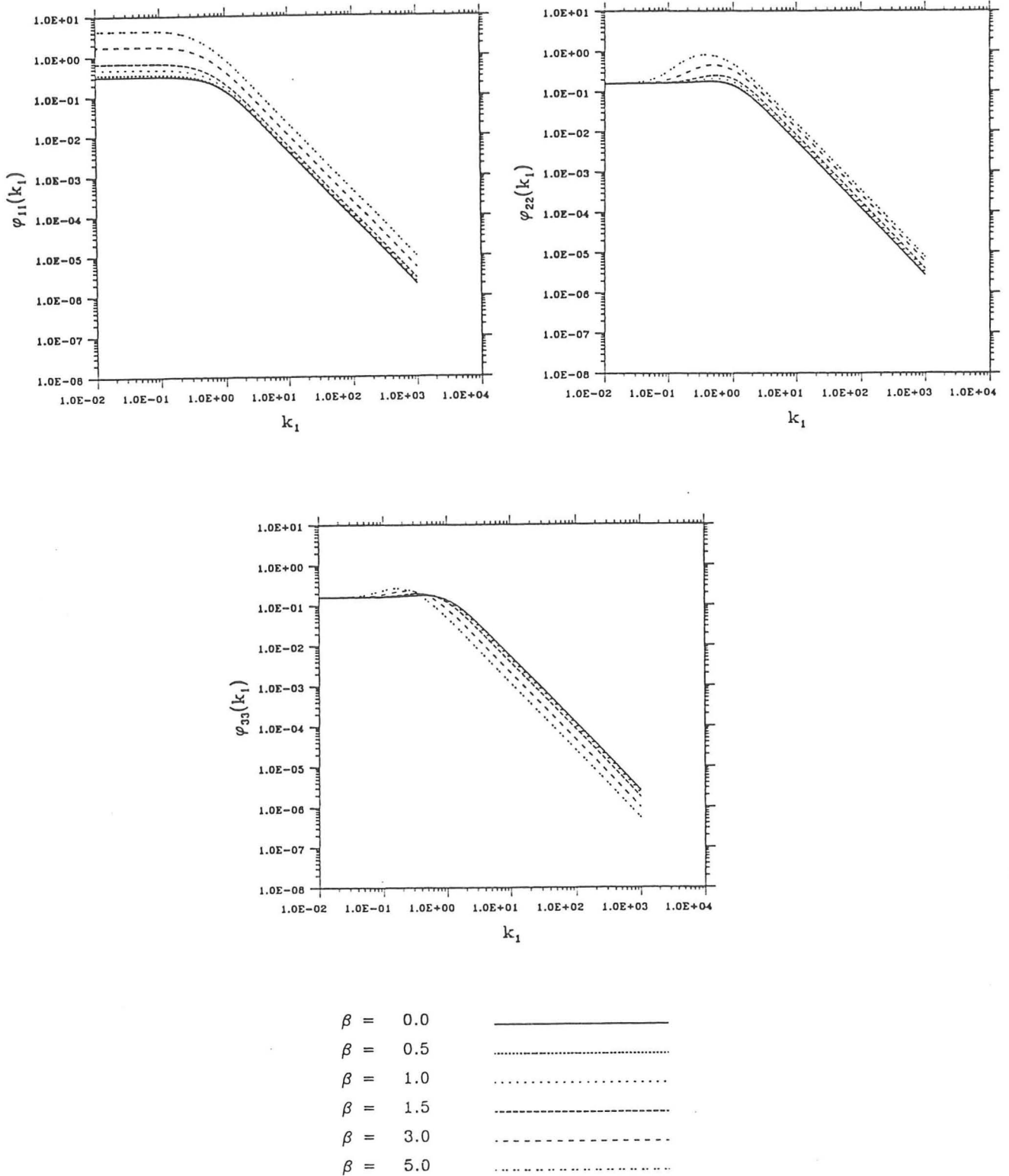
Fig. 4.6 The one-dimensional energy spectra $\phi_{ii}(k_1, \beta)$ in homogeneous turbulent shear flow obtained from RDT.
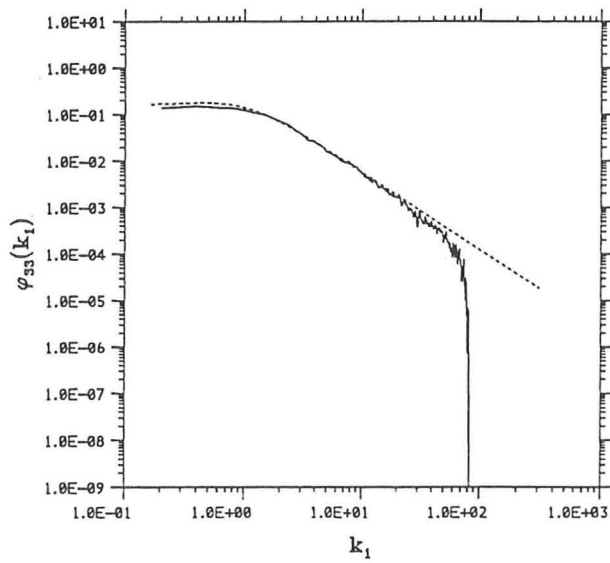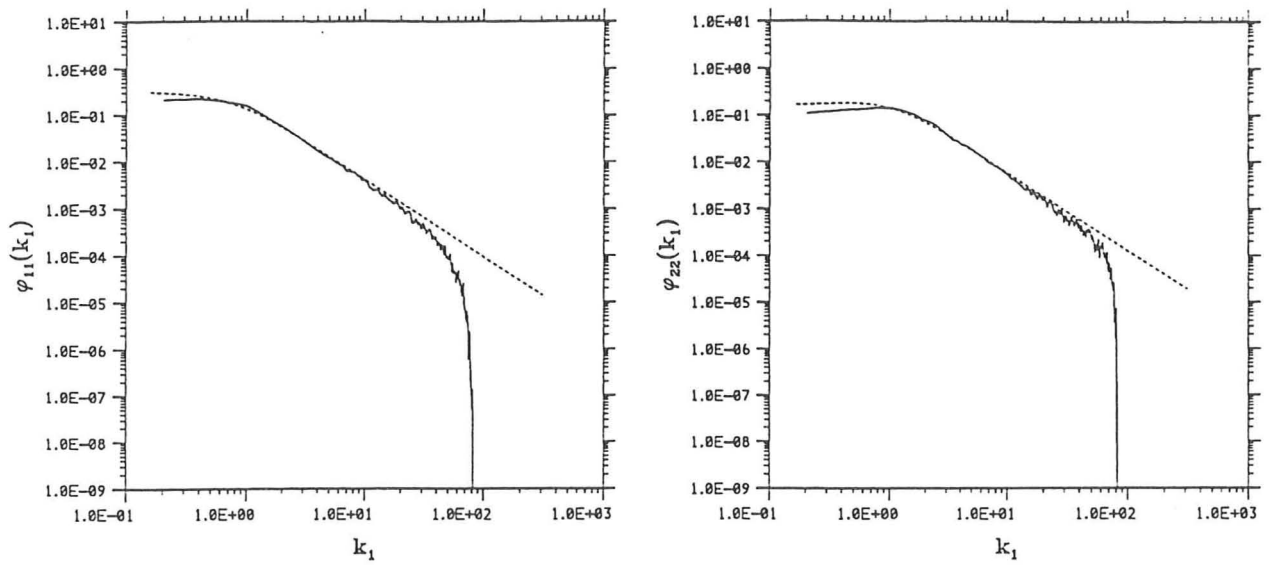
$\beta = 0.0$

| KS | $\varphi_{ii}(k_1)$ | ———————— |
| RDT | $\varphi_{ii}(k_1)$ | ------------------------ |

(a)

Fig. 4.7 Comparison of the one-dimensional energy spectra $\phi_{ii}(k_1, \beta)$ in homogeneous turbulent shear flow between RDT and KS simulation at (a) $\beta = 0.0$; (b) $\beta = 1.5$.

$\beta = 1.5$
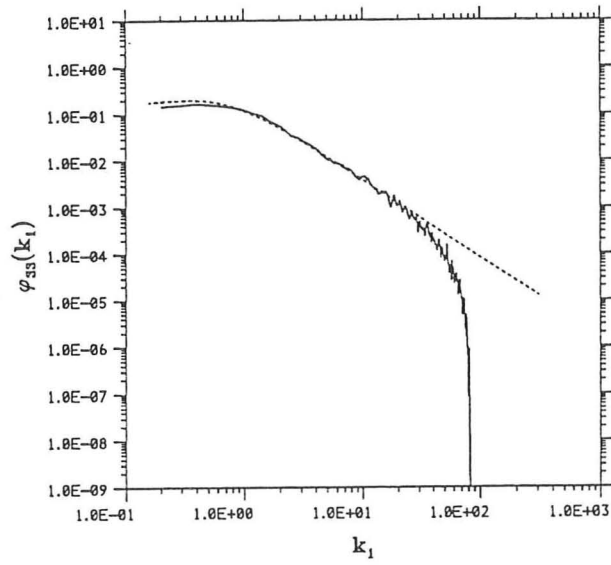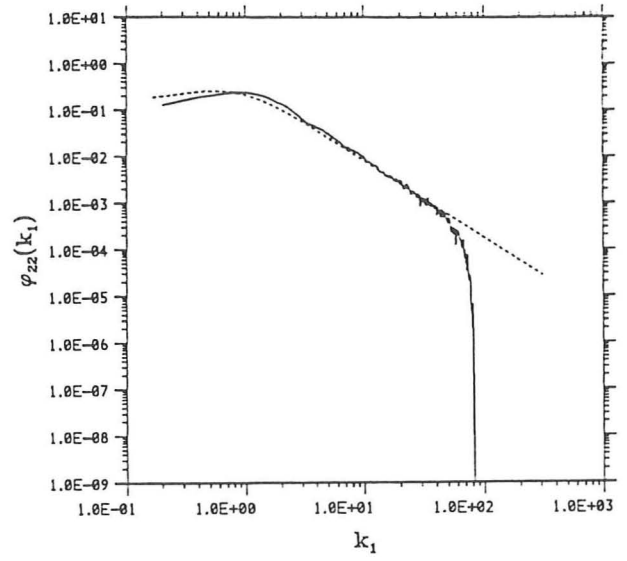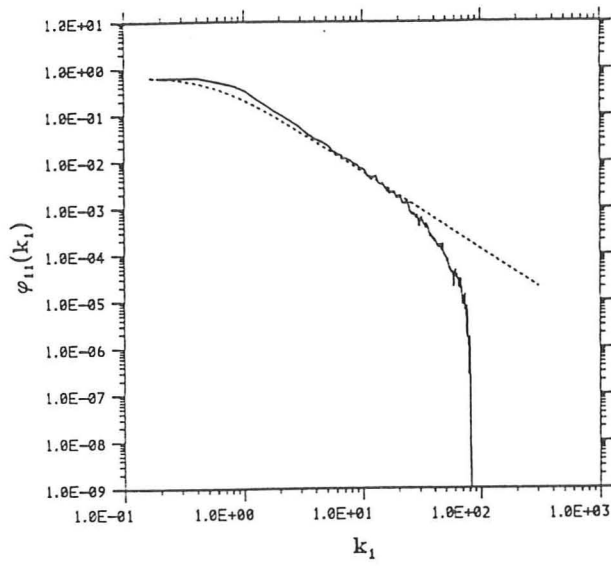
| KS | $\varphi_{11}(k_1)$ | ———— |
| RDT | $\varphi_{11}(k_1)$ | -------- |

(b)
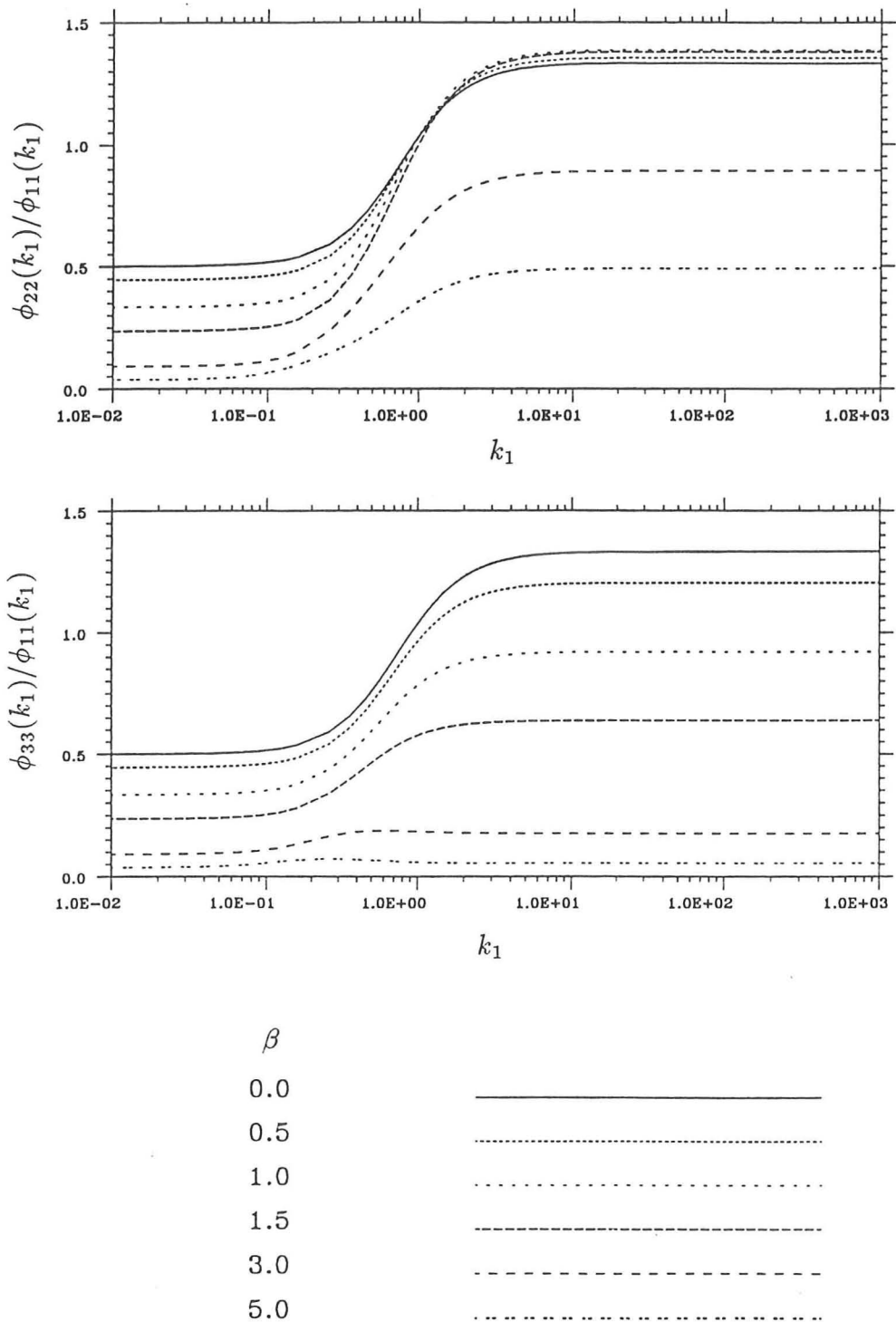
Fig. 4.8   Plots of the ratios of spectra from RDT. (a) $\phi_{22}(k_1)/\phi_{11}(k_1)$; (b) $\phi_{33}(k_1)/\phi_{11}(k_1)$ showing at $\beta = 0.0$ approach to the 4/3 ratio required for isotropy.
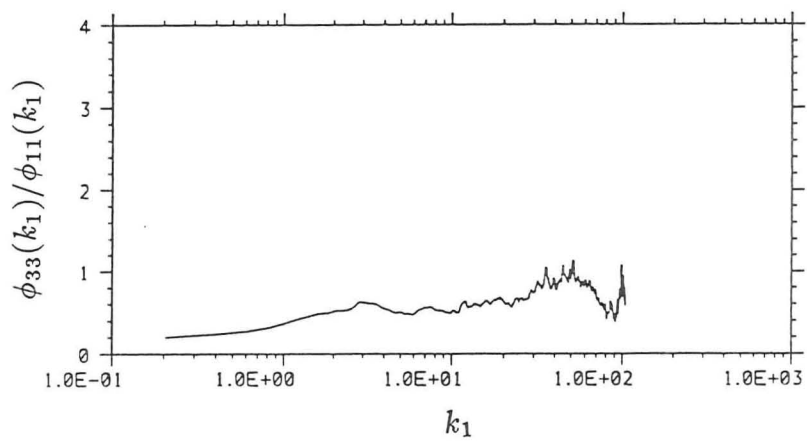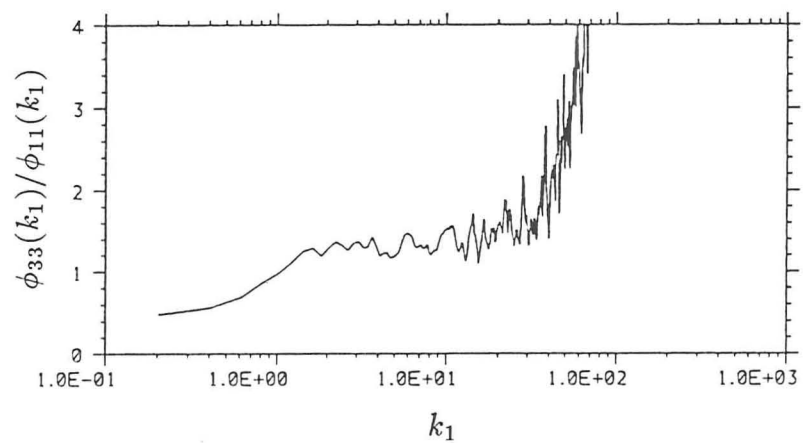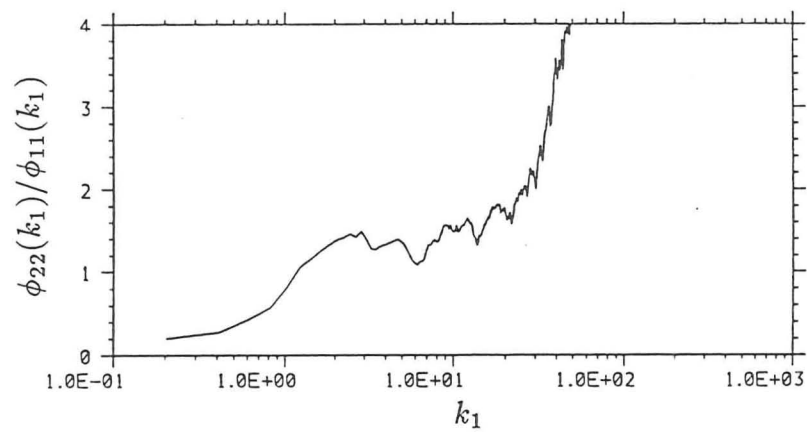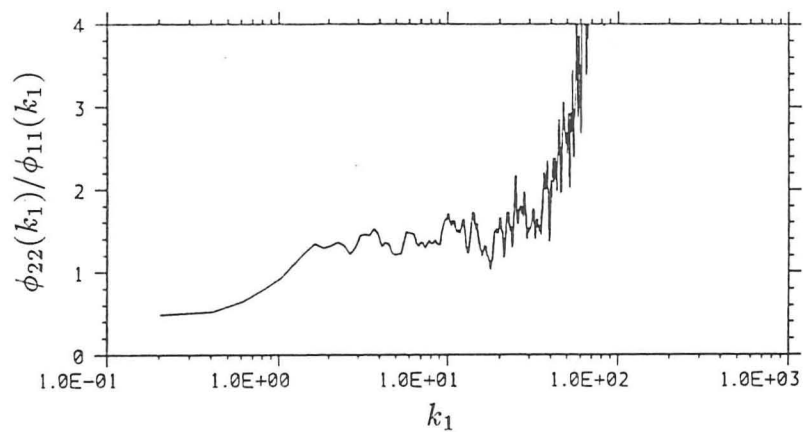
Fig. 4.9   Plot of the ratios of spectra $\phi_{22}(k_1)/\phi_{11}(k_1)$ and $\phi_{33}(k_1)/\phi_{11}(k_1)$ from KS, with total no. of modes of 46. (a) $\beta = 0.0$ and (b) $\beta = 1.5$.
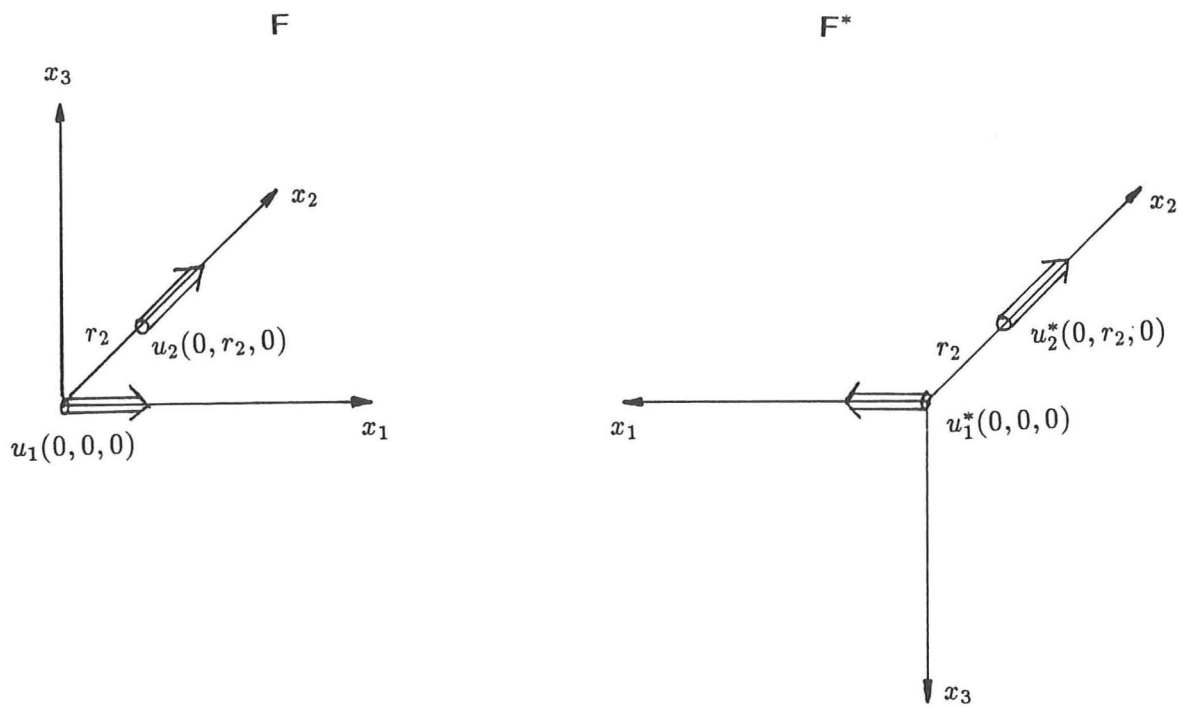
Fig. 4.10 Velocity correlation $R_{12}(0, r_2, 0)$ computed in the coordinate system F and F^*.
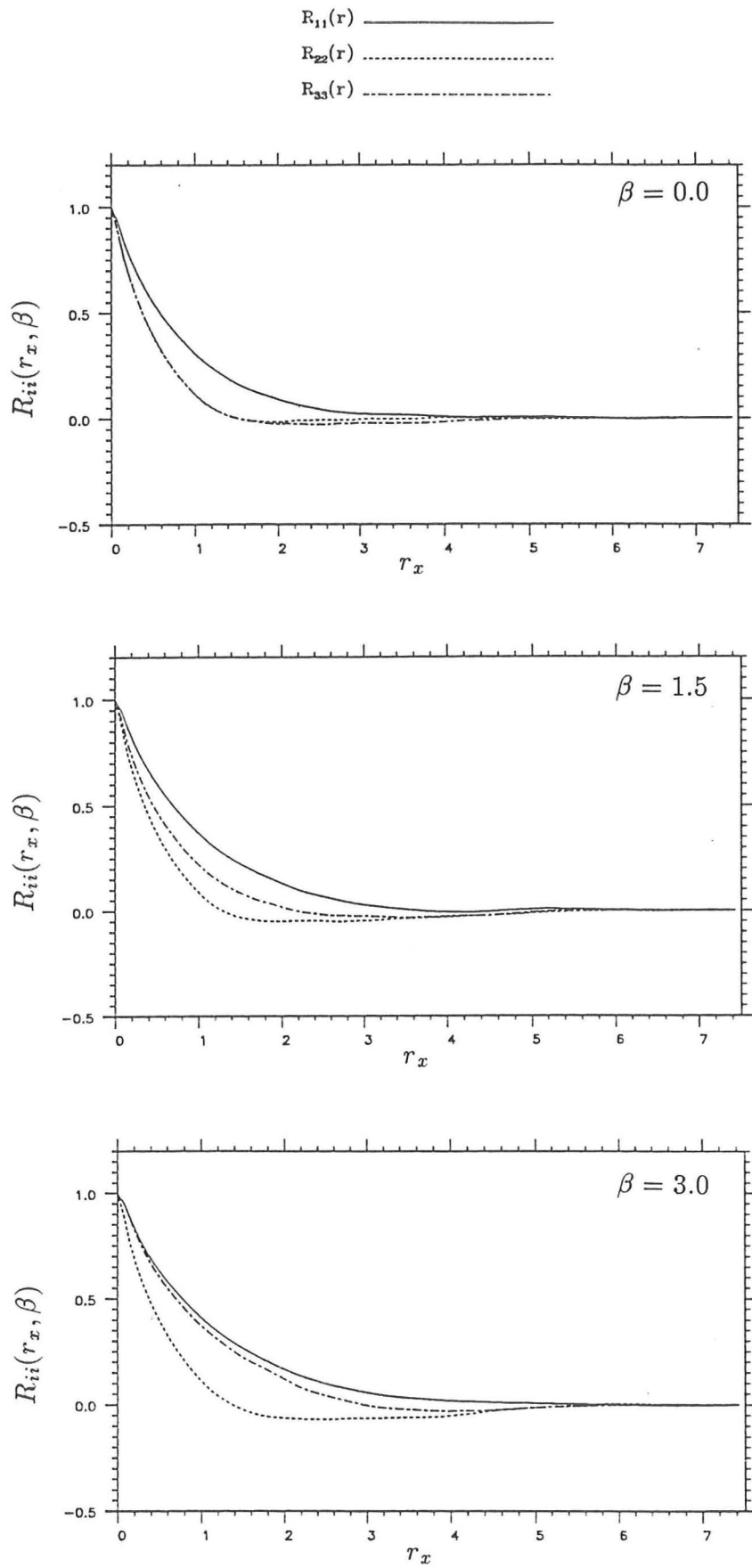
Fig. 4.11 The streamwise two-point correlations of the velocity component from KS with total shear (a) $\beta = 0.0$; (b) 1.5; (c) 3.0. R_{11}(solid line) is for the u component, R_{22}(dotted) for v and R_{33}(dash-dot) for w.
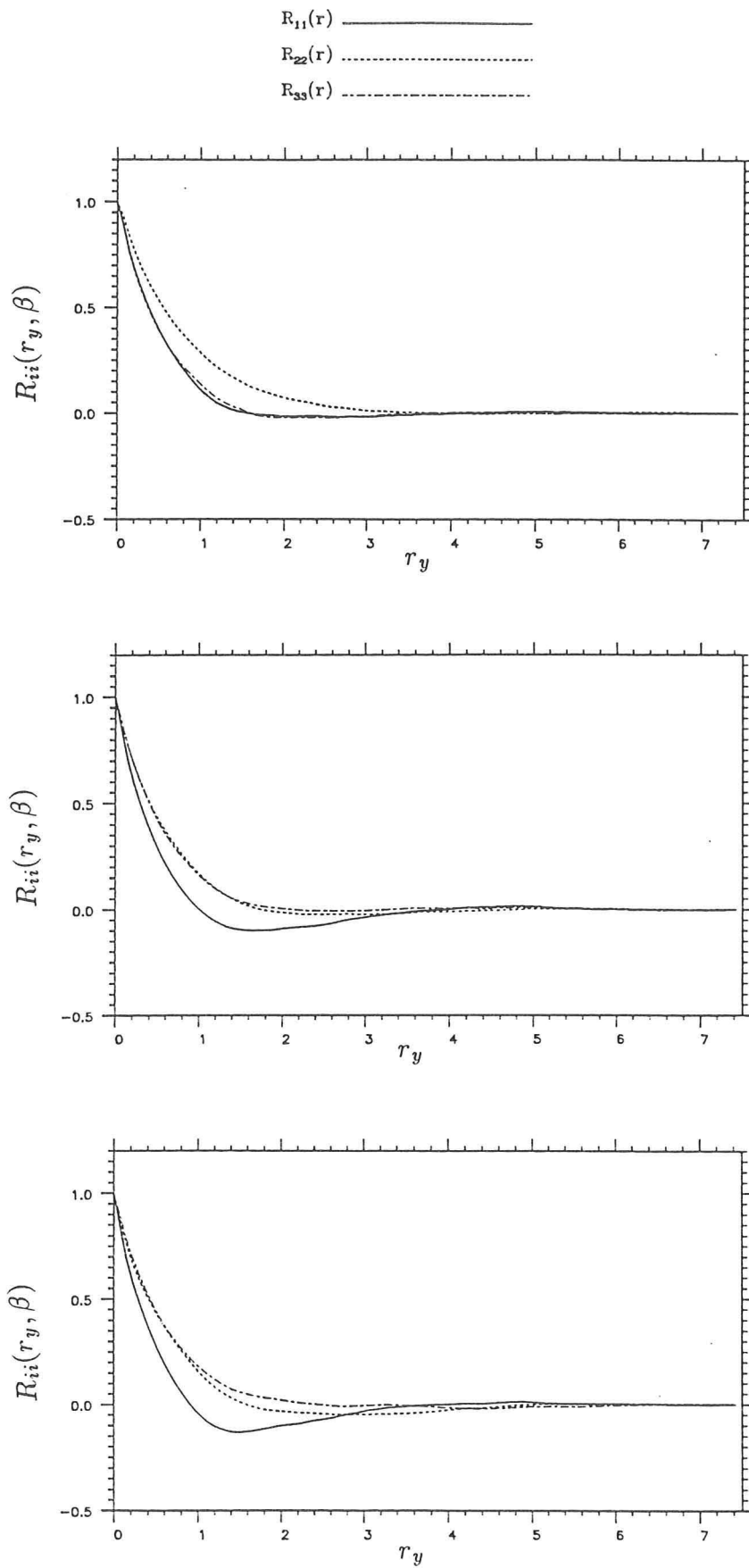
Fig. 4.12 The spanwise two-point correlations of the velocity component from KS with total shear (a) $\beta = 0.0$; (b) 1.5; (c) 3.0. R_{11}(solid line) is for the u component, R_{22}(dotted) for v and R_{33}(dash-dot) for w.
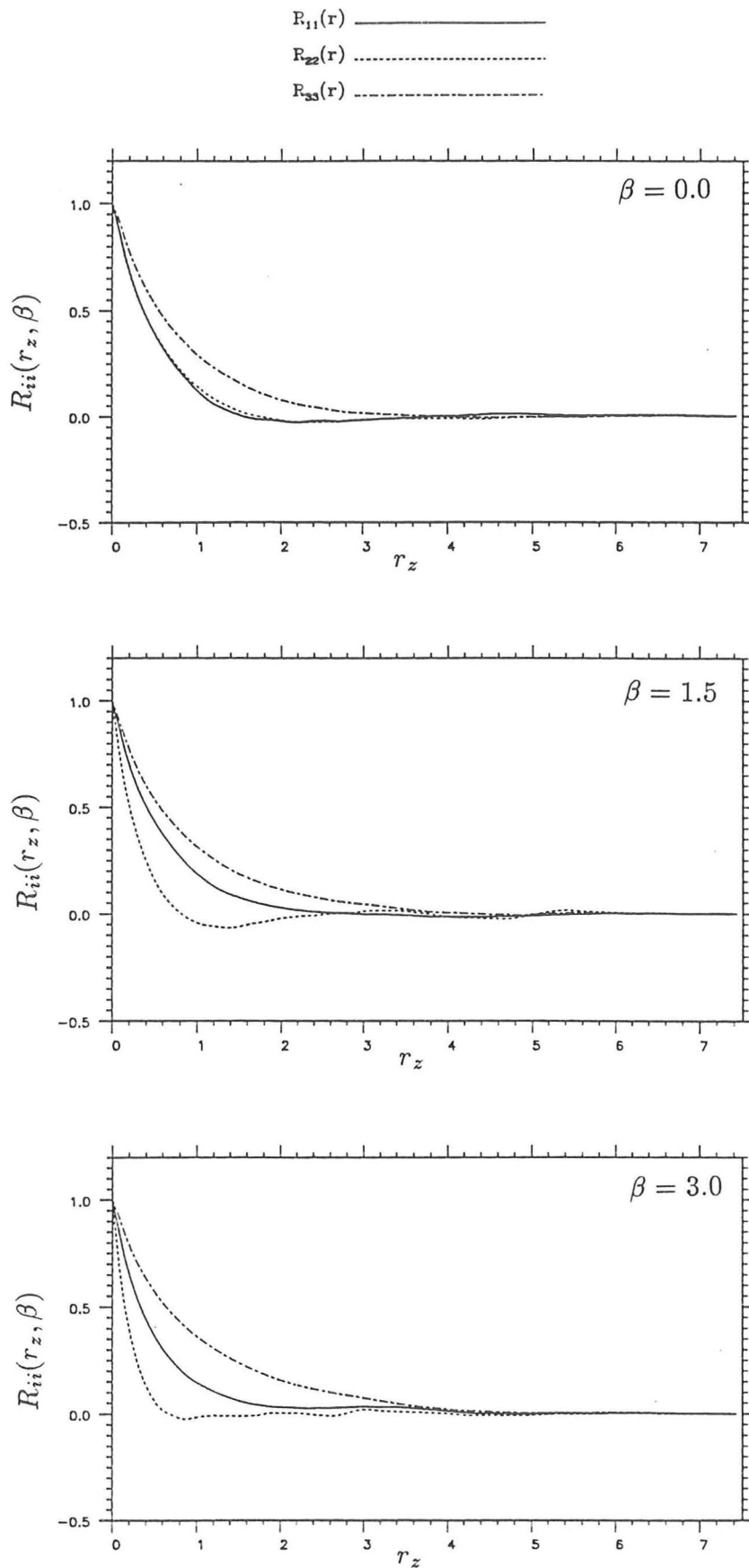
Fig. 4.13 The vertical two-point correlations of the velocity component from KS with total shear (a) $\beta = 0.0$; (b) 1.5; (c) 3.0. R_{11}(solid line) is for the u component, R_{22}(dotted) for v and R_{33}(dash-dot) for w.
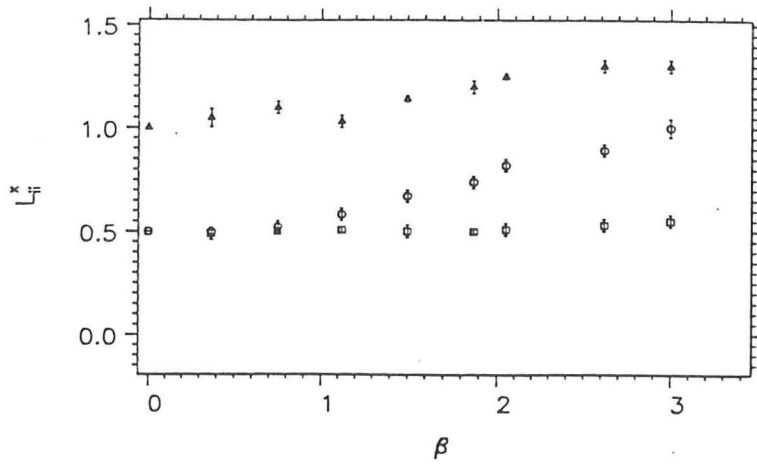
Fig. 4.14 Plots of the changes of the streamwise integral length scale $L_{ii}^x(\beta)$ as a function of total shear β. $\triangle\,\triangle\,\triangle$, L_{uu}^x; $\square\,\square\,\square$, L_{vv}^x; $\circ\,\circ\,\circ$, L_{ww}^x.
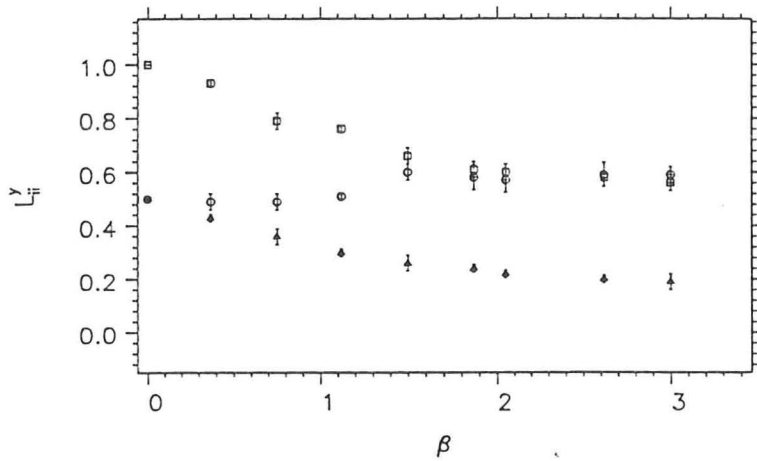
Fig. 4.15 Plots of the changes of the spanwise integral length scale $L_{ii}^y(\beta)$ as a function of total shear β. $\triangle\,\triangle\,\triangle$, L_{uu}^y; $\square\,\square\,\square$, L_{vv}^y; $\circ\,\circ\,\circ$, L_{ww}^y.
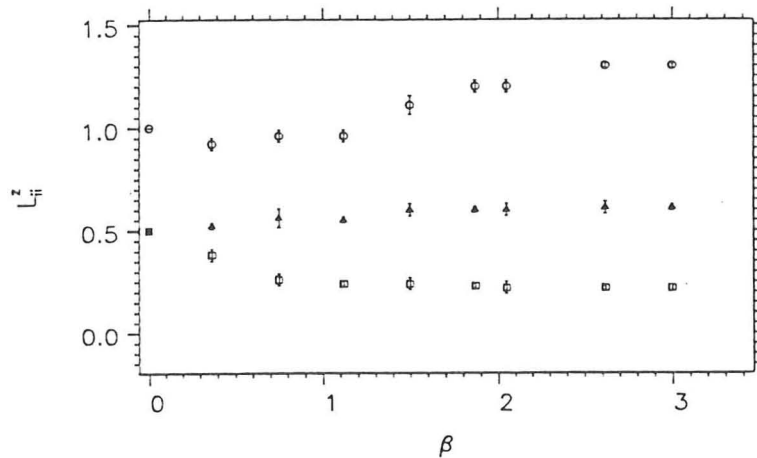
Fig. 4.16 Plots of the changes of the vertical integral length scale $L_{ii}^z(\beta)$ as a function of total shear β. $\triangle\,\triangle\,\triangle$, L_{uu}^z; $\square\,\square\,\square$, L_{vv}^z; $\circ\,\circ\,\circ$, L_{ww}^z.
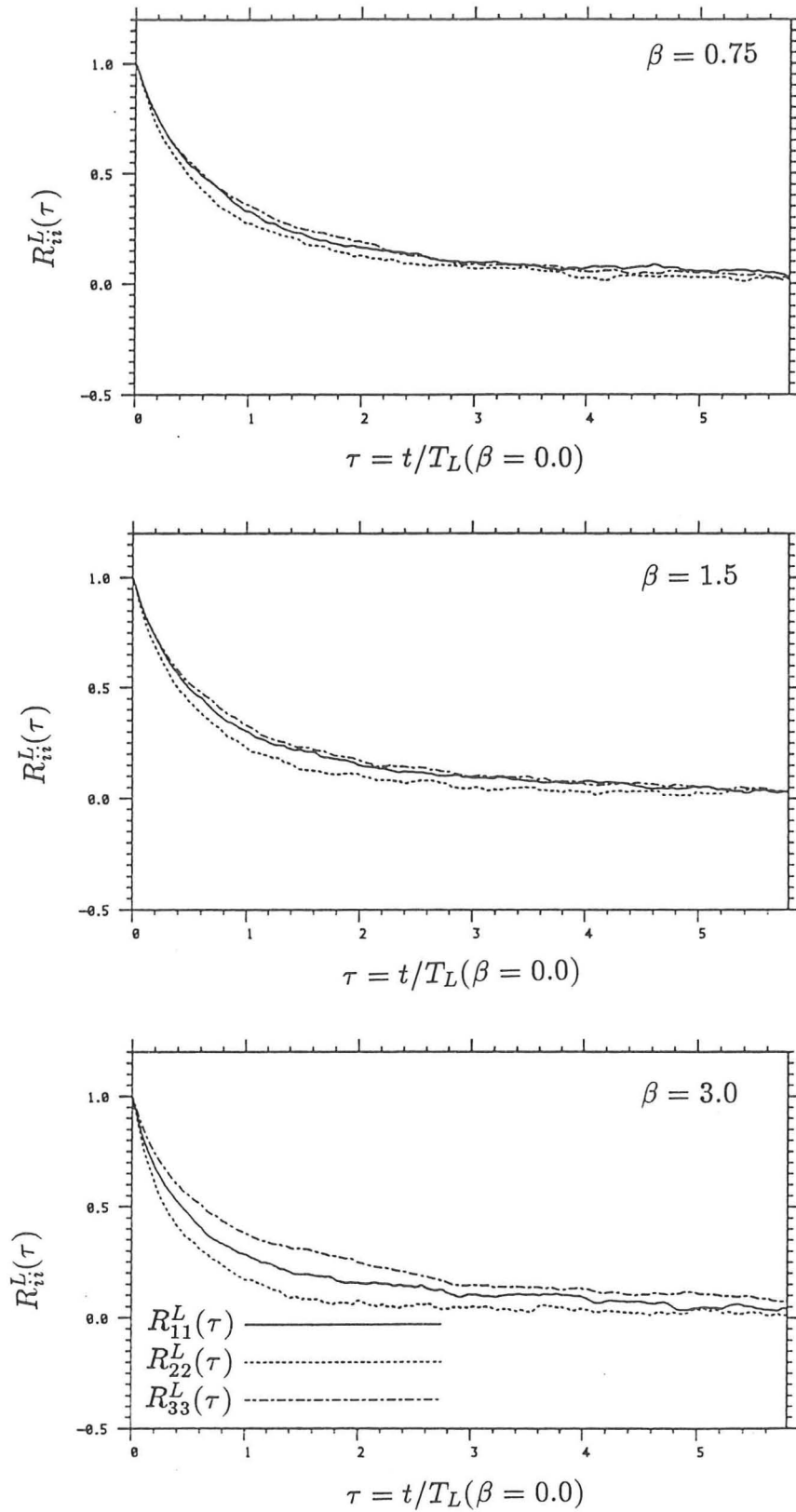
Fig. 4.17 The Lagrangian velocity auto-correlation functions. (a) $\beta = 0.75$; (b) 1.5 and (c) 3.0.
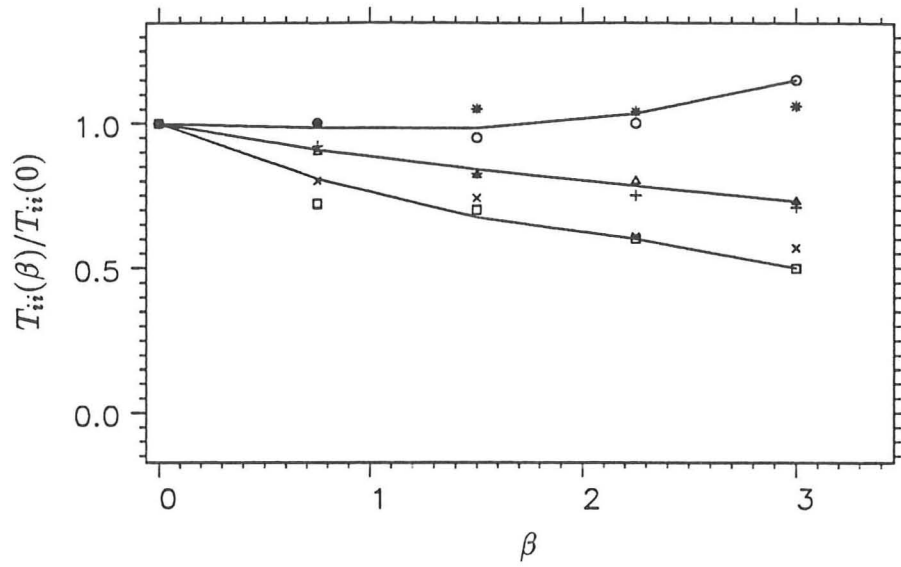
$$T_{11}(\beta)/T_{11}(0) \quad \triangle \; \triangle \; \triangle \; \triangle \qquad L_{uu}^x/\sigma_u \quad + \; + \; + \; +$$

$$T_{22}(\beta)/T_{22}(0) \quad \square \; \square \; \square \; \square \qquad L_{vv}^x/\sigma_u \quad \times \; \times \; \times \; \times$$

$$T_{33}(\beta)/T_{33}(0) \quad \circ \; \circ \; \circ \; \circ \qquad L_{ww}^x/\sigma_u \quad * \; * \; * \; *$$

Fig. 4.18 Plots of the changes of the Lagrangian integral time scales as a function of total shear β.
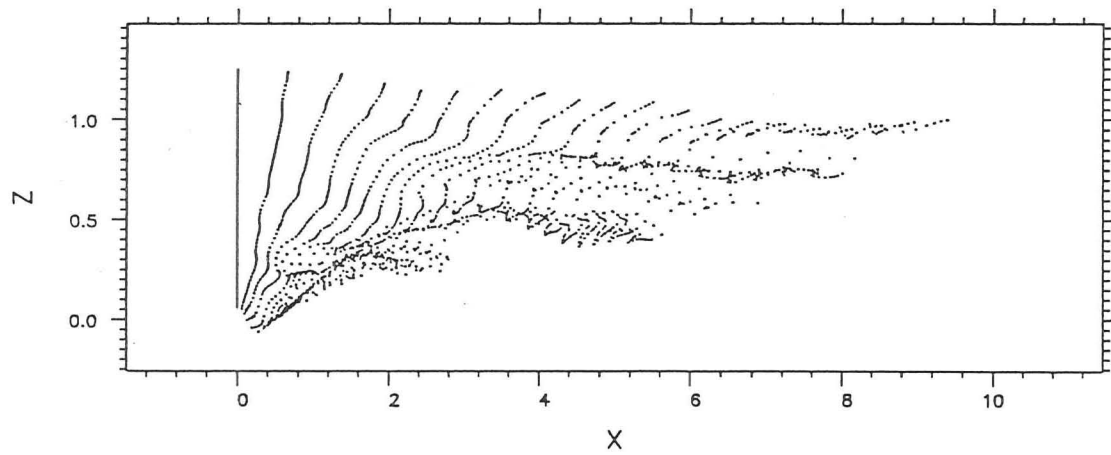
Fig. 4.19 Typical fluid particle trajectories released parallel to z-axis in turbulent shear flow simulated by KS.
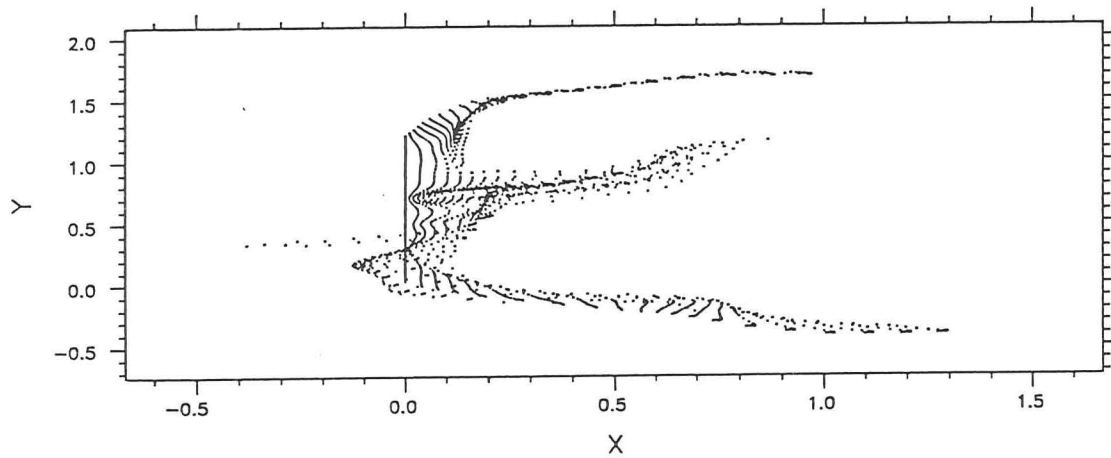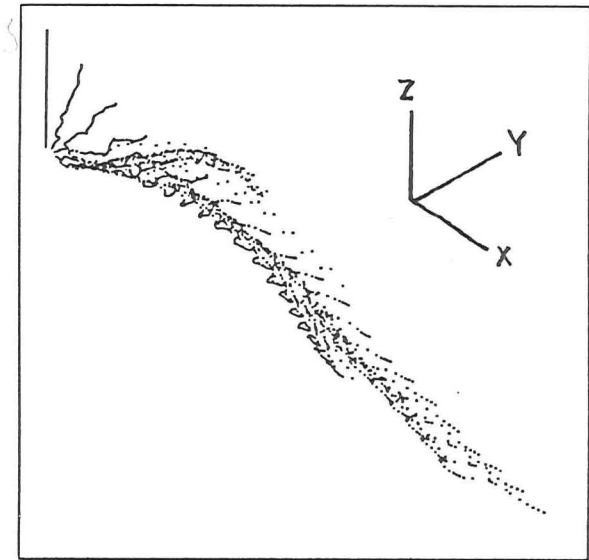
Fig. 4.20 Typical fluid particle trajectories released parallel to x-axis in turbulent shear flow simulated by KS.
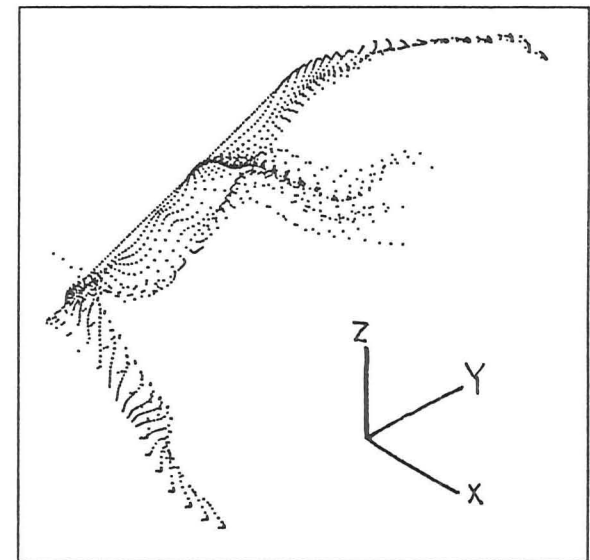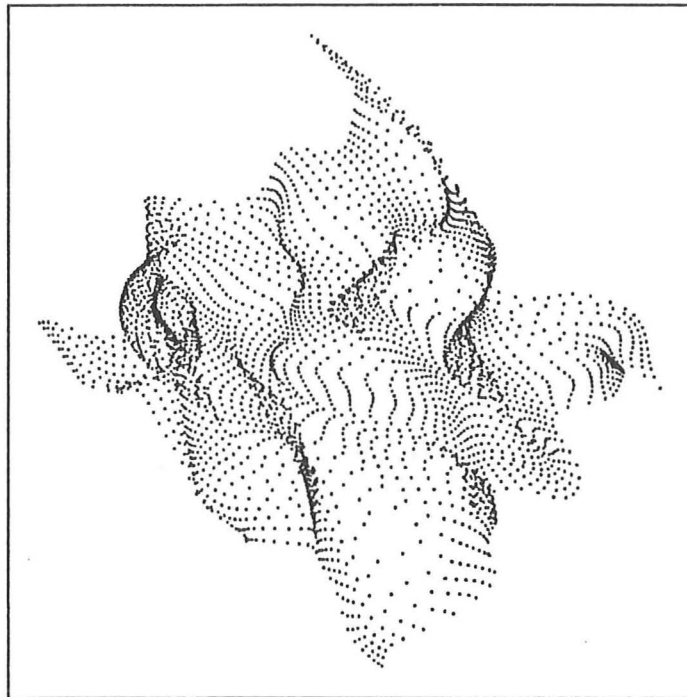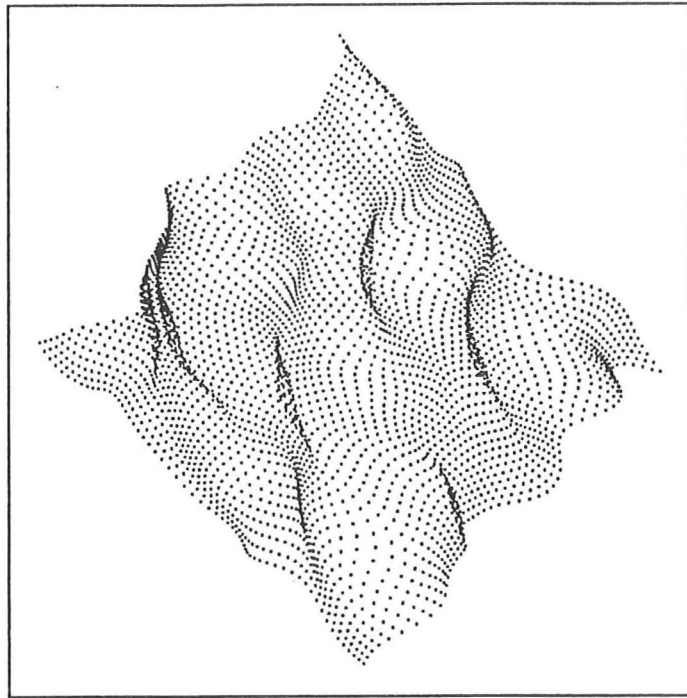
Fig. 4.21 Material surface distorting in shear flow. Particles are initially distributed uniformly on a plane parallel to the xOy-plane with $z = 0.1L$ (top view).
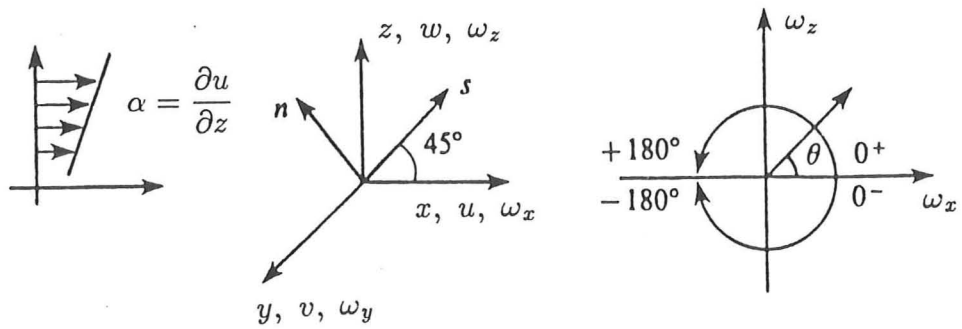
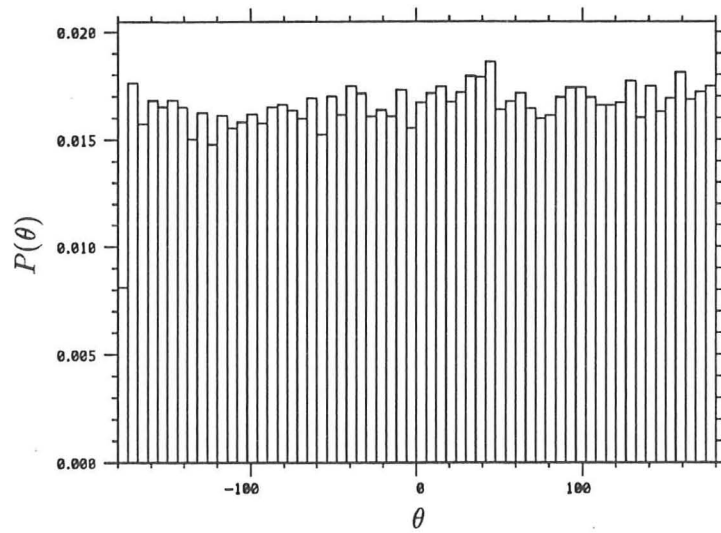Fig. 4.22 Coordinate system and sign convention for angle θ.

Fig. 4.23 Distribution of the inclination angle of the projection of the vorticity vectors in (x, z)-plane for the initial field.
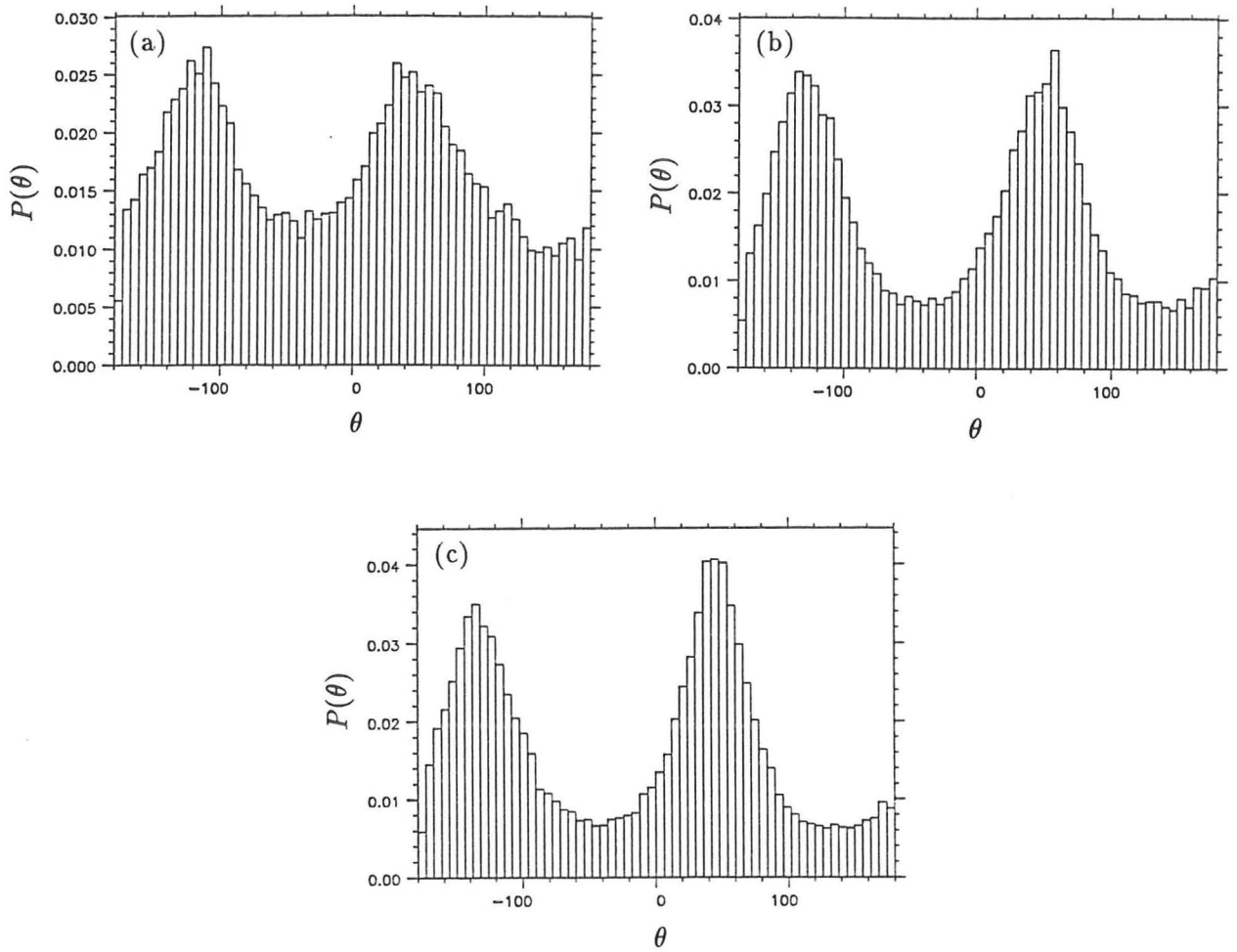
Fig. 4.24 Distribution of the inclination angle of the projection of the vorticity vectors in (x, z)-plane at total shear (a) $\beta = 0.5$; (b) 1.0; (c) 1.5; data weighted with the magnitude of the projected vorticity.
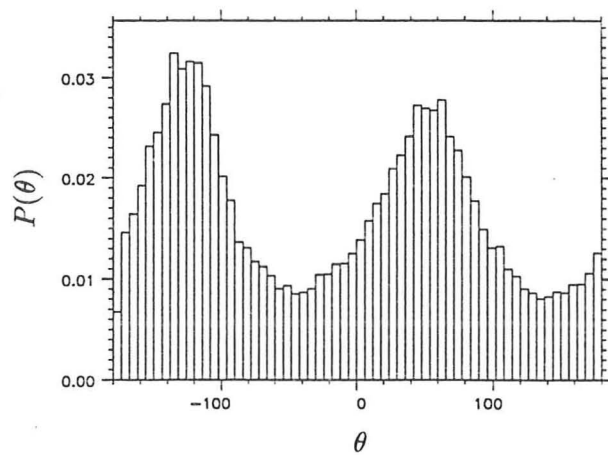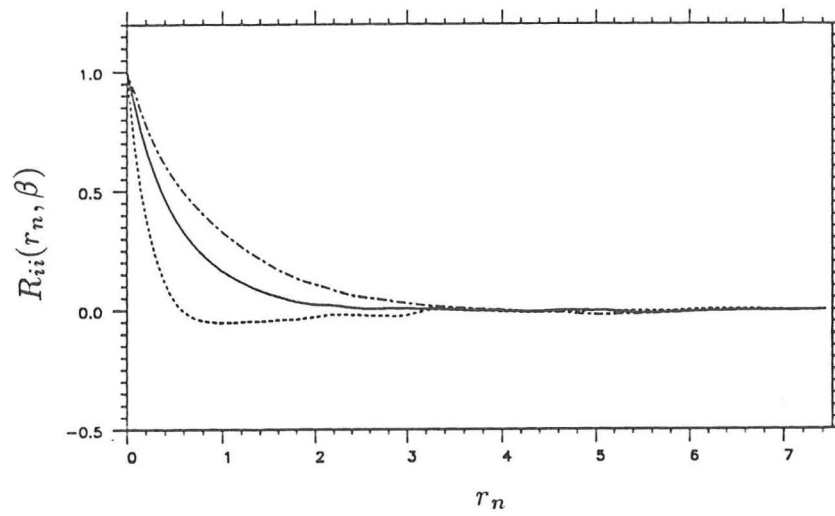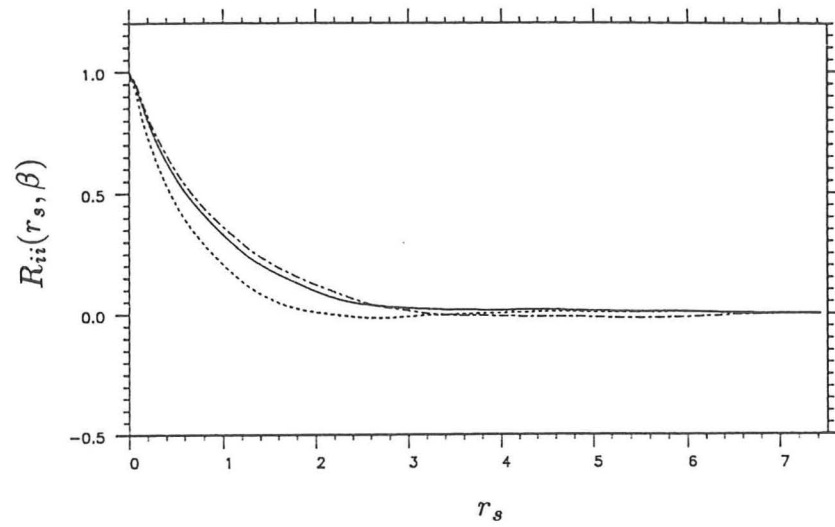

Fig. 4.25 Same as 4.24(c) but with the data not weighted.

$R_{11}(r)$ ——————————

$R_{22}(r)$ ······························

$R_{33}(r)$ ——·——·——·——·——

Fig. 4.26 Two-point correlations of the velocity components at $\beta = 3.0$ with direction of separation in the (a) s-direction; (b) n-direction.
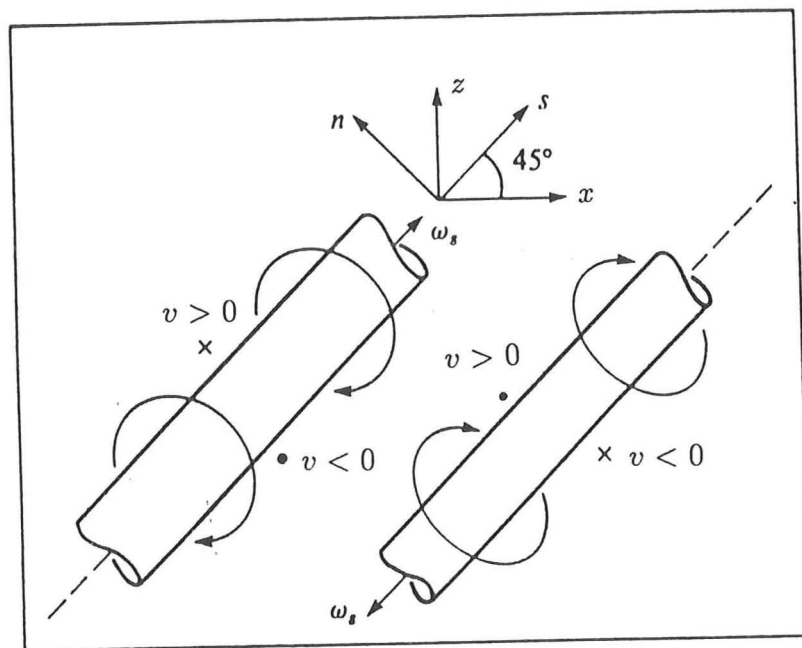
Fig. 4.27 Sketch of the vortical structure inclined at 45° to the flow direction.

Flow direction

Flow direction

plane

View

Inclined feature

45°

View

plane

Inclined feature

45°
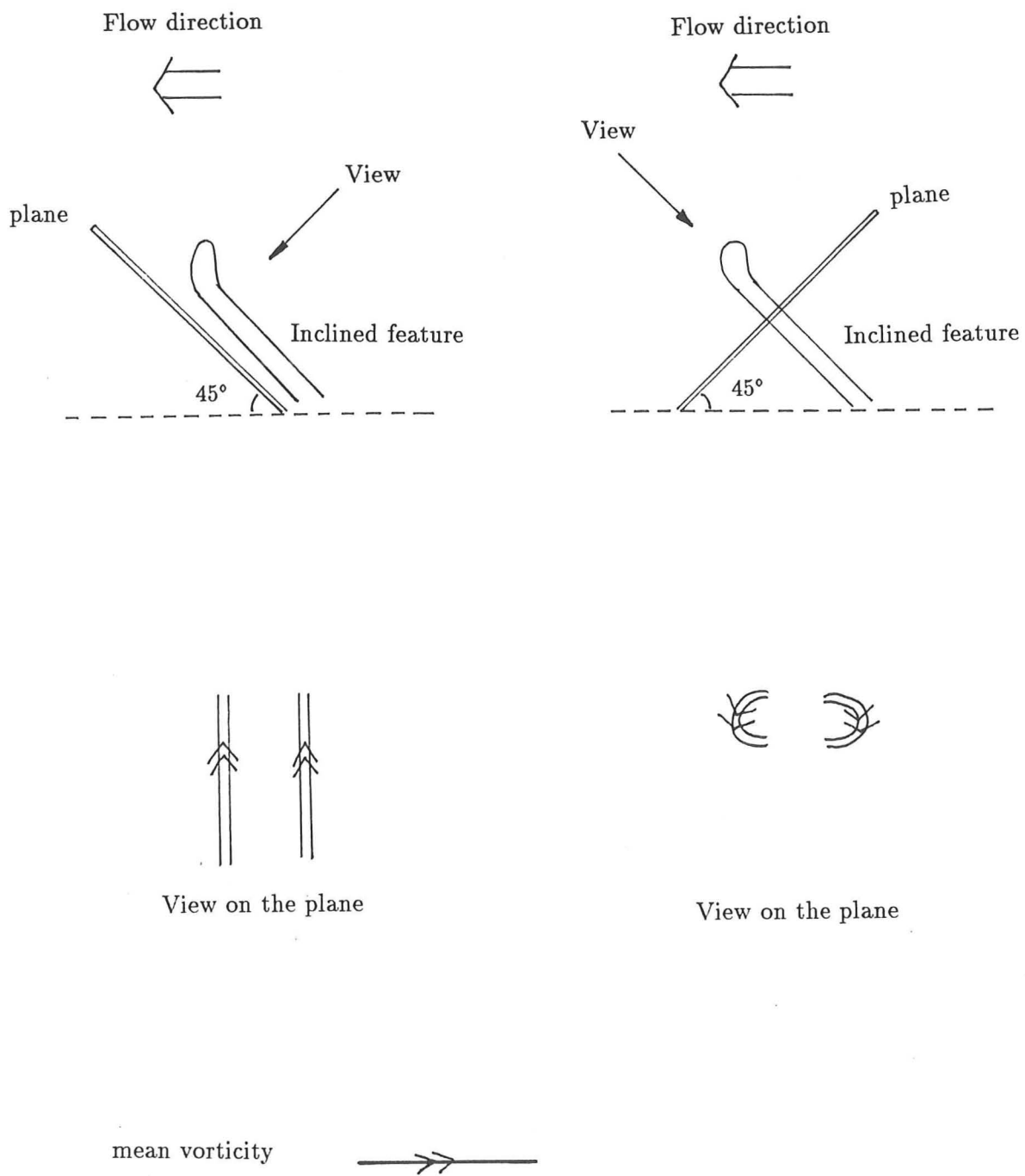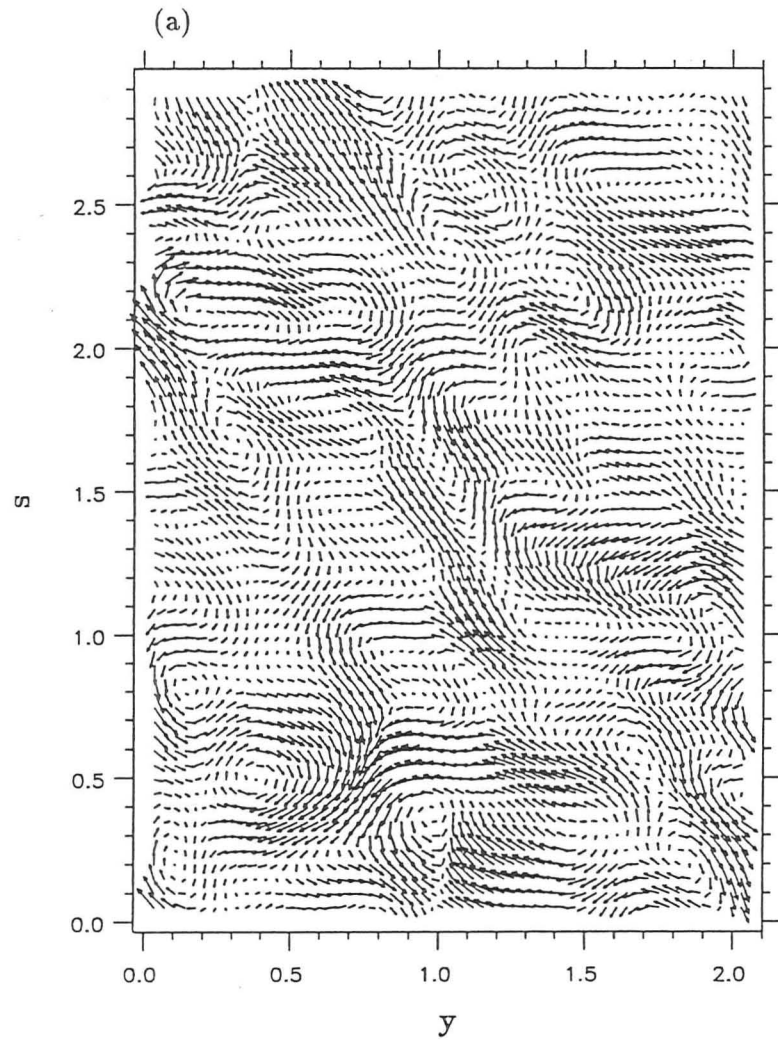
View on the plane

View on the plane

mean vorticity

Fig. 4.28   Inclined features being converted past the plane (a) 45°; (b) 135° to the flow direction respectively.
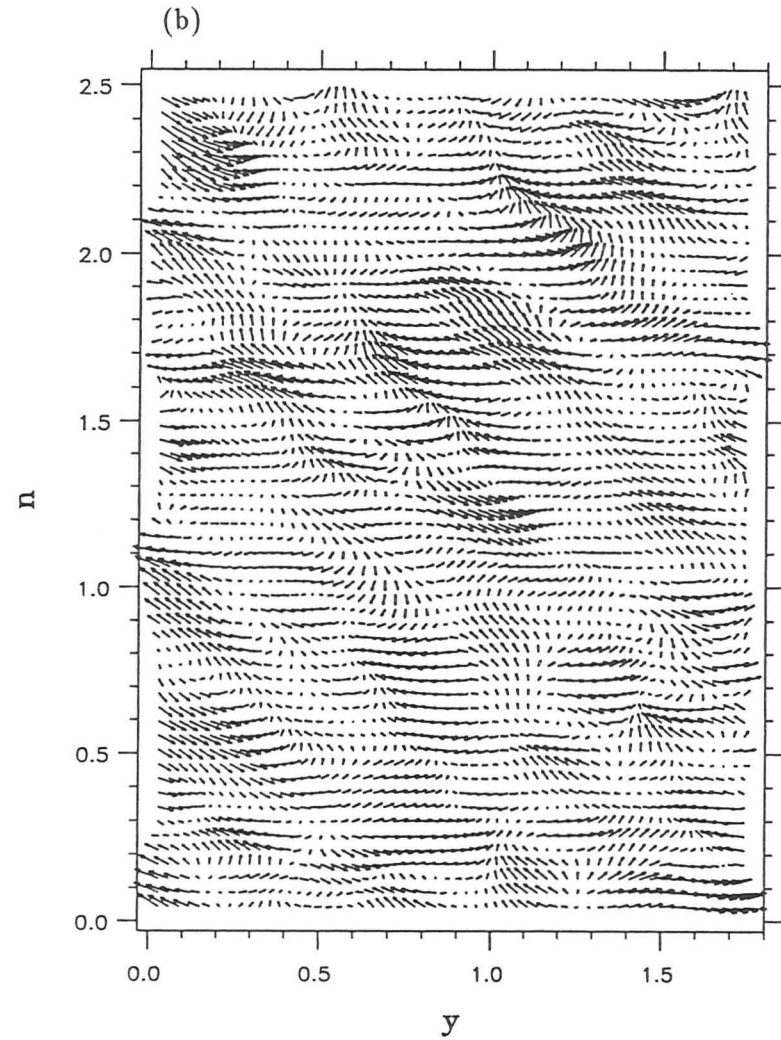
VORTICITY VECTORS

VORTICITY VECTORS

(a)

(b)

Fig. 4.29 Projection of the instantaneous vorticity vectors at $\beta = 7.2$ in (a) (y, r_s)-plane (inclined at $45°$); (b) (y, r_n)-plane (inclined at $135°$). The vectors are drawn on the inclined planes.

Fig. 4.30 Contours of the streamwise turbulent velocity u for a homogeneous turbulent field with von Kármán energy spectrum at low shear rate: $\alpha = 20.0$ and $\beta = 9.4$. Positive values are contoured by solid lines and negative values are contoured by dashed lines.
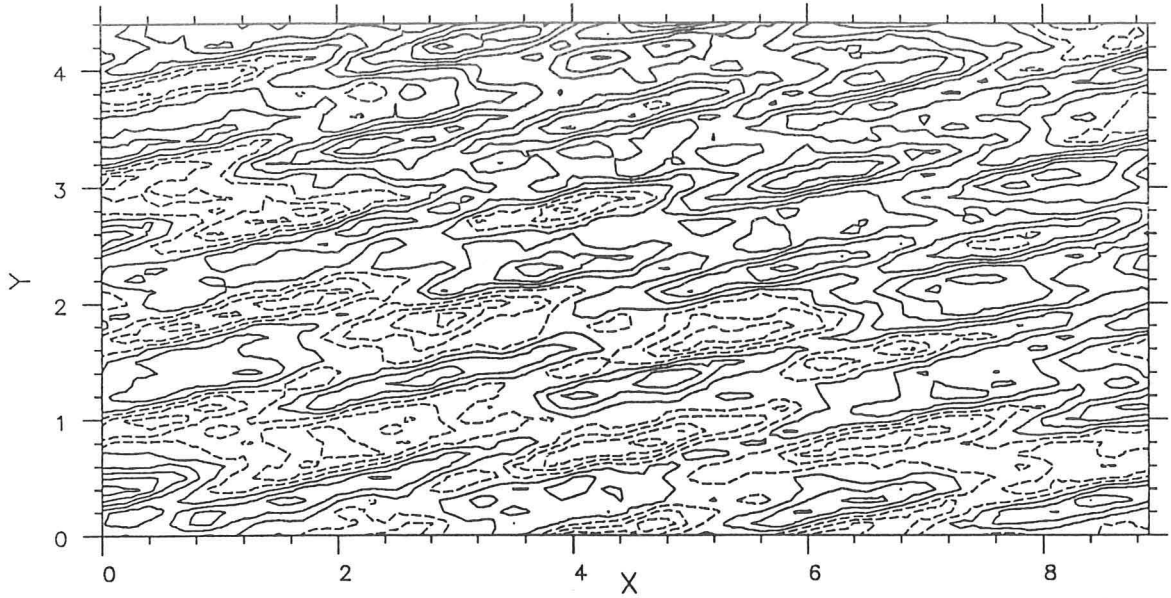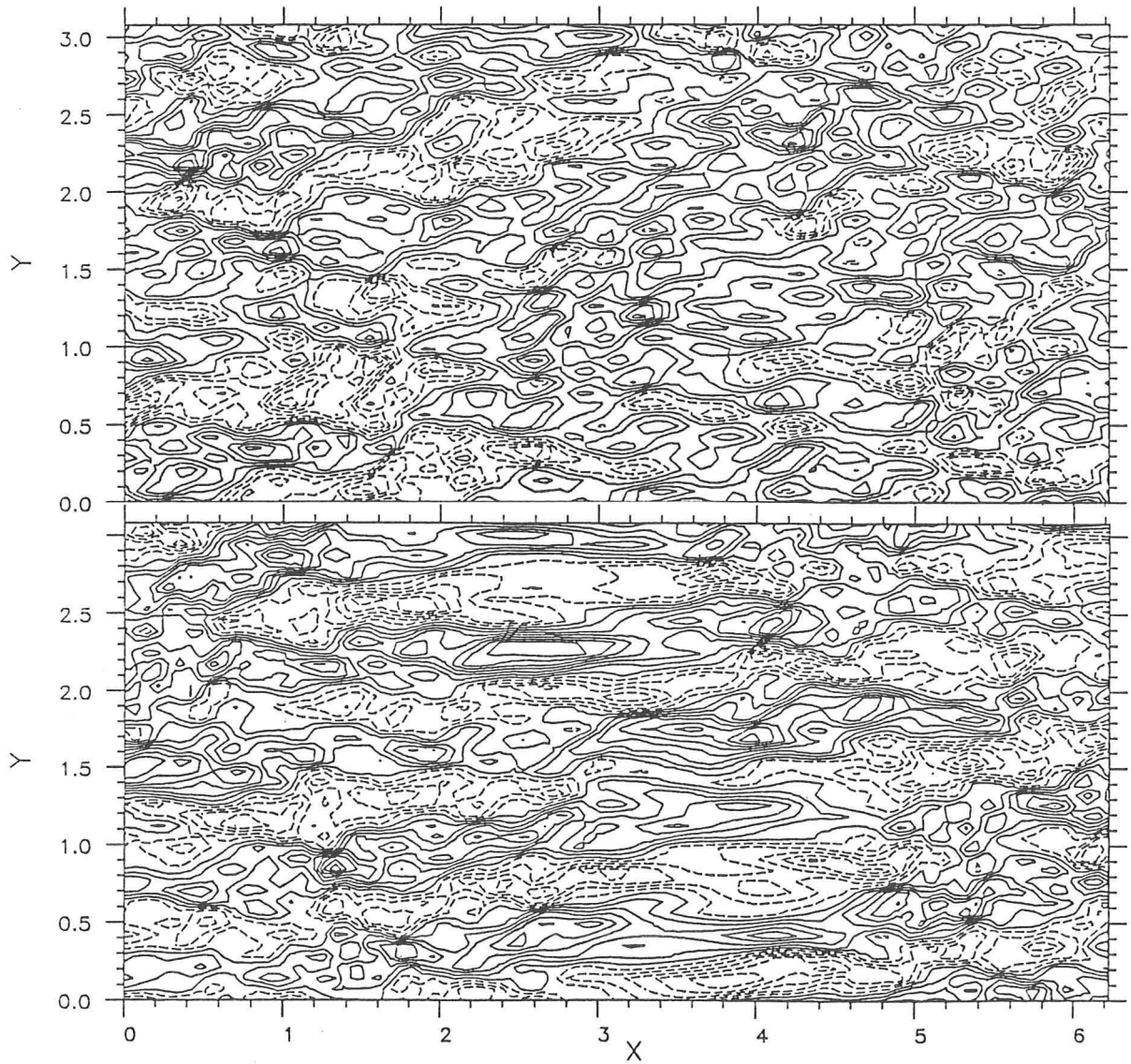

Fig. 4.31 Contours of the streamwise turbulent velocity u for a homogeneous turbulent field with von Kármán energy spectrum at high shear rate: $\alpha = 43.2$ and (a) $\beta = 4.7$; (b) $\beta = 9.4$.
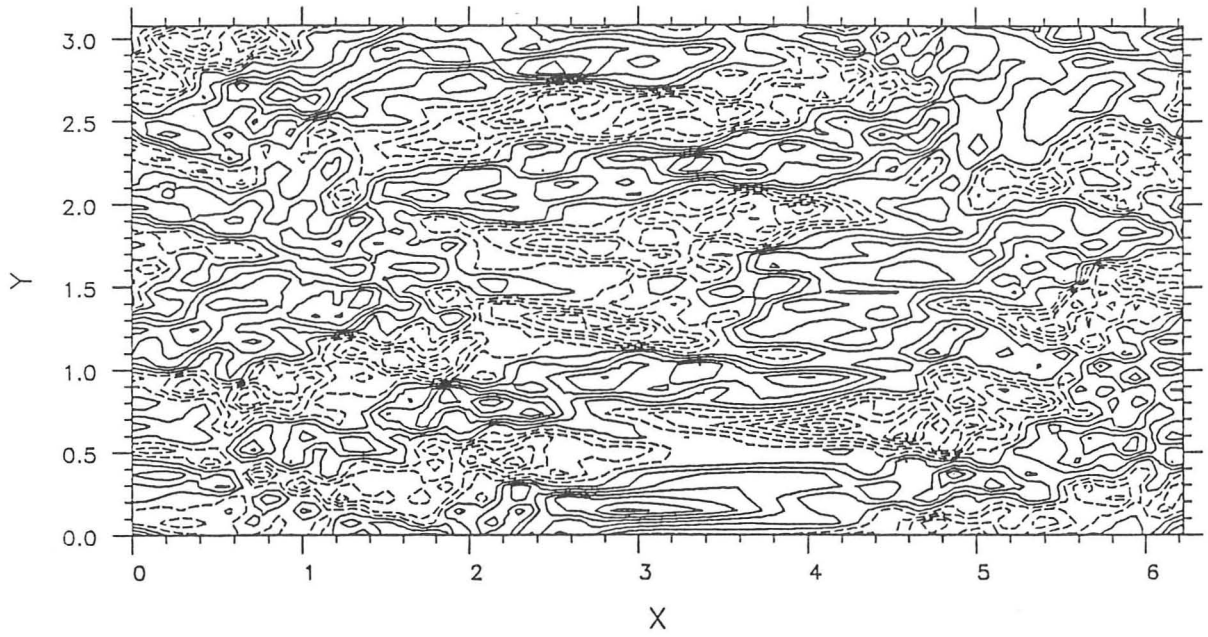
Fig. 4.32 Contours of spanwise vorticity fluctuation ω_y in the (x, y)-plane.
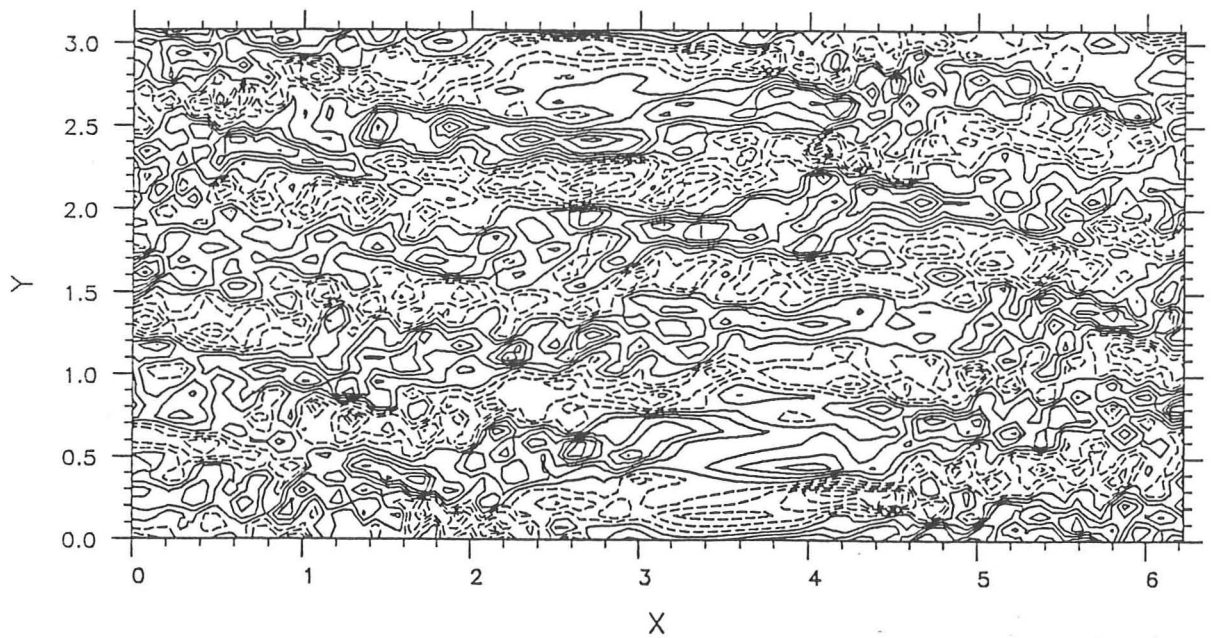
Fig. 4.33 Contours of vertical vorticity fluctuation ω_z in the (x, y)-plane.
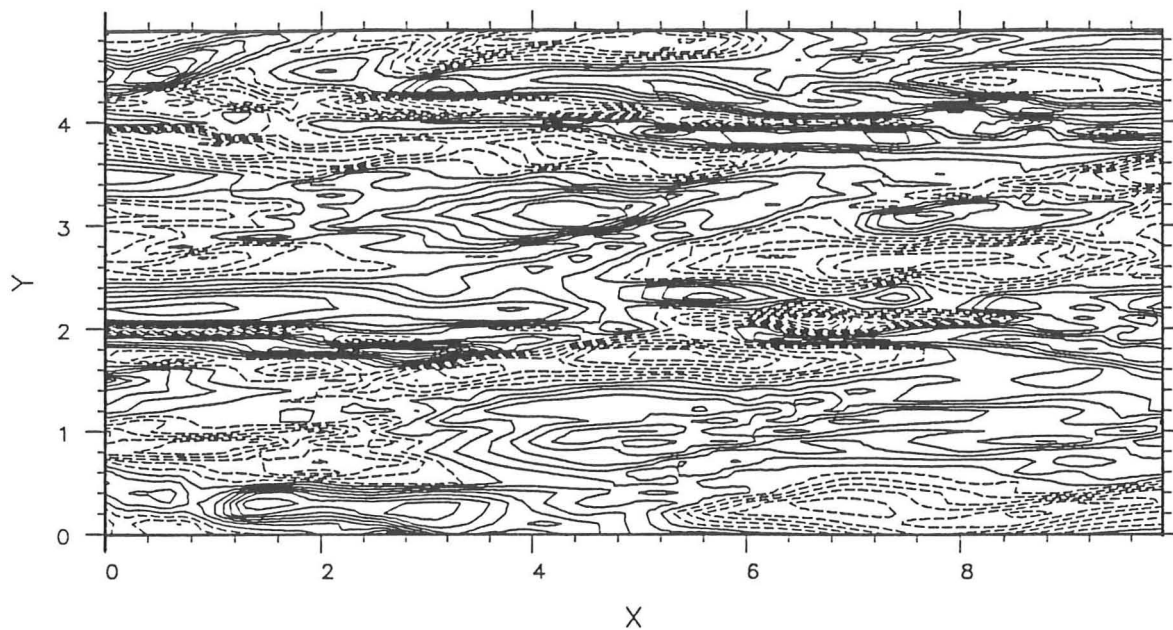
Fig. 4.34 Contours of the streamwise turbulent velocity u for a homogeneous turbulent field with energy spectrum E_1: $\alpha = 43.2$ and $\beta = 25.6$.
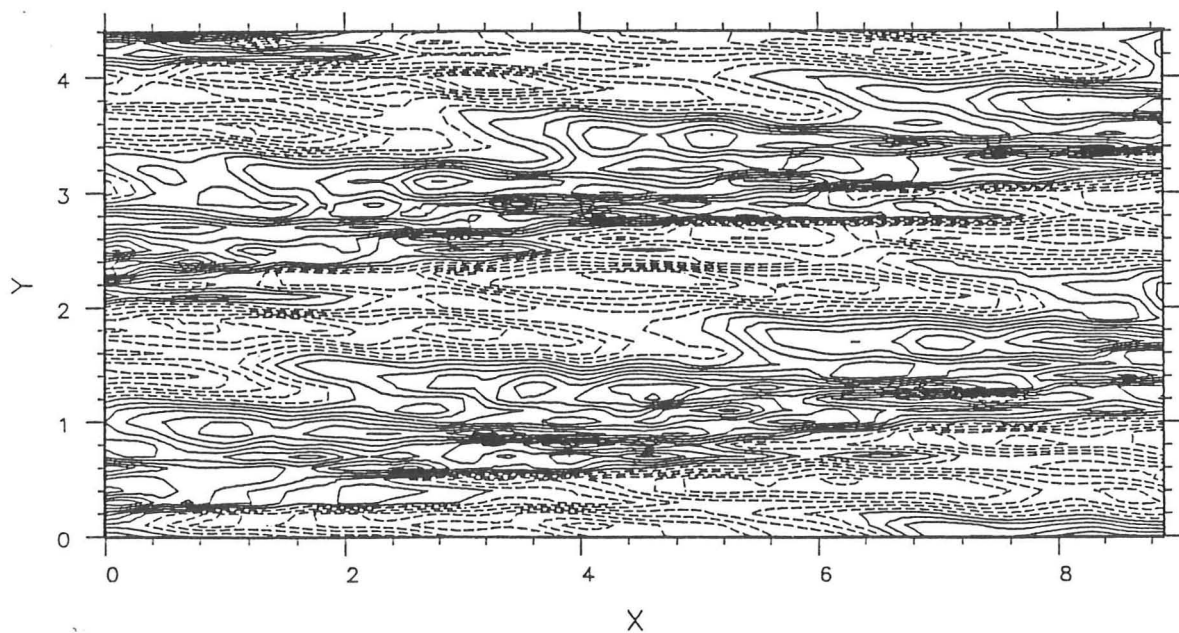
Fig. 4.35 Contours of the streamwise turbulent velocity u for a homogeneous turbulent field with energy spectrum E_2: $\alpha = 43.2$ and $\beta = 25.6$.

(a)

(b)
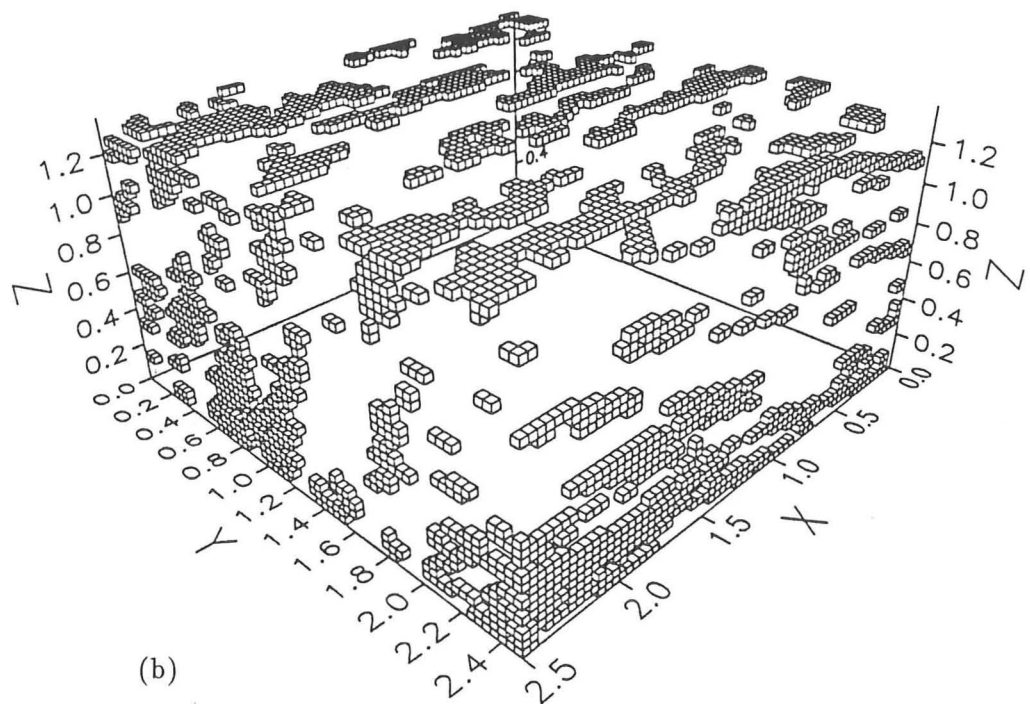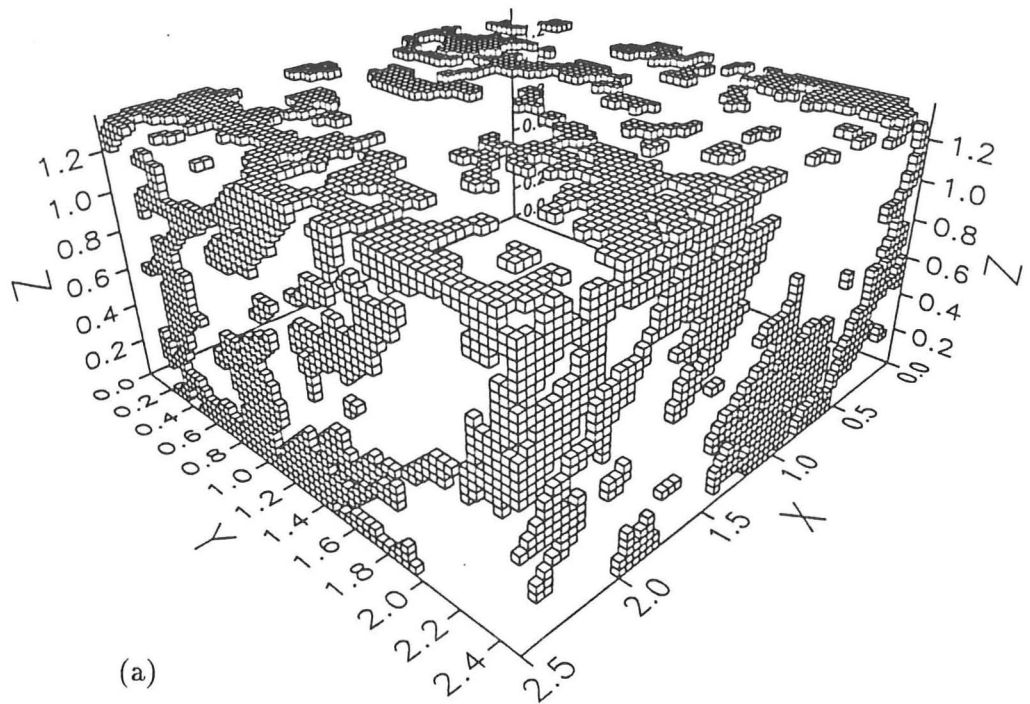
Fig. 4.36 Streaming regions plotted only on the surface of a cuboid (a) initially homogeneous, isotropic turbulence with $\beta = 0.0$; (b) after shear is applied with $\beta = 5.0$.
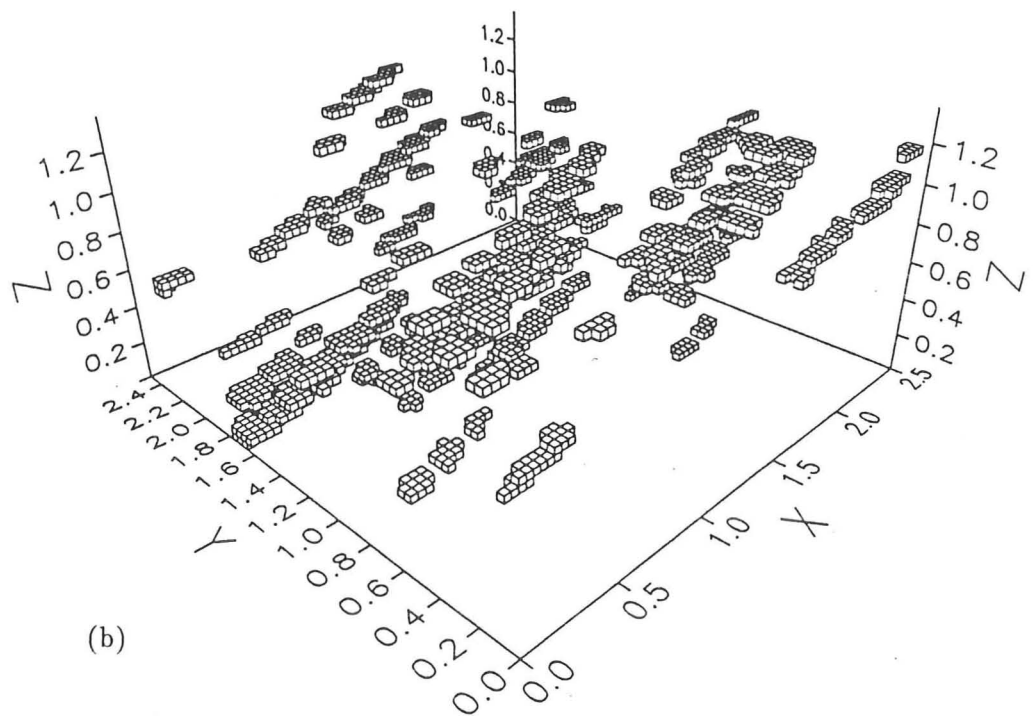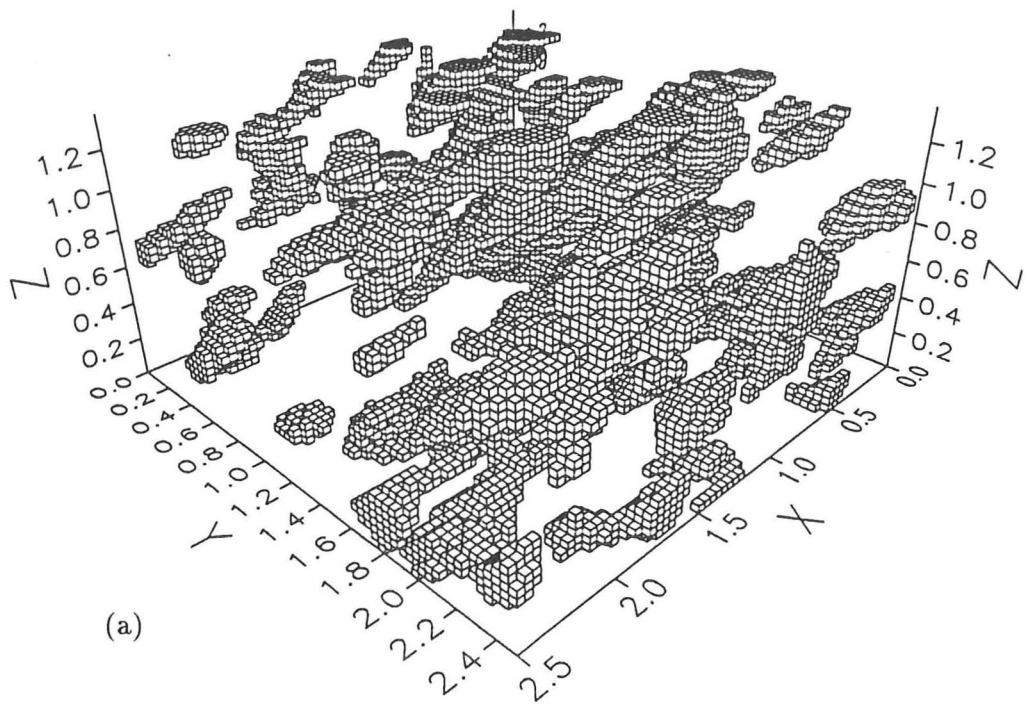
Fig. 4.37 Eddy regions plotted only in the volume of a cuboid (a) initially homogeneous, isotropic turbulence with $\beta = 0.0$; (b) after shear is applied with $\beta = 5.0$.

Fig. 4.38 Convergence regions plotted in the volume of a cuboid (a) initially homogeneous, isotropic turbulence with $\beta = 0.0$; (b) after shear is applied with $\beta = 5.0$.

Eddy regions

(a)

Streaming regions

(b)

Convergence regions

(c)

Fig. 4.39 Elliptics have been fitted to (a) eddy regions; (b) streaming regions and (c) convergence regions.

REFERENCES

ARNOLD, L. 1974 *Stochastic Differential Equation: Theory and Application.* Wiley, London.

AUTON, T.R. 1983 The dynamics of bubbles, drops and particles in motion in liquids. Ph.D dissertation *University of Cambridge.*
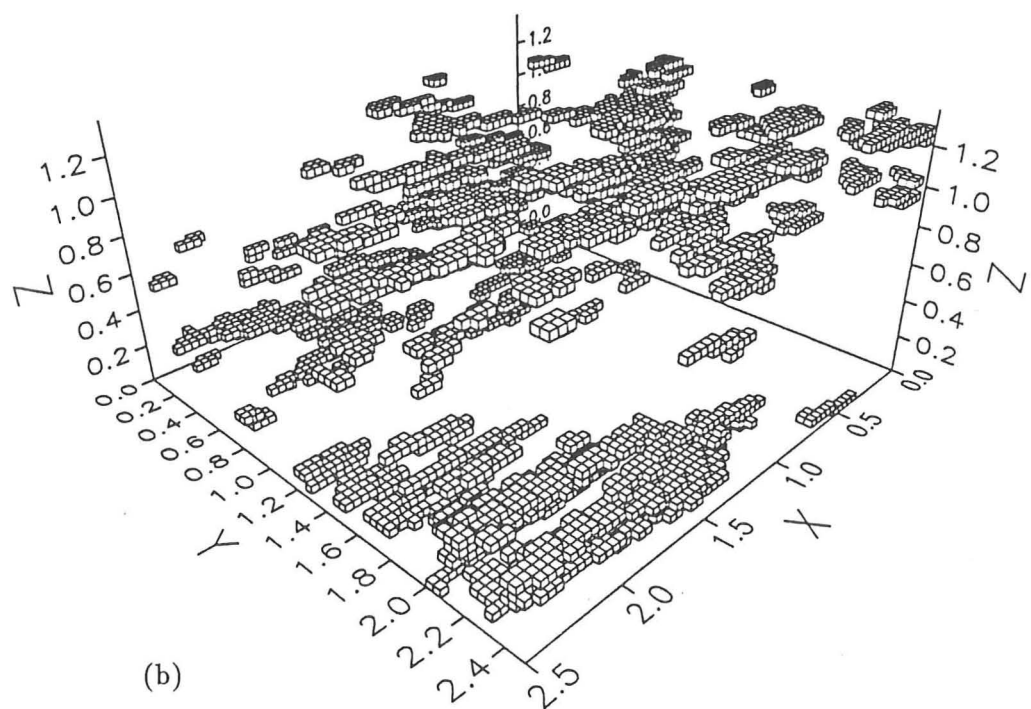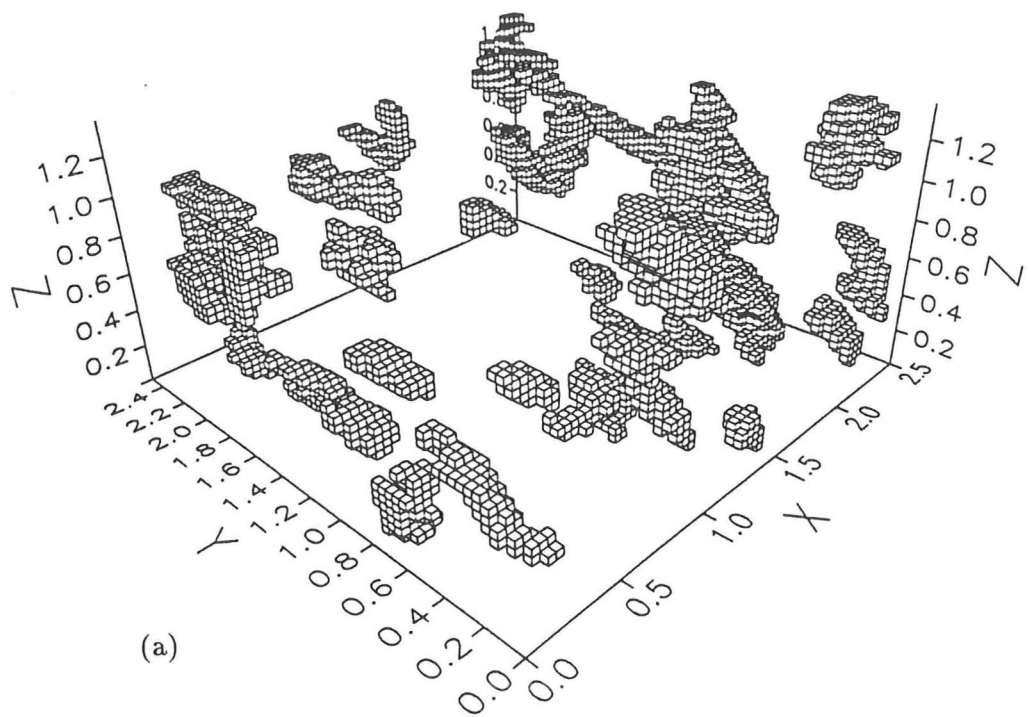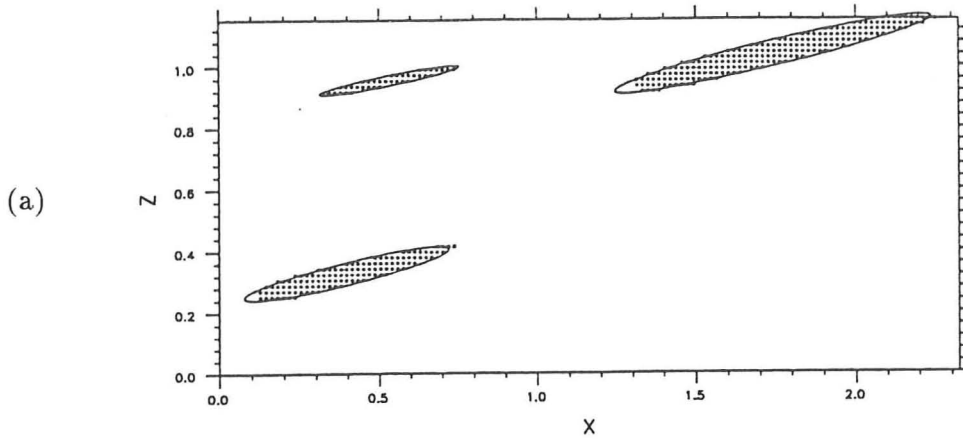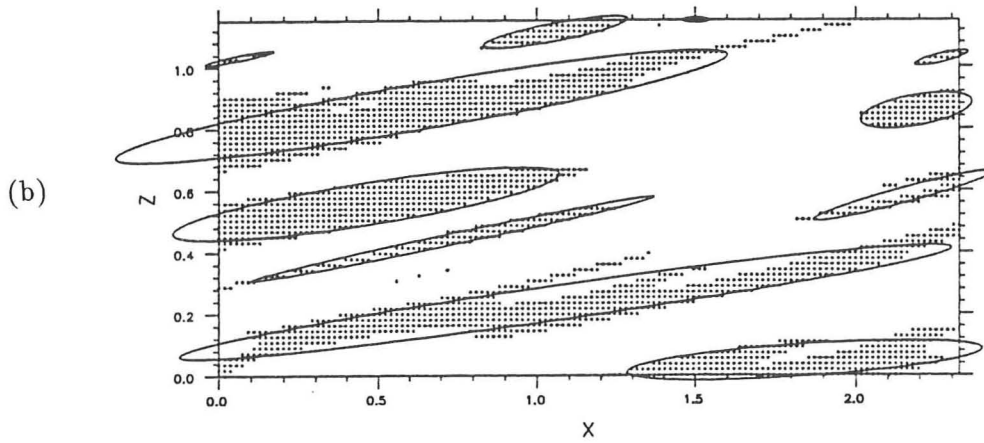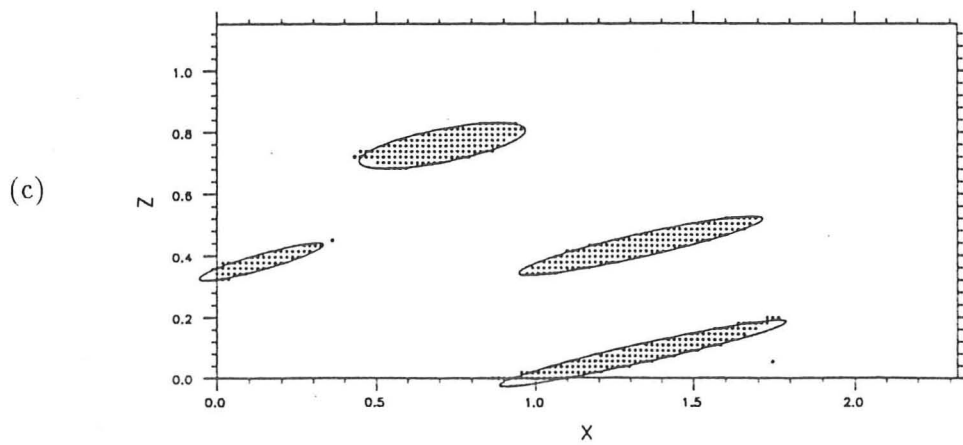
AUTON, T.R. 1987 The lift force on a spherical body in a rotational flow. *J. Fluid Mech.* **183**, 199–218.

AUTON, T.R., HUNT, J.C.R. & PRUD'HOMME, M. 1988 The force exerted on a body in inviscid unsteady non-uniform rotational flow. *J. Fluid Mech.* **197**, 241–257.

BASSET, A.B. 1888 *A treatise on Hydrodynamics.* Vol2 Ch5 Deighton, Bell and Co., Cambridge, England.

BATCHELOR, G.K. 1949 Diffusion in a field of homogeneous turbulence. *Austral. J. Sci. Res.* **A2**, 437–450.

BATCHELOR, G.K. 1952 Diffusion in a field of homogeneous turbulence, part II, the relative motion of particles. *Proc. Camb. Phil. Soc.* **48**, 345–362.

BATCHELOR, G.K. 1953 *The theory of homogeneous turbulence.* CUP, New York.

BATCHELOR, G.K. 1959 Small-scale variation of convected quantities like temperature in turbulent fluid (Part 1. General discussion and the the case of small conductivity. *J. Fluid Mech.* **5**, 113–133.

BATCHELOR, G.K. & PROUDMAN, I. 1954 The effect of rapid distortion of a fluid in turbulent motion. *Q. J. Mech. Appl. Math.* **7**, 83–103.

BATCHELOR, G.K. & TOWNSEND, A.A. 1947 Decay of vorticity in isotropic turbulence. *Proc. Roy. Soc. A,* **190**, 534–560.

BATCHELOR, G.K. & TOWNSEND, A.A. 1956 Turbulence diffusion. In *Surveys in Mechanics* (ed. G.K. Batchelor & R.M. Davies), p. 352. Cambridge University Press.

BAYERLEIN, S.W. 1981 *Mechanisms in bubble transport in turbulent flow. MSc Thesis,* Thayer School of Engineering, Dartmonth College, Hanover New Hamshire, U.S.A.

BOUSSINESQ, J. 1903 *Théorie analytique de la chaleur,* vol2 p. 224 Cauthier-Villars, Paris.

BROADWELL, J.F. & BREIDENTHAL, R.E. 1982 A simple model of mixing and chemical reaction in a turbulent shear layer. *J. Fluid Mech.* **125**, 397–410.

BROWN, D.J. & HUTCHINSON, P. 1979 The interaction of solid or liquid particles and turbulent fluid fields — a numerical simulation. *J. Fluids Eng.* **101**, 265–269.

CARRUTHERS, D.J. & HUNT, J.C.R. 1986 Velocity fluctuations near an interface between a turbulent region and a stably stratified layer. *J. Fluid Mech.* **165**, 475–501.

CARRUTHERS, D.J. 1989 *private communication.*

CHAMPAGNE, F.H., HARRIS, V.G. & CORRSIN, S. 1970 Experiment on nearly homogeneous turbulent shear flow. *J. Fluid Mech.* **41**, 81–139.

CHASE, D.M. 1970 Space-time correlations of velocity and pressure and the role of convection for homogeneous turbulence in the universal range. *Acustica* **22**, 303–320.

CHUNG, J.N. & THOUTT, T.R. 1988 Simulation of particle dispersion in an axisymmetric jet. *J. Fluid Mech.* **186**, 199–222.

CLIFT, R., GRACE, J.R. & WEBER, M.E. 1978 *Bubbles, Drops and Particles.* Academic Press.

COMTE-BELLOT, G. & CORRSIN, S. 1971 Simple Eulerian time correlation of full- and narrow-band velocity signals in grid-generated, isotropic turbulence. *J. Fluid Mech.* **48**, 273–337.

CORRSIN, S. & LUMLEY, J.L. 1956 On the equation of motion for a particle in turbulent fluid. *Appl. Sci. Res.* **6A**, 114–116.

CROW, S.C. 1970 Stability theory of a pair of trailing vortices simulated helical turbulence with molecular diffusivity. *A.I.A.A.* **J.8**, 2172–2179.

CSANADY, G.T. 1963 Turbulent Diffusion of heavy particle in the atmosphere. *J. Atmos. Sci.* **20**, 201–208.

DEARDORFF, J.W. 1970 A numerical study of three-dimensional turbulent channel flow of large Reynolds numbers. *J. Fluid Mech.* **44**, 453–480.

DRUMMOND, I.T., DUANE, S. & HORGAN, R.R. 1984 Scalar diffusion in simulated helical turbulence with molecular diffusivity. *J. Fluid Mech.* **138**, 75–91.

DURBIN, P.A. 1980a A stochastic model of two-particle dispersion and concentration fluctuations in homogeneous turbulence. *J. Fluid Mech.* **100**, 279–302.

DURBIN, P.A. 1980b A random flight model of inhomogeneous turbulent dispersion. *Phys. Fluid* **23**, 2151–2153.

DURBIN, P.A. & HUNT, J.C.R. 1980 Dispersion from elevated line sources in turbulent boundary layers. *J. de Mecanique* **19**, 679–695..

EDWARDS, S.F. 1964 The statistical dynamics of homogeneous turbulence. *J. Fluid Mech.* **18**, 239–273.

FAVRE, A.J., CRANGLIO, J.J. & DUMAS, R. 1957 Space-time double correlations and spectra in a turbulent boundary layer. *J. Fluid Mech.* **2**, 313–342.

FUCHS, N.A. 1964 *The Mechanics of Aerosols.* Macmillan.

GEORGE, W.K., BEUTHER, P.D. & ARNDT, R.E.A. 1984 Pressure spectra in turbulent free shear flows. *J. Fluid Mech.* **148**, 155–191.

GIBSON, M.M. 1963 Spectra of turbulence in a round jet. *J. Fluid Mech.* **15**, 161–173.

GOUESBET, G., DESJONQUÉRES, P. & BERLEMONT, A. 1987 *Eulerian and Lagrangian approaches to turbulent dispersion of particles.* Seminaire International "Transient Phenomena in Multiphase Flow", Int. Center for Heat and Mass Transfer, Dubrovnic.

GOSMAN, A.D. 1981 *Aspect of Computer simulation of liquid-fueled combustors.* AIAA paper 81-0323, 19th Aerospace Sciences Meeting, St. Louis.

GRANT, H.L. 1958 The large eddies of turbulent motion. *J. Fluid Mech.* **4**, 149–190.

GRANT, H.L., STEWART, R.W. & MOILLIET, A. 1962 Turbulent spectra from a tidal channel. *J. Fluid Mech.* **12**, 241–268.

GRAHAM, J.M.R. 1980 The force on sharp-edged cylinders in oscillatory flow at low Keulegan-Carpenter numbers. *J. Fluid Mech.* **97**, 331–346.

HANNA, S.R. 1980 Lagrangian and Eulerian time-scale relation in the daytime boundary layer. *J. Appl. Meteor.* **20**, 242–249.

HARRIS, V.G., GRAHAM, J.H.H. & CORRSIN, S. 1977 Further experiment in nearly homogeneous turbulent shear flow. *J. Fluid Mech.* **81**, 657–687.

HEAD, M.R. & BANDYOPADHYAY, P. 1981 New aspects of turbulent boundary-layer structure. *J. Fluid Mech.* **107**, 297–338.

HELLAND, K.N., VAN ATTA, C.W. & STEGEN, G.R. 1977 Spectral energy transfer in high Reynolds number turbulence. *J. Fluid Mech.* **79**, 337–359.

HINZE, J.O. 1975 *Turbulence.* McGraw-Hill, New York.

HUNT, J.C.R. 1973 A theory of turbulent flow round two-dimensional bluff bodies. *J. Fluid Mech.* **61**, 625–706.

HUNT, J.C.R. 1985 Turbulent Diffusion from sources in complex flows. *Ann. Rev. Fluid Mech.* **17**, 447–485.

HUNT, J.C.R. 1987 Vorticity and vortex dynamics in complex turbulence flow. Proc. CANCAM (Canadian Congress of Applied Mechanics, London Ontorio). *Trans. Can. Soc. Mech. Engng* **11**, 21–35.

HUNT, J.C.R., AUTON, T.R., SENE, K., THOMAS, N.H. & KOWE, R. 1988a Bubble motions in large eddies and turbulent flows. *Transient phenomena in multiphase flow (ed. N.H. Afgan)* HPC.

HUNT, J.C.R., BUELL, J.C. & WRAY, A.A. 1987 Big whorls carry little whorls. *NASA Report CTR-S87.*

HUNT, J.C.R. & CARRUTHERS, D.J. 1990 Rapid distort theory and the 'problem' of turbulence. *To be appeared in J. Fluid Mech.*

HUNT, J.C.R., MOIN, P. & WRAY, A.A. 1988b Eddies, stream and convergence zones in turbulent flows. *NASA Report CTR-S88.*

HUNT, J.C.R. & NALPANIS, P. 1985 'Saltating and suspended particles over flat and sloping surfaces', in O. E. Barndorff-Nielsen(ed.) Academic Press. *Proceedings of the International Workshop on the Physics of Blown Sand,* Aarhus, Denmark.

INOUE, E. 1951 On turbulent diffusion in the atmosphere. *J. Met. Soc. Japan* **29**, 246–252.

KAIMAL, J.C., WYNGAARD, J.C., LZUMI, Y. & COTE, O.R. 1972 Spectral characteristics of surface-layer turbulence. *Quart. J. R. Met. Soc.* **98**, 563–589.

KIM, J., MOIN, P. & MOSER, R.D. 1987 Turbulence statistics in full-developed channel flow at low Reynolds number. *J. Fluid Mech.* **177**, 133–166.

KLINE, S.J., REYNOLDS, W.C., SCHRAUB, F.A. & RUNSTADLER, P.W. 1967 The structure of turbulent boundary layers. *J. Fluid Mech.* **30**, 741–773.

KOLMOGOROV, A.N. 1941 The local structure of turbulence in incompressible viscous fluid for very large Reynolds numbers. *Acad. Sci., USSR* **30**, 301–305.

KRAICHNAN, R.H. 1970 Diffusion by a random velocity field. *Phys. Fluid* **13**, 22–31.

LANCE, M., MARIÉ, J.L. & BATAILLE, J. 1980 Homogeneous turbulence in bubbly flows. Internal report, Lyon, 1–8.

LANDAHL, M.T. 1967 A wave-guide model for turbulent shear flow. *J. Fluid Mech.* **29**, 441–459.

LEE, M.J., KIM, J. & MOIN, P. 1987 Turbulent structure at high shear rate. *In: Sixth Symposium on Turbulence Shear Flows, Toulouse, France* (ed. F. Durst *et al.*). pp 22.6.1–22.6.6.

LESIEUR, M. 1987 *Turbulence in fluids: stochastic and numerical modelling.* M. Nijhoff, Dordrecht, Netherlands.

LESLIE, D.C. 1973 *Developments in the theory of turbulence.* Clarendon Press, Oxford.

LIGHTHILL, M.J. 1956 The image system of a vortex element in a rigid sphere. *Proc. Camb. Phil. Soc.* **52**, 31–53.

LUMLEY, J.L. 1957 Some problems connected with the motion of small particles in turbulent fluid. Ph.D. dissertation *The John Hopkins University.*

LUMLEY, J.L. 1962 The mathematical nature of the problem of relating Lagrangian and Eulerian statistical functions in turbulence. *In Mécanique de la Turbulence (ed. A Frave) pp. 17–26. Paris, CRNS.*

MALIK, N.A. 1990 Two-particle dispersion in turbulent flow. Ph.D dissertation *University of Cambridge.*

MANTON, M.J. 1973 On the motion of a small particle in the atmosphere. *Boundary-Layer Meteorol.* **6**, 487–504.

MAXEY, M.R. & RILEY J.J. 1983 Equation of motion for a small rigid sphere in a non-uniform flow. *Phys. Fluid* **26**, 883–889.

MAXEY, M.R. & CORRSIN, S. 1986 Gravitation settling of aerosol particles in randomly oriented cellular flow fields. *J. Atmos. Sci.* **43**, 1112–1134.

MAXEY, M.R. 1987 The motion of small spherical particles in a cellular flow field. *Phys. Fluid* **30**, 1915–1928.

MENEGUZZI, M. 1989 CERFACS: Scientific Report.

METCALFE, J.R. 1988 *private communication.*

MOFFATT, H.K. 1965 The interaction of turbulence with strong wind shear *In Atmospheric Turbulence and Radio Waves Propagation: Proc. of intern. Collq., Moscow,* (eds. A.N. Yaglom & V.I. Tatarsky), pp. 139–156. Publishing House ⟪NAUKA⟫: Moscow.

MOIN, P. & KIM, J. 1982 Numerical investigation of turbulent channel flow. *J. Fluid Mech.* **118**, 341–377.

MOIN, P. & KIM, J. 1985 The structure of the vorticity field in turbulent channel flow. Part 1. Analysis of the vorticity fields and statistical correlations. *J. Fluid Mech.* **155**, 441–464.

MONIN, A.S.& YAGLOM, A.M. 1971 *Statistical Fluid Mechanics.* Vol. 1, M.I.T. Press.

MONIN, A.S.& YAGLOM, A.M. 1975 *Statistical Fluid Mechanics.* Vol. 2, M.I.T. Press.

MORSI, S.A. & ALEXANDER, A.J. 1972 An investigation of particle trajectories in two-phase flow systems. *J. Fluid Mech.* **55**, 193–208.

NIELSEN, P. 1984 On the motion of suspended sand particles. *J. Geophys Res.* **89**, 616–626.

ORSZAG, S.A. & PATTERSON, G.S. 1972 "Numerical simulations of turbulence" in "Statistical models and turbulence" edited by M. Rosenblatt & C. Van Atta. *Springer Verlag* **12**, 127–147.

OSEEN, C.W. 1927 *Hydrodynamik* p. 132, Leipzig.

PAO, Y.H. 1965 Structure of turbulent velocity and scalar field at large wavenumbers. *Phys. Fluid* **8**, 1063–1070.

PASQUILL, F. 1974 *Atmospheric diffusion.* 2nd edn. Wiley.

PEARSON, J.R.A. 1959 The effect of uniform distortion on weak homogeneous. *J. Fluid Mech.* **5**, 274–288.

PERKINS, R.J. & HUNT, J.C.R. 1986 *Particle transport in turbulent shear flow.* Report to SERC.

PERKINS, R.J. & HUNT, J.C.R. 1987 *Particle transport in turbulent report.* Final report to SERC.

PERRY, A.E. & CHONG, M.S. 1987 A description of eddying motions and flow patterns using critical-point concepts. *Ann. Rev. Fluid Mech.*, 125–155.

PETERS, N.& WILLIAMS, F.A. 1988 22nd Symposium on Combustion, *Seattle.*

PHILIP, J.R. 1967 Relation between Eulerian and Lagrangian statistics. *Boundary Layers and Turbulence, Physics of Fluid Supplement*, 69–71.

PHYTHIAN, R. 1975 Dispersion by random velocity fields. *J. Fluid Mech.* **67**, 145–153.

PISMEN, L.M. & NIR, A. 1979 The effect of a steady drift on the dispersion of a particle in turbulent fluid. *J. Fluid Mech.* **94**, 369–381.

POPE, S.B. 1983 Consistent modelling of scalars in turbulent flows. *Phys. Fluid* **26**, 404–408.

PROUDMAN, I. 1951 A comparison of Heisenberg's spectrum of turbulence with experiment. *Proc. Camb. Phil. Soc.* **47**, 158–176.

REEKS, M.W. 1977 On the dispersion of small particles suspended in an isotropic turbulent fluid. *J. Fluid Mech.* **83**, 529–546.

REEKS, M.W. 1980 Eulerian direct interaction applied to the statistical motion of particles in turbulent fluid. *J. Fluid Mech.* **97**, 569–590.

RILEY, J.J. 1971 Ph.D. dissertation *The John Hopkins University.*

RILEY, J.J. & PATTERSON, G.S. 1974 Diffusion experiments with numerically integration isotropic turbulence. *Phys. Fluid.* **17(2)**, 292–297.

ROGALLO, R.S. 1981 *Numerical experiments in homogeneous turbulence.* NASA Tech. Memo. 81315.

ROGALLO, R.S. & MOIN, P. 1984 Numerical simulation of turbulent flows. *Ann. Rev. Fluid Mech.* **16**, 99–157.

ROGERS, N.M. & MOIN, P. 1987 The structure of the vorticity field in homogeneous turbulent flows. *J. Fluid Mech.* **176**, 33–66.

SATO, Y. & YAMAMOTO, K. 1987 Lagrangian measurement of fluid- particle motion in an isotropic turbulent field. *J. Fluid Mech.* **175**, 183–199.

SHIH, TSAN-HSING & LUMLEY, J.L. 1986 Second-order modelling of particle dispersion in a turbulent flow. *J. Fluid Mech.* **163**, 349–363.

SHLIEN, D.J. & CORRSIN, S. 1974 A measurement of Lagrangian velocity autocorrelations in approximately isotropic turbulence. *J. Fluid Mech.* **62**, 225–271.

SNYDER, W.H. & LUMLEY, J.L. 1971 Some measurements of particle velocity autocorrelation functions in a turbulent flow. *J. Fluid Mech.* **48**, 47–71.

SOO, S.L. 1967 *Fluid dynamics of multiphase systems.* Blaisdell.

SPALDING D.B. 1971 Concentration fluctuations in a round free jet. *Chem. Eng. Sci.* **26**, 95–107.

SQUIRES, J. 1988 *private communication.*

STEWART, R.W. 1951 Triple velocity correlations in isotropic turbulence. *Proc. Roy. Soc. A,* **165**, 73–92.

TAYLOR, G.I. 1921 Diffusion by continuous movements. *Proc. London Math. Soc.* **20**, 196–211.

TCHEN, C.M. 1947 Mean value correlation problems connected with the motion of small particles suspended in a turbulent fluid. Ph.D. dissertation *University of Delft.*

TENNEKES, H. 1975 Eulerian and Lagrangian time microscales in isotropic turbulence. *J. Fluid Mech.* **67**, 561–567.

TENNEKES, H. & LUMLEY, J.L. 1972 *A first course in Turbulence.* M.I.T. Press.

THEODORSEN, T. 1952 *Mechanism of turbulence.* In Proc. 2nd Midwestern Conf. on Fluid Mech. Ohio State University, Columbus Ohio.

THOMSON, D.J. 1984 Random walk modelling of diffusion in inhomogeneous turbulence. *Quart. J. R. Met. Soc.* **110**, 1107–1120.

TOLLMEIN, W. 1938 Uber Krafte und momente in schwach gekrummten oder konvergenten stromungen. *Ing-Arch.* **9**, 308–319.

TOOBY, P.F., WICK, G.L. & ISAACS, J.D. 1977 The motion of a small sphere in a rotating velocity field: A possible mechanism for suspending particles in turbulence. *J. Geophys. Res.* **82(15)**, 2096–2100.

TOWNSEND, A.A. 1966 Internal waves produced by a convective layer. *J. Fluid Mech.* **65**, 475–501.

TOWNSEND, A.A. 1970 Entrainment and the structure of turbulent flow. *J. Fluid Mech.* **41**, 13–46.

TOWNSEND, A.A. 1976 *The structure of turbulent shear flow.* Cambridge University Press.

TOWNSEND, A.A. 1980 The response of sheared turbulence to additional distortion. *J. Fluid Mech.* **98**, 171–191.

TURFUS, C. 1983 Stochastic Modelling of turbulent dispersion near surface. Ph.D. dissertation *University of Cambridge.*

TURFUS, C. & HUNT, J.C.R. 1986 A stochastic analysis of the displacements of fluid elements in inhomogeneous turbulence using Kraichnan's method of random modes. *In Advances in Turbulence*, 191–203 ed. G. Comte-Bellot & J. Mathieu.

UBEROI, M.S. 1953 Quadruple velocity correlations and pressure fluctuations in isotropic turbulence. *J. Atoms. Sci.* **20**, 197–204.

WRAY, A.A. & HUNT, J.C.R. 1989 Algorithms for classification of turbulent structures. IUTAM, symposium on 'Topological Fluid Mechanics'. *Cambridge, CUP.*

WALKLATE, P.J. 1987 A random-walk model for dispersion of heavy particles in turbulent air flow. *Boundary-Layer Meteorol.* **39**, 175–190.

WEINSTOCK, J. 1978 Analytical approximations in the theory of turbulent diffusion. *Phys. Fluid* **21**, 887–890.

WELLS, M.R. & STOCK, D.E. 1983 The effects of crossing trajectories on the dispersion of particles in a turbulent flow. *J. Fluid Mech.* **136**, 31–61.

WHITE, B.R 1982 Two phase measurements on saltating particles in a turbulent boundary layer flow. *Int. J. Multiphase Flow* **8**, 459–467.

WYNGAARD, J.C. & COTE, O.R. 1972 Modelling buoyancy driven mixed layer. *J. Atmos. Sci.* **33**, 1974–1988.

YAKIMOV, Y.L. 1973 Forces acting on a small body in a flowing incompressible liquid, and equations of motion of a two-phase medium. *Fluid Dynamics.* **8**, 411–430.

YEUNG, P.K. & POPE, S.B. 1989 Lagrangian statistics from direct numerical simulations of isotropic turbulence. *J. Fluid Mech.* **207**, 531–586.

YUDINE, M.I. 1959 Physical consideration on heavy particle diffusion. *Adv. Geophys.* **6**, 185-191.

YULE, A.J. 1980 Investigations of eddy coherence in jet flows. In the role of coherent structures in modelling turbulence and mixing. (ed. J. Jinenez) *pp 188–207 Springer.*

APPENDIX A: **Implication on the choice of** $\mathbf{W}_n(t)$

In the following, we obtain a choice of $\mathbf{W}_n(t)$ which ensures that the velocity $\mathbf{u}_\ell(\mathbf{x}, t)$ has the small and large time behaviour of the Eulerian velocity correlation function.

The Eulerian time correlation function of $\mathbf{u}_\ell(\mathbf{x}, t)$ is

$$\langle \mathbf{u}_\ell(\mathbf{x}, t).\mathbf{u}_\ell(\mathbf{x}, t')\rangle = \sum_n \langle \mathbf{a}_n \wedge \widehat{\boldsymbol{\kappa}}_n.\mathbf{a}_n \wedge \widehat{\boldsymbol{\kappa}}_n \cos \boldsymbol{\kappa}_n.[\mathbf{x} + \boldsymbol{\chi}_n(\boldsymbol{\kappa}_n, t)] \cos \boldsymbol{\kappa}_n.[\mathbf{x} + \boldsymbol{\chi}_n(\boldsymbol{\kappa}_n, t')]\rangle$$

$$+ \sum_n \langle \mathbf{b}_n \wedge \widehat{\boldsymbol{\kappa}}_n.\mathbf{b}_n \wedge \widehat{\boldsymbol{\kappa}}_n \sin \boldsymbol{\kappa}_n.[\mathbf{x} + \boldsymbol{\chi}_n(\boldsymbol{\kappa}_n, t)] \sin \boldsymbol{\kappa}_n.[\mathbf{x} + \boldsymbol{\chi}_n(\boldsymbol{\kappa}_n, t')]\rangle$$

$$+ \sum_{n \neq m} \langle \mathbf{a}_n \wedge \widehat{\boldsymbol{\kappa}}_n.\mathbf{a}_m \wedge \widehat{\boldsymbol{\kappa}}_m \cos \boldsymbol{\kappa}_n.[\mathbf{x} + \boldsymbol{\chi}_n(\boldsymbol{\kappa}_n, t)] \cos \boldsymbol{\kappa}_m.[\mathbf{x} + \boldsymbol{\chi}_m(\boldsymbol{\kappa}_m, t')]\rangle$$

$$+ \sum_{n \neq m} \langle \mathbf{b}_n \wedge \widehat{\boldsymbol{\kappa}}_n.\mathbf{b}_m \wedge \widehat{\boldsymbol{\kappa}}_m \sin \boldsymbol{\kappa}_n.[\mathbf{x} + \boldsymbol{\chi}_n(\boldsymbol{\kappa}_n, t)] \sin \boldsymbol{\kappa}_m.[\mathbf{x} + \boldsymbol{\chi}_m(\boldsymbol{\kappa}_m, t')]\rangle$$

$$+ 2\sum_{n,m} \langle \mathbf{a}_n \wedge \widehat{\boldsymbol{\kappa}}_n.\mathbf{b}_m \wedge \widehat{\boldsymbol{\kappa}}_m \cos \boldsymbol{\kappa}_n.[\mathbf{x} + \boldsymbol{\chi}_n(\boldsymbol{\kappa}_n, t)] \sin \boldsymbol{\kappa}_m.[\mathbf{x} + \boldsymbol{\chi}_m(\boldsymbol{\kappa}_m, t')]\rangle. \quad (A1)$$

It can be easily shown that the third, forth and fifth terms are zero and let us consider the first and second terms together, we obtain

$$\langle \mathbf{u}_\ell(\mathbf{x}, t).\mathbf{u}_\ell(\mathbf{x}, t')\rangle = \frac{2}{3} \sum_n \langle \mathbf{a}_n^2 \rangle \cdot \left\langle \widehat{\boldsymbol{\kappa}}_n^2 \cos \boldsymbol{\kappa}_n.[\boldsymbol{\chi}_n(\boldsymbol{\kappa}_n, t') - \boldsymbol{\chi}_n(\boldsymbol{\kappa}_n, t)]\right\rangle$$

$$= \frac{2}{3} \sum_n \langle \mathbf{a}_n^2 \rangle \cdot \langle \cos \boldsymbol{\kappa}_n.[\boldsymbol{\chi}_n(\boldsymbol{\kappa}_n, t') - \boldsymbol{\chi}_n(\boldsymbol{\kappa}_n, t)]\rangle. \quad (A2)$$

Therefore, in normalised form, the Eulerian correlation function is

$$R^{(E)}(\mathbf{x}; t, t') = \frac{\langle \mathbf{u}_\ell(\mathbf{x}, t).\mathbf{u}_\ell(\mathbf{x}, t')\rangle}{\sqrt{\langle \mathbf{u}_\ell^2(\mathbf{x}, t)\rangle} \cdot \sqrt{\langle \mathbf{u}_\ell^2(\mathbf{x}, t')\rangle}}. \quad (A3)$$

But $\mathbf{u}_\ell(\mathbf{x}, t)$ is a stationary function, therefore the auto-correlation function depends only upon the difference $t - t'$, substituting (A2) into above (A3) and let $t' = 0$, we obtain

$$R^{(E)}(\mathbf{x}, t) = \sum_n \langle a_n^2 \rangle \cdot \langle \cos \boldsymbol{\kappa}_n.[-\boldsymbol{\chi}_n(\boldsymbol{\kappa}_n, t)]\rangle \bigg/ \sum_n \langle a_n^2 \rangle. \quad (A4)$$

This can be conveniently written in a complex form, i.e.

$$R^{(E)}(\mathbf{x}, t) = \sum_n \langle a_n^2 \rangle \cdot \langle \exp\{-i\boldsymbol{\kappa}_n.\boldsymbol{\chi}_n(\boldsymbol{\kappa}_n, t)\}\rangle \bigg/ \sum_n \langle a_n^2 \rangle. \quad (A5)$$

Let us consider only one particular mode,

$$R_n^{(E)}(\mathbf{x}, t) = A_n \langle \exp\{-i\boldsymbol{\kappa}_n.\boldsymbol{\chi}_n(\boldsymbol{\kappa}_n, t)\}\rangle, \quad (A6)$$

where $A_n = \langle a_n^2 \rangle \big/ \sum_n \langle a_n^2 \rangle$. The average $\langle \exp(i\boldsymbol{\kappa}_n.\boldsymbol{\chi}_n) \rangle$ is calculated using the assumption that the random function $\mathbf{W}_n(t)$ is joint normal and therefore depends only on the second moment, i.e. $\langle \mathbf{W}_n.\mathbf{W}_n \rangle$ (Weinstock 1978). The characteristic functional of a joint normal distribution is

$$
\mathbf{Q}\left(\mathbf{q}(t)\right) = \left\langle \exp\left\{-i\int_{-\infty}^{\infty} \mathbf{W}_n(t).\mathbf{q}(t)\,dt\right\}\right\rangle
$$

$$
= \exp\left\{-\frac{1}{2}\int_{-\infty}^{\infty} \mathbf{q}(t_1).\left\langle \mathbf{W}_n(t_1).\mathbf{W}_n(t_2)\right\rangle \mathbf{q}(t_2)\,dt_1 dt_2\right\}. \qquad (A7)
$$

Substituting

$$
\mathbf{q}(t_1) = \boldsymbol{\kappa} \quad \text{for} \quad 0 < t_1 < t \qquad \text{and} \qquad \mathbf{q}(t_1) = 0 \qquad \text{otherwise}
$$

in (A7), we find

$$
\langle \exp\left\{-i\boldsymbol{\kappa}_n.\boldsymbol{\chi}_n(t)\right\}\rangle = \left\langle \exp\left[-i\boldsymbol{\kappa}.\int_0^t \mathbf{W}_n(t)\,dt\right]\right\rangle
$$

$$
= \exp\left[-\frac{1}{2}\int_0^t dt_1 \int_0^t dt_2 \boldsymbol{\kappa}_n.\left\langle \mathbf{W}_n(t_1).\mathbf{W}_n(t_2)\right\rangle.\boldsymbol{\kappa}_n\right]. \qquad (A8)
$$

The above equation can be put into a better form by introducing the mean-square random displacement of a fluid particle,

$$
\langle \boldsymbol{\chi}_n(\boldsymbol{\kappa}_n, t)\boldsymbol{\chi}_n(\boldsymbol{\kappa}_n, t)\rangle = \int_0^t dt_1 \int_0^t dt_2 \left\langle \mathbf{W}_n(t_1).\mathbf{W}_n(t_2)\right\rangle, \qquad (A9)
$$

as a new variable, also if one restrict to isotropic flow, then $\langle \boldsymbol{\chi}_n(\boldsymbol{\kappa}_n, t).\boldsymbol{\chi}_n(\boldsymbol{\kappa}_n, t)\rangle$ must be of the form

$$
\langle \boldsymbol{\chi}_n(\boldsymbol{\kappa}_n, t).\boldsymbol{\chi}_n(\boldsymbol{\kappa}_n, t)\rangle = 3\sigma^2_{\boldsymbol{\chi}_n(t)}.\mathbf{I}, \qquad (A10)
$$

where $\mathbf{I}$ is the identity tensor. Therefore substituting (A9), (A10) into (A6), we obtain

$$
R_n^{(E)}(\mathbf{x}, t) = A_n \exp\left\{-\frac{1}{2}k_n^2 \sigma^2_{\boldsymbol{\chi}_n(t)}\right\}. \qquad (A11)
$$

Because there are some similarities between these trajectories and those of microscopic particles under the action of Brownian motion, the changes in the velocity of the large eddies for each wavenumber k is, in homogeneous conditions, most simply modelled by the Langevin equation

$$
\frac{d\mathbf{W}_n}{dt} = -\frac{1}{T_n}\mathbf{W}_n + a_2\boldsymbol{\xi}_t, \qquad (A12)
$$

where the coefficient a_2 is to be specified by the physics of the process, $\mathbf{W}_n$ and T_n are the large eddy velocity and the time scale for the motion with wave number $\boldsymbol{\kappa}$ and $\boldsymbol{\xi}_t$ is a random function. This is a stochastic differential equation but can be manipulated formally in many respects like an ordinary differential equation.

In homogeneous turbulence, the solution to (A12) is simple, by taking the initial condition to be $\mathbf{W}_n(t=0) = \mathbf{W}_{n0}$, where $\mathbf{W}_{n0}$ is drawn from a three dimensional Gaussian distribution with zero mean and equal variance which has the value $\sigma^2_{\mathbf{W}_0} = \langle \mathbf{u}^n_\ell(\mathbf{x}, t)^2 \rangle$ where n denoted the n-th mode. It can be shown (Durbin 1980) that with this initial condition, $a_2 = [2\sigma^2_{\mathbf{W}_n}/T_n]^{1/2}$.

By integration of the random velocity $\mathbf{W}_n$, we obtain an expression for $\boldsymbol{\chi}_n$, i.e.

$$\boldsymbol{\chi}_n(\boldsymbol{\kappa}_n, t) = \int_0^t \mathbf{W}_n(t')\, dt', \tag{A13}$$

for a particular wavenumber $\boldsymbol{\kappa}_n$. Since $\mathbf{W}_n$ is normally distributed, $\boldsymbol{\chi}_n(\boldsymbol{\kappa}_n, t)$ is a Gaussian process, the so-called Ornstein-Uhlenbeck process.

It can be shown that (Arnold 1974)

$$\langle \boldsymbol{\chi}_n(\boldsymbol{\kappa}_n, t) \rangle = T_n(1 - e^{-t/T_n})\sigma_{\mathbf{W}_n} \tag{A14}$$

and

$$C_\chi(\boldsymbol{\kappa}, t, t') = \frac{1}{3} \langle \boldsymbol{\chi}_n(\boldsymbol{\kappa}_n, t) . \boldsymbol{\chi}_n(\boldsymbol{\kappa}_n, t') \rangle$$
$$= \sigma^2_{\mathbf{W}_n} T_n^2 \left\{ \frac{2}{T_n} t' - 1 + e^{t/T_n} + e^{t'/T_n} - e^{-(t-t')/T_n} \right\}. \tag{A15}$$

By letting $\Delta\boldsymbol{\chi}_n = \boldsymbol{\chi}_n(\boldsymbol{\kappa}_n, t') - \boldsymbol{\chi}_n(\boldsymbol{\kappa}_n, t)$, we have

$$\sigma^2_{\Delta\chi} = C_\chi(\boldsymbol{\kappa}, t, t) + C_\chi(\boldsymbol{\kappa}, t', t') - 2C_\chi(\boldsymbol{\kappa}, t, t')$$
$$= 2\sigma^2_{\mathbf{W}_n} T_n^2 \left\{ \frac{|t - t'|}{T_n} - 1 + e^{-t-t'/T_n} \right\}. \tag{A16}$$

Substituting (A16) into (A11) and let $t' = 0$, we obtain

$$R_n^{(E)}(\mathbf{x}, t) = A_n \exp \left\{ -k_n^2 \sigma^2_{\mathbf{W}_n} T_n^2 \left[\frac{|t|}{T_n} - 1 + e^{-|t|/T_n} \right] \right\}. \tag{A17}$$

If we assume that the turbulent velocity fields has a correlation decay time about one turn around time of a large eddy, i.e. $T_n = 1/\omega_n = 1/\sigma_{\mathbf{W}_n} k_n$, it has the property that the time scale decreases with increasing wave number, a well known property of turbulent flow. (It seem more natural, within the general context of the model, to relate the decay time of each component of the turbulence spectra to its respective wavenumber k rather than to use arbitrary constant

decay rate k_o, where k_o is the wavenumber often energy containing eddies.) Substituting (A17) into (A5), we have

$$R^{(E)}(\mathbf{x}, t) = \sum_{n=1}^{N} A_n \exp\left\{-\left[\sigma_{\mathbf{W}_n} k_n t - 1 + e^{-\sigma_{\mathbf{W}_n} k_n t}\right]\right\}. \tag{A18}$$

If we model the large scale eddies as described above, i.e. for each wavenumber k, it moves randomly with some random Gaussian velocity which is different for different k, then the Eulerian velocity correlation is given by

$$R^{(E)}(\mathbf{x}, t) = \sum_{n=1}^{N} A_n \exp\left\{-\frac{1}{2} k^2 \sigma_{\mathbf{W}_n}^2 t^2\right\}, \qquad \text{if} \qquad t \ll T_n \tag{A19}$$

and

$$R^{(E)}(\mathbf{x}, t) = \sum_{n=1}^{N} A_n \exp\left\{-k\sigma_{\mathbf{W}_n} t\right\}, \qquad \text{if} \qquad t \gg T_n. \tag{A20}$$

The corresponding stochastic differential equation of the Langevin equation (A12) is

$$d\mathbf{W}_n(t) = -\frac{\mathbf{W}_n(t)}{T_n} dt + \sigma_{\mathbf{W}_n} \left(\frac{2}{T_n}\right)^{1/2} d\xi_t, \tag{A21}$$

where $d\xi_t$ is a three dimension Gaussian, white-noise stochastic process with zero mean and variance dt. The Langevin equation models "memory" through the integral time scale T_n. Note that the acceleration is modelled as white noise ($d\xi_t$ is white noise).

If the subscript i denotes a value at the ith time step, then the discrete version of (A21) becomes the so-called Markov-chain Model used originally by Taylor (1921)

$$\mathbf{W}_{n(i+1)} = \left(1 - \frac{\Delta t}{T_n}\right) \mathbf{W}_{n(i)} + \sigma_{\mathbf{W}_n} \sqrt{\frac{2\Delta t}{T_n}} \mathbf{W}'_{n(i+1)}, \tag{A22}$$

with initial condition $\mathbf{W}_{n(0)} = \mathbf{W}_{n0}$ and $\mathbf{W}''$s are random vectors with zero mean and unit variance.

APPENDIX B: **Eulerian-Lagrangian velocity auto-correlation function**

To simulate the small scale eddies as well as the large scales, consider a set of small eddies moved by a random large scale velocity $\mathbf{u}_\ell(\mathbf{x}, t)$, then

$$\mathbf{u}_s(\mathbf{x}, t) = \sum_{n=-N}^{N} \mathbf{a}_n \exp i\left\{\boldsymbol{\kappa}_n \cdot \left(\mathbf{x} - \int_0^t \mathbf{u}_\ell(\mathbf{x}, t') \, dt'\right) + \omega'_n t\right\}, \tag{B1}$$

where ω'_n is the frequency in the advected frame, and is determined from the spectra (or structure function) which must be correct in a frame moving with $\mathbf{u}_\ell$.

Since the local fluid velocity $\mathbf{u}(\mathbf{x}, t)$ is mainly determined by the large eddies, it is relatively constant over the space-time region of $r \ll L$ and $\tau \ll L/|\mathbf{u}_\ell|$ (since $\mathbf{u}_\ell(\mathbf{x}, t)$ changes slowly with time). Therefore, over short times $\tau_L \ll \tau \ll T_L$, where $\tau_L \sim \mathrm{Re}^{-1/4} T_L$, the Eulerian-Lagrangian auto-correlation function of $\mathbf{u}_s(\mathbf{x}, t)$ in a frame moving with the large scale eddies has a form

$$R^{EL}(\tau) = \langle \mathbf{u}_s(\mathbf{x}(t), t).\mathbf{u}_s(\mathbf{x}(t+\tau), t+\tau) \rangle^{EL}$$

$$= \left\langle \mathbf{u}_s(\mathbf{x}, t).\mathbf{u}_s \left(\mathbf{x} + \int_t^{t+\tau} \mathbf{u}_\ell(\mathbf{x}, t) \, dt, t+\tau \right) \right\rangle^{EL}$$

$$= \sum_{n=-N}^{N} \sum_{m=-N}^{N} \langle \mathbf{a}_n.\mathbf{a}_m^* \rangle e^{i\omega_n' \tau}$$

$$= 2 \sum_{n=N_c}^{N_\eta} \langle |\mathbf{a}_n|^2 \rangle e^{i\omega_n' \tau}, \tag{B2}$$

we have used the condition that the modes are independent of each other, i.e. $\langle \mathbf{a}_n.\mathbf{a}_m^* \rangle = \delta_{mn}$. This represents an average over the motion of scale small compared with L only. If we let

$$\omega_n' = \lambda \varepsilon^{1/3} k_n^{2/3} , \tag{B3}$$

where λ is a constant of proportion and of order unity. This is the 'natural' eddy time scale introduced by Edwards (1964) – see Leslie (1973). We will show that such choice of ω_n is consistent with the Eulerian-Lagrangian result of $R_{11}^{EL}(\tau) = \langle u_1^2 \rangle - 2\pi C_{11}^{EL} \varepsilon \tau$, where ε is the dissipation of turbulent kinetic energy per unit mass and C_{11}^{EL} is a constant.

By letting $k_n = n k_c \ \omega_n' = \lambda \varepsilon^{1/3} k_c^{2/3} n^{2/3}$, we have

$$R^{EL}(\tau) = 2A \sum_{n=N_c}^{N_\eta} n^{-5/3} \exp(in^{2/3} p), \tag{B4}$$

where $p = \lambda \varepsilon^{1/3} k_c^{2/3} \tau$ and $A = \alpha_k \varepsilon^{2/3} k_c^{-2/3}$. To compute the sum in (B4), we assume n/n_c is large so that the finite sum reduces to an integral, i.e.

$$R^{EL}(\tau) = 2A \int_{n_c}^{n_\eta} n^{-5/3} e^{in^{2/3} p} \, dn.$$

Let $q = pn^{2/3}$, then

$$R^{EL}(\tau) = 3Ap \int_{q_o}^{q_\eta} q^{-2} e^{iq} \, dq$$

$$\approx \langle u_s^2 \rangle - \frac{3}{2} \pi \alpha_k \lambda \varepsilon \tau + 3\alpha_k \lambda^2 \varepsilon^{4/3} k_c^{2/3} \tau^2 - 6\alpha_k \varepsilon^{2/3} k_\eta^{-2/3} \cos(\omega_\eta \tau).$$

In idealised model of turbulence with $k_c \to 0$ and $k_\eta \to \infty$, R^{EL} reduces to

$$\approx \langle u_s^2 \rangle - \pi C^{EL} \varepsilon \tau, \tag{B5}$$

where $q_c = pn_c^{2/3}$ and $C^{EL} \approx 3\alpha_k \lambda/2$.

If we define $\mathbf{u}_s(\mathbf{x}, t)$ as scales *less* than, say, $10t^{3/2}\varepsilon^{1/2}$, and from the similarity law, $\varepsilon \sim u_s^3/\ell_s \sim u_s^2/\tau$, then the displacement due to the small scales eddies in time τ is

$$\mathbf{x}_s = \int_0^\tau \mathbf{u}_s(\mathbf{x}, t') \, dt' \sim O\left(\tau \varepsilon^{1/3} \ell_s^{1/3}\right) \sim O\left(\tau^{3/2} \varepsilon^{1/2}\right). \tag{B6}$$

Now consider the Lagrangian velocity correlation function of $\mathbf{u}_s(\mathbf{x}, t)$, along the fluid element trajectories, i.e.

$$\begin{aligned}
R^L(\tau) &= \langle \mathbf{u}_s(t).\mathbf{u}_s(t+\tau)\rangle^L \\
&= \langle \mathbf{u}_s(\mathbf{x}, t).\mathbf{u}_s(\mathbf{x}+\mathbf{x}_L+\mathbf{x}_s, t+\tau)\rangle^E \\
&= R^{EL}(\tau) + \Delta R^L,
\end{aligned} \tag{B7}$$

where ΔR^L is the difference in the correlation between A^L and A and A^{EL} and A (the dispersive due to small scale correction), i.e.

$$\Delta R^L = \langle \mathbf{u}_s(\mathbf{x}, t).\mathbf{u}_s(\mathbf{x}+\mathbf{x}_L+\mathbf{x}_s, t+\tau)\rangle - \langle \mathbf{u}_s(\mathbf{x}, t).\mathbf{u}_s(\mathbf{x}+\mathbf{x}_L, t+\tau)\rangle.$$

Assuming

$$\Delta R^L \leq |\langle \mathbf{u}_s(\mathbf{x}, t).\mathbf{u}_s(\mathbf{x}+\mathbf{x}_L+\mathbf{x}_s, t)\rangle - \langle \mathbf{u}_s(\mathbf{x}, t).\mathbf{u}_s(\mathbf{x}+\mathbf{x}_L, t)\rangle|,$$

then from (B6), we have

$$\Delta R^L \sim (|\mathbf{x}_s|^{2/3}\varepsilon^{2/3})^{1/2}(\varepsilon\ell_s)^{1/3} \sim (\tau^{1/2}\varepsilon^{1/6+1/3})^2 \sim \varepsilon\tau. \tag{B8}$$

Therefore, we have

$$R^L(\tau) = \langle \mathbf{u}_s^2 \rangle - \pi C^L \varepsilon \tau, \tag{B9}$$

where $C^L \sim C^{EL}$.

APPENDIX C: **Test the sensitivity of the assumptions and statistical variability**

When two or more simulations are performed with identical parameters (k_c, $k_{\max}$, no. of modes, etc.) but with different random numbers used in the simulations, then some statistical variability between the simulation is expected.

The standard deviation of the sampling distribution of a statistic such as the mean or a proportion is often used as a measure of the reliability of the statistic. Suppose there exists a random process θ whose mean value M we want to compute. We denote a random sample of

N independent realisations of the process θ by $\{\alpha_i, \quad i = 1, 2, \ldots N\}$. Then the mean and the standard deviations are given by

$$M = \langle \alpha_i \rangle \quad \text{and} \quad \sigma^2 = \langle [\alpha_i - M]^2 \rangle \tag{C1}$$

respectively, where $\langle \ \rangle$ denotes ensemble average. Let the average $\overline{\theta_N}$ be defined by

$$\overline{\theta_N} = \frac{1}{N} \sum_{i=1}^{N} \alpha_i. \tag{C2}$$

Note that $\overline{\theta_N}$, the sum of a finite number of random function, is itself a random function. Its mean, M_N, is given by $M_N = \langle \overline{\theta_N} \rangle$, with its standard deviation, σ_N, is

$$\sigma_N^2 = \left\langle \left[\overline{\theta_N} - M \right]^2 \right\rangle = \sigma^2 / N. \tag{C3}$$

The average $\overline{\theta_N}$ will be used to approximate M, so the random error involve, $e_N = \overline{\theta_N} - M$, is approximately normally distributed (since $\overline{\theta_N}$ is the sum of independent, identically distributed event, by the Central Limit Theorem, as $N \to \infty$, the pdf is normal). The standard error of the mean is of particular interest. It can be easily shown that $\text{Var}(\overline{\theta_N}) = \sigma^2 / N$, and the standard error of the mean in a random sample of size N is $\sigma / \sqrt{N}$. And the standard deviation of these α_i was found from

$$\sigma^2 = \frac{1}{N-1} \sum_{i=1}^{N} \left(\alpha_i - \overline{\theta_N} \right)^2 \tag{C4}$$

(the divisor $N - 1$ is often called the degree of freedom on which the estimated variance is based).

In order to gauge the extent of this variability, six simulations $\{\alpha_i, \quad i = 1, 2, \ldots, 6\}$, with identical parameters, but with different initial random numbers, were studied, and the degree of uncertainty after averaging over the six simulations is determined via the standard deviation. In other words, for a control flow the mean $\overline{\theta_6}$ had an expected standard deviation of $\overline{\theta_6}/\sqrt{5}$.

Addition studies were made with slightly different assumptions about the trajectory calculation method, with the purpose of checking the sensitivity of the method to these various assumptions. By making successive estimates, $\{\alpha_i, \quad i = 1, 2, \ldots, 6\}$, of the quantity, each based on a different control run of 15 realisations (i.e. 405 particles). The error expected in evaluating each of these quantities can then be found. This enabled comparison to be made between the computed quantities of the test runs and that of the control.

Description	$\langle x^2 \rangle$	$\sigma_{\langle x^2 \rangle}$	T_L	σ_{T_L}
Control	2.2473	0.0235	0.5180	0.0007
$\Delta t = 0.015$	2.4536	0.0364	0.5832	0.0087
$\Delta t = 0.00375$	2.2398	0.0134	0.5100	0.0043
$k_c = 5.0$, $k_{\max} = 100$	2.2622	0.0097	0.5273	0.0007
$k_c = 5.0$, $k_{\max} = 25$	2.2213	0.0027	0.5130	0.0018
$k_c = 10.0, k_{\max} = 50$	2.2391	0.1032	0.4810	0.0066
$k_c = 2.5$, $k_{\max} = 50$	2.4067	0.0329	0.5280	0.0066
$\text{Modes}_{u_\ell} = 6$ and $\text{Modes}_{u_s} = 16$	2.2133	0.0363	0.4863	0.0015
$\text{Modes}_{u_\ell} = 6$ and $\text{Modes}_{u_s} = 64$	2.2133	0.0788	0.5163	0.0043
$\text{Modes}_{u_\ell} = 3$ and $\text{Modes}_{u_s} = 32$	2.2083	0.0144	0.5113	0.0358
$\text{Modes}_{u_\ell} = 12$ and $\text{Modes}_{u_s} = 32$	2.3833	0.0336	0.5247	0.0033

Table C1.

$\langle x^2 \rangle$ is the mean square displacement of the fluid point and T_L is the Lagrangian integral time scale of the flow.

The parameters which it was decided to examine were the mean square displacement $\langle x^2 \rangle$ and the Lagrangian integral time scale T_L of the flow. The mean square displacement was evaluated at $t = 3$ where any divergence between methods would most likely be maximised and the Lagrangian integral time scale was evaluated when it reaches its asymptotic value (This was done by plotting $\langle x^2 \rangle$ against t; by the theory of Taylor (1921), this curve should asymptote to $2 \langle u^2 \rangle T_L t$). The results of the analysis are presented in table C1. The first row of data represent the control flow. (i.e. $\Delta t = 0.0075$, $\text{Modes}_{u_\ell} = 6$, $\text{Modes}_{u_s} = 32$, $k_c = 5.0$, $k_{\max} = 5.0$.). Besides each variable is its estimated statistical uncertainty.

First, we doubled the time step of integration and shows that this change of mean square displacement $\langle x^2 \rangle$ and the Lagrangian time scale T_L are considerable. i.e. a discrepancy well beyond the error bounds. These results are shown in row two.

The third row is the results of a test with Δt reduced to the half of the time step of the control run. The differences in comparison with the control run is small. This indicated that the chosen time-step of integration $\Delta t = 0.0075$ was small enough not to influence the evaluation of the quantities of interest.

In order to test the sensitivity of the choice of $k_{\max}$, two runs with half and double the size of $k_{\max}$ was computed and the results shows that the changes of the mean square displacement and the Lagrangian integral time scale are small and thus we conclude that the dependence on $k_{\max}$ was small, this results shows in row 4 and 5.

Two runs with half and double the size of the critical wavenumber k_c was computed and in comparison with the control run, the different is considerable. By doubling the size of k_c, the mean square displacement of the fluid point is less compared with that of the control and also the Lagrangian integral time scale is approximately 10% less than that of control. By reducing the size of k_c to half, we obtain the opposite trend. This indicates that the dispersion strongly depends on the ratio of energy between the energy containing and the small scale eddies. In other words, it depends on how fast does the small eddies being advected by the large eddies.

Finally, the test of the variation with the mode density also being investigated. If the number of modes were infinite so that the discretised version of the velocity field might closely approximate the analytic, continuous version of the velocity field. However, because of the computational cost, a minimum number of modes was required to represent as closely as possible to the modelled velocity field. We have chosen $\text{Modes}_{u_\ell} = 6$ and $\text{Modes}_{u_s} = 32$, this was justified by, first we reduce the number of modes in half in the small scale and the difference was considerable; by doubling the number of modes to 64, there were hardly any difference compared with the control run. From the evidence presented above, it does seem that variation with mode density in the small scale is probably weak provided the 'minimum' number of modes were chosen, i.e. as in the control run. Secondly, two runs with half and double the number of modes in the large scales, there is a small difference both in the $\langle x^2 \rangle$ and T_L in the simulations, the results are by decreasing the number of modes in the large scale motion, both $\langle x^2 \rangle$ and T_L decrease whereas by increasing that the opposite trend occurs. This evidence suggests that both the $\langle x^2 \rangle$ and T_L are, to a degree, sensitive to the number of mode being used to model the large scale. This can readily be explained that since there is no universal characteristic in this range, and it has more energy than in the small scale.

We conclude that within the stated limited of statistical uncertainty, the quantities $\langle x^2 \rangle$ and T_L, derived here using the modelled velocity field, are not sensitive to the particular assumption made.

APPENDIX D: **The stability and the error estimation of PC method**

To study stability, we write

$$\mathbf{x}_n = \mathbf{x}(t_n) + \mathbf{e}_n,$$

$$h\mathbf{x}'_n = h\mathbf{x}'(t_n) + \mathbf{f}_n,$$

$$\frac{1}{2}h^2\mathbf{x}''_n = \frac{1}{2}h^2\mathbf{x}_n''(t_n) + \mathbf{g}_n, \qquad (D1)$$

$$\mathbf{x}_n^{(p)} = \mathbf{x}(t_n) + \mathbf{e}_n^{(p)},$$

$$\mathbf{u}_n^{(p)} = \mathbf{u}\left(\mathbf{x}(t_n), t_n\right) + \eta \mathbf{e}_n^{(p)}.$$

We also set

$$\boldsymbol{\psi}_3 = h^3 \mathbf{x}_{n-\frac{1}{2}}''' \,, \qquad \boldsymbol{\psi}_4 = h^4 \mathbf{x}_{n-\frac{1}{2}}^{(iv)} \,, \tag{D2}$$

and

$$\theta = h^2 \eta \Big/ \left(\tau_p + \frac{1}{2}h\right), \qquad \phi = h \Big/ \left(\tau_p + \frac{1}{2}h\right). \tag{D3}$$

We note that, because of the trigonometric terms in $\mathbf{u}$, η (and therefore θ) is typically of the form $b \cos(\ )$. If $\mathbf{u}$ contains a term $\mathbf{a} \sin\left[\boldsymbol{\kappa}.(\mathbf{x} + \mathbf{X}(t)) + \alpha\right]$, then

$$\theta = \frac{h^2 \mathbf{a}.\boldsymbol{\kappa}}{\tau_p + \frac{1}{2}h} \cos\left[\boldsymbol{\kappa}.(\mathbf{x} + \mathbf{X}(t)) + \alpha\right].$$

The true solution satisfies

$$\mathbf{x}(t_n) = \mathbf{x}(t_{n-1}) + h\mathbf{x}'(t_{n-1}) + \frac{1}{2}h^2\mathbf{x}''(t_{n-1})$$

$$+ \frac{1}{6}\left(\boldsymbol{\psi}_3 - \frac{1}{2}\boldsymbol{\psi}_4\right) + \frac{1}{24}\boldsymbol{\psi}_4 + O(h^5), \tag{D4}$$

so that neglecting terms $O(h^5)$,

$$\mathbf{e}_n^{(p)} = \mathbf{e}_{n-1} + \mathbf{f}_{n-1} + \mathbf{g}_{n-1} - \frac{1}{6}\boldsymbol{\psi}_3 + \frac{1}{24}\boldsymbol{\psi}_4 \,. \tag{D5}$$

Also

$$h\mathbf{x}'(t_n) = h\mathbf{x}'(t_{n-1}) + \frac{1}{2}h^2\left(\mathbf{x}''(t_n) + \mathbf{x}''(t_{n-1})\right) - \frac{1}{12}\boldsymbol{\psi}_4 + O(h^6), \tag{D6}$$

and

$$\mathbf{x}(t_n) = \mathbf{x}(t_{n-1}) + \frac{1}{2}h\left(\mathbf{x}'(t_n) + \mathbf{x}'(t_{n-1})\right) - \frac{1}{12}\boldsymbol{\psi}_3 + O(h^5)$$

$$= \mathbf{x}(t_{n-1}) + \frac{1}{2}h\left(\mathbf{x}'(t_n) + \mathbf{x}'(t_{n-1})\right) - \frac{1}{12}h^2\left(\mathbf{x}''(t_n) - \mathbf{x}''(t_{n-1})\right) + O(h^5), \tag{D7}$$

so that from (3.5.4a) and (D5)

$$2\tau_p \mathbf{g}_n + h\mathbf{f}_n - h^2\eta\left(\mathbf{e}_{n-1} + \mathbf{f}_{n-1} + \mathbf{g}_{n-1} - \frac{1}{6}\boldsymbol{\psi}_3 + \frac{1}{12}\boldsymbol{\psi}_4\right) = 0, \tag{D8}$$

and from (3.5.4b) and (D4)

$$\mathbf{f}_n - \mathbf{f}_{n-1} - \mathbf{g}_n - \mathbf{g}_{n-1} - \frac{1}{12}\boldsymbol{\psi}_4 = 0. \tag{D9}$$

Solving these gives

$$\mathbf{f}_n = \left(\tau_p + \frac{1}{2}h\right)^{-1}\left\{\frac{1}{2}h^2\eta\,\mathbf{e}_{n-1} + \left(\tau_p + \frac{1}{2}h^2\eta\right)(\mathbf{f}_{n-1} + \mathbf{g}_{n-1})\right.$$

$$\left. - \frac{1}{12}h^2\eta\,\boldsymbol{\psi}_3 - \frac{1}{12}\left(\tau_p - \frac{1}{4}h^2\eta\right)\boldsymbol{\psi}_4\right\},\tag{D10}$$

and

$$\mathbf{g}_n = \left(\tau_p + \frac{1}{2}h\right)^{-1}\left\{\frac{1}{2}h^2\eta\,\mathbf{e}_{n-1} + \left(\frac{1}{2}h^2\eta - \frac{1}{2}h\right)(\mathbf{f}_{n-1} + \mathbf{g}_{n-1})\right.$$

$$\left. - \frac{1}{12}h^2\eta\,\boldsymbol{\psi}_3 - \frac{1}{24}\left(h - \frac{1}{2}h^2\eta\right)\boldsymbol{\psi}_4\right\},\tag{D11}$$

Substituting these into the equation for $\mathbf{e}_n$, from (3.5.3a or b) and (D7)

$$\mathbf{e}_n = \mathbf{e}_{n-1} + \frac{1}{2}(\mathbf{f}_n + \mathbf{f}_{n-1}) + \frac{1}{12}\boldsymbol{\psi}_3 \,,\tag{D12a}$$

or

$$\mathbf{e}_n = \mathbf{e}_{n-1} + \frac{1}{2}(\mathbf{f}_n + \mathbf{f}_{n-1}) - \frac{1}{6}(\mathbf{g}_n - \mathbf{g}_{n-1}),\tag{D12b}$$

gives finally

$$\mathbf{e}_n = (1 + c\theta)\mathbf{e}_{n-1} + (1 + c(\theta - \phi))\,\mathbf{f}_{n-1} + (d + c(\theta - \phi))\,\mathbf{g}_{n-1} + \boldsymbol{\delta}\,,\tag{D13}$$

$$\mathbf{f}_n = \frac{1}{2}\theta\mathbf{e}_{n-1} + \left(1 + \frac{1}{2}(\theta - \phi)\right)\mathbf{f}_{n-1} + \left(1 + \frac{1}{2}(\theta - \phi)\right)\mathbf{g}_{n-1}$$

$$- \frac{1}{12}\theta\boldsymbol{\psi}_3 - \frac{1}{12}\left(1 - \frac{1}{4}\theta - \frac{1}{2}\phi\right)\boldsymbol{\psi}_4\,,\tag{D14}$$

and

$$\mathbf{g}_n = \frac{1}{2}\theta\mathbf{e}_{n-1} + \frac{1}{2}(\theta - \phi)\mathbf{f}_{n-1} + \frac{1}{2}(\theta - \phi)\mathbf{g}_{n-1} - \frac{1}{12}\theta\boldsymbol{\psi}_3 - \frac{1}{24}\left(\phi - \frac{1}{2}\theta\right)\boldsymbol{\psi}_4\,,\tag{D15}$$

where for case a

$$c = \frac{1}{4}, \qquad d = \frac{1}{2}, \qquad \boldsymbol{\delta} = \frac{1}{12}\left(1 - \frac{1}{2}\theta\right)\boldsymbol{\psi}_3 - \frac{1}{24}\left(1 - \frac{1}{4}\theta - \frac{1}{2}\phi\right)\boldsymbol{\psi}_4\,,\tag{D16}$$

or for case b

$$c = \frac{1}{6}, \qquad d = \frac{2}{3}, \qquad \boldsymbol{\delta} = -\frac{1}{36}\theta\boldsymbol{\psi}_3 - \frac{1}{24}\left(1 - \frac{1}{6}\theta - \frac{2}{3}\phi\right)\boldsymbol{\psi}_4\,.\tag{D17}$$

We use these equations in two ways. First, setting $\boldsymbol{\psi}_3 = \boldsymbol{\psi}_4 = 0$, we study the stability of the method. Secondly, we take θ to be slowly varying and seek a solution with $(\mathbf{e}, \mathbf{f}, \mathbf{g}) = (\mathbf{e}_n, \mathbf{f}_n, \mathbf{g}_n) = (\mathbf{e}_{n-1}, \mathbf{f}_{n-1}, \mathbf{g}_{n-1})$ in order to get error estimates.

For the stability investigation we first take $\theta = 0$, then estimate the perturbation from a small θ. We need the eigenvalues of the matrix

$$A = \begin{pmatrix} 1 + c\theta & 1 + c(\theta - \phi) & d + c(\theta - \phi) \\ \frac{1}{2}\theta & 1 + \frac{1}{2}(\theta - \phi) & 1 + \frac{1}{2}(\theta - \phi) \\ \frac{1}{2}\theta & \frac{1}{2}(\theta - \phi) & \frac{1}{2}(\theta - \phi) \end{pmatrix} . \tag{D18}$$

For $\theta = 0$, A is reducible, with an eigenvalue 1 corresponding to the eigenvector $\begin{pmatrix} 1 \\ 0 \\ 0 \end{pmatrix}$.

The other eigenvalues are those of the submatrix

$$B = \begin{pmatrix} 1 - \frac{1}{2}\phi & 1 - \frac{1}{2}\phi \\ -\frac{1}{2}\phi & -\frac{1}{2}\phi \end{pmatrix} , \tag{D19}$$

which are 0 and $1 - \theta$. The corresponding eigenvectors of B are

$$\begin{pmatrix} 1 - d \\ -1 \\ 1 \end{pmatrix} \quad \text{and} \quad \begin{pmatrix} 1 + \frac{1}{2}d\phi \\ -\phi + \frac{1}{2}\phi^2 \\ -\frac{1}{2}\phi^2 \end{pmatrix} .$$

The latter is nearly parallel to $\begin{pmatrix} 1 \\ 0 \\ 0 \end{pmatrix}$, and its eigenvalue $1 - \phi$ is close to 1, so the matrix is nearly defective; in the limit $\phi \to 0$, it is defective.

This makes the eigenvalues very sensitive to perturbation. Clearly perturbations of the eigenvalue close to 1 are most likely to lead to instability, so we seek eigenvalues of the form $(1 + \epsilon)$ with vectors whose first component is the largest one. Ignoring higher powers of θ and ϕ, we find that the eigenvector must be $\begin{pmatrix} 1 \\ \theta/\left(\epsilon + \frac{1}{2}(\theta - \phi)\right) \\ \frac{1}{2}\theta \end{pmatrix}$ approximately, and that the

determinant of

$$\begin{pmatrix} c\theta - \epsilon & 1 + c(\theta - \phi) & d + c(\theta - \phi) \\ \frac{1}{2}\theta & \frac{1}{2}(\theta - \phi) - \epsilon & 1 + \frac{1}{2}(\theta - \phi) \\ \frac{1}{2}\theta & \frac{1}{2}(\theta - \phi) & \frac{1}{2}(\theta - \phi) - 1 - \epsilon \end{pmatrix} ,$$

must vanish. Subtract the third row from the second to get

$$\begin{pmatrix} c\theta - \epsilon & 1 + c(\theta - \phi) & d + c(\theta - \phi) \\ 0 & -\epsilon & 2 + \epsilon \\ \frac{1}{2}\theta & \frac{1}{2}(\theta - \phi) & \frac{1}{2}(\theta - \phi) - 1 - \epsilon \end{pmatrix} .$$

Now subtract $1 - \phi/\theta$ times the first column from the second and third, to get

$$\begin{pmatrix} c\theta - \epsilon & 1 + \left(1 + \frac{\phi}{\theta}\right)\epsilon & d + \left(1 - \frac{\phi}{\theta}\right)\epsilon \\ 0 & -\epsilon & 2 + \epsilon \\ \frac{1}{2}\theta & 0 & -1 - \epsilon \end{pmatrix} ,$$

of which the determinant is

$$\epsilon^3 + \epsilon^2(1 - c\theta - \theta + \phi) + \epsilon\left(\frac{3 + d}{2} + \phi - c\theta\right) - \theta = 0 \ .$$

For small ϵ, we must have $\epsilon^2 - \theta \approx 0$, all other terms then being of order $\theta^{3/2}$. Thus the eigenvalues near 1 are perturbed to $1 \pm \sqrt{+\theta}$ approximately.

For $\theta = \dfrac{h^2 \mathbf{a}.\boldsymbol{\kappa}}{\tau_p + \frac{1}{2}h} \cos\left[\boldsymbol{\kappa}.(\mathbf{x} + \mathbf{X}(t)) + \alpha\right]$, and since $\mathbf{X}(t)$ varies slowly with time, thus

$$\left|1 + \sqrt{+\theta}\right| \approx 1 + h\sqrt{\frac{\mathbf{a}.\boldsymbol{\kappa}}{\tau_p}\cos\left[\boldsymbol{\kappa}.(\mathbf{x} + \mathbf{X}(t)) + \alpha\right]} \ .$$

Thus there is an error mode growing like

$$\exp\left\{t\sqrt{\frac{\mathbf{a}.\boldsymbol{\kappa}}{\tau_p}\cos\left[\boldsymbol{\kappa}.(\mathbf{x} + \mathbf{X}(t)) + \alpha\right]}\right\} \ ,$$

approximately.

This imposes a limit on the range of t over which error are expected to remain small. Turning now to the error estimation, we must have (in the steady state)

$$(A - I)\begin{pmatrix} \mathbf{e} \\ \mathbf{f} \\ \mathbf{g} \end{pmatrix} + \begin{pmatrix} \boldsymbol{\delta} \\ \beta \\ \gamma \end{pmatrix} \ , \tag{D20}$$

where

$$\beta = -\frac{1}{12}\theta\psi_3 - \frac{1}{12}\left(1 - \frac{1}{4}\theta - \frac{1}{2}\phi\right)\psi_4 \ ,$$

$$\gamma = -\frac{1}{12}\theta\psi_3 - \frac{1}{24}\left(\phi - \frac{1}{2}\phi\right)\psi_4 \ . \tag{D21}$$

Subtracting the third row from the second gives

$$2\mathbf{g} + \beta - \gamma = 0 \ , \tag{D22}$$

whence

$$\mathbf{g} = \frac{1}{24}\psi_4(1 - \phi) \ . \tag{D23}$$

It is noteworthy that this does not involve ψ_3, so that the error in $\mathbf{x}''$ is of order h^2, rather than h as it might have been. Subtracting $2c$ times the third row from the first gives

$$\mathbf{f} + (d + 2c)\mathbf{g} = -(\boldsymbol{\delta} - 2c\gamma) \ , \tag{D24}$$

so that

$$\mathbf{f} = -\left[\delta - 2c\gamma + \frac{1}{24}\psi_4(1-\phi)(d+2c)\right],$$

for case a

$$= \frac{1}{24}\psi_4\left[1 - \frac{1}{4}\phi - \frac{1}{2}\phi - (1-\phi) - \frac{1}{2}\phi + \frac{1}{4}\theta\right] - \frac{1}{12}\psi_3$$

$$= -\frac{1}{12}\psi_3, \qquad (D25a)$$

for case b

$$= \frac{1}{24}\psi_4\left[1 - \frac{1}{6}\theta - \frac{2}{3}\phi - (1-\phi) - \frac{1}{3}\phi + \frac{1}{6}\theta\right]$$

$$= 0. \qquad (D26b)$$

Thus in case a the error in $\mathbf{x}'$ is of order $h^2\mathbf{x}'''/12$, but in case b it is of order h^4, so case b is clearly superior. In either case we find $\mathbf{e}$ from the third equation. It is of order h^3, so we ignore the terms in ψ_4, obtaining

$$\mathbf{e} = -\frac{1}{6}\psi_3 - \left(1 - \frac{\phi}{\theta}\right)\mathbf{f},$$

for case a

$$= -\frac{1}{12}\left(1 + \frac{\phi}{\theta}\right)\psi_3, \qquad (D27a)$$

for case b

$$= -\frac{1}{6}\psi_3. \qquad (D27b)$$

Again case (b) is better, since ϕ/θ is of order h^{-1}, making $\mathbf{e}$ of order h^2 instead of h^3. We note that in case b, if $\mathbf{e}_{n-1} \approx -\frac{1}{6}\psi_3$, then $\mathbf{f}_{n-1} \approx 0 \approx \mathbf{g}_{n-1}$, then $\mathbf{e}_n^{(p)} \approx 0$, thus explaining the high accuracy. In practice, at the start of a range we shall have $\mathbf{e}_o = \mathbf{f}_o = \mathbf{g}_o = 0$, giving

$$\mathbf{e}_1 = \delta \approx -\frac{1}{36}\theta\psi_3, \qquad \mathbf{f}_1 \approx -\frac{1}{12}\theta\psi_3 \approx \mathbf{g}_1,$$

so the steady state will not be obtained. Nevertheless, it seems worthwhile to use method b.

Returning to the unstable eigenvalue $1 + \sqrt{\dfrac{\mathbf{a}.\boldsymbol{\kappa}}{\tau_p}}\,\cos[\boldsymbol{\kappa}.(\mathbf{x} + \mathbf{X}(t)) + \alpha]$ approximately, the corresponding eigenvector is

$$\begin{pmatrix} \mathbf{e} \\ \mathbf{f} \\ \mathbf{g} \end{pmatrix} \propto \begin{pmatrix} 1 \\ h\sqrt{\dfrac{\mathbf{a}.\boldsymbol{\kappa}}{\tau_p}}\,\cos[\boldsymbol{\kappa}.(\mathbf{x}+\mathbf{X}(t))+\alpha] \\ \dfrac{h^2\mathbf{a}.\boldsymbol{\kappa}}{2\tau_p}\,\cos[\boldsymbol{\kappa}.(\mathbf{x}+\mathbf{X}(t))+\alpha] \end{pmatrix},$$

and we expect this to be the dominant error mode after a number of steps. We have already seen that $\mathbf{e} = -\frac{1}{6}\boldsymbol{\psi}_3$ is a plausible estimate for method b, so we may expect the maximum error in the velocity to be of order

$$\left| h^{-1}\mathbf{f} \right| \approx \left(\frac{\mathbf{a.\kappa}}{\tau_p} \right)^{\frac{1}{2}} \left| \frac{1}{6}\boldsymbol{\psi}_3 \right| = \left(\frac{\mathbf{a.\kappa}}{\tau_p} \right)^{\frac{1}{2}} \left| \frac{1}{6}h^3\mathbf{x}''' \right|.$$

All this is on the assumptions that linearisation is justified, i.e. that $|\boldsymbol{\kappa}.\mathbf{e}| \ll 1$, that the exponential error growth is not severe, i.e. $t\sqrt{\mathbf{a.\kappa}/2\tau_p}$ is moderate, and that maximum $|\theta| \approx h^2\mathbf{a.\kappa}/\tau_p$ is small.